Time-gated detection of near-infrared emitting quantum dots for in vivo cell tracking

Sophie Bouccara

THÈSE DE DOCTORAT

présentée par

Sophie BOUCCARA

pour l'obtention du grade de

Docteur de l'UNIVERSITÉ PARIS DIDEROT (Paris 7)

ÉCOLE DOCTORALE FRONTIÈRE DU VIVANT

Specialité: Physique du vivant

Laboratoire de Physique et d'Étude des Matériaux

Time-gated detection of near-infrared emitting quantum dots for *in vivo* cell tracking in small animals

soutenue le 22 septembre 2014

devant le jury constitué de :

Mme.	**Sandrine LÉVÊQUE-FORT**	Rapporteur
M.	**Stéphane PETOUD**	Rapporteur
Mme.	**Geneviève BOURG-HECKLY**	Examinateur
M.	**Frédéric DUCONGÉ**	Examinateur
M.	**François TREUSSART**	Examinateur
M.	**Paul FRENCH**	Examinateur
Mme.	**Alexandra FRAGOLA**	Invitée
M.	**Vincent LORIETTE**	Directeur de thèse

Remerciements

Je pense que la partie “Remerciements” est la partie la plus difficile à écrire dans un manuscrit de thèse. Je remercie tous ceux qui m'ont permis de mener cette thèse en espérant n'oublier personne.

J'aimerais commencer par remercier les membres de mon jury. Merci à Sandrine Lévêque-Fort et Stéphane Petoud d'avoir accepté de rapporter ma thèse. Je remercie Sandrine Lévêque-Fort de m'avoir suivie tout au long de ma thèse, merci pour les discussions autours du time-gated et le coaching professionnel dans le bus d'ELMI. Merci Stéphane Petoud d'avoir trouvé autant d'intérêt au travail que j'ai fourni. Je remercie aussi Frédéric Ducongé qui m'a également suivie tout au long de ma thèse. Je te remercie pour les discussions que nous avons pu avoir et surtout pour ton expertise en biologie durant les “Thesis Advisory Committees”. Merci à Paul French d'être venu de Londres pour assister à ma soutenance et merci pour les échanges que nous avons pu avoir. Merci à François Treussart d'avoir accepté d'examiner ma thèse et merci pour les remarques scientifiques intéressantes que vous avez fournies le jour de la soutenance. Un merci particulier à la présidente du jury Geneviève Bourg-Heckly qui m'a donné le goût de la recherche biomédicale et qui a été pour moi un modèle scientifique tout au long de mes études universitaires.

Ma thèse n'aurait pas été possible sans Alexandra Fragola. Merci Alexandra d'avoir eu confiance en moi et d'avoir pensé ce sujet qui m'a tant passionnée. C'est grâce à toi que j'ai pu découvrir ce laboratoire et cet environnement scientifique que j'ai adoré. Merci pour les discussions scientifiques et le rôle de maman que tu as si bien tenu pendant ces dernières années. Merci à Vincent Loriette, mon directeur de thèse pour qui l'optique n'a aucun secret. Merci d'avoir accepté de me prendre en thèse alors que tu ne croyais pas au sujet. J'espère que ce sujet t'a donné envie de commencer une carrière en synthèse de quantum dots. Merci à Thomas Pons pour ta présence et ton excellence scientifique. J'ai eu énormément

de chance de travailler avec toi, c'était un véritable plaisir et cela va beaucoup me manquer. Merci à Nicolas Lequeux pour ton savoir en matière de ligands, ton sens de l'humour et tes critiques sur ma façon de m'habiller qui m'ont, dans le fond, souvent amusées. Merci à Sandrine Ithurria Lhuillier pour nos discussions de commérage, j'ai jamais vu une commère comme toi. Merci à Benoît Dubertret de m'avoir accueillie dans son équipe. Merci à Ivan Maksimovic pour ton humour sarcastique qui m'a fait tant rire. Merci à Xiangzhen Xu pour les heures passées au TEM.

J'aimerais remercier maintenant mes co-bureaux. Je dois bien sûr commencer par mon binôme de thèse Gary Sitbon sans qui ma thèse n'aurait pas été aussi belle. Merci Gary d'avoir supporté mon stress, mes humeurs, mon bordel et merci d'être devenu l'ami que tu es. Tu es quelqu'un de génial ne l'oublie pas s'il te plait. Merci Emerson Giovanelli pour tes conseils et ton excellente pédagogie en chimie, heureusement que tu es patient. Merci pour tes gentilles attentions et pour ton soutien à San Francisco. Je ne te souhaite que des bonnes choses. Merci Michel Nasilowski alias Mich Mich. Tu es quelqu'un d'adorable, ne te laisse pas marcher dessus et ne doute pas de toi. Vous avez été tous les trois d'excellents co-bureaux pendant ces trois années je vous remercie grandement pour ces beaux moments qu'on a partagés.

J'aimerais remercier tous les anciens de l'équipe qui m'ont rapidement manqué après leur départ :

- Eleonora Muro : j'ai été triste qu'on se croise si peu au labo et j'aurais adoré maniper avec toi. Nous nous sommes tout de suite bien entendues et nous avons eu tellement de fous rires ensemble. Heureusement, c'est parti pour continuer.

- Clémentine Javaux : merci pour ton caractère et ta générosité. Tu nous reçois toujours tellement bien. Tu es une fille déterminée et une amie super.

- Pierre Vermeulen : mon frère de thèse. J'ai été complètement perdue quand tu es parti et tu m'as beaucoup manqué dans les salles d'optique que j'arpentais seule. Merci d'être venu m'écouter j'ai été très touchée.

- Benoît Mahler : merci pour les fous rires inter-bureaux et les clopes qu'on fumait ensemble en cachette. Tu es un bon vivant et ton rire nous a vite manqué au labo.

- Elsa Cassette : merci pour ta rigueur en salle de manip car quand tu es partie ça a vite été l'anarchie. Tu es une grande scientifique je te souhaite de réussir.

- Cécile Bouet : merci ma coach sportive. Tu m'as donné le goût de la course et ce n'était pas gagné. Merci pour ta gentillesse et ta douceur.

- Mickaël Tessier : merci pour ton aide lors de la préparation des TD et pour tous ces vendredis soirs qu'on a passé à discuter.

- Arjen Dijksman : merci pour tes conseils lorsque je suis arrivée au laboratoire.

- Botao Ji : Merci Botao d'avoir partagé ces trois années de thèse avec moi et bon courage pour la suite.

Je remercie les membres de Nextdot, la start up du labo. Je remercie Brice Nadal pour sa gentillesse et son altruisme. Merci pour ton aide et ta présence durant ces trois années dans les moments joyeux comme les plus tristes. Je remercie Chloé Grazon pour sa spontanéité, ses rires qui mettent de l'ambiance au labo et ses discussions "girly-girly" . Je remercie Hadrien Heuclin pour son aide précieuse pendant la rédaction, Emmanuel Lhuillier pour son art à déplaire et Martin Guilloux pour ses remarques de business man qui donnent une autre dimension aux discussions. Merci aussi à la bella Silvia Pedetti pour son sourire et son art de la fête, que de bons souvenirs à Copenhague.

Merci ensuite à Aurore Bournigault ma stagiaire préférée, Aude Buffard la jolie rousse (sois forte), Marianna Tasso l'argentine grâce à qui j'ai pratiqué (un peu) mon espagnol, Piernicola Spinicelli l'un des meilleurs cuisiniers de Paris, Anusuya Banerjee pour sa douceur, Adrien Robin le Lincoln de l'ESPCI, Patrick Hease le jeune paresseux (ne te laisse pas faire par les autres), Fatima, Céline et Laura les nouvelles à qui je souhaite de passer d'excellents moments dans l'équipe.

Je remercie les membres du laboratoire de Neurobiologie avec qui j'ai travaillé : Sophie Pezet et Zsolt Lenkei pour les manips sur souris, Anne Simon pour la culture cellulaire et Delphine Ladarré pour son soutien pendant la rédaction.

Je remercie également Jérôme Lesueur et Ricardo Lobo les directeurs du LPEM pendant ma thèse. Merci à Sophie Demonchaux pour sa disponibilité et ses conseils avisés pendant ces trois années, Marie-Claude Theme pour sa

gentillesse et sa disponibilité et Josiane Racine. Merci aussi à tous les membres du LPEM, et en particulier Maxime Malnou et Simon Hurand.

Je remercie aussi mon école doctorale, FDV, qui m'a permis de rencontrer un grand nombre de scientifiques de qualité. Je remercie également les Laboratoires Servier d'avoir financé ma thèse ainsi que de m'avoir donné les moyens de participer à un nombre incalculable de conférences. Un merci particulier à Olivier Nosjean pour tous tes conseils et la confiance que tu m'as accordée pendant ces trois années.

Enfin j'aimerais remercier tous mes amis de Vanves, de Montréal et d'ailleurs qui sont venus me voir le jour de la soutenance. Vous m'avez donné beaucoup de force et de courage. Merci également aux membres de Transapi, association dans laquelle je me suis investie en thèse et dont le projet est génial. Je remercie bien sûr ma famille, mes parents pour leur soutien, leur amour et leur confiance depuis toujours, mes soeurs Boubou et Bubu que j'aime fort et ma tante Michèle toujours prête à me faire plaisir. Pour finir j'aimerais remercier Samuel Peillon pour m'avoir supporté pendant la thèse, je sais que ce n'était pas facile tous les jours. Merci mon Sam de ta patience et de ton soutien, sans toi j'aurais pu perdre pied.

Contents

Introduction

In the last decades, cancer therapies have become a large field of researches. Cell tracking techniques would allow a better understanding of the metastatic processes. Today, identifying the spread of cancer cells from a primary tumour to seed secondary tumours in distant site, is one of the greatest challenges in cancer understanding and treatments. It has been shown that only one in five patients will survive once diagnosed with metastases. For this reason, many researches in oncology have been developed to better diagnosing primary tumours and better detecting first metastases in order to implement new therapies.

In vivo detection of unique cell remains a challenge because few techniques are sensitive enough to allow the detection of rare individual and isolated events. Primary Intraocular Lymphoma is a lymphoma of the eye that creates brain metastases. The metastatic migration pathway of circulating tumour cells (CTC) from the eye to the brain is still unknown. A best knowledge about the CTC migration pathway should allow finding new therapies. Moreover, quantitative and kinetic CTC studies in an *in vivo* PIOL model would test the efficiency of different treatments. Therefore fluorescence microscopy that is very sensitive and allows detection of only a few probes, is a diagnostic adapted tool. Nevertheless its sensitivity is limited by two major factors. First, the low visible light penetration depth. In order to reduce this limitation there is a wavelength range where absorption and scattering by tissues are limited. This range of wavelengths goes from 680 to 900 nm. The other factor that limits the sensitivity is the tissue autofluorescence. Autofluorescence is the natural emission of photon-excited tissues. In order to reduce these two limitations, the fluorescence signal peak wavelength of the nanoprobes should lie in an absorption and diffusion free region and should be distinguishable, either spectrally or temporally, from the autofluorescence background.

During my PhD thesis, I've worked on the synthesis of fluorescent nanoparticles with adapted optical properties for *in vivo* imaging. These fluorescent nanoprobes

should have an emission wavelength in the optical therapeutic window and should be bright, small and biocompatible. They also should have a long fluorescent lifetime to be coupled to a time-gated detection. Indeed, autofluorescence has a short fluorescence lifetime (<5 ns). By coupling long fluorescence lifetime with a time gated detection, we could enhance the sensitivity and reduce autofluorescence signal. I've also developed the optical set up to perform time-gated detection and have obtained promising preliminary *in vivo* results. The manuscript is divided in five chapters.

The FIRST CHAPTER is a state of the art of the different cell tracking techniques that have been developed and used in the last years. I will focus on our choice to work with optical microscopy and develop the different limitations we had to get ride of.

The SECOND CHAPTER describes the synthesis, characterisation of near-infrared long fluorescence lifetime quantum dots. I will report the protocol of water-solubilzation and the technique of cell labelling used in order to obtain massively loaded cells. I will also present some toxicity tests performed with our nanoprobes.

The THIRD CHAPTER is a description and characterization of the optical set up I developed. As we want to detect few and rare cells, we have to be highly sensitive. I will present our set up behaviour regarding noise sources. I will also determine our imaging system spatial resolution.

The FOURTH CHAPTER is my results chapter. I will present how we have managed to enhance sensitivity by reducing autofluorescence signal. I will present three types of experiments from *in vitro* results to our last *in vivo* promising results.

The FIFTH CHAPTER is a protocol chapter. I will list all chemical and biological products used for my experiments. I will also report the different protocols for the different steps of this project.

I

In vivo cell tracking: state of the art

In vivo cell tracking is an interesting tool to understand many biological processes. In tissue engineering, the ability to track implanted cells is essential to finely control the tissue monitoring and to direct tissue growth [1]. For immunotherapy that consists in administrating substances to induce an immune response, *in vivo* cell tracking could allow us to understand the molecular basis of immune cell biodistribution and trafficking [2]. Finally, tumour cell tracking can allow us to study their biodistribution and *in vivo* activity in order to improve our understanding of cancer development and metastatic processes. These examples of applications of *in vivo* cell tracking require the detection of isolated cells, which still remains a challenge today. Some of these applications require the detection of few cells previously stained with a contrast agent.

The spread of cancer cells from a primary tumour to seed secondary tumours at distant sites, commonly called metastasis, is one of the greatest challenges in cancer treatment today. In 2011, the National Cancer Institute has published alarming data about the survival prognosis of patients diagnosed with metastases. Indeed, across all cancer types, only one in five patients diagnosed with metastatic cancer will survive more than 5 years (data from the National Cancer Institute in USA) [3]. It is crucial for the mechanisms of metastatic migration to be established because each step represents an opportunity for a new therapy. Moreover, tumour targeting for delivery treatments is also crucial [4]. Figure I.1 is a scheme of the different steps of metastasis. Briefly, tumour cells from the primary site break the epithelial cell barrier and clear a path for migration into the vasculature rich stroma. Cells are then introduced in the body bloodstream and reach a second host site. To proliferate in the secondary site, cancer cells release pro-inflammatory compounds and proteinases that induce growth factor releasing by their neighbours [5][6]. Here, tumour cells spread through the bloodstream but the lymphatic system is also a possible pathway. An other interesting challenge is to determine the migration pathway by detecting the tumour cells when leaving the original tumour site in order to reach another one. These type of cells are called circulating tumour cells (CTC).

Circulating tumour cells are spilled by primary tumours to invade other organs. In 1869 Thomas Ashworth, an Australian physician, after observing microscopically circulating tumour cells in the blood of a man with metastatic cancer, postulated that "cells identical with those of the cancer itself being seen in the blood" [8][9]. Then, researchers started to study this type of cancer cells and understood that the number of CTC can be a sensitive biomarker for tumour progression and metastasis

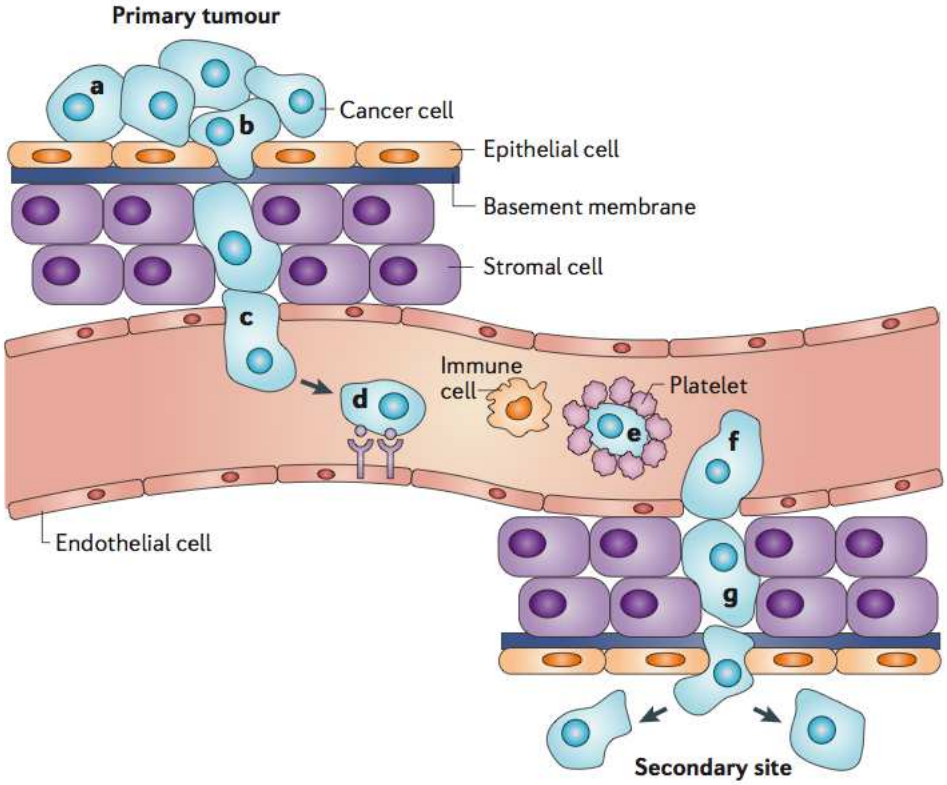

Figure I.1 – Scheme of the different steps of metastasis [7].

in some cases of cancers. In 2004, Cristofanilli *et al.* showed that the level of CTC can predict survival in metastatic breast cancer [10]. Therefore, the detection of CTC is useful for diagnosis and "staging" of cancers, to estimate the efficiency of treatments and to evaluate the presence of residual metastasis. However, the number of CTC in the blood or in lymphatic circulation is very low (few cells per mL). Therefore, the detection of CTC require a high sensitivity that could allow the detection of individual and isolated cells.

For my PhD project, we started a collaboration with Sylvain Fisson's group in the Centre de Recherche des Cordeliers in Paris. His group works on the influence of the microenvironement in metastasis spread and one of the unsolved issue is the determination of the metastatic migration pathway for some cancers, such as the Primary IntraOcular Lymphoma. Primary intraOcular lymphoma (PIOL) is a high-grade non Hodgkin lymphoma: a cancer originating from white blood cells called lymphocytes. Most patients show non-specific visual symptoms and are often initially diagnosed with uveitis (inflammation of the uvea) or retinitis (inflammation of the retina). Unfortunately, the definitive diagnosis is obtained when clinical symptoms of cerebral lymphoma appear [11]. Indeed, it has been shown that up to 80% of the patients who initially present ocular lymphoma will develop cerebral lymphoma [11][12][13][14][15]. A better understanding and prevent of the spread of tumour cells to the brain could improve the survival diagnosis. However, the migration pathways from the eye to the brain are still unknown. There are two suspected pathways: via the lymphatic system or via the bloodstream. In 2007, the group of Sylvain Fisson developed a murine model in order to study the immune microenvironmenent which is known to be crucial in controlling tumour growth and maintenance [16]. In this model, they implanted a tumour cell line derived from A20 tumour cells into the eye of an immunocompetent syngenic mice: they injected a fixed quantity of tumour cells and waited for several days before the observation of the first brain metastases. This model is interesting in order to understand immune escape mechanisms and to design new therapies to block metastatic spread. It can also be useful for the development of techniques to determine early tumour cell spread, such as cell tracking techniques. As previously mentioned, the understanding of the metastatic migration pathways requires the detection of isolated circulating tumour cells. Therefore, the imaging instrument has to be highly sensitive. In the case of the PIOL, we have access to the cells that are injected in the mouse model, which will allow us to previously stain cells with an adapted contrast agent.

There are many imaging techniques used in oncology as illustrated in Fig. I.2. For cancer cells, these techniques mainly include bioluminescence, positron emission tomography (PET), magnetic resonance imaging (MRI) and fluorescence imaging [17].

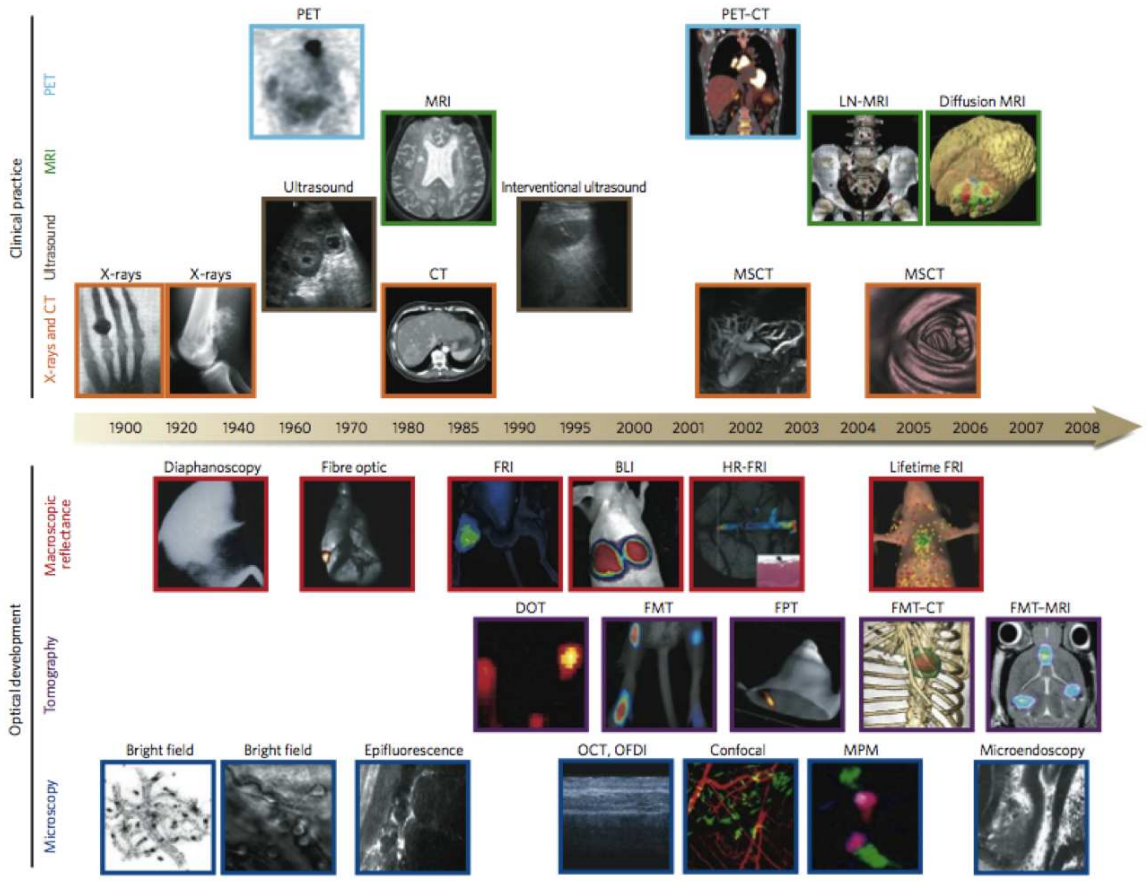

Figure I.2 – Imaging technologies used in oncology[18]. Abreviations: BLI, bioluminescence imaging; CT, computed tomography; DOT, diffuse optical tomography; FMT, fluorescence-mediated tomography; FPT, fluorescence protein tomography; FRI, fluorescence reflectance imaging; HR-FRI, high-resolution FRI; LN-MRI, lymphotropic nanoparticle-enhanced MRI; MPM, multiphoton microscopy; MRI, magnetic resonance imaging; MSCT, multislice CT; OCT, optical coherence tomography; OFDI, optical frequency-domain imaging; PET, positron-emission tomography.

The CTC tracking for the PIOL application requires several technically challenging characteristics:

- a high sensitivity because it requires the detection of a few isolated *in vivo* cells,
- a good spatial resolution (hundred of micrometers) to ensure an identification of the migration pathway,
- a good temporal resolution (ms to s) to follow dynamic events,
- a good biocompatibility and a low invasiveness.

In the next part of this introduction, I will describe the different imaging techniques previously mentioned and determine among all, the technique we chose for circulating tumour cells tracking.

I.1 Cell tracking techniques

Each of the imaging techniques presented here has its own advantages and disadvantages and they are more complementary than competitive. However, this listing of imaging techniques is an accurate description that allowed us to motivate our final choice.

I.1.1 PET

Positron emission tomography (PET) is a nuclear medicine and functional imaging technique that produces a three-dimensional image of functional processes in the body. The system detects pairs of gamma rays emitted indirectly by a positron-emitting radionuclide (tracer), which is introduced into the body via a biologically active molecule. Typically, the molecule used for this purpose is fluorodeoxyglucose (FDG). This tracer is similar to glucose: it binds tissues that consume large quantities of this sugar such as cancer tissues, the cardiac muscle or the brain. The FDG is chemically modified to be radioactive and ensure the detection. The spatial resolution is the millimeter, and the temporal resolution is the minute [19]. For these reasons, PET is not a good candidate for *in vivo* circulating tumour cell tracking for the PIOL application.

I.1.2 Magnetic Resonance Imaging

The signal used for magnetic resonance imaging (MRI) is derived from endogenous mobile water protons (^{1}H) or fluorinated molecules (such as ^{19}F) that are present or introduced in the subject. When the subject is placed in a large static magnetic field, the magnetic moment associated with ^{1}H or ^{19}F tends to align along the direction of the magnetic field. A radio-frequency radiation perturbs the ^{1}H or ^{19}F nuclei from their equilibrium state. The nuclei then recover their equilibrium state and induce a transient voltage in a receiver antenna. This transient voltage constitutes the nuclear magnetic resonance (NMR) signal. There are two types of contrast given by two characteristic times: T1 and T2. MRI provides an image of the density of nuclei which is responsible for contrast. This nuclei density depends on the tissue properties. Thus, T1 gives information about the nuclear spin-lattice relaxation time. T1 parametrizes the alignment of the nuclei along the magnetic field direction that is not instantaneous. T2 gives information about the spin-spin relaxation time. T2 is the characteristic time constant during which nuclei remain in "phase" with each other, and its value is reflected in the duration of the transient NMR signal. MRI-based cell tracking involves detecting cells that exhibit a differential signal. There are also labelled agents that can be used in order to enhance contrast in MRI. The superparamagnetic iron oxide (SPIO) nanoparticles have a strong magnetic moment [20]. They are composed of small particles of ferrous and ferric oxides coated with dextran. These particles induce a strong local magnetic field. Therefore, water protons are affected by inhomogeneous magnetic fields around SPIO particles, which induces a signal loss (negative contrast). For example, Fig. I.3 shows MRI images used to monitor the location and the target-accuracy of injected SPIO-stained cells. The black arrow indicates the targeted delivery area and the white arrow indicates the SPIO-labelled cells location after injection. MRI is a sensitive technique but its temporal and spatial resolutions are not adapted for rare event and individual cell tracking.

I.1.3 Bioluminescence imaging

Bioluminescence imaging (BLI) is a commonly used technique for whole-body *in vivo* imaging [22][23]. Bioluminescence is a chemical reaction between a substrate and an enzyme that creates photons. A famous substrate/enzyme system used in BLI is the luciferine/luciferase one. A reporter gene is transferred to cells of interest via a vector and the luciferase enzyme is then expressed in the transfected cells. Luciferase-

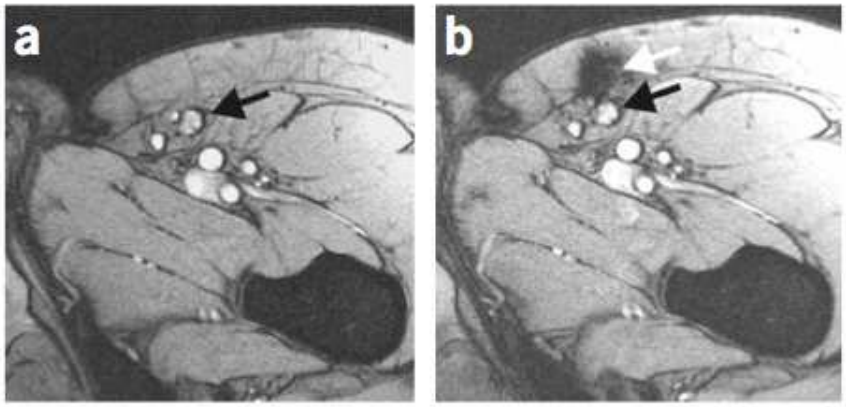

Figure I.3 – Monitoring the delivery of SPIO-labelled cells using MRI. (a) MRI before cell injection; the targeted delivery area is indicated with the black arrow. (b) MRI after injection; SPIO-stained cells were not accurately delivered into the targeted area but in the vicinity, as indicated by the white arrow [21].

expressing cells are transplanted to animals and the luciferine substrate is injected to perform cell tracking. BLI is an adapted technique to test the antitumour effect of a molecule. For example, Toll-like receptors (TLRs) are recognition receptors that initiate adaptive immune responses. Agonists of TLR have been identified as new drugs to treat cancer [24]. Ben Abdelwahed *et al.* have shown by BLI that the injection of agonists for Toll-like receptors (the CpG) appears to prevent lymph node invasion. However, it has no detectable effect on the primary eye tumour (PIOL), as shown in Fig. I.4

BLI is an adapted tool in order to track a hundred of cells. The field of view allows the whole-body imaging of small animals as shown in Fig. I.4. The spatial resolution is in the range of several milimeters and it requires a few minutes to acquire an image. BLI is often used as an imaging technique to localize tumour cells and identify their anatomic localisation. The detection of rare, isolated and quick events can not be performed using BLI.

I.1.4 Fluorescence microscopy

Fluorescence imaging is one of the most versatile and widely used visualization methods in biomedical research. It has become a dominant *in vitro* and *in vivo* imaging method due to its high spatial and temporal resolutions, its high sensitivity and its ease of use [26]. Fluorescence is a luminescence process. This phenomenon is characterized by the absorption and emission of photons. A molecule absorbs

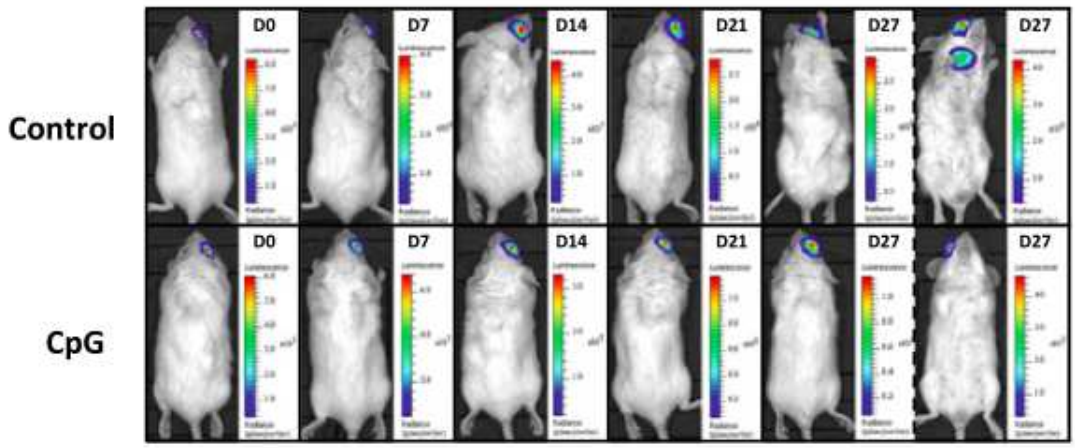

Figure I.4 – Bioluminescence images of a mouse inoculated with the PIOL and treated with an antitumour drug. The drug prevent lymph node invasion at day 27 but has no detectable effect on the PIOL [25].

photons and changes from the fundamental state to an excited state. In order to get back to the fundamental state, the molecule emits a photon with a lower energy [27]. The corresponding fluorescence lifetime is a property of each fluorophore for a given environment. Physically, it corresponds to the time during which the fluorophore remains in the excited state. Using the lifetime properties of the different components of a tissue as source of contrast in the image, fluorescence lifetime imaging microscopy has emerged and has provided lifetime maps of tissues. Figure I.5 shows three images of an unstained section of a rat ear. The left image is the typical epifluorescence wide-field image, the middle one is the lifetime map and the right image corresponds to the superposition of both previous images. This illustrates the possibility of tissue mapping using lifetime properties.

Moreover, fluorescence imaging is an imaging technique compatible with a wide variety of *in vitro* and *in vivo* samples. Figure I.6 illustrates the different fluorescence imaging paths for preclinical studies relating to brain imaging.

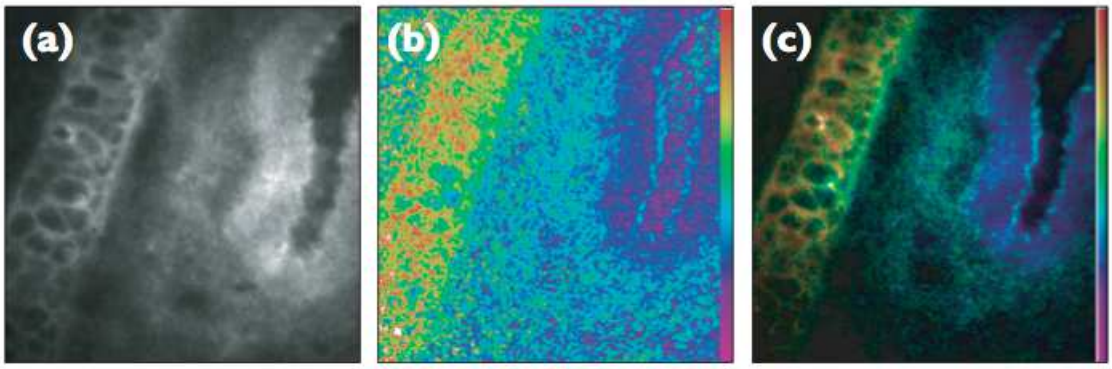

Figure I.5 – Images of an unstained section of a rat ear. a) Classical wide-field fluorescence image. b) Lifetime map image. c) Superposition of the classical image and lifetime map. (False color scale: 800-3500ps)[28].

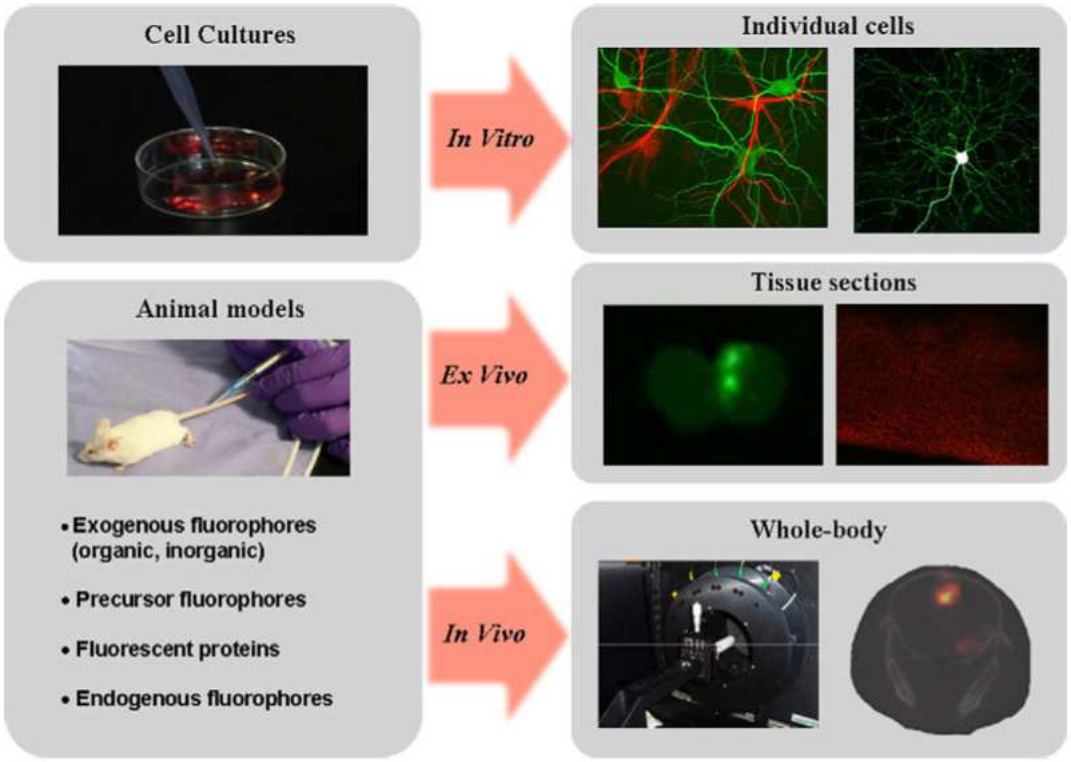

Figure I.6 – Illustration of the different types of samples compatible with fluorescence imaging relating to brain imaging [26].

Fluorescence microscopy is a sensitive technique and present a high spatial (μm) and temporal (ms) resolutions. It's an adapted candidate for the CTC tracking and for the identification of CTC migration pathways.

I.1.5 Summary of the different imaging techniques characteristics

Table I.1 summarizes the characteristics of the imaging techniques used for cell tracking previously mentioned. The spatial resolution corresponds to the minimum distance between two independently measured objects. The temporal resolution is the final time at which the interpretable version of the image can be recorded. Sensitivity can be defined as the ability to detect a nanoprobe when it is present, relative to the background.

Technique	Range of wavelengths	Spatial resolution	Temporal resolution	Sensitivity
PET	High energy γ rays	1-2 mm	10 s to min	++
MRI	radiowaves	25-100 μm	min to h	+
BLI	visible light	3-5 mm	s to min	++
Fluorescence imaging	visible to near-infrared	from μm to mm (depending on the depth)	ms to s	+++

Table I.1 – Characteristics of the main imaging techniques used for cell tracking [29].

Therefore, fluorescence imaging seems to be the most adapted imaging technique for *in vivo* CTC tracking. Nevertheless, fluorescence imaging is not a perfect technique and present some limitations.

I.2 Fluorescence microscopy limitations

In fluorescence *in vivo* imaging, the sensitivity is limited by two major factors: the low visible light penetration depth and the high tissue autofluorescence.

I.2.1 Visible light scattering and absorption

There is a range of wavelengths where the absorption and scattering of tissues are limited. This "optical therapeutic window" goes from 650 to 950 nm [30][31], where

water, hemoglobin and oxyhemoglobin absorb less, as shown in Fig. I.7. Photon diffusion depends on the wavelength. The higher is the wavelength the lower is the diffusion ($\propto 1/\lambda^n$). Consequently, to enhance sensitivity in *in vivo* fluorescence imaging, fluorescent probes have to absorb and emit in this near-infrared range.

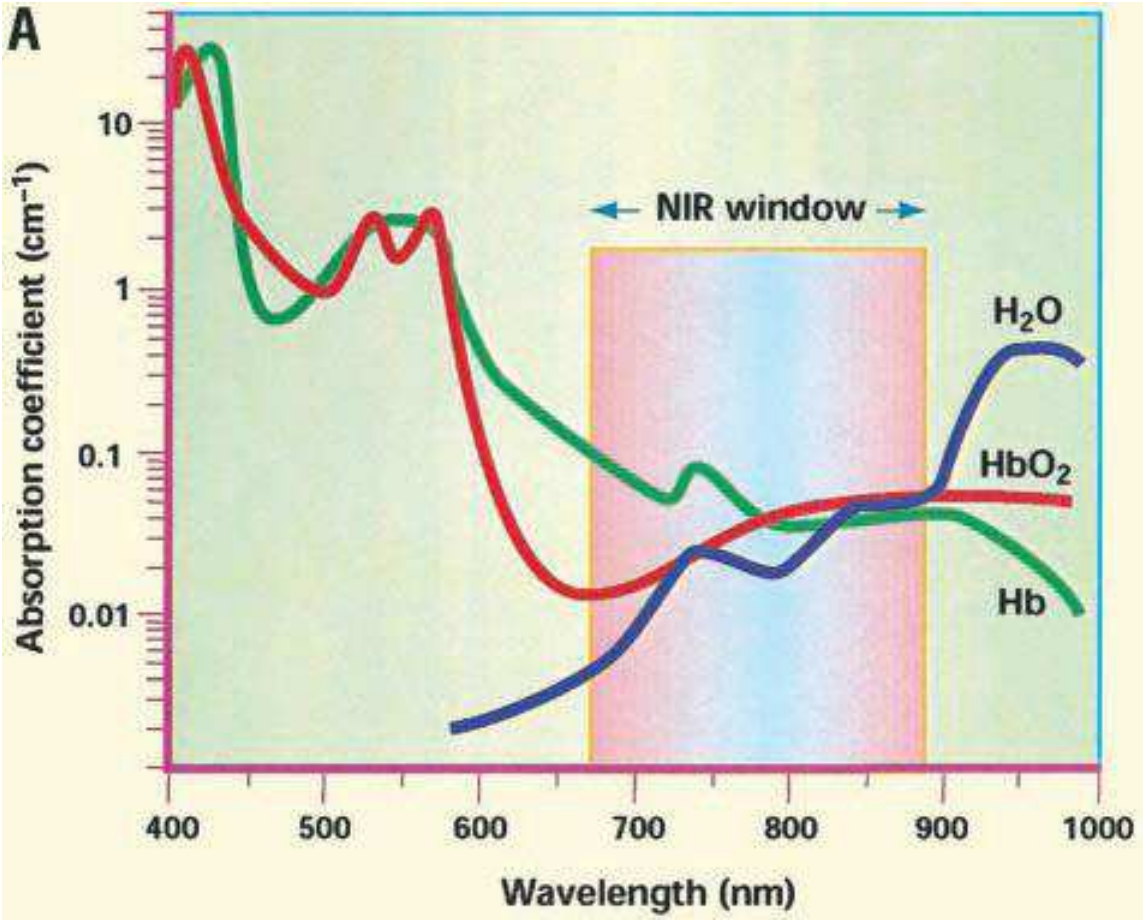

Figure I.7 – Extinction coefficients of water (in blue), hemoglobin (in green) and oxyhemoglobin (in blue) as a function of the wavelength. (*Image taken from the website of the International cancer therapy center: http://www.internationalcancertherapy.com/faq.php).*

I.2.2 Tissue autofluorescence

Visible autofluoresence

The autofluorescence is the natural emission of photon-excited tissues. Figure I.8 presents the autofluorescence signal of vital organs depending on the excitation and emission filters chosen. As illustrated in these pictures, the autofluorescence signal

highly depends on the excitation and emission wavelengths. In the NIR region this signal is lower than in the rest of the electromagnetic spectrum.

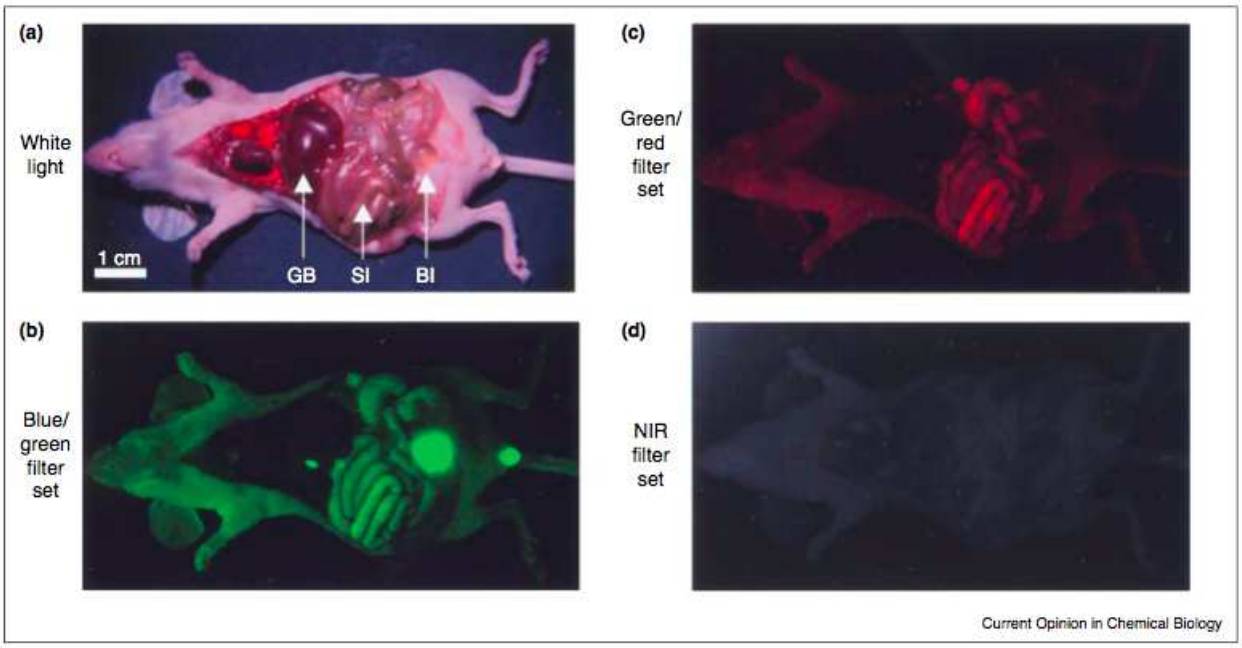

Figure I.8 – Wavelenght dependency of the autofluorescence of vital organs with various excitation/emission filters. a) Image acquired in white light b) blue/green (460-500 nm/505-560 nm) c) green/red (525-555 nm/590-650 nm) d) NIR (725-775 nm/790-830 nm) (GB, SI and BI stand for respectively, gallbladder, small intestine and bladder) [30].

Many endogenous fluorophores present in the tissues have been identified to be responsible for the visible autofluorescence signals. Figure I.9 presents the excitation and emission spectra of endogenous tissue fluorophores.

Fluorescence lifetimes of endogenous fluorophores vary typically between 2 and 10 ns [33].

Near-infrared autofluorescence

Near infrared autofluorescence has not been well reported. However, in 2006, Fournier *et al.* studied the *in vivo* detection of mammary tumor in a rat model using autofluorescence alterations in the red and far-red regions [34]. They showed that there are significant autofluorescence signal differences in the NIR region between healthy tissue and malignant and benign tumours. Figure I.10 shows, on the left side, a light scattering image of a rat mammary tissue under ambient light. On the right

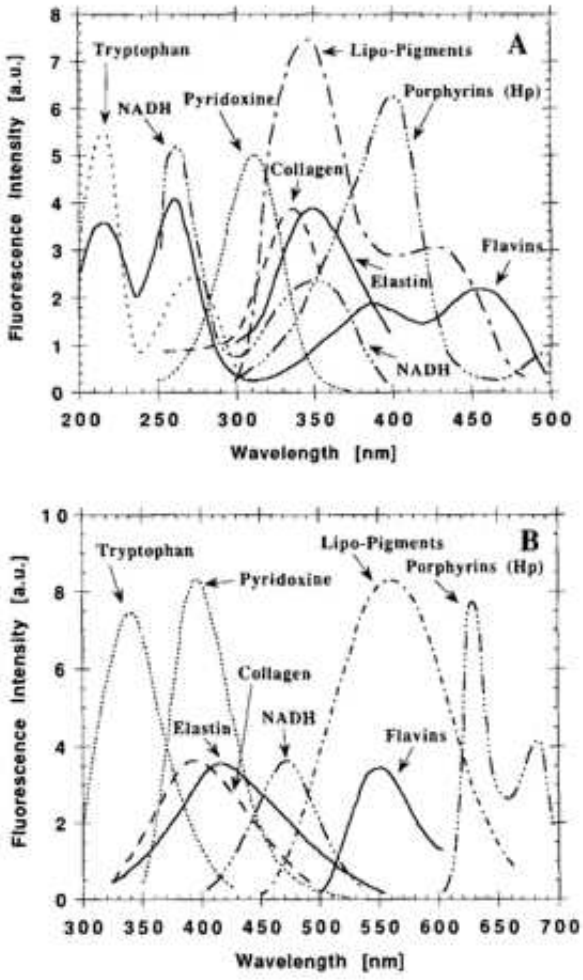

Figure I.9 – Fluorescence excitation (A) and emission (B) spectra of endogenous tissue fluorophores in the visible range of wavelengths [32][33].

side, the corresponding autofluorescence image is presented with an excitation at 670 nm and a detection at 800 nm. The tumour (indicated by the white arrow) is less fluorescent than the adjacent normal tissue. We can also note the possibility to visualize blood vessels that absorb light (black arrow). By calculating the tumour-to-normal tissue ratios they managed to discriminate normal tissue from malignant or benign tumours with a sensitivity of 76% (probability for a test to be positive when a person is sick: reveals the percentage of true positive) and a specificity of 75% (probability for a test to be negative when a person is healthy: reveals the percentage of false negative). They attributed the signal difference to a difference in the porphyrin concentration in tumour tissue as compared to corresponding normal tissue.

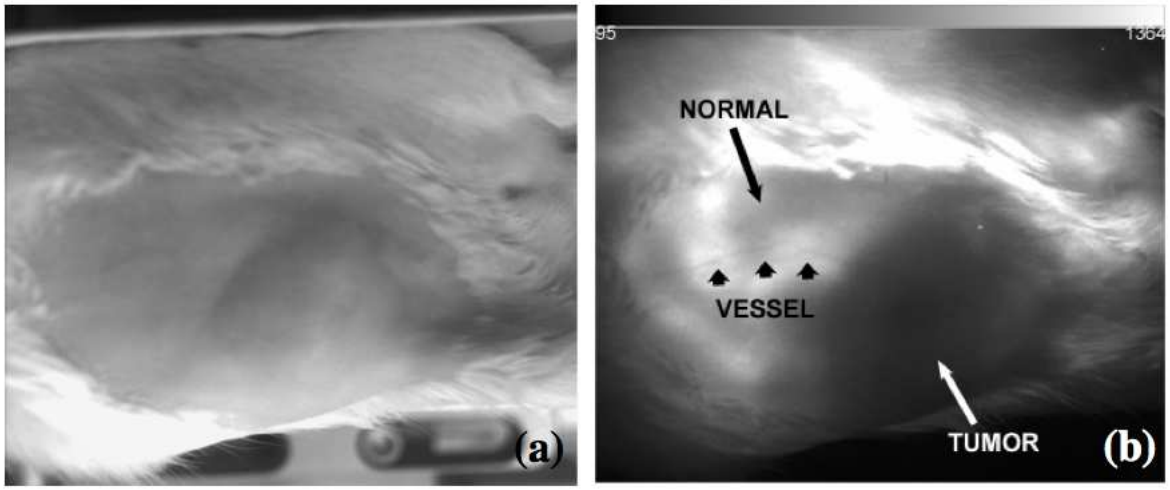

Figure I.10 – a) Light scattering image under ambient light. b) Corresponding autofluorescence image with an excitation at 670 nm and a detection at 800 nm [34].

Among the endogenous and exogenous fluorophores emitting in the near-infrared region, porphyrins are suspected to be responsible for the near-infrared autofluorescence. Many porphyrins are naturally occurring: one of the most famous is the heme, the pigment of red blood cells. The chlorines such as the chlorophylles can also be responsible for autofluorescence. In 1988, Weagle *et al.* observed that normal mouse skin had a fluorescence peak at 674 nm [35]. They attributed this fluorescence to a degradation product of chlorophyll derived from the mouse food (see spectra in Fig.I.11). By illuminating a mouse whole-body using a preoperative probe at 785 nm, Montcuquet observed an autofluorescent prevailing signal in the stomach and the intestines (see Fig. I.12).

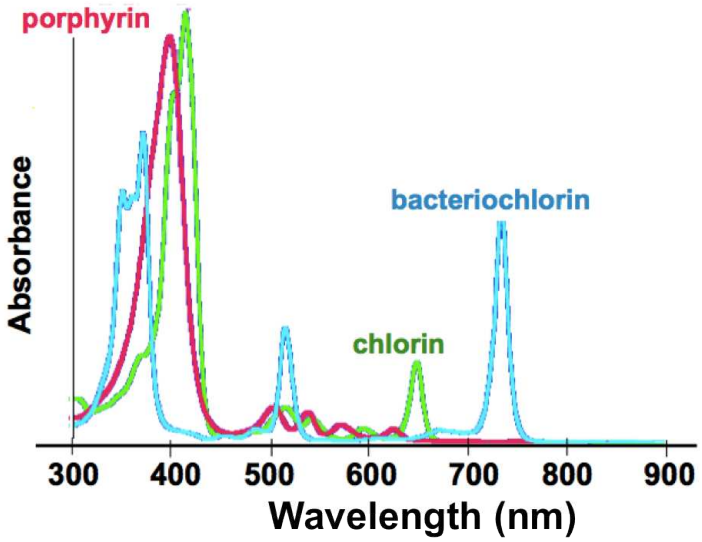

Figure I.11 – Absorbance spectra of porphyrin and chlorine *Adapted from http: www.genopole.fr/IMG/pdf/Brault*$_A$*telier*$_B$*iophotonique.*

The autofluorescence in the near-infrared region can be due to the presence of porphyrin in the bloodstream and we have seen that the food can be fluorescent too. The hypothesis of porphyrins is possible but not consistent with the quantity of porphyrins in the body. Porphyrins remain the only described endogenous fluorophores that emit in the near-infrared region [26]. However, in order to avoid any autofluorescence signal Funovis *et al.* [36] fed their mice with chlorophyll-free food seven days before the near-infrared imaging. They still observed non identified autofluorescence signals in the near-infrared region. Finally, the autofluorescence sources in the near-infrared region are still not well-identified. Because we aim to track rare and individual cells we have to reduce spurious signals, such as autofluorescence in order to increase the signal-to-noise ratio.

I.3 Solution proposed to reduce the autofluorescence signal

In order to solve this problem, the fluorescence signal peak wavelength should lie in an absorption and diffusion free region and should be distinguishable, either spectrally or temporally, from the autofluorescence background. Therefore, we have to work with probes that absorb and emit in the near-infrared region. They must also have a high fluorescence quantum yield, be biocompatible and present a low

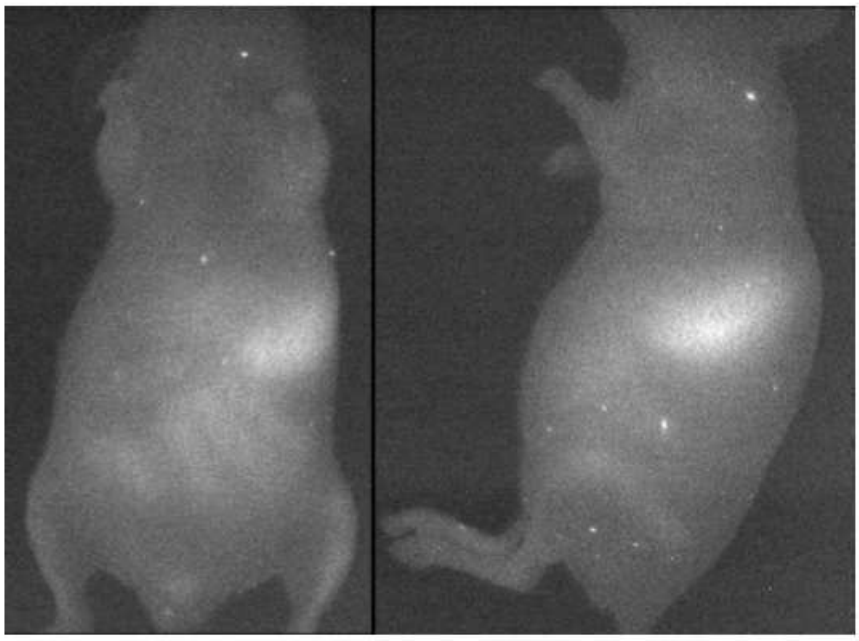

Figure I.12 – Whole-body autofluorescence signal of a normal mouse obtained using a preoperative probe with an excitation at 785 nm [37].

toxicity.

I.3.1 Time-gated detection coupled to long lifetime nanoprobes

In the last few years, several groups have worked on time-gated detection in order to reduce autofluorescence for biological imaging. Fluorescence decay rate consists in isolating a time-decaying signal from other signals having a different (longer or shorter) timescale. In our case, autofluorescence has a short fluorescence lifetime so, time-gated detection using probes having longer fluorescence decay rates than autofluorescence would enable autofluorescence rejection and a substantial increase in the signal-to-noise ratio (principle in Fig. I.13). I will present the different techniques developed by several groups and describe one of the probes and imaging system chosen for each.

I.3.2 Current applications of time-gated detection for autofluorescence rejection

Confocal microscopy

Several groups have used time-gated detection in order to reduce autofluorescence signals. In 2001, Dahan *et al.* [38] built a stage-scanning confocal microscope with

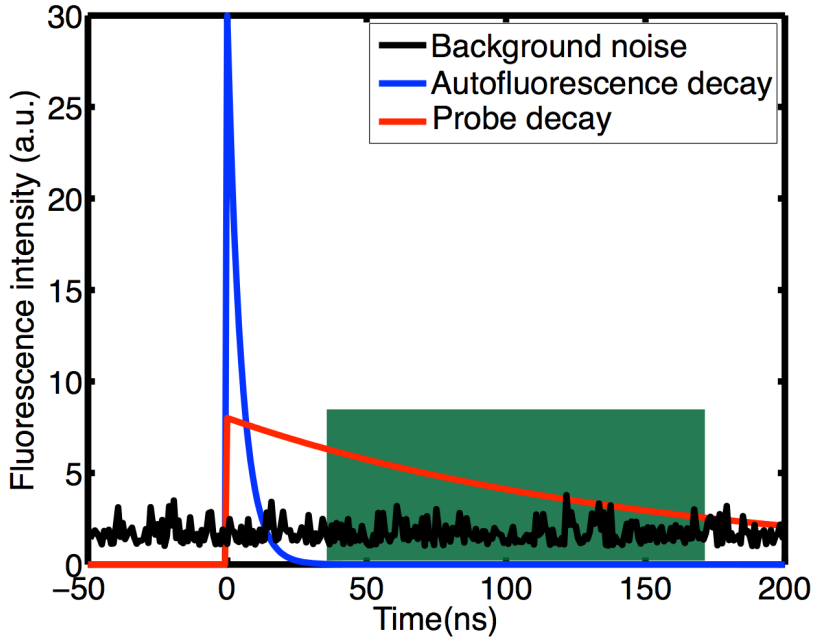

Figure I.13 – Scheme of the principle of time-gated detection. In green adapted detection window.

a nanometer resolution closed-loop piezo-stage scanner. The excitation is provided by a Ti:sapphire laser, with an excitation at 503 nm and a 5 MHz repetition rate. At each piezo-stage step, the scanning controller generates a Transistor-Transistor Logic (TTL) pulse and a computer (which contains a time-correlated single-photon counting card) acquires the detected fluorescence photons. The start and stop pulses are provided by an avalanche photodiode and laser electronics, respectively (reverse mode). Thus, for each pixel of the image, they get histograms of photons arrivals. These histograms can be analysed in time-gated applications by selecting a time range of photons' arrival and form an image with them. They incubated 3T3 mouse fibroblasts with a small amount of silanized visible quantum dots ($\lambda = 575$ nm, QY = 40%) overnight and fixed them. The QDs fluorescence decay could be described by a sum of three exponentials with characteristic times of 2, 8 and 24 ns that corresponds respectively to 11, 49 and 40 % of the fluorescence. Figure I.14 shows time-resolved confocal images. On top, the image corresponds to all detected photons. At the bottom, the image is obtained from photons that arrived between 35 and 65 ns after the laser pulse. The image was taken with a 25-ms integration time per pixel. The gated image allows the observation of bright, localized spots with enhanced signal-to-background ratio. Here, with the parameters used, they obtained a signal-to-noise

ratio of 15.

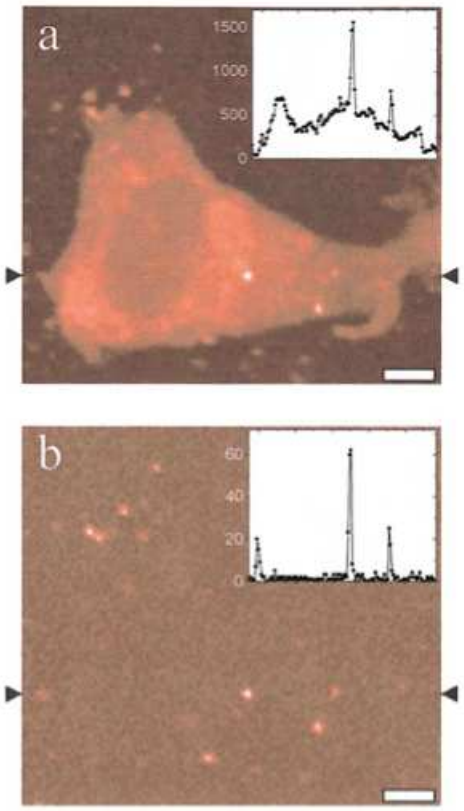

Figure I.14 – Time-resolved confocal image of a fibroblast previously incubated with quantum dots. a) Image obtained for all detected photons. b) Gated image built with photons that arrived between 35 and 65 ns after the laser pulse. [38]

This application of time-gated detection allows them to enhance the detection sensitivity by one order of magnitude. However, they used visible-emitting quantum dots, which are often made of cadmium (in this range of emission wavelength). In addition, excitation and emission wavelengths used here are not in the optical therapeutic window. Finally, with a 25-ms integration time per pixel, it requires several minutes to get an image. Such a time scale is not compatible with cell tracking measurements.

Whole-body imaging using near-infrared-emitting quantum dots

In 2009, May and co-workers [39] built a wide-field time-gated preclinical imaging system for detection of near-infrared-emitting quantum dots by suppression of the short-lifetime background autofluorescence. The near-infrared-emitting quantum

dots used here have a fluorescence lifetime superior to 20 ns. The imaging system consists in a pulsed high-power 630-nm LED excitation (2 MHz repetition rate) and a gated intensified CCD camera for fluorescence detection. The excitation light was bandpass filtered with filters at 615±20 nm to discriminate excitation light that overlapped with the quantum dot emission peak. The emission signal is similarly filtered using filters at 710 ± 25 nm to select fluorescence from quantum dots. The laser pulse and the intensifier are controlled by phase-locked generators and the intensifier is imaged on a CCD camera. In order to compare the efficiency of their time-gated detection compared to conventional fluorescence imaging, they synthesized images by overlapping the excitation pulse and intensifier detection window times during the image exposure (image called CW for continuous wave excitation). Alternatively, time-gated images were obtained by inserting a delay between the end of the excitation pulse and start of the detection gate. They injected a solution of QDs in Phosphate buffered saline (PBS) at different concentrations along the back of three anaesthetized nude mice and imaged the injection points. Figure I.15 shows images of the three mice previously injected with QDs in CW (on the left) and superposition of CW (in green) and the time-gated (in red) images on the right. Time-gated detection greatly improved contrast of QDs, allowing a detection of QD concentrations down to 0.25 nM. Depending on the concentration, the exposure time was variable, from 125 ms to 5 s. The delay is empirically fixed at 50 ns after the laser pulse. The image contrast, defined as the ratio between QDs signal and the autofluorescence, increased by a factor from 3 to 10 using time-gated detection.

This application of time-gated detection allows an enhancement of near-infrared quantum dots detection. Moreover, the quantum dots used have an emission wavelength in the optical therapeutic window. However, this type of quantum dots is composed of heavy metals (cadmium and tellurium). The imaging set up is a whole-body imaging system, which has not the spatial and temporal resolutions necessary for individual cell tracking.

Whole-body imaging using silicon nanoparticules

Recently, Gu *et al.* have imaged a human ovarian cancer xenograft in a mouse model using porous silicon nanoparticules introduced via intravenous injection [40]. Synthesized porous silicon nanoparticles have a mean hydrodynamic diameter of 168 nm. Their emission wavelength is centered at 800 nm (QY = 10%) and their fluorescence lifetime is 12 μs, about 1000 times longer than the autofluorescence. A

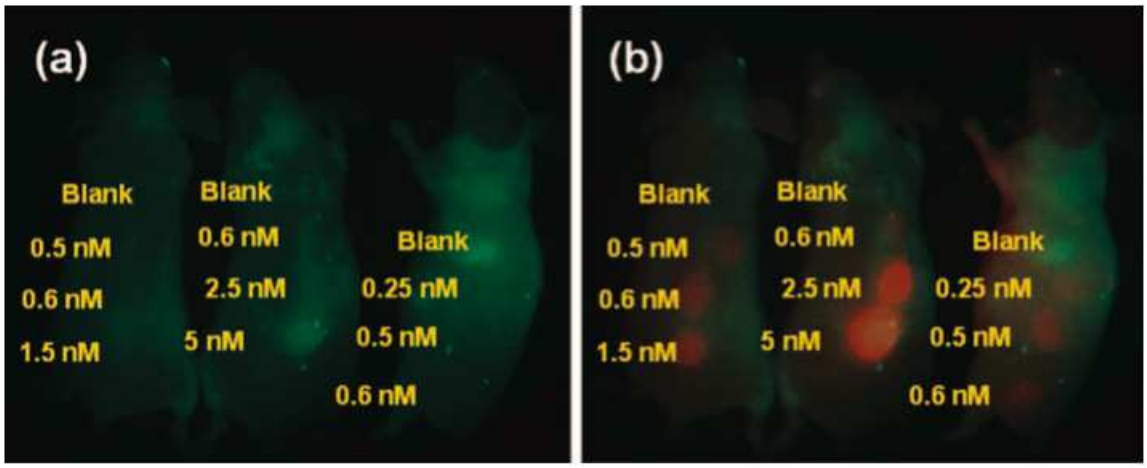

Figure I.15 – Wide-field images of 3 nude mice subcutaneously injected with near-infrared-emitting QDs at different concentrations along their backs. a) Image obtained with continuous wave (CW) illumintation. b) Superposition of CW images (in green) and time-gated images (in red) with a 50 ns delay after the laser impulsion [39].

time-domain fluorescence imaging system eXplore Optix is used to image mice *in vivo*. The system was used with a 470-nm excitation laser with a repetition rate of 40 MHz, corresponding to a 25 ns time window between pulses. CW fluorescence images are obtained by reconstructing the photoluminescence signal collected using the full 25 ns time-window from the data. For time-gated (TG) fluorescence images the photoluminescence signal was collected between 20.5 and 21.5 ns of the imaging time-window from the full data. Figure I.16 presents CW and TG images of a nude mouse bearing a human ovarian cancer xenograft at different time after injection of silicon nanoparticules. The white arrow indicates the tumour localization. Just after injection, no signal from nanoparticles is observed in the tumour location. One hour after injection, CW image does not indicate difference of contrast between normal tissue and tumour tissue. However, time-gated image shows a weak photoluminescent signal at the tumour location. Four hours post-injection, the authors observe a different contrast between CW and TG images at the tumour location. Silicon nanoparticles have accumulated in the tumour location are their presence was clearly revealed using the TG detection. The signal at the tumour location decreases 24 hours post-injection, which suggests that a degradation and clearance from the host occur [41].

This experiment uses nanoparticles that emit in the optical therapeutic window.

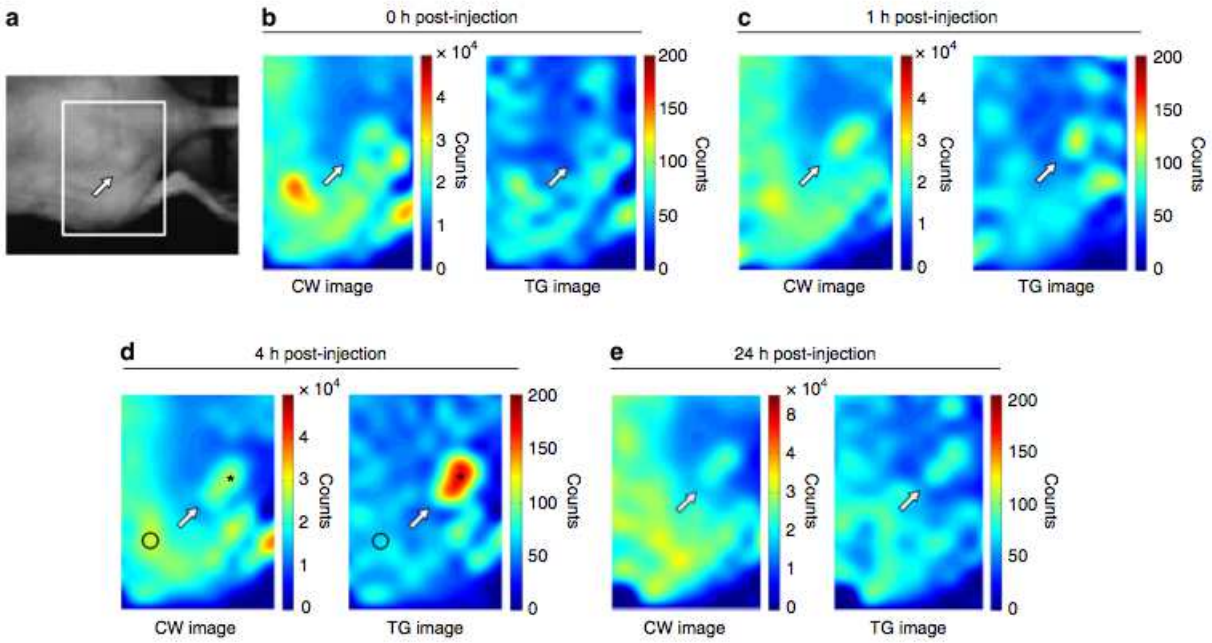

Figure I.16 – CW and time-gated images of nude mouse bearing a human ovarian carcinoma SKOV3 xenograft tumour at different time after the porous silicon nanoparticles injection [40].

Their fluorescence quantum yield is relatively high (10%) in this range of emission wavelengths. These nanoparticles are biodegradable, which ensures a low level of toxicity. Because we aim to track cells over a few days, they need to be massively charged with nanoprobes. Indeed, the cell division leads to a probes dilution between the two daughter cells. Here, the high hydrodynamic diameter of the nanoparticles limits the massive loading of cells with nanoprobes and decreases the number of days during which cells can be tracked. Moreover, this optical system by photons counting requires a long acquisition time and important analysis treatments in order to obtain the definitive image. In our application, because we want to determine the metastatic migration pathway we need to track dynamic cells. Finally, this system does not allow a cell-scale detection, and therefore a detection of isolated and rare cells.

Wide-field imaging and flow cytometric analysis

Nanodiamonds are promising fluorescent biomarkers because they are highly photostable and biocompatible [42]. Very recently, Hui *et al.* [43] reported their use to detect cancer cells in blood analysis. Here, nanodiamonds have an emission wave-

length centered at 700 nm, their fluorescence lifetime is around 20 ns and their diameter is 100 nm.

The optical set up was a wide-field microscope with an excitation at 600 nm. The detection was performed by a nanosecond intensified charge-coupled device. Figure I.17 shows images of HeLa cells stained with nanodiamonds and immersed in human blood in order to mimic *in vivo* autofluorescence signal. The left image is a typical wide-field fluorescence image and the right image is a wide-field time-gated image. The exposure time used for fluorescence images is 0.1 s and for time-gated images 0.3 s. They use a 100X immersion oil objective. They clearly observed a sensitivity enhancement with the time-gated detection that was confirmed by the intensity profiles of both images.

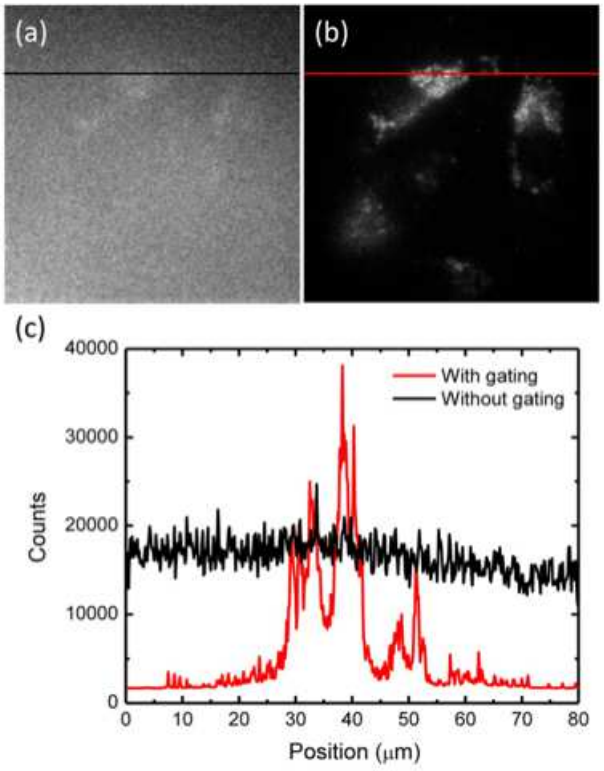

Figure I.17 – *In vitro* images of HeLa cells stained with nanodiamonds and immersed in human blood. a) Wide-field fluorescence classical image. b) Time-gated image. c) Intensity profiles along the black and red color lines of images just above [43].

They also performed flow cytometry using their system. They used microchannel devices with dimension compatible to mouse and rate blood capillaries. The cell counting was performed using a MATLAB program that also allowed measuring

fluorescence intensity of nanodiamond-labelled cells. Finally, to demonstrate the principle that their wide-field imaging system may serve as a useful instrument for *in vivo* flow cytometry they labelled mouse lung cancer cells with nanodiamonds and then injected them into a mouse via its tail vein. Figure I.18 presents *in vivo* images of mouse blood vessel where a stained cell pass though.

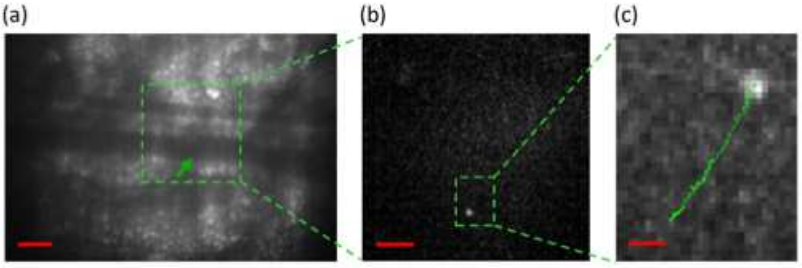

Figure I.18 – *In vivo* images of mouse lung cancer cells stained with nanodiamonds and injected in a mouse bloodstream via the tail vein. [43].

The experiments use nanodiamonds that are biocompatible and easily taken up by cells for labelling. Their diameter is 100 nm and their fluorescence lifetime is 20 ns. The optical set up developed allows a cell-scale imaging with an enhance in sensitivity by autofluorescence rejection. However, the fluorescence lifetime of nanodiamonds is not so far from the autofluorescence one. This limits a total rejection of the autofluorescence. To the best of our knowledge, this article is the first one that clearly shows images of isolated cells in an *in vivo* sample using time-gated detection.

I.4 Conclusion

This state of the art of the current imaging techniques for *in vivo* cell tracking allowed us to determine that fluorescence imaging is a sensitive technique that should permit the detection of isolated circulating cells. To overcome the two limitations in fluorescence imaging, we propose to stain cells with near-infrared long fluorescence lifetime probes and to couple them to a time-gated detection to reduce the autofluorescence signal and improve the sensitivity. Several groups have worked on the development of time-gated imaging systems in order to reduce autofluorescence signals. The here-reported experiments utilize different types of nanoprobes with various fluorescence decays. Indeed, nanoprobes fluorescence decay has to be longer than the autofluorescence one.

To conclude, optical microscopy seems to be the most adapted imaging technique. In this manuscript, I will present our probe choice, their synthesis and optical characterization. Then, I will describe the optical set up we developed and the results obtained using both optical set up and nanoprobes. In order to determine the metastatic migration pathway, for the PIOL application, we plan to label cells with near-infrared-emitting long fluorescence lifetime probes. Toxicity test will be performed on these cells. Stained cells will be injected in the eye of a mouse model of PIOL, and we plan to observe them in the blood vessels of a mouse ear, as illustrated in Fig. I.19.

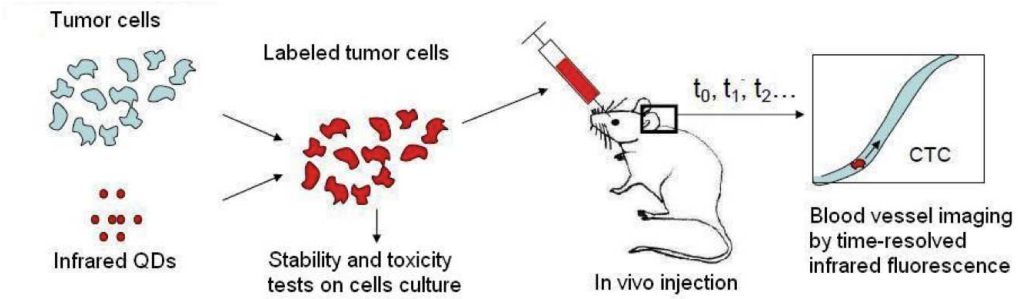

Figure I.19 – Scheme of the CTC detection principle using near-infrared-emitting nanoprobes coupled to time-gated detection (*Scheme from Thomas Pons*).

II

Near-infrared-emitting quantum dots for cell labelling

II.1 Introduction

In order to efficiently detect *in vivo* circulating tumour cells, we have to be highly sensitive. Fluorescence microscopy is a technique that is very sensitive. Nevertheless, this sensitivity is limited by the low visible light penetration depth and the tissue autofluorescence. In order to reduce these two limitations, the fluorescent probes must have well-defined specifications. Indeed, we need probes with an emission wavelength in the "optical therapeutic window" and that present long fluorescence lifetime compared to the autofluorescence one. Nanoprobes also have to be small (to massively charge biological cells), biocompatible and present a low cytotoxic. Finally, as we aim to track cells over a few days, they need to keep their chemical and photo-stability in a biological environment.

There are several materials that have an emission in the near-infrared region [44]. We can remove from the list organic molecules that have fluorescence lifetimes too close from the autofluorescence. Among the existing materials, we selected different near-infrared emission and long fluorescence lifetimes nanoparticles : silicon nanoparticles, rare earth doped nanoparticles and quantum dots.

Silicon nanoparticles have the advantage of being non cytotoxic and biodegradable. Indeed, in 2009, Park *et al.* have reported that silicon nanoparticules self-destruct in a mouse model into renally cleared components in a relatively short period of time with no evidence of toxicity [41]. Their fluorescence lifetime is long (around 1-10 μs) but their fluorescence quantum yield is not enough high to detect rare and individual event (around 10 %). Rare earth also have excitation and emission properties adapted for *in vivo* imaging. In 2013, Foucault-Collet *et al.* have synthesized near-infrared emitting lanthanides and have managed to obtain *in vitro* images of HeLa cells after probes incubation. Their fluorescence lifetime is long, however their diameter is high (a fraction of micrometer) and their fluorescence quantum yield is too low for our application of single cell tracking (a few percents) [45].

Quantum dots (QDs) are nanocrystals of semiconductors with an emission wavelength depending on their size and on their composition [46][47]. Their emission wavelength can be tuned from 300 nm to 5 μm. Because of their small size (around 5 to 10 nm), these nanocrystals present a different behaviour from the corresponding bulk semiconductor. QDs are composed of an inorganic core surrounded by an organic outer layer of surfactant molecules (ligands) which aims to ensure the colloidal dispersion and to passivate the QD surface. The small size of these nanocrystals

implies great importance of surface effects that can degrade the fluorescence. An interesting strategy to improve nanocrystals surface passivation, and thus preserve a high quantum yield, is their overgrowth with a shell of a second semiconductor (typically ZnS) resulting in core/shell systems.

A nanocrystal can be considered as a nano-sized quantum box in which electrons are confined. The wave function associated with an electron in a nanocrystal is less spread compared to the bulk semiconductor. The electron is confined which costs energy and induces an increase of the band gap. This affects the electronic structure and tends to separate the electronic levels from each other, especially as the radius of the nanocrystal gets smaller: this effect is called quantum confinement. This leads to a red shift of the QD fluorescence as the size increases.

In the last few years, quantum dots have been used for biological applications [48][49] because they combine a high resistance to photobleaching and interesting optical properties. Figure II.1 shows a HeLa cell previously labelled with the Green Fluorescence Protein (GFP) on the top and with QDs on the bottom. The cell stained with QDs can be observed for a longer time compared to the GFP cell that photobleaches more rapidly.

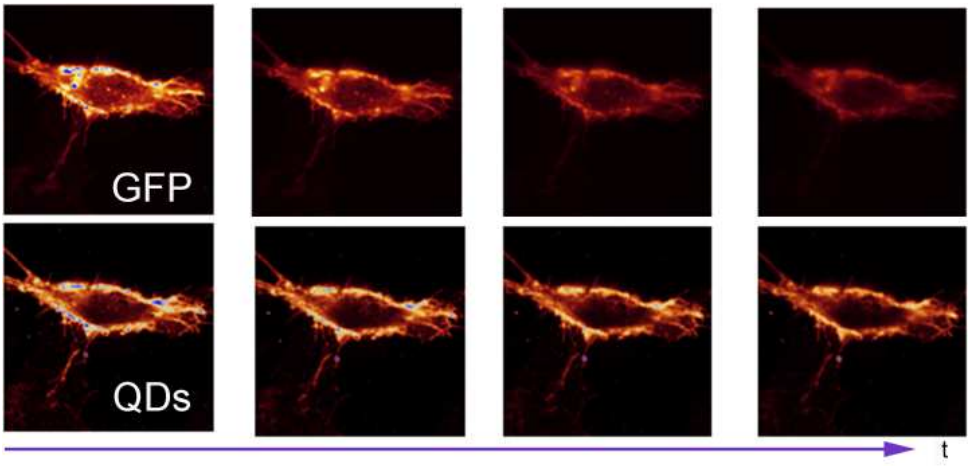

Figure II.1 – Comparision of the photobleaching between a cell stained with GFP (on the top) and QDs (on the bottom). *Images from Alexandra Fragola.*

Many nanocrystals have a bandgap which yields an emission wavelength in the near-infrared region [50]: CdHgTe/ZnS [51], InAs [52] and CdTe [53]. However, the use of these kind of materials is limited because of the high toxicity of their heavy metals composition such as lead, cadmium or arsenic. Indium phosphide (InP) seems a good alternative as it can theorically reach emission wavelengths in

the optical therapeutic window. Unfortunately, the phosphorus precursors are rare and expensive [54], or release a deadly gas PH_3 during the reaction [55]. Moreover, it is difficult to provide InP nanocrystals big enough to reach near-infrared emission wavelength.

New types of quantum dots, commonly called I-III-VI (because of their chemical composition) have been synthesized [56][57][58]. They have the advantage of being composed of low toxic elements and their emission is tunable from green to near-infrared regions. $CuInSe_2$ nanocrystals have a bandgap of 1.04 eV at 300 K (corresponding to a theoretical maximum emission wavelength of 1.2 μm) and their Bohr radius is equal to 5.4 nm, which enables the confinement regime for smaller nanocrystals sizes. These materials have first been used for solar cells because of their low cost, abundance, optimal bandgap energy and their broad absorption spectra [59][60]. Then, they have been synthesized as colloidal nanocrystals via different methods : precursors decomposition [61][62][63], autoclave [64] or high temperature injection in organic medium [65]. Several groups have been interested in these materials and have worked on their synthesis in order to improve their fluorescence quantum yield [65][66][67]. A solution to increase the fluorescence quantum yield was to add a shell, with a higher bandgap, around the core in order to confine the charges (electrons and holes) inside the cores [58][68]. This shell also allowed the preservation of the fluorescence properties after solubilization in water for *in vivo* biological fluorescence imaging [56][58][68][69][70].

Furthermore, most of the reported QDs syntheses are performed in organic solvent. Thus, QDs are surrounded by long organic strings as ligands and are not directly biocompatible. For this reason, we have to modify the quantum dots surface to provide biocompatible nanocrystals. It has been shown that QD surface chemistry is not only responsible for the biocompatibility but also for the toxicity since it determines the biodistribution [71]. The ligand has to present different functions: one part which allows the QDs anchoring and another hydrophilic part which allows the water solubilization and biocompatibility. There are two main techniques [72] to water-solubilize nanoparticles: QDs encapsulation in amphiphilic polymers or phospholipid surfactants and ligand exchange [73][74].

This chapter will focus on the synthesis and characterization of nanocrystals and on their water solubilization before cell labelling. We will show that this type of quantum dots have adapted optical properties for *in vivo* time-gated and cell tracking imaging. We will then describe our chosen method in order to massively

label cells with near-infrared-emitting quantum dots (NIR QDs) previously made biocompatible using a ligand exchange.

II.2 Zn-Cu-In-Se cores

II.2.1 Synthesis

The core synthesis is inspired from the synthesis that Elsa Cassette *et al.* developed three years ago in our lab [58]. For this synthesis, all metal precursors (copper chloride, indium chloride, selenourea and zinc acetate) are mixed together in a three-neck flask in the presence of a solvent (octadecene) and some ligands (oleylamine, trioctyphosphine and dodecanethiol). The solution is heated at 265°C. Figure II.2 shows a scheme of the set up used for quantum dots synthesis. The solvent commonly used for quantum dots synthesis is the octadecene (ODE) because its boiling point is sufficiently high (around 315°C). Trioctylphosphine (TOP) behaves as a ligand. Oleylamine (OLA) acts as a ligand and also activates the reaction with the selenium precursor. Dodecanethiol (DDT) has a high boiling point (280°C) and stabilizes the nanocrystals during the temperature increase. Figure II.3 presents the chemical formula of the different molecules used during the core synthesis. The nanocrystals are formed from 90°C where the solution becomes yellow then red at 120°C and brown at 200°C (see Fig II.4). The nucleation and growth of the nanocrystals occur as the temperature increases. Figure II.5 shows the normalized photoluminescence spectra of Zn-Cu-In-Se cores with respect to the temperature. The more the temperature increases, the more the nanocrystals emit in the near-infrared region because of the quantum confinement. Heating is stopped immediately after the targeted emission wavelength is reached (about 820 nm) and the flask is quickly cooled down to room temperature to stop the reaction.

Cu-In-Se nanocrystals emission is due to defects or other trap states in the crystal structure. These defects are also responsible for the low fluorescence quantum yield and create deep-traps for the exciton. We noted that the incorporation of zinc during the core synthesis improves a lot the fluorescence quantum yield [75][76]. This may be attributed to defect passivation and filling of vacancy sites by Zn atoms inside the core. Figure II.6 shows the emission spectra divided by the absorbance at the excitation wavelength of CuInSe cores from Cassette *et al.* synthesis and Zn-Cu-In-Se cores I have developed. This figure shows that for the same emission wavelength Zn-Cu-In-Se cores are brighter up to 7 times than CuInSe cores without zinc.

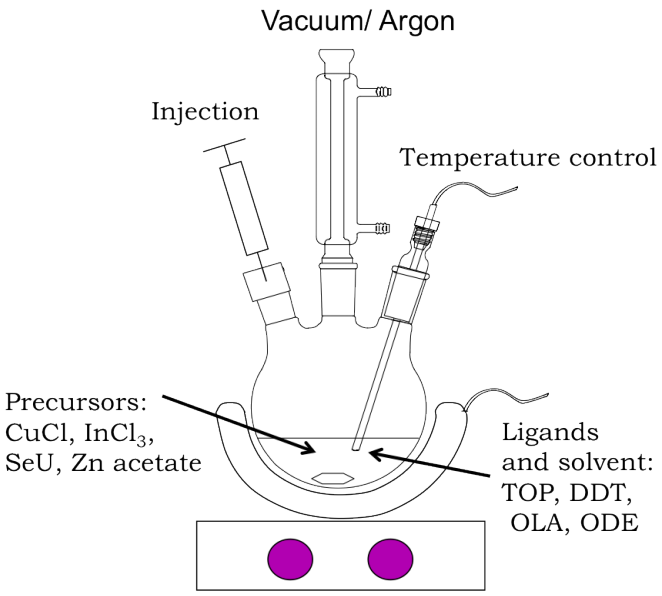

Figure II.2 – Experimental set up for the QDs synthesis.

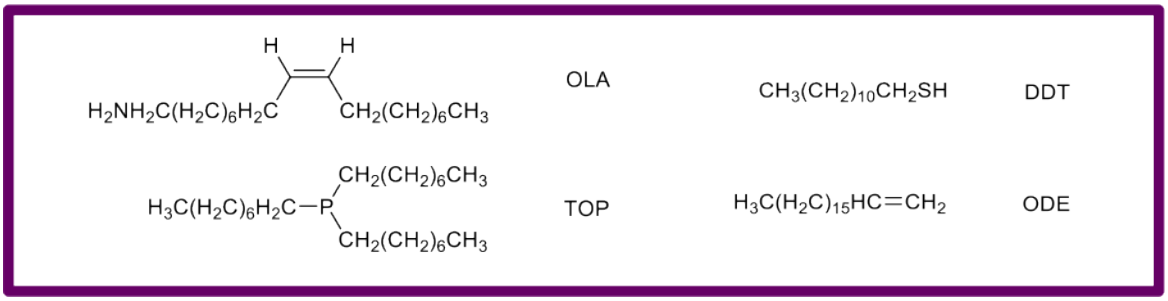

Figure II.3 – Chemical formula of the different ligands and solvents used for core synthesis.

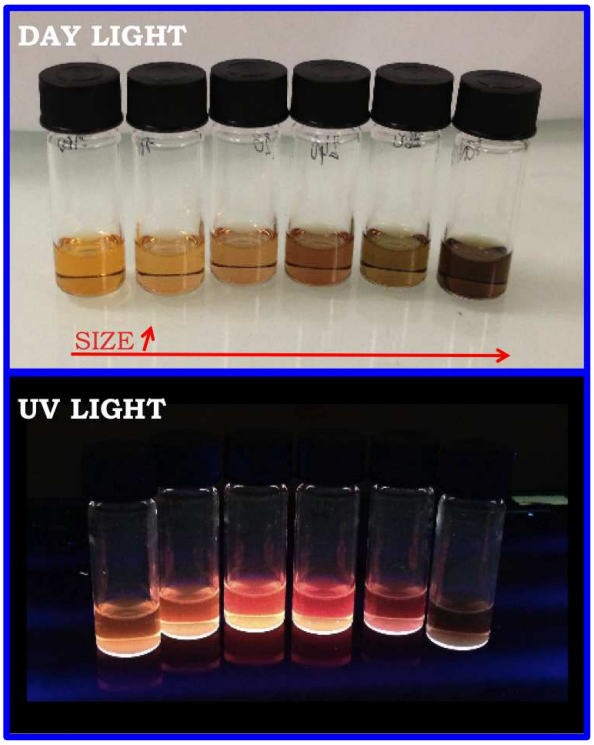

Figure II.4 – Colloidal nanocrystals in hexane obtained at different temperatures under visible light (top) and UV lamp excitation (bottom).

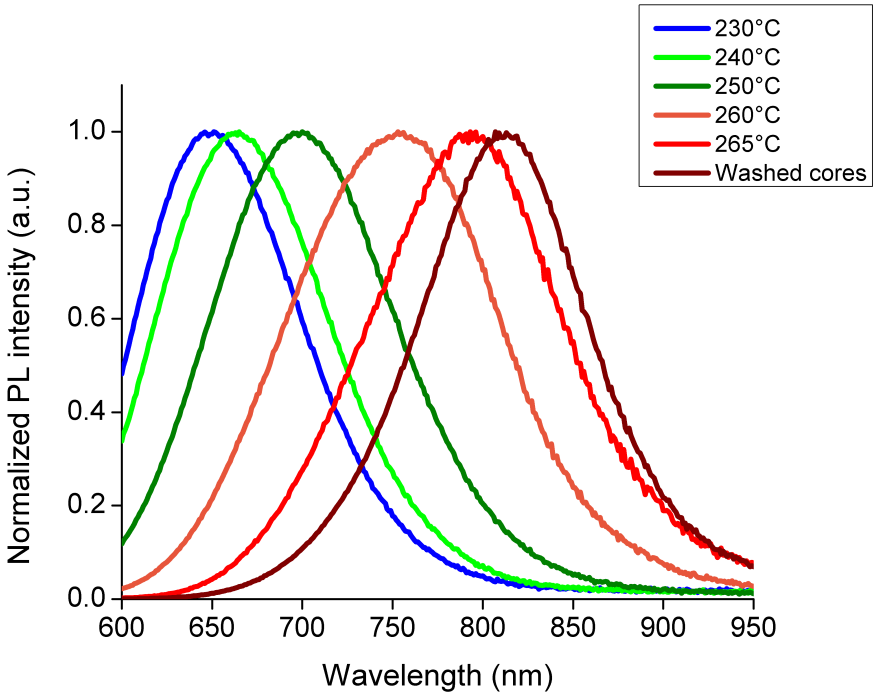

Figure II.5 – Normalized photoluminescence (PL) intensity spectra of Zn-Cu-In-Se cores obtained at different temperatures.

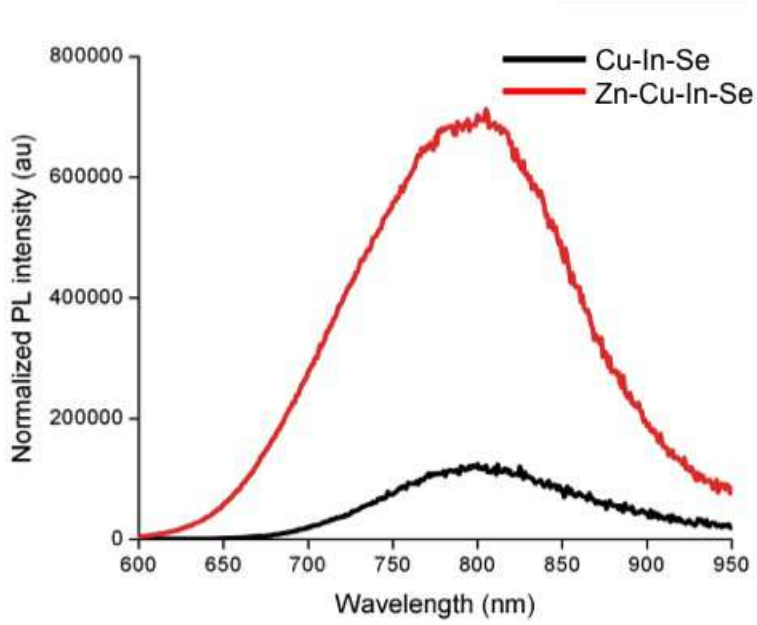

Figure II.6 – Photoluminescence (PL) intensity spectra normalized by the absorbance at the excitation wavelength of Zn-Cu-In-Se cores and CuInSe cores.

II.2.2 Structural properties

We have characterized the Zn-Cu-In-Se nanocrystals using several techniques:

- X-ray diffraction (XRD) informs us about the cristallographic structure and alloy composition,
- transmission electronic microscopy (TEM) allows us to determine the shape and to estimate the size distribution,
- energy dispersive X-ray spectrometry (EDX) is an analytical technique used for the elemental analysis or chemical element characterization of a sample.

X-ray diffraction (XRD)

This method uses an X-ray beam that interacts with the crystal. It causes the diffraction of the light beam in specific directions. The angles and the intensity of the diffracted rays are measured. By comparing the diffractogram obtained with reference crystal peaks, we determine the cristallographic structure of our crystal.

I-III-VI semiconductors generally have a chalcopyrite cristallographic structure as described in the scheme II.7(a). It corresponds to a quadratic structure. I-III-VI semiconductors can also exist in a cubic structure called zinc blende. Cations

(Copper, Indium and Zinc), represented as grey atoms in Scheme II.7(b), form a face-centered cubic lattice. Compared to the chalcopyrite structure, cations are located in the center of half tetraedric sites formed by the selenium atoms network (yellow atoms) and also form a face-centred cubic lattice. In this case, it forms a cubic structure because the cations are not ordered.

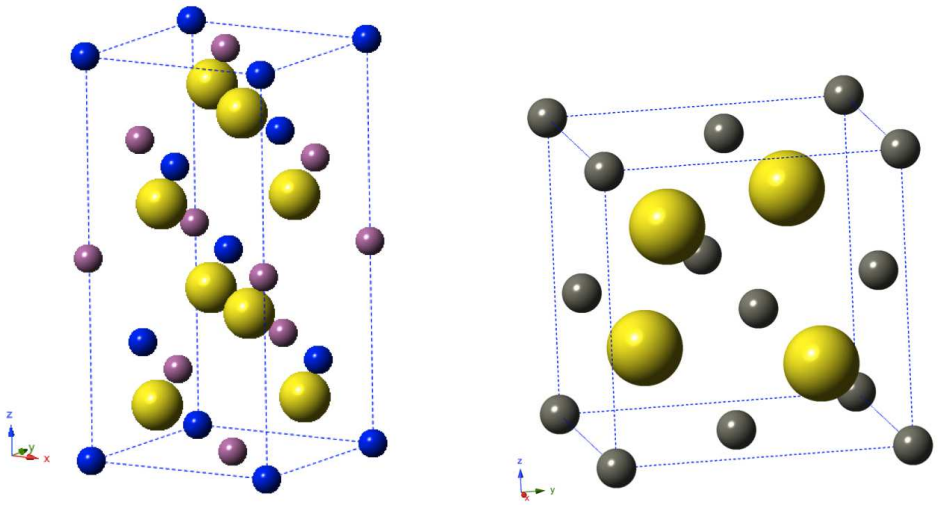

(a) (b)

Figure II.7 – Scheme of the different cristallographic structures for Cu-In-Se based nanocrystals. a) Quadratic structure. b) Cubic structure. Yellow atoms stand for selenium atoms, grey atoms, blue atoms and pink atoms stand for cations.

In order to determine the crystallographic structure of our cores we performed X-ray diffraction measurements. Figure II.8 presents a diffractogram of our cores in purple and the reference peaks of cubic $CuInSe_2$ and ZnSe. Our core nanocrystals diffractogram fits well with the $CuInSe_2$ and ZnSe diffractograms in cubic structure as shown in Fig. II.8 (cyan and orange peaks). We can now determine the percentage of each element in the alloy using Vegard's law (see Appendix A). This law gives a relationship between the crystal lattice parameter of an alloy and the proportions of the constituent elements. If we assume that our QDs are an alloy of $CuInSe_2$ and ZnSe, we obtain as composition 56% of $CuInSe_2$ and 44% of ZnSe in cubic structure. Using these results we can determine the ratio between each elements, as show in Table II.1.

These data allow us to determine the cores composition and density and estimate the cores concentration (see Appendix A).

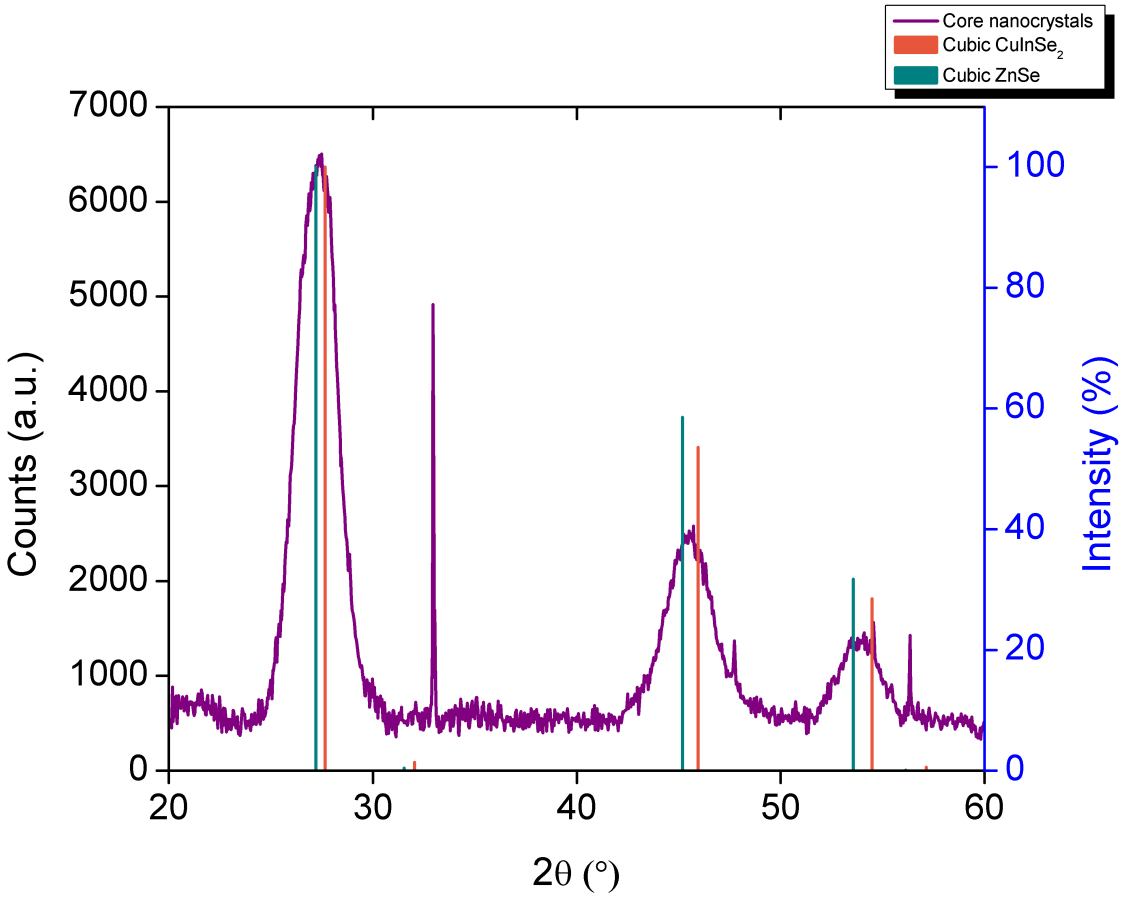

Figure II.8 – Diffractogram of Zn-Cu-In-Se core nanocrystals and reference peaks of cubic $CuInSe_2$ and ZnSe nanocrystals (*PDF 01-088-2345 (ZnSe) and PDF 01-070-3084 ($CuInSe_2$)*).

Cu/Zn	Cu/Se
1.27	0.36

Table II.1 – Ratios between the different elements that compose the cores obtained using the Vegard's law.

We conclude that the cores are composed of an alloy of 56% of $CuInSe_2$ and 44% of ZnSe in cubic structure.

Transmission Electron Microscopy

Transmission electron microscopy (TEM) is a technique in which a beam of electrons is transmitted through a thin sample. The beam of electrons interacts with the sample as it passes through. An image is formed with the electrons transmitted through the sample.

We can determine the nanoparticle shape and size using transmission electron microscopy (TEM). Figure II.9 presents TEM images of the Zn-Cu-In-Se at different magnifications. The higher magnification allows us to visualize the crystalline planes of our cores. The cores have a diameter of 4.1±0.4 nm.

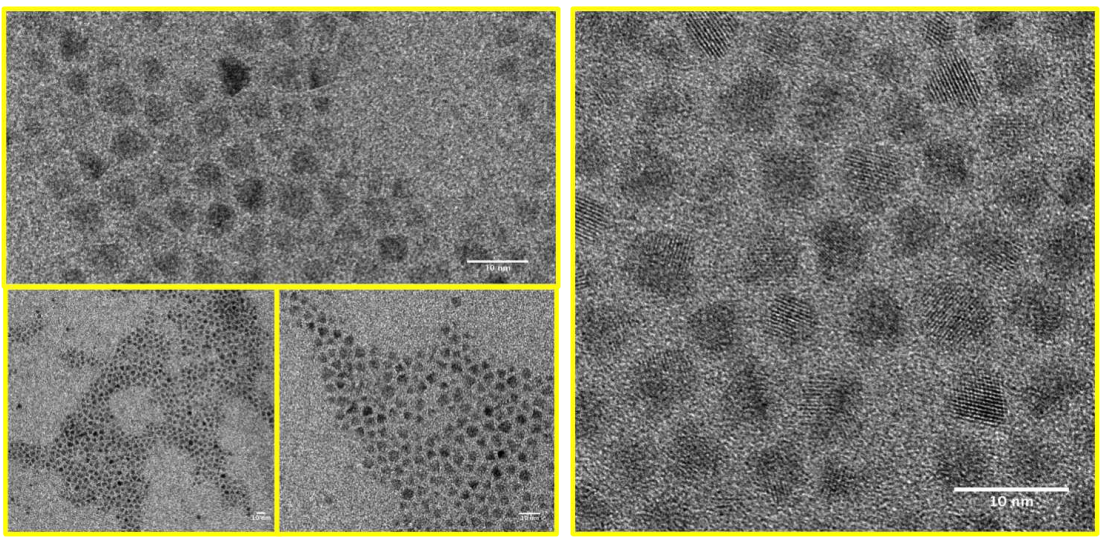

(a) (b)

Figure II.9 – TEM images of Zn-Cu-In-Se core nanocrystals (scale bars: 10 nm).

EDX measurements

In EDX measurements, an incident electron beam excites a core electron of an atom, ejecting it and thus creating an electron hole where the electron was. An electron from an outer higher-energy orbital fills the hole, and the energy difference may be released in the form of an X-ray. The number and energy of the X-rays emitted from a transition can be measured by an energy-dispersive spectrometer. Since the X-rays energy is characteristic of the energy difference between the two electronic levels and of the electronic structure of the element. This allows us to determine the relative composition of the sample measured.

The different ratios between all elements present in the cores are presented in the table II.2.

Cu/In	Cu/Zn	Cu/Se	Cu/S
1.10±0.05	1.020± 0.002	0.61± 0.03	0.470±0.003

Table II.2 – Ratios between the different elements that compose the cores

These results confirm the presence of zinc in high quantity in the cores. However, these results are slightly different from those obtained in XRD. The ratio Cu/S reports the presence of sulfur in our cores samples. The presence of sulfur may be attributed to the dodecanethiol as ligand or to the dodecanthiol that can be decomposed and incorporated in the core during the synthesis. However, if the amount of sulfur was higher, XRD peaks would have been shifted to the higher angles because ZnS or $CuInS_2$ have a smaller lattice parameter (Bragg's law). Therefore, for the concentration calculation we will consider that the cores are only composed of $CuInSe_2$ and ZnSe (see Appendix A).

This analysis confirms the presence of copper, indium, selenium and zinc in the cores, as observed in XRD. This also confirms a high incorporation of zinc in the core nanocrystals.

II.3 ZnS shell

In order to preserve the fluorescence and minimize the oxidation when a ligand exchange is performed, it was necessary to add a shell of another semiconductor material. The choice of the shell material depends on two main criteria. First, it has to have a larger bandgap in order to confine the charges (electron and hole)

inside the core. Second it has to have a lattice parameter close to the core's one in order to allow the growth.

Zinc sulfide is a good candidate with a bandgap of 3.61 eV and a lattice parameter of 5.41 Å (5.78 Å for $CuInSe_2$) [47]. Moreover, it is composed of non toxic elements and has a good resistance towards oxidation allowing a better photostability. A final argument for the choice of a ZnS shell is the good affinity of the cationic atoms (Zn^{2+}) with the dithiol function of the anchoring function of the poly(dithiol-co-sulfobetaine) ligand noted PDSB, used for water solubilization.

II.3.1 Synthesis

The precursors synthesis is described in the Protocols chapter and their formula are illustrated in Fig.II.10.

For the shell synthesis, 4 mL of as-prepared cores was dispersed in 4mL of ODE and 1mL OAm into a new three-neck flask. The mixture is degassed under vacuum at 40°C. A solution of zinc ethylxanthate ($Zn(EtX)_2$) and zinc oleate ($Zn(OA)_2$) (0.13 and 0.8 mmol, respectively) dissolved in ODE (2 mL), TOP (3 mL), and dioctylamine (1 mL) is loaded into an injection syringe. The dioctylamine is added to facilitate the precursors dissolution in ODE.

The flask is heated to 190°C under argon atmosphere and these ZnS precursors are added dropwise during one hour. At the end of the injection, the reaction flask is cooled down to room temperature. The resulting Zn-Cu-In-Se/ZnS QDs are finally precipitated with ethanol and redispersed in 10 mL of hexane.

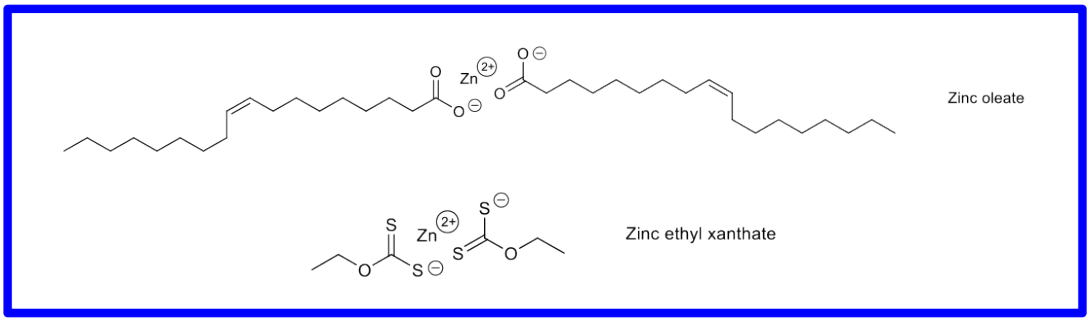

Figure II.10 – Chemical formulas of zinc and sulfur precursors used for the shell synthesis.

II.3.2 Structural properties

Transmission electron micrscopy images

In order to verify the presence of a shell around our cores, we performed transmission electronic microscopy (TEM). Indeed, the size of the core is compared to the size of the resulting core/shell. Because of the size dispersion and their low contrast in TEM we did not observe a significant size difference between the core and the core/shell nanocrystals. The ZnS shell must be thin. TEM images do not show nucleation of ZnS as illustrated in Fig.II.11. From TEM data, we estimated the NIR QDs diameter to be 4.5 ± 0.3 nm.

In order to verify the presence of a shell around our cores we performed XRD analysis and optical spectroscopy characterizations.

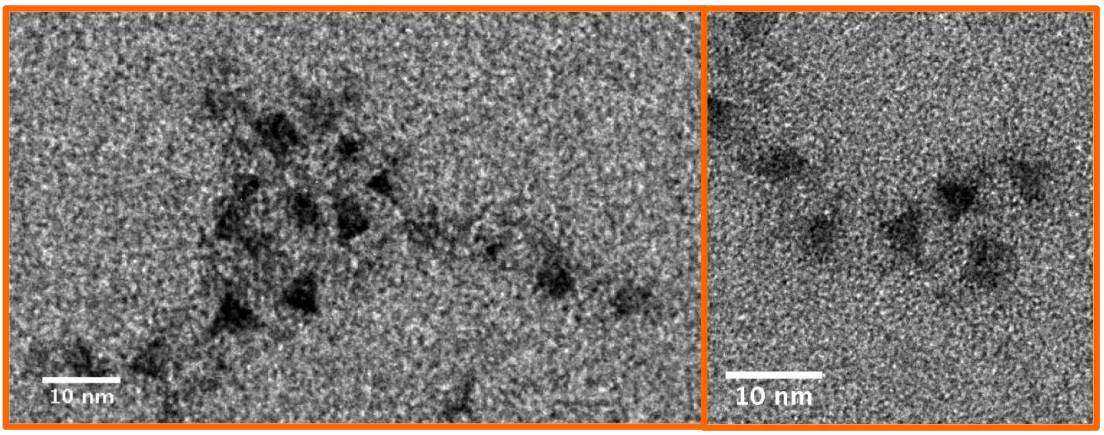

Figure II.11 – TEM images of core/shell nanocrystals at different magnifications.

XRD measurements

The Zn-Cu-In-Se/ZnS nanocrystals synthesized were analysed by XRD (Fig.II.12). The purple and orange curves are respectively the diffractograms of the core nanocrystals and the core/shell nanocrystals. The synthesis retains the crystalline structure of the core. The shift of the core/shell nanocrystals peaks with respect to those of the cores, indicates a slight decrease of the lattice parameter. This is consistent with the growth of a ZnS shell on Zn-Cu-In-Se cores since ZnS has a smaller lattice parameter. This is in favor of a ZnS shell growth or at least incorporation of these elements in the crystal. However, the core/shell nanocrystals peaks width is similar to the core nanocrystals ones. This suggests that the shell is very thin, limited to a few monolayers.

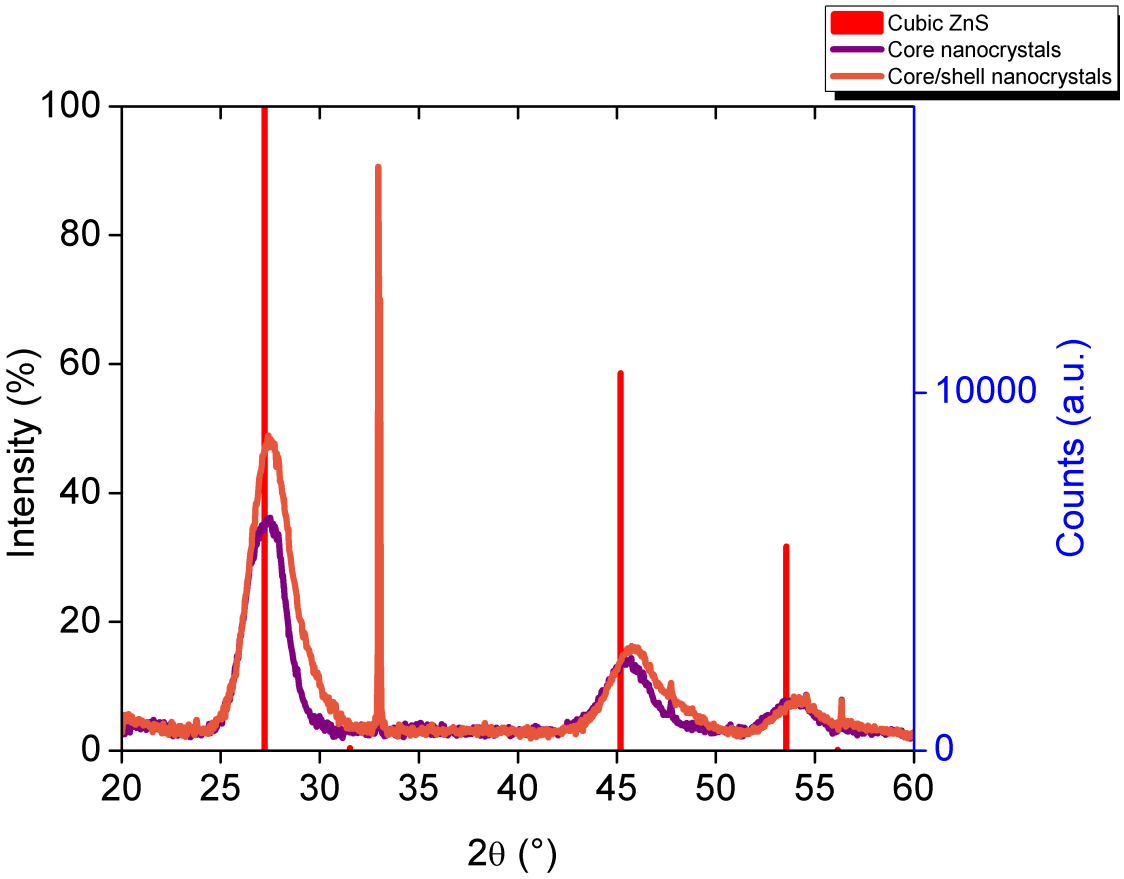

Figure II.12 – Diffractograms of Zn-Cu-In-Se cores (in purple) and Zn-Cu-In-Se/ZnS core/shell (in orange).

EDX measurements

We also performed EDX measurements in order to determine the composition of the core/shell nanocrystals. Table II.3 presents the different ratios between all the chemical elements they are composed. The Cu/In and Cu/Se ratios are more or less preserved compared to the core nanocrystals. However, the ratios Zn/Cu and S/Cu inrease for the core/shell nanocrystals. This confirms the presence of ZnS and is consistent with the formation of a ZnS shell. The final Cu/Zn ratio allows us to estimate a shell thickness of about 0.5 nm, which is consistent with the TEM observations.

Cu/In	Cu/Zn	Cu/Se	Cu/S
0.98±0.11	0.10± 0.001	0.58± 0.02	0.11±0.008

Table II.3 – Ratios between the different elements that compose the core/shell nanocrystals

II.3.3 Spectral properties

We can characterize the shell growth by spectroscopy measurements.

By dividing the fluorescence spectra of the nanocrystals by their optical density at the excitation wavelength, we can see that the quantum yield of fluorescence increases during the growth of ZnS, up to 35 %, as shown in Figure II.13.

Figure II.14 represents the photoluminescence excitation spectra (PLE) of the core nanocrystals in purple and core/shell nanocrystals in orange normalized at 550 nm where only cores absorb. The increase of the PLE below 400 nm for the core/shell nanocrystals is characteristic of the presence of ZnS because ZnS absorb in this spectral range ($E_g = 3.54$ eV for ZnS in zinc blende structure).

To summarize, for the core/shell nanocrystals (and to compare with the only core ones), we observed:

- an increase of the absorbance below 400 nm,
- a peak shift in XRD measurements,
- an increase of the Zn/Cu and S/Cu ratios,
- an absence of secondary nucleation in TEM,
- an increase of the QY during the shell synthesis.

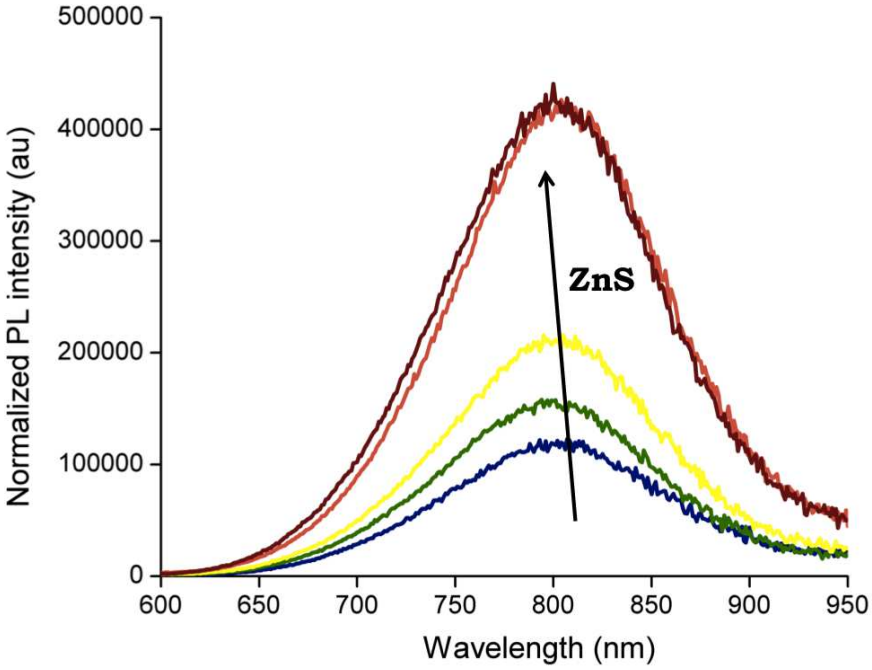

Figure II.13 – Fluorescence spectra normalized by the absorbance at the excitation wavelength of the nanocrystals Zn-Cu-In-Se cores before (blue curve) and during the progressive growth of a shell of ZnS (green to red curves).

All these observations suggest that a thin shell has grown around the core nanocrystals.

II.4 Influence of trap states on the optical properties

I-III-VI nanocrystals have a large full width at half maximum (FWHM) ranging between 110 and 150 nm. Many factors can cause this broadening of the emission spectra :

- the size dispersion of the nanocrystals,
- the composition dispersion,
- a non excitonic emission.

In the first two cases, the broadening is due to an ensemble effect while the last broadening is intrinsic to the nanocrystal and would be visible in single nanocrystals spectroscopy. Due to the ternary composition of nanocrystals, it is possible to have

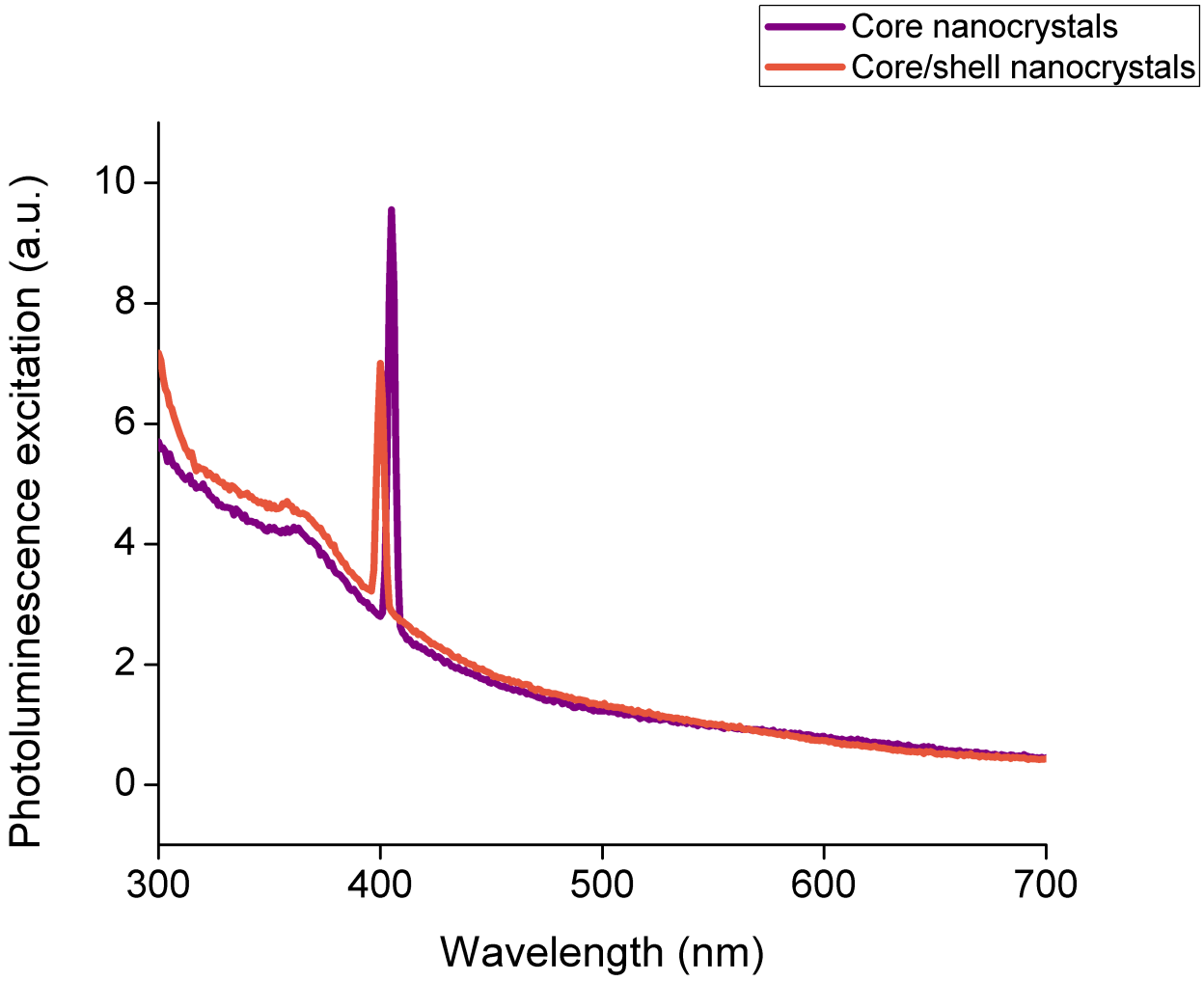

Figure II.14 – Photoluminescence excitation spectra of core nanocrystals (in purple) and core/shell nanocrystals (in orange).

some defects (vacancies, substitutions) in the crystal [77]. These can create a new distribution of trap energy levels located inside the bandgap. Radiative transitions can occur via these new levels, which will indeed lead to a broad emission due to the different defect levels present in a nanocrystal (see diagram in Fig. II.15). If the emission broadening is due to recombination via levels created by defects, these defects are not located at the surface of the nanocrystals. Indeed, if it was the case, the passivation of the cores by a shell of ZnS would sharpen emission spectra. This sharpening is not observed as shown in Fig. II.16.

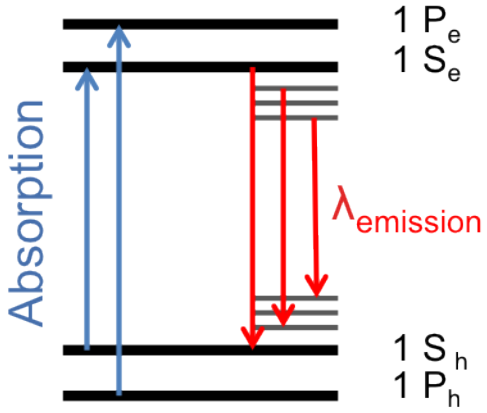

Figure II.15 – Scheme of the different possible radiative transitions. New energy levels can be created near the conduction and/or valence band because of the defects in the nanocrystals structure.

Another argument in favour of an emission due to energy levels created near to the conduction and/or the valence band is their long fluorescence lifetimes. The fluorescence intensity decays of NIR QDs are not monoexponential and present a high proportion of long component (between 80-95%), around 150 ns as shown in Fig.II.17. This long lifetime observed for core/shell nanocrystals is consistent with a transition involving an extended electron quantized state and a localized trapped hole [70]. This situation would be characterized by a large disparity in localization volumes of the electron and the hole that provides a reduced spatial overlap of their wave functions and a slow radiative decay according to the Fermi's golden rule.

We have reported the synthesis and characterization of long fluorescence lifetime and near-infrared quantum dots. They have a high fluorescence quantum yield (up to 35% in organic solvent) and are small. As this QDs synthesis is performed in organic solvent we have to modify the QD surface to provide biocompatible nanocrystals.

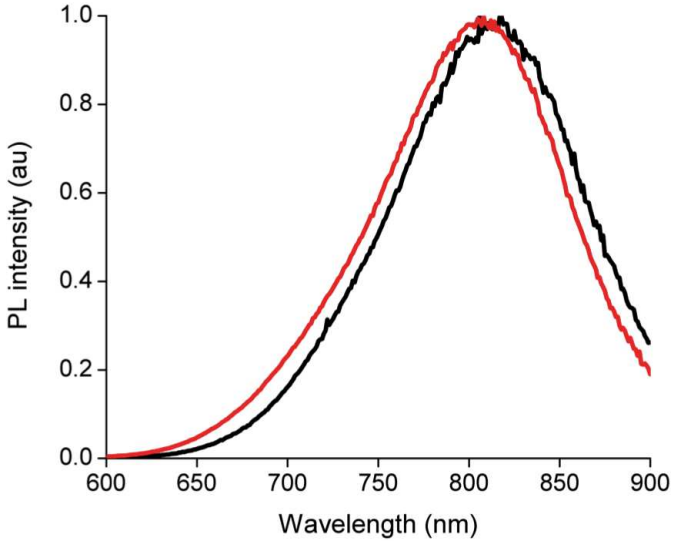

Figure II.16 – Photomumescence intensity of NIR emitting cores (in black) and core/shell nanocrystals (in red).

II.5 QDs as probes for biological applications

As we intend to track cells over a few days they need to be massively loaded with nanoprobes that are stable in the cell cytoplasm with time.

II.5.1 Solubilization in water

There are two main techniques to solubilize nanoparticles in water:

- QDs encapsulation in amphiphilic polymers or phospholipid surfactants,
- ligands exchange.

The hydrophobic part of the amphiphilic molecules used for encapsulation interacts with the organic shell of ligands at the QD surface whereas the hydrophilic part ensures the water solubilization as illustrated in Fig. II.18. Typically, quantum dots and amphiphilic molecules are mixed together in chloroform. Then, water is added and the chloroform is evaporated to induce micelle formation. This technique preserves QDs optical properties. Indeed, the hydrophobic shell formed by the synthesis ligands and the hydrophobic part of the polymer acts as a barrier against water molecules and oxidation. Nevertheless, the obtained systems are not very stable [78] because the hydrophilic interactions are weak and are thus not compatible with long term stability. Moreover, because of the polymer shell, the obtained

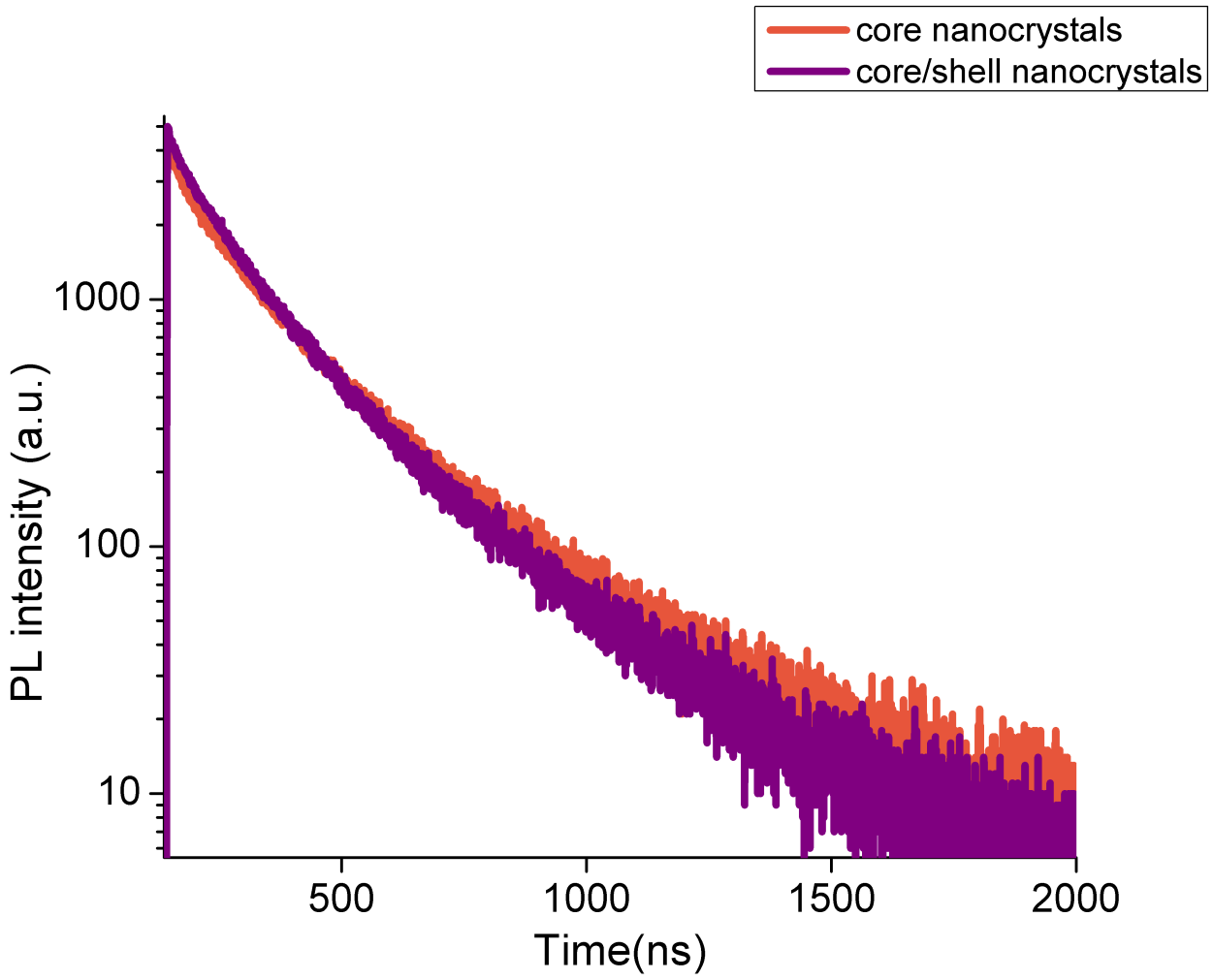

Figure II.17 – Photoluminescence intensity decay of NIR emitting cores (in orange) and core/shell nanocrystals (in purple).

systems present a high hydrodynamic radius which is not well adapted for biological applications such as protein targeting and renal clearance [79].

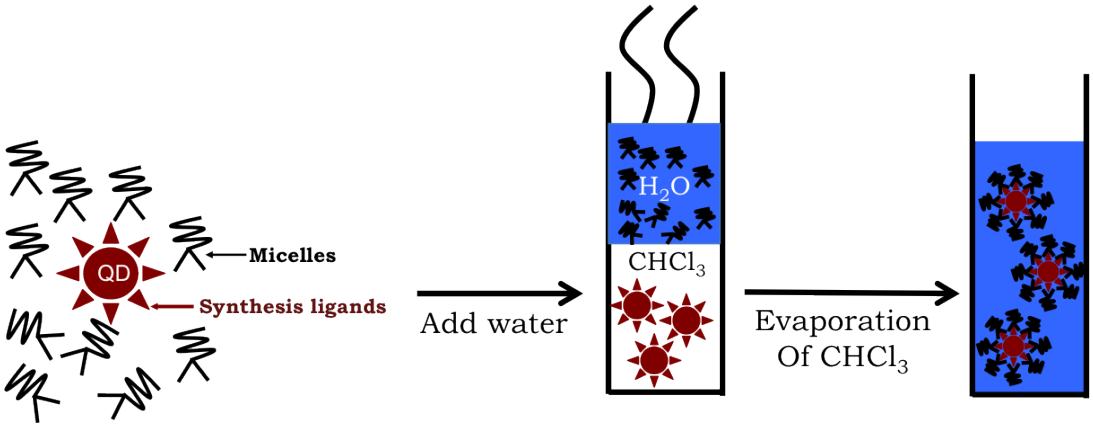

Figure II.18 – Scheme of encapsulation into micelles.

The other strategy consists in performing a ligand exchange. Ligand exchange consists in substituting the synthesis ligands by hydrophilic ones. In our laboratory, we have focused on ligand exchange as it leads to smaller and more stable QDs, including in an intracellular environment [78]. This technique is based on the balance between adsorption and desorption of the ligands at the surface of the nanocrystals in solution by addition of an excess of the new ligand. It consists in replacing initial hydrophobic ligands with hydrophilic ligands to make nanoparticles water-soluble. These ligands have two different parts : one group to anchor to the QD surface and another one to ensure the water solubilization. The anchoring part usually used is the thiol function because it has a good affinity with cationic metal ions (Zn^{2+}) at the QD surface [80][39]. In order to increase the anchoring strength, it has been proposed to use bidentate ligands such as the dihydrolipoic acid (DHLA) [74]. This ligand has a dithiol group which allows a stronger anchoring and provides a better stability (see Fig.II.19) .

Different solubilization chemical functions have been used. For DHLA, the solubilization is provided by the carboxylate function. The stability is due to electrostatic repulsion between negatively charged nanoparticles which prevents formation of aggregates. But this stability is reduced in saline medium by electrostatic screening. Moreover, these anionic groups can interact with positively charged biomacromolecules [74][81]. These electrostatic issues were resolved by the use of polyethylene glycol groups known to limit non specific interactions but to provide larger systems [82].

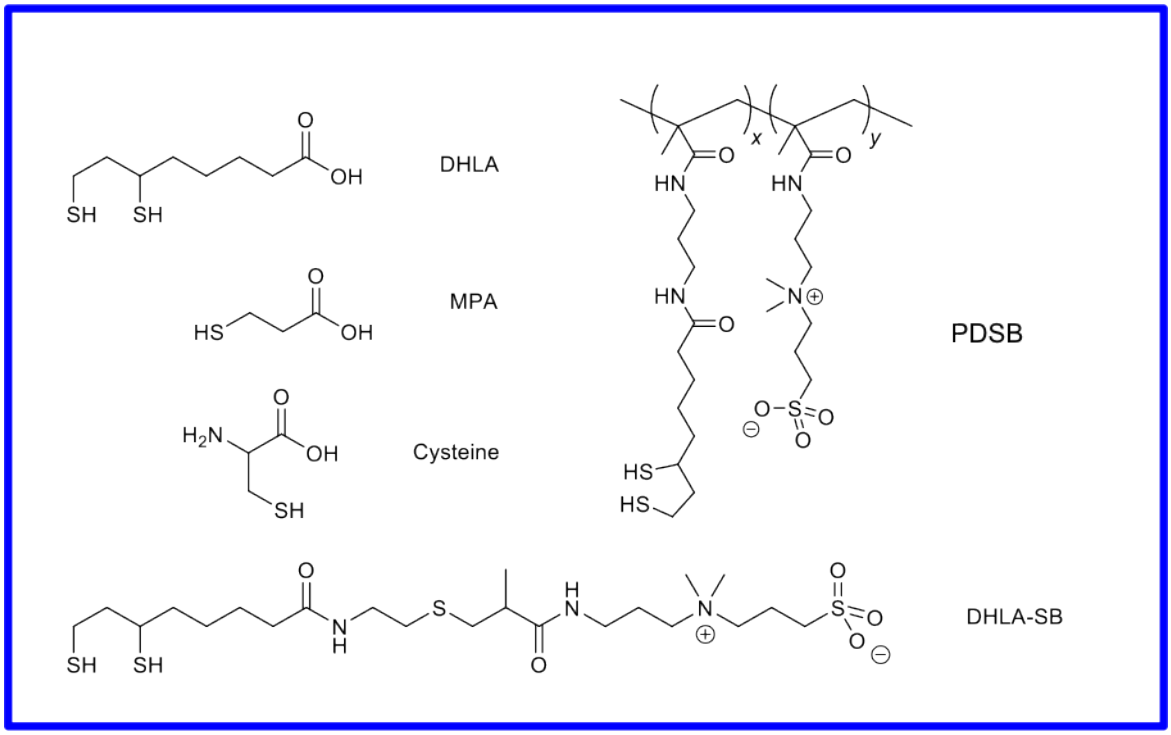

Figure II.19 – Chemical formula of the different ligands.

In order to obtain small and low non specific adsorption nanoparticles, zwitterionic groups are a good alternative. They are formed by a positive and a negative charge close to each other, which ensures a global neutral charge. In 2007, Bawendi *et al.* proposed to use the cysteine as a zwiterrionic ligand for QDs [83]. This ligand exhibits weak nonspecific interactions with proteins, small size and good resistance to pH variations and salinity. Nonetheless, QDs coated with cysteine quickly aggregate after a few days because of the low stability of monothiol anchor groups. For this reason, in the laboratory, Muro *et al.* developed a new ligand composed of a dithiol as an anchoring function and a zwitterionic part as a water solubilization function (DHLA-SB)[84]. The DHLA-SB-QDs were stable in a large pH range but started to aggregate after a few days in the cell cytoplasm. This can be attributed to a low stability in diluted media due to the ligand desorption. For this purpose, Giovanelli *et al.* have developed a new ligand, noted PDSB, with several anchoring and solubilization functions per ligand [85]. This ligand is a co-polymer composed of two monomers: one contains the dithiol functionand the other one includes the zwitterionic function in a 20/80 ratio (See the synthesis in the Protocol part). Moreover, the multiplicity of the different functions leads to a better QDs stability in diluted media and in the cell cytoplasm up to 54 hours after labelling.

Figure II.20 shows HeLa cells previously electroporated with CdSe/CdS/ZnS QDs coated with DHLA-SB (on the left) and CdSe/CdS/ZnS QDs coated with the PDSB (on the right), 54 hours after electroporation. The DHLA-SB-QDs start to aggregate in the cell cytoplasm whereas PDSB-QDs remain individualized, freely diffusing and homogeneously distributed in the cell cytoplasm.

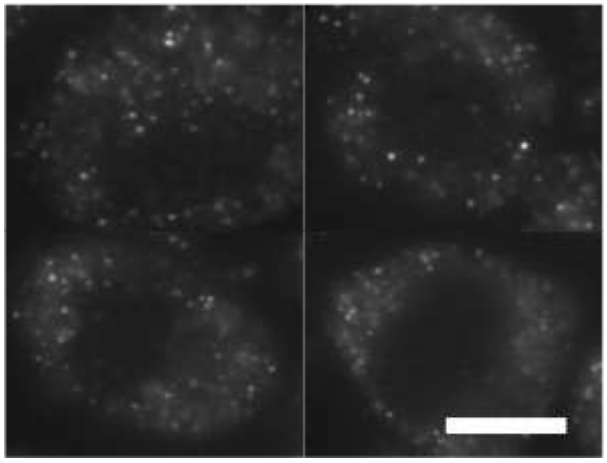

(a)

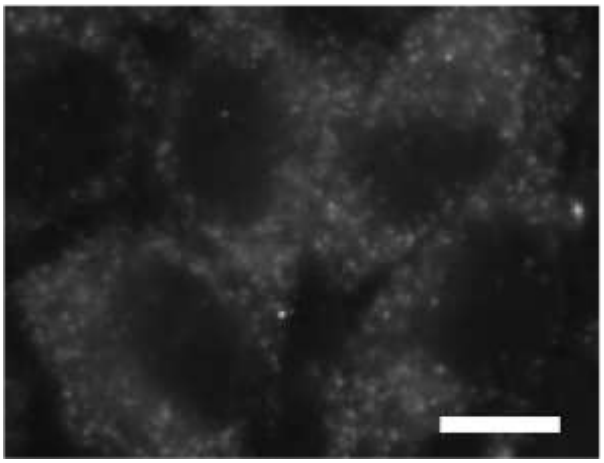

(b)

Figure II.20 – (a) Fluorescence microscopy images of HeLa cells, 54 hours after the electroporation with DHLA-SB-QDs. (b) Fluorescence microscopy images of HeLa cells, 54 hours after electroporation with PDSB-QDs. Scale bars 5 μm. (*Images from Eleonora Muro*).

For our application, we need long-term stable QDs. The ligand exchange can not be performed directly with the PDSB because of low organic solubility of the PDSB (more than 80% of hydrophilic part). Thus we have to perform a first ligand

exchange (with a weak ligand) to provide water soluble QDs. Then, the first ligand can be replaced with the strong ligand as shown in Fig.II.21. The detailed protocol of ligand exchange is described in the Protocols part.

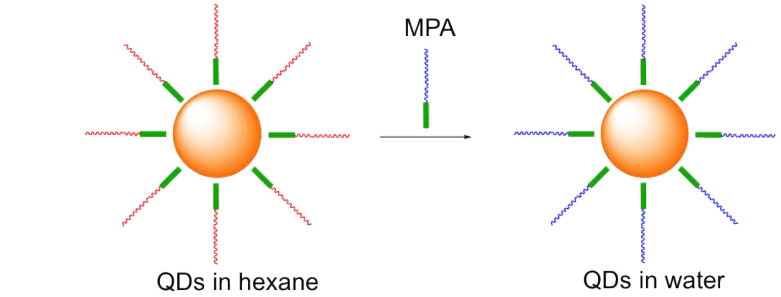

(a)

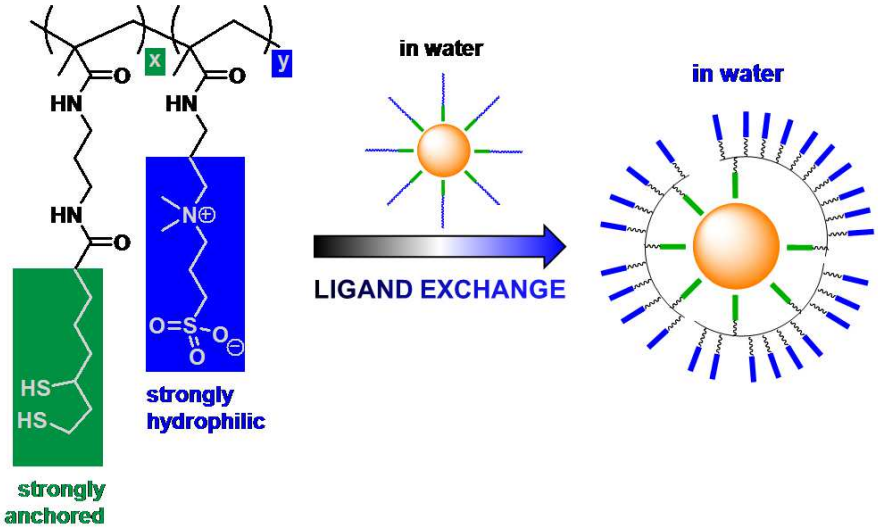

(b)

Figure II.21 – Scheme of the ligand exchange procedure. (a) First ligand exchange with mercaptopropionic acid to obtain water-soluble QDs (b) Second ligand exchange with PDSB (poly(dithiol-co-sulfobetaine) zwitterionic) ligand to provide long-term stable water-soluble QDs [85].

We have observed that the emission is slightly blue shifted after ligand exchange (see Fig.II.22), which could be attributed to a slight etching of the QD surface.

We used indocyanine green as a reference for quantum yield measurements because it emits in the near-infrared region. Fluorescence QY measurements gave typical values of 35% for QDs in hexane and 20% for QDs in aqueous solution after ligand exchange with an emission wavelength around 800 nm. All these properties make them interesting probes for cell labelling and *in vivo* imaging.

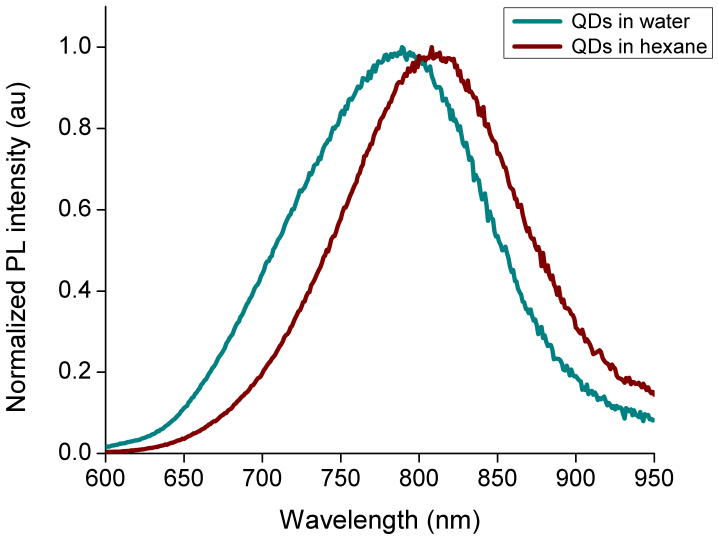

(a)

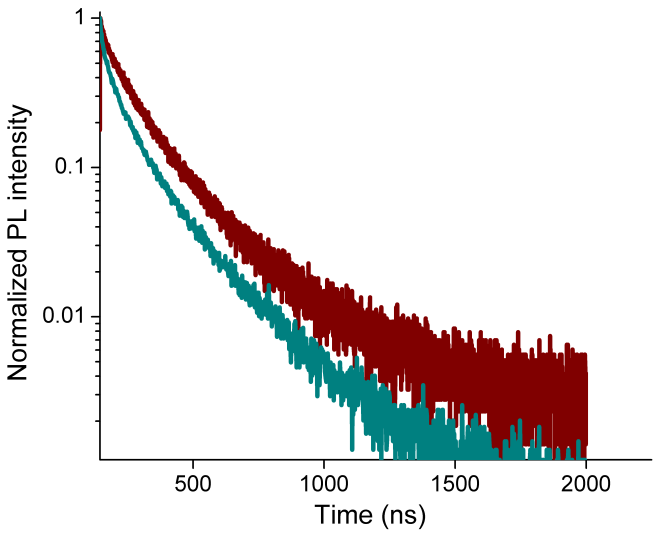

(b)

Figure II.22 – (a) Normalized Photoluminescence intensity spectra of NIR QDs in hexane (red curve) and in water (blue curve). (b) Normalized photoluminescence intensity decays of near-infrared-emitting quantum dots (NIR QDs) in hexane (red curve) and water (blue curve).

II.5.2 Cell labelling technique

Many techniques can be used to deliver QDs in the living cell cytoplasm. Many of them require the QDs functionalization in order to target membrane receptors and induce endocytosis. Nevertheless, there are other methods such as pynocytosis, microinjection or electroporation that allow QD delivery in the living cell cytoplasm without any supplementary modification of the QD surface. As we aim to track cells over a few days, they need to be massively loaded with nanoprobes. Indeed, because of cell division, which leads to a QD's dilution between two daughter cells, cells have to be initially loaded with a high number of nanoprobres.

Pinocytosis is a process that induces endocytosis using a hypertonic shock. This phenomenon allows the introduction of extracellular material inside the cell thanks to pynocytic vesicles broken in the cell cytoplasm by hypotonic shock. This allows the release of nanoparticles inside the cell. Delehanty *et al.* [86] have shown that this technique induces QD aggregation if the concentration is too high. Moreover, Eleonora Muro has noticed that the fluorescence signal strongly decreases with time compared to other delivery techniques. She observed that 24 hours after the internalization of the QDs by pinocytosis, the fluorescence signal measured was equal to 15 % of the initial value one hour after the delivery. The current hypothesis is the establishment of an active cellular process such as the exocytosis due to the hypotonic shock [87]. For this reason, we didn't choose pinocytosis as a labelling technique because we aim to track tumour cells over a few days and therefore need long term staining.

Microinjection is another way to deliver quantum dots into the cell cytoplasm. It allows the mechanical introduction of small volumes (around nL) of a high concentrated solution of QDs thanks to a capillary guided by fluorescence microscopy into the cell cytoplasm. This technique is of a low toxicity for cells, but each cell has to be injected individually which is not adapted for our applications.

Electroporation refers to the application of an external electric field that increases the permeability of the cell membrane's phospholipid bilayer by creating small holes, thus allowing the extracellular materials to directly enter the cytoplasm during an electric pulse by diffusion [88][89]. The pores then close and the cell membrane recovers more or less its integrity. Electroporation causes the loss of about one half of the initial cell population. As we want to track cells over a few days, we selected this technique because it provides cells that are massively loaded with QDs in their cytoplasm.

All electroporation experiments have been performed on 500,000 cells in suspension in a complete medium with various concentrations of QDs. Cells are placed in a 2 mm electroporation cuvette. The cuvette is subjected to a 0.15 kV (for HeLa cells) or a 0.13 kV (for A20 cells) pulse for about 30 ms using a Gene Pulser electroporator.

Electroporation experiments are a good means to compare the behaviour of different QD batches in the cell cytoplasm. It allowed us to quantitatively compare the two QD batches. The two QD solutions were prepared with identical optical density at the excitation wavelength. We performed electroporation on HeLa cells (because it is a cell line well-known in the laboratory and electroporation conditions were established by Eleonora Muro during her PhD). Figure II.23 presents fluorescence microscopy images of HeLa cells, 5 hours after electroporation with two different batches of NIR QDs. The top image corresponds to cells electroporated with NIR QDs composed of cores with a low percentage of zinc in their composition. The bottom image corresponds to cells electroporated with NIR QDs synthesized with our new protocol. Both images have been obtained with the same optical parameters (exposure time, objective, diaphragm aperture).

These images show that NIR QDs are still bright in the cell cytoplasm and are homogeneously distributed. We do not observe QDs aggregates, but instead QDs freely diffuse in the cell cytoplasm. These images also show that the new synthesis of NIR QDs provided us brighter QDs in the cell cytoplasm compared to QDs synthesized without zinc in their cores.

Once we demonstrated that Zn-Cu-In-Se/ZnS QDs are homogeneously distributed in the cell cytoplasm we wanted to determine the evolution of the QD signal in the cell cytoplasm with time. Cells were electroporated with NIR QDs and we imaged them over a few days. Figure II.24 shows images of living HeLa cells electroporated with NIR QDs, obtained at different times after the electroporation (5, 24, and 48 h). In order to visually compensate for the diminution of the fluorescence signal induced by QD dilution after each cell division, the intensity level of the middle image (24 h) was doubled and the level of the last image (48 h) was quadrupled according to the number of cell divisions. The original images exhibit average intensity levels compatible with one and two division stages and no leaking of QDs out of the cell. The images in Fig. II.24 show that NIR QDs coated with this surface chemistry stay bright and homogeneously distributed in the cell cytoplasm for several days. Moreover, while initial free-floating cells look round (Fig. II.24, 5 h), they become adherent on the coverslip the day after electroporation (Fig. II.24, 24 h). This,

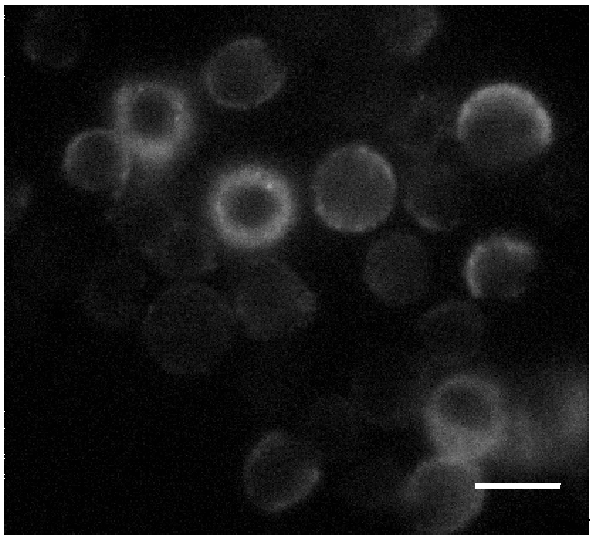

(a)

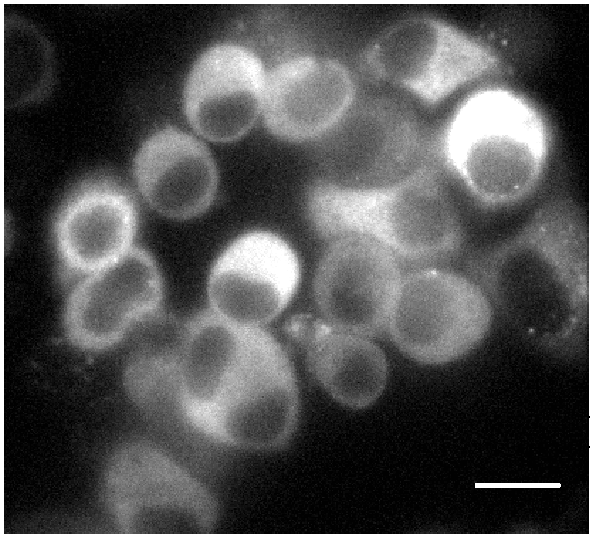

(b)

Figure II.23 – Fluorescence microscopy images of HeLa cells, 5 hours after electroporation. (a) Cells electroporated with Cu-In-Se/ZnS (b) Cells electroporated with Zn-Cu-In-Se/ZnS. Scale bar = 16 μm.

together with their preserved mitotic activity, suggests a low level of toxicity. In order to determine the NIR QDs toxicity we performed two types of tests described in the next section.

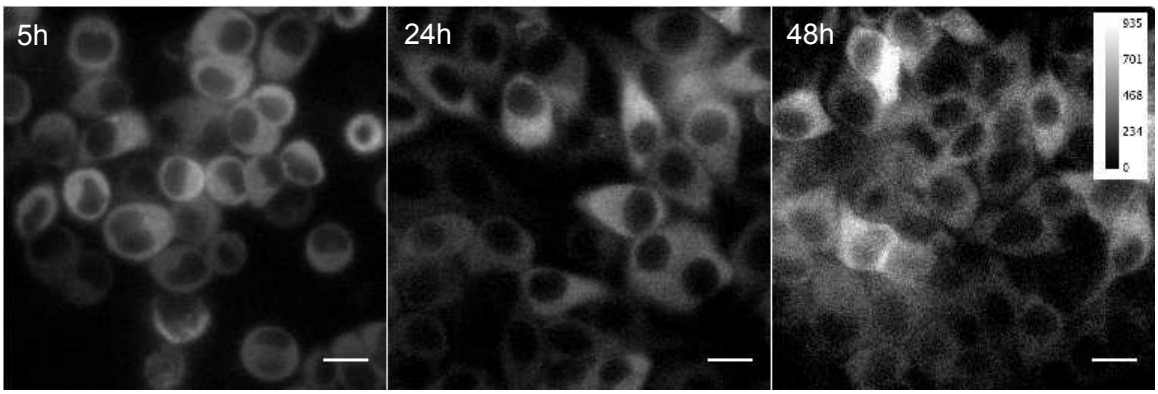

Figure II.24 – Fluorescence microscopy images of HeLa cells electroporated with NIR QDs at different times after the electroporation: 5, 24, and 48 h. Scale bar: 16 μm.

II.5.3 QDs toxicity

For the Primary Intraocular Lymphoma (PIOL) application, the group of Sylvain Fisson has developed and characterized a murine model of the PIOL [16]. In this model, the injection of T-lymphocytes, called A20 cells, in the eye of a mouse creates the eye tumour. Because we want to use these cells for *in vivo* studies, we performed toxicity tests on this cell line. Many toxicity tests have been done on visible CdSe nanocrystals [90][91] and near-infrared cadmium based quantum dots [92]. But to our knowledge, few groups have studied I-III-VI cytotoxicity. The toxicity is evaluated by two tests. The first one, using FACS, compares the percentage of live cells in each sample. The second one, an MTT assay, compares the number and metabolismof cells in each sample.

FACS measurements: testing the percentage of live cells

We decided to evaluate the NIR QDs toxicity in the cell cytoplasm of A20 cells at different times after electroporation. For this, we compared the cell viability of two samples over time:

- cells electroporated with NIR QDs called QD-electroporated cells
- cells electroporated without NIR QDs called control cells.

We incubated the different samples with a 1 nM solution of fluorescence dead cell dye emitting at 530 nm. The fluorescent dead cell dye is diluted in complete medium for incubation. SYTOX Green nucleic acid stain is a high-affinity nucleic acid stain that easily penetrates cells with compromised plasma membranes and yet will not cross the membranes of living cells. After 10 minutes of incubation, we centrifuge our solution in order to replace complete medium with medium without FBS, which is recommended in FACS measurements. We measured cell viability after electroporation. The obtained data are not quantitative and only aims to compare the percentage of live cells for the two samples at different time after electroporation.

Flow cytometry allows the precise study of individual cells previously labelled with a fluorophore and moving through a flow channel. The cell suspension (see Fig. II.25) is entrained in the center of a narrow, rapidly flowing stream of liquid. A nozzle tip allows the cell alignment before the analysis by fluorescence. A laser illuminates the cell and the response is measured by two detectors placed at 90°with respect to

each other. The forward scatter (FSC) intensity value gives an information about the size of the cells. The side scatter (SSC) intensity value gives an information about the cell granulometry.

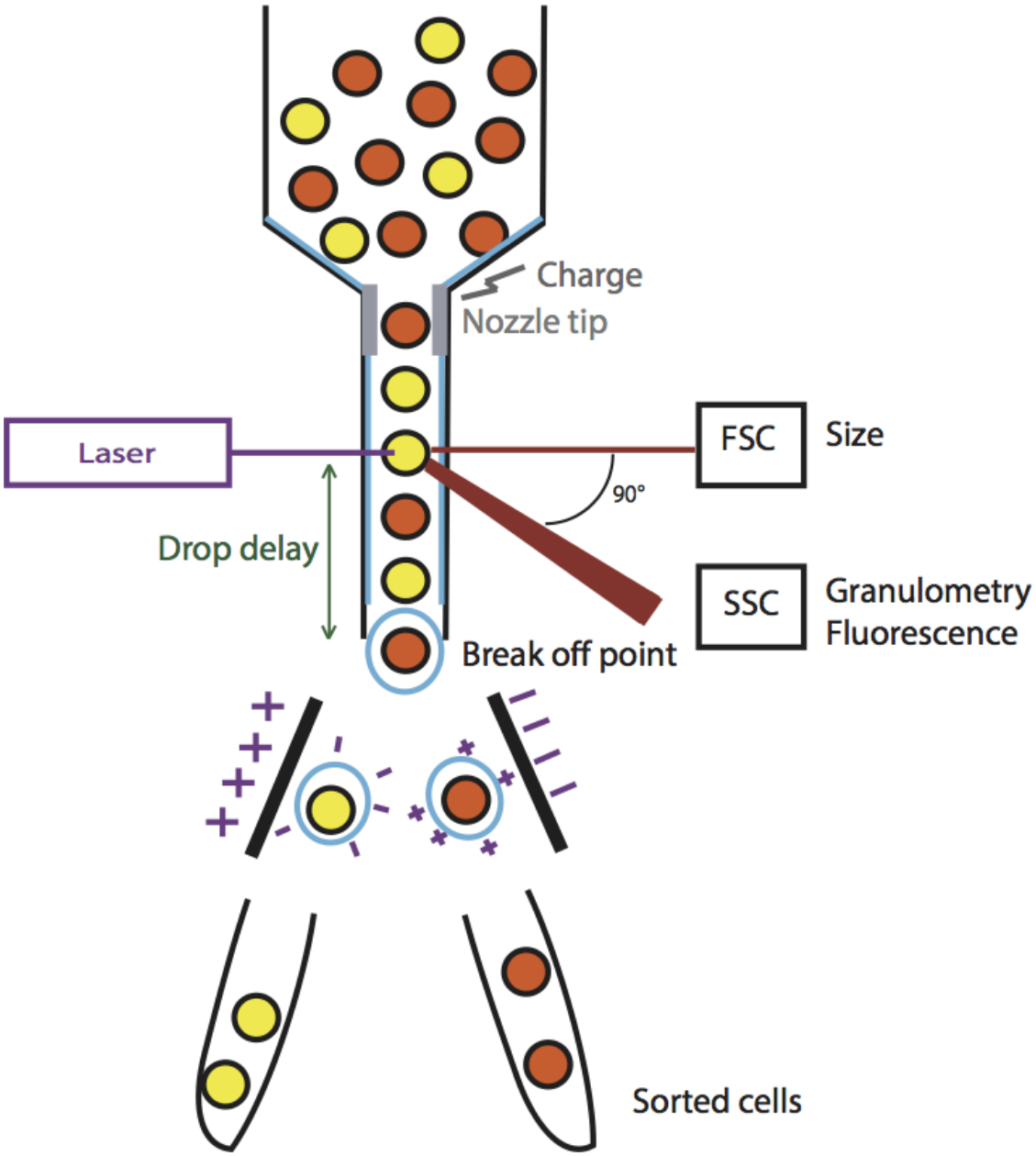

Figure II.25 – Flow cytometry scheme principle.

Figure II.26 presents FACS data for the two measured samples at different times after electroporation. We chose to represent the mortality dye signal together with the forward scattering signal, which is representative of the cell size. First, we eliminated all cell doublets by plotting the amplitude of the FSC signal as a function

of the area of the FSC signal. All events that are not in the diagonal is considered as doublet. The doublet treatment is performed in order to discriminate an autofluorescence signal from a fluorescent interest signal and is commonly done for FACS data treatments. Figure II.26 depicts the FACS results obtained with time. Each graph represents the signal of the dye versus the cell size. We chose an arbitrary threshold on the y-axis in order to separate the living cells from the dead ones. All elements that are above the horizontal line in Fig.II.26 are considered as dead cells. All elements below the threshold are considered to be living. The same threshold is used for each sample and each day. Results are summarized in Table II.4, which presents the percentages of living cells in our sample at different time after electroporation.

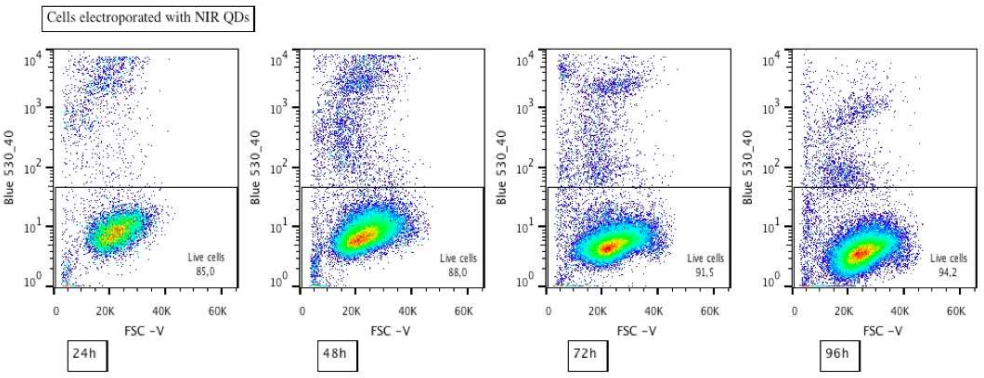

(a)

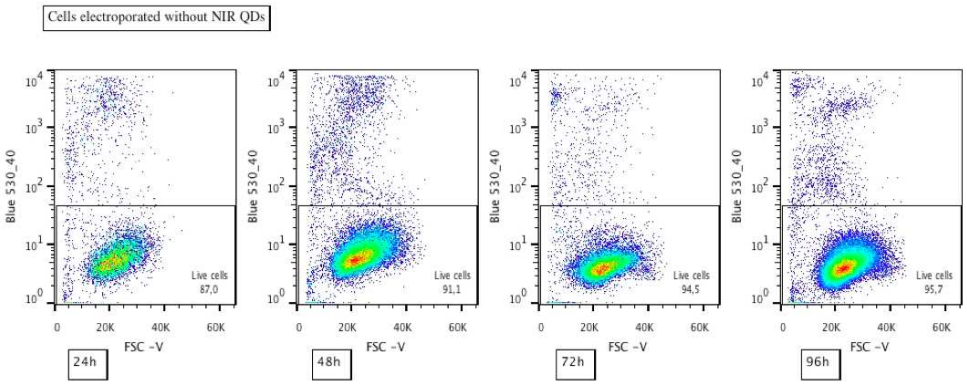

(b)

Figure II.26 – FACS analysis of A20 cells electroporated with time. (a) Electroporated with NIR QDs (b) Electroporated without any QDs.

Sample	% of live cells D1	% of live cells D2	% of live cells D3	% of live cells D4
Control cells	87	91	94	95
QD-electroporated cells	85	88	91	94

Table II.4 – Cell viability after 1, 2, 3 or 4 days for cells electroporated without QDs and cells electroporated with NIR QDs.

From these measurements, we observe that:

- There is only a limited difference at each time point between cells electroporated with QDs and cells electroporated without QDs.
- As time increases after electroporation, there is a slight increase in the percentage of live cells measured on both samples. This may reflect the population recovery that occurs after electroporation. In fact, a few hours after electroporation the effects of the electric field applied to the cells translate into an overall diminished cell survival, which translates in higher numbers of dead cells. The survival of those cells that have been less affected by the electric field mark the recovery of the electroporated cell population and the overall reduction in the total number of counted dead cells.

To summarize, FACS data show that cells electroporated with NIR QDs and cells electroporated without NIR QDs behave essentially in the same way regarding their survival. The small difference between both samples can not be considered as significant concerning the cell survival and suggests that NIR QDs do not induce cell mortality. Moreover, as time increases after electroporation, we observe an increase of survival . It may be attributed to a main loss of cells just after electroporation, then cells continue to divide and for this reason, the percentage of live cell increases. In order to be more quantitative and to probe if cell metabolism is similar or not between these two cases, we performed MTT assays.

MTT assays

The MTT assay is a classical test to determine and quantify cell activity and cell viability. We performed this test to confirm FACS results and to compare the cell activity of cells electroporated with and without NIR QDs and unperturbed cells.

The reagent used is the tetrazolium salt MTT (3 - (4,5-dimethylthiazol-2-yl) -2,5-diphenyl tetrazolium). In active living cells, the tetrazolium rings is reduced by mitochondrial succinate dehydrogenase, to a formazan. This forms a purple precipitate in the mitochondria. The amount of precipitate formed is proportional to the amount of living cells (but also to the metabolic activity of each cell). In a typical assay, cells are incubated (37°C, 5 % CO_2) with NIR QDs in complete cell medium, then rinsed and exposed to the MTT reagent in cell medium for 2 hours at 37°C. Finally, cells are rinsed and lysed by exposure to a detergent solution (isopropanol: Triton, 9:1 vol %). Cell lysis enables the release of the purple product formazan, which is then detected via absorbance spectroscopy in a plate reader.

As previously said, we performed the test for 3 different samples at different time after electroporation, 5h, 24h and 48h in triplicate:

- Cells electroporated with NIR QDs, called QD-electroporated cells,
- Cells electroporated without QDs, called control
- Unperturbed cells, called Cells.

Figure II.27 shows the absorbance values of each sample at different times after electroporation on the left and the absorbance values of the both electroporated samples on the right graph. We observe that the absorbance of the unperturbed cells is higher than the absorbance of the two other samples. This suggests that the activity and/or the number of cells are higher. However, the absorbance of both electroporated samples are similar with time. The cell activity and the metabolism are therefore affected by the electroporation. However, the presence of QDs does not seem to further disturb the cell activity.

The difference between unperturbed and electroporated cells could be due to either higher number of cells or a higher activity per cell in the unperturbed sample. To discriminate between these hypotheses, we have normalized the absorbance by the number of live cells.

Figure II.28 presents the absorbance of each sample at different time after electroporation normalized by the number of cells. Errors bars are very high because of the disparity of the number of cells on each sample of each triplicate just after electroporation. However, error bars decrease with time, and we can not explain that for the moment. Because of the high values of error bars it is difficult to interpret correctly this graph. However, this graph shows that both electroporated samples have a similar absorbance which suggests a same cellular activity. In order to be

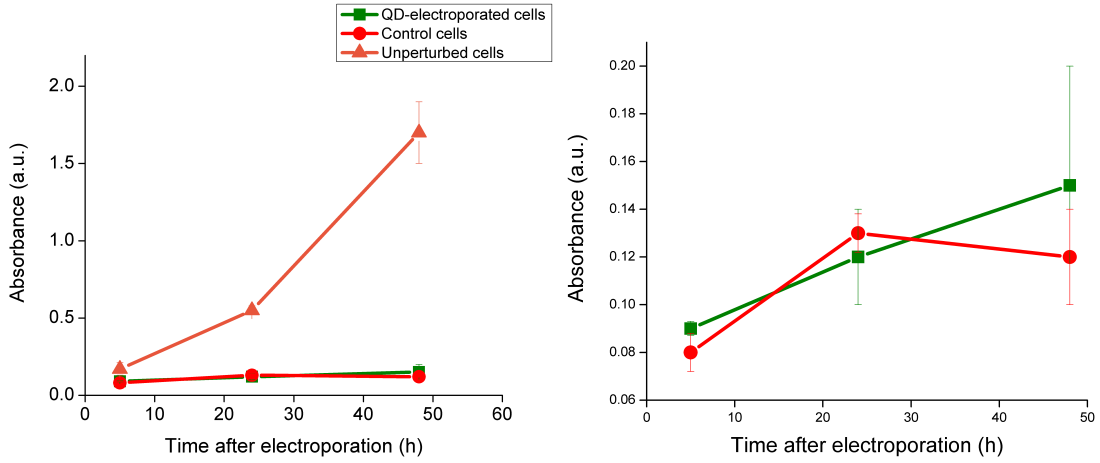

(a) (b)

Figure II.27 – Absorbance of the different samples. a) All samples are presented. b) Zoom on the electroporated samples.

more relevant it could be interesting to repeat these experiments but it requires a high quantity of quantum dots, which requires a long preparation. Thus, to determine if the cell activities and metabolism are changed by electroporation, it could be interesting to inject electroporated cells (with or without QDs) in the murine model of the PIOL and compare the tumour development and spread to a control sample with unperturbed cells.

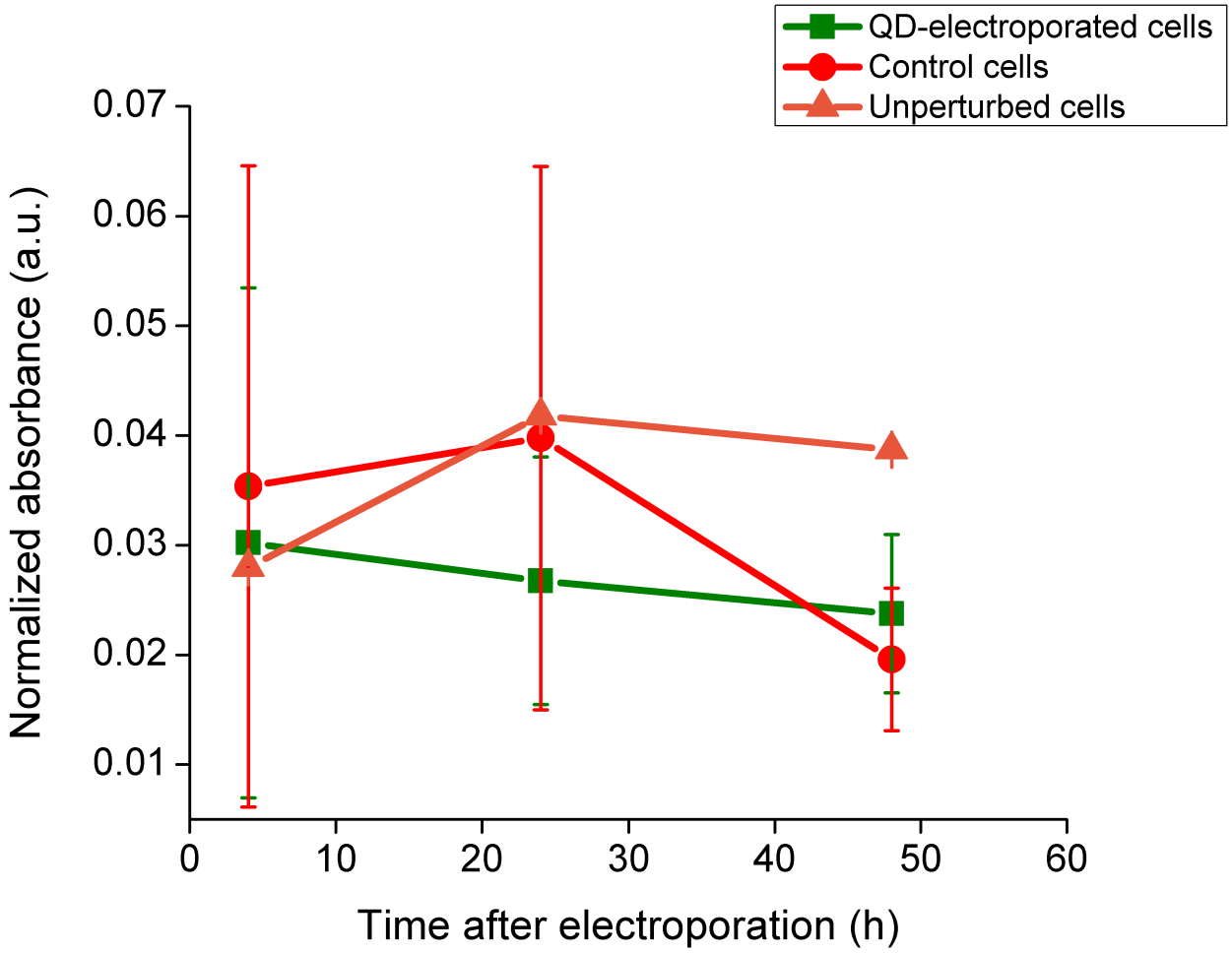

Figure II.28 – Absorbance of the different samples normalized by the number of cells.

II.6 Conclusion

We reported the synthesis and characterization of near-infrared-emitting quantum dots based on low toxic materials. Their emission wavelength is tunable in the "optical therapeutic window" around 800 nm. Thanks to the introduction of zinc in the core synthesis, we succeeded in synthesizing small nanoparticles with a high fluorescence quantum yield for this range of wavelengths. We also synthesized a thin shell around the cores in order to enhance the fluorescence and enable ligands exchange. This type of nanocrystals have optical properties that are linked to the trap states that create intermediate energy levels: large emission spectrum and slow fluorescence decay.

After a ligand exchange, these nanocrystals stay bright and keep their optical properties (emission wavelength and fluorescence lifetime). The PDSB ligand allows the water-solubilization and the QDs' biocompatibility. This ligand enables a strong anchoring at the QD surface and provides long term stable quantum dots in biological media.

We also presented the electroporation, technique used to label massively living cells with a high concentration of nanoparticles. We have shown that NIR QDs stay bright, freely diffusing and homogeneously distributed in the cell cytoplasm after electroporation. Toxicity tests revealed that NIR QDs seem to present a low toxicity: they do not induce cell mortality but we could not definitely conclude on the electroporation effect on cell metabolism.

These probes have the adapted optical properties for *in vivo* studies (emission wavelength, fluorescence quantum yield, size). We have now to develop an optical set up that could limit and reduce the autofluorescence, the second factor that limit sensitivity in fluorescence imaging.

III

Optical set-up, characterization and operation modes

III.1 Introduction

Fluorescence microscopy is an essential tool for better understanding many biological phenomena [93][94]. It provides information at different scales of space (single molecule dynamics, cellular processes, embryonic development, tissue organization, behaviour of small animals ...) and time (from the millisecond for proteins interaction tracking to the day for stem cells tracking or embryogenesis processes). Thus, wide field microscopes and confocal microscopes are routine instruments in biology laboratories. Yet, technical and more fundamental bottlenecks still restrict the capability of fluorescence microscopy. The study of individual and rare events at the cell scale in live tissues is still out of reach. Actually, it requires a cell scale resolution and a high sensitivity. Autofluorescence, even if it is reduced in the near-infrared region still decreases sensitivity and signal to noise ratio. In order to solve this problem, the fluorescence signal peak wavelength should lie in an absorption and diffusion free region and should be distinguishable, either spectrally or temporally, from the autofluorescence background. In our optical set up, we use dichroic and emission filters with optical densities close to OD=8 for wavelengths longer than 715 nm (see Appendix B). Indeed, we estimated an order of magnitude of the acheivable SNR by measuring the signal to noise ratio of a cell, previously stained with NIR QDs and embedded in an autofluorescent signal from beef tissue, we have obtained a kind of signal-to-noise ratio (SNR) of 0.7. Thus, spectral filtering alone is not efficient to increase sensitivity and have a SNR >1. Time-gated detection is a good alternative and allows a temporal separation between two signals having different time scales. Autofluorescence has a shorter fluorescence lifetime (<5 ns) compared to NIR QDs (150 ns). Using a time-gated detection together with spectral filtering, we managed to obtain a SNR >15 and this increase is mainly due to reduction of autofluorescence signal using temporal separation (details in chapter IV). However, the efficiency of the time-gated detection depends strongly on the gate characteristics (duration and delay between the laser pulse and the opening). The optimal values of these parameters depend on the autofluorescence and QDs lifetimes but also on the relative magnitudes of signals and noise levels.

Therefore, it is essential to characterize the noise sources behaviours in order to determine the optimal experimental conditions and improve the SNR. As we want to determine the migration pathway of CTC, we also need to have a spatial resolution allowing the precise cell location (few micrometers). Therefore, spatial resolution measurements are also required.

I describe an optical set up which brings a solution to the mentioned specifications. It consists in a detection which is temporally separated from the excitation in order to reduce short fluorescence lifetime signals such as autofluorescence. This system acts like a gate which opening, closing and width can be controlled at the nanosecond scale. Thus, the instrument developed can be used for two different applications : time-gated detection where the detection window is fixed (see scheme in Fig.IV.1), and fluorescence lifetime measurements where the detection window is shifted regarding the laser pulse (see scheme in Fig.III.12) [28].

In this chapter, we will present spatial resolution measurements and present noise measurements and characterization. Finally, we report fluorescence lifetime measurements performed using our optical set up.

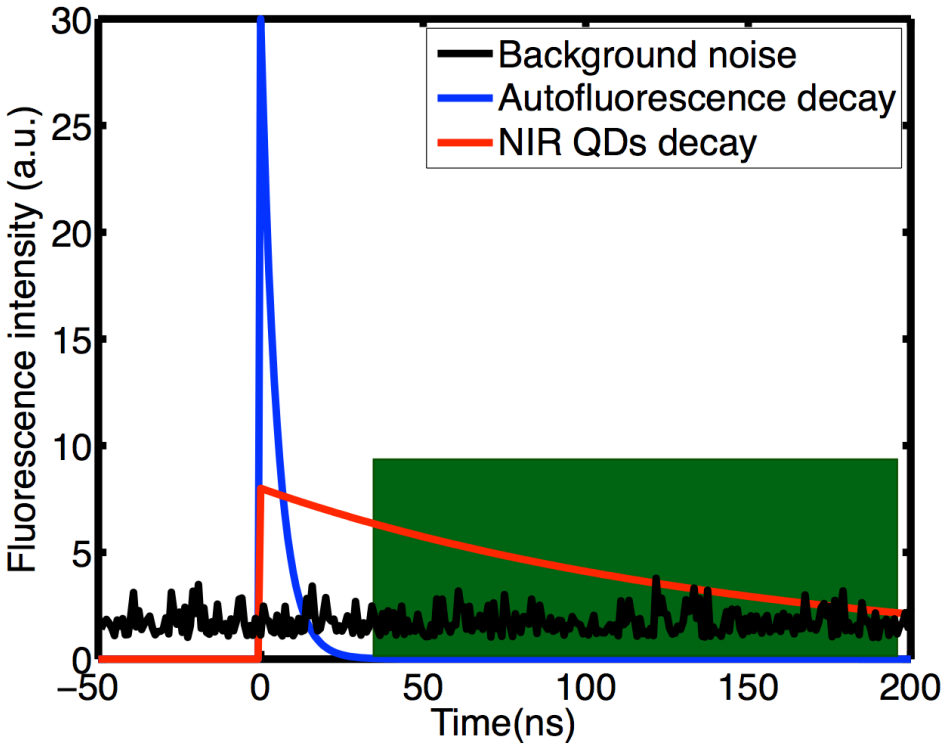

Figure III.1 – Scheme of the time-gated detection. In green, an adapted detection window in order to get rid of signal from autofluorescence.

III.2 Experimental set up

III.2.1 Description

The light source used for time-gated imaging (setup shown in Fig. III.2) is a picosecond pulsed laser diode, emitting at 659 nm, with variable repetition rates (from 1 MHz to 80 MHz) injected in the epi-illumination path of a commercial microscope body. The beam spot size and position in the focus plane of the objective are controlled by an external telescope and periscope. Depending on the sample, we use a 60× water immersion Olympus objective (NA = 1), a 40× Olympus objective (NA = 0.6) or a 20× water immersion Olympus objective (NA = 0.7). We use emission filters to eliminate most of the excitation photons that may enter the detection path, usually due to reflections on optical surfaces. As already mentioned we use dichroic and emission filters that have a transmission T=2.4826×10^{-8} at the excitation wavelength. A relay achromatic pair of lenses matches the image size to the intensifier and gate surface. The same relay system is placed head to tail between the intensifier and the electron multiplying charge-coupled device (EMCCD) camera. The laser diode and the intensifier are synchronized by two phase-locked function generators. (See filters specifications and HRI quantum efficiency in Appendix B).

III.2.2 Operation of the intensifier

The intensifier (Picostar HRI, LaVision) is composed of a photocathode, a microchannel plate and a phosphore screen as described in Fig.III.3. Emission photons hit the photocathode and produce photoelectrons. A high voltage applied between the photocatode and the microchannel plate accelerates and directs the electrons into the channels. At the output of the microchannel plate the electrons strike a phosphor screen and their kinetic energy is converted into light. The spectral response of the photocathode is provided by the manufacturer (it covers all the visible and near infrared with a maximum sensitivity in the red, see Appendix B), and the emission of the phosphor screen is centered around the maximum of emission of this element, at 540 nm which corresponds to the maximum of the spectral response of the EMCCD (see Appendix B).

The intensifier can be used in different modes. For our experiments, we worked with a mode called RF mode. In this mode, the gate is driven by a waveform synthesizer. This mode is suited to perform time-gated detection as well as fluorescence intensity decay measurements. In this mode we control two different parameters : the microchannel plate voltage (MCP gain) which fixes the electrons amplification

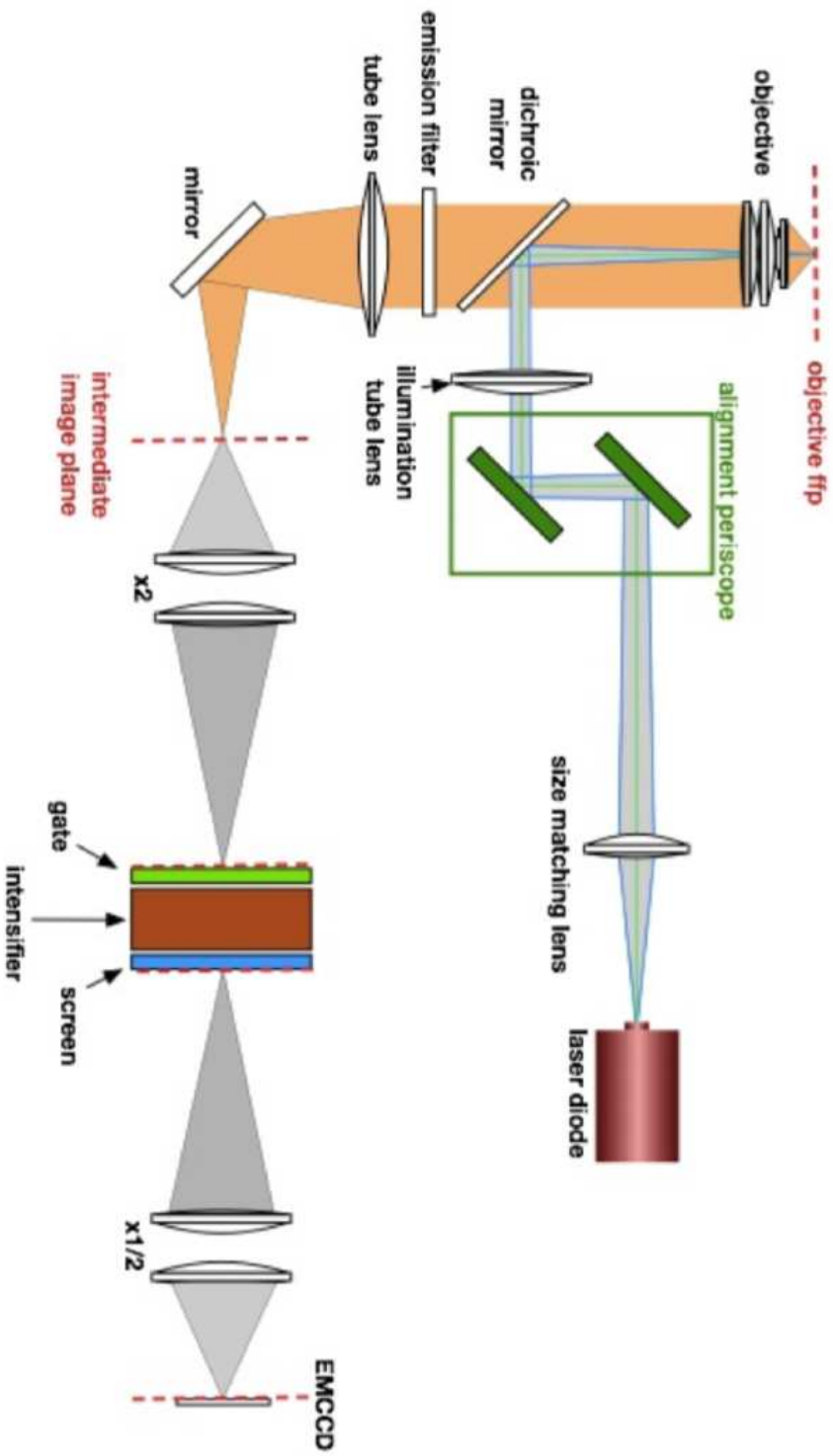

Figure III.2 – Optical setup. The sample is illuminated by a pulsed laser diode with a 1 or 5 MHz repetion rate and emitting at 659 nm. The laser and the intensifier are synchronized by two phase-locked function generators.

and the RF gain which activates the photocathode and convert photons into primary electrons that are accelerated toward the microchannel plate. Both parameters have to be set so as to maximize the signal to noise ratio.

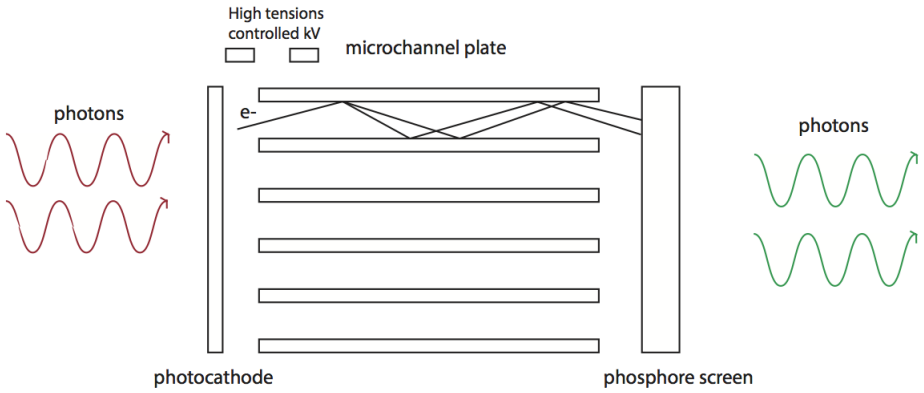

Figure III.3 – Scheme of the intensifier operation

III.2.3 Set up flexibility

To determine if our NIR QDs are saturated using our excitation we lead a calculation to determine the number of photons absorbed by a QD using our excitation laser. Calculations were performed with a 20X objective a repetition rate of 5 MHz and a laser with a repetition rate of 5 MHz and a maximum intensity. If we consider that a QD has a fluorescence lifetime of 150 ns, it can absorb at saturation:

$$N_{\text{sat}} = \frac{1}{150 \times 10^{-9}} \simeq 7 \times 10^{6} \text{photons/s}$$

We have now to calculate the number of photons sent to our sample using our laser diode. We measured an average power equal to $P = 0.190$ mW for a repetition rate of 5 MHz to the output of the objective. Our laser emits at 659 nm, thus the energy of a photon is given by :

$$E = \frac{hc}{\lambda} = 3 \times 10^{-19} \text{J}$$

We can then determine the number of photons by second on our sample:

$$N_{\text{laser}} = \frac{P}{E} = 6 \times 10^{14} \text{photons/s}$$

The surface illuminated by the laser using a 20× objective is $S = 1.28 \times 10^{-3} \text{cm}^2$

Thus, we can determine the illuminance given by:

$$I = \frac{N}{S} = 4.7 \times 10^{17} \text{photons/cm}^2\text{/s}$$

Depending on its size and composition and on the excitation wavelength, a reasonable order of magnitude of a QD absorption cross section is about σ=10^{-15} cm^2 [95]. Therefore, the number of absorbed photons by a QD during one second is given by :

$$N_{QD} = I \times \sigma = 470 \text{photons/s}$$

By comparing N_{QD} and N_{sat} there are 5 orders of magnitude. QDs are not saturated using our excitation. Therefore, if we do not manage to detect *in vivo* isolated cells we will increase the QD fluorescence signal by increasing the excitation illumination. This can be either realized by reducing the laser spot size or by replacing the actual laser diode by a more powerful source.

III.3 Set up characterization

Because we want to track cell and identify their pathway, we need a cell scale spatial resolution (10 μm). Moreover, because the final goal is to detect circulating tumour cells, the microscope has to be highly sensitive and able to detect few signal photons. For this reason, we have to characterize all "noise photons". Thus, this section will deal with the spatial resolution value and characterize noise sources we are subjected to.

III.3.1 Spatial resolution

This section presents resolution measurements performed using near-infrared emitting 200 nm-diameter beads.

One of the main limitation of conventional optical microscopy is the resolution limit imposed by diffraction, which prevents observation smaller than half of the emission wavelength structures. This can be calculated knowing the point spread function (PSF), which is described by the equation bellow and is given for a classical wide field microscope with a circular pupil:

$$I(r) = I_0 \left| \frac{J_1(kNAr)}{kNAr} \right|^2 \quad \text{(III.1)}$$

where r is the distance to the center of the diffraction spot, $k = \frac{2\pi}{\lambda}$ the wave number, NA the numerical aperture of the objective and J_1 the first order Bessel function.

We measured the PSF by depositing infrared emitting ($\lambda \simeq 750$ nm) 200 nm-diameter beads on a coverslip and imaging them using a 20× objective ($NA = 0.7$, corrected for coverslip). Repetition rate of the laser was fixed to 5 MHz. We compared the PSF measurements with a model that took into account the beads shape and both microscope and gate transfer functions.

We used two bead models that are illustrated in Fig.III.4 :

- a cylindric bead with an intensity profile corresponding to a gate function,
- a spherical bead for which the signal level depends on the local thickness of the bead.

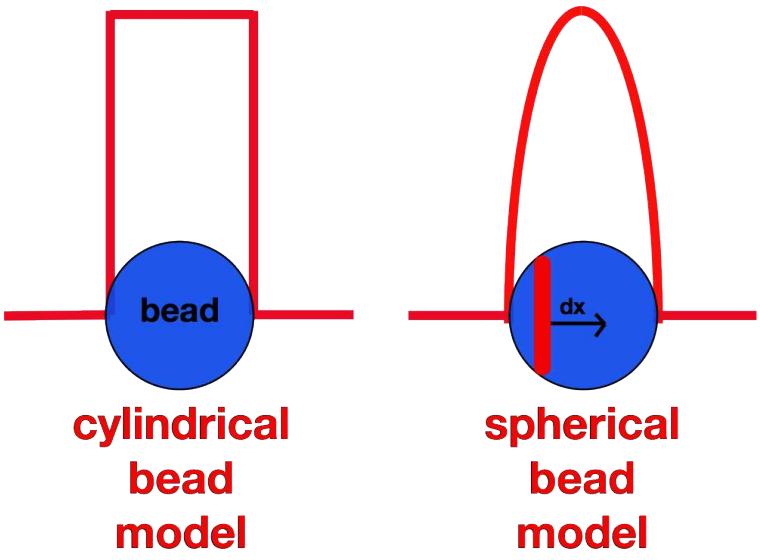

Figure III.4 – Scheme of the bead models used and their respective intensity profiles for the simulation.

Figure III.5 presents the intensity profiles of the two different modeling of beads corresponding to the convolution of the PSF of the objective with the signal bead models described above. The profiles are similar for the two beads models initially chosen and are similar to the PSF of the objective. Thus, if the resolution is limited by the diffraction at the objective level, the FWHM of the intensity profile of the beads would be equal to 0.65 μm around 750 nm.

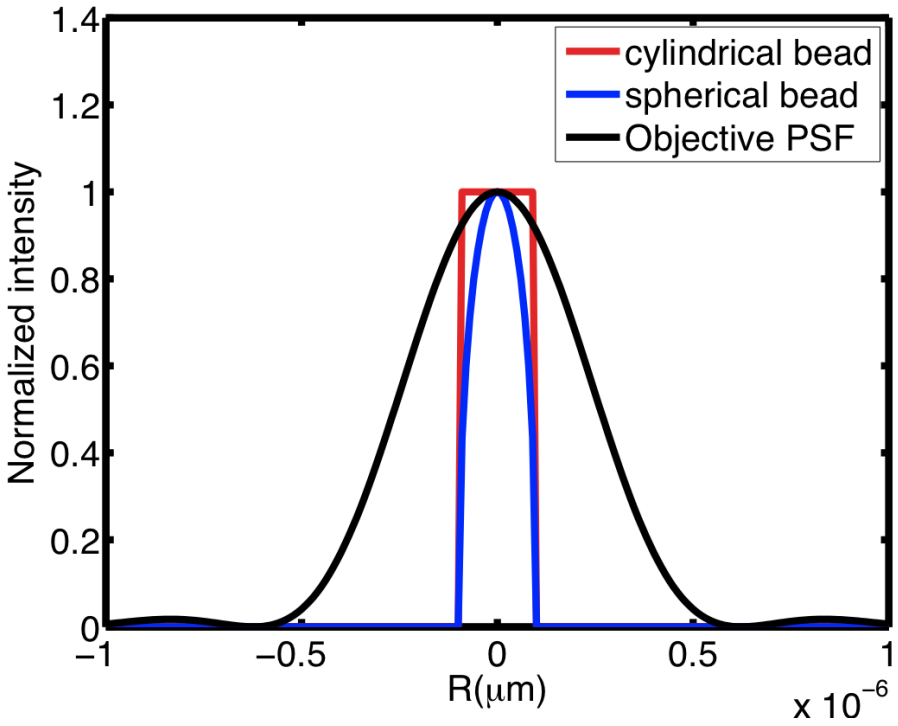

(a)

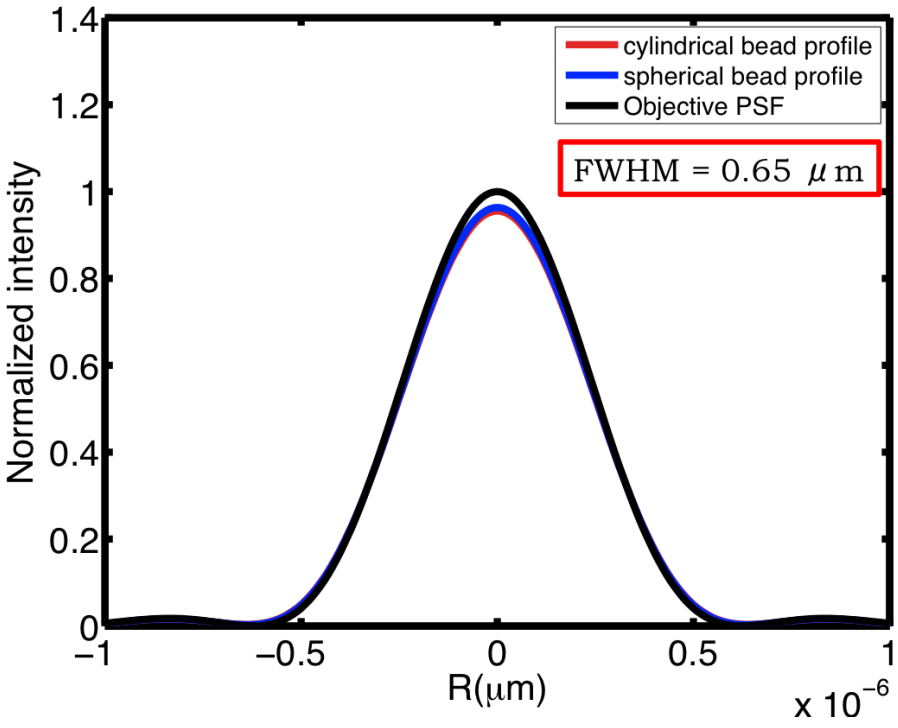

(b)

Figure III.5 – (a) Representation of the objective PSF and the bead models used. (b) Theoretical bead profiles obtained with our optical set up if we take into account a resolution limitation only due to diffraction by the objective pupil.

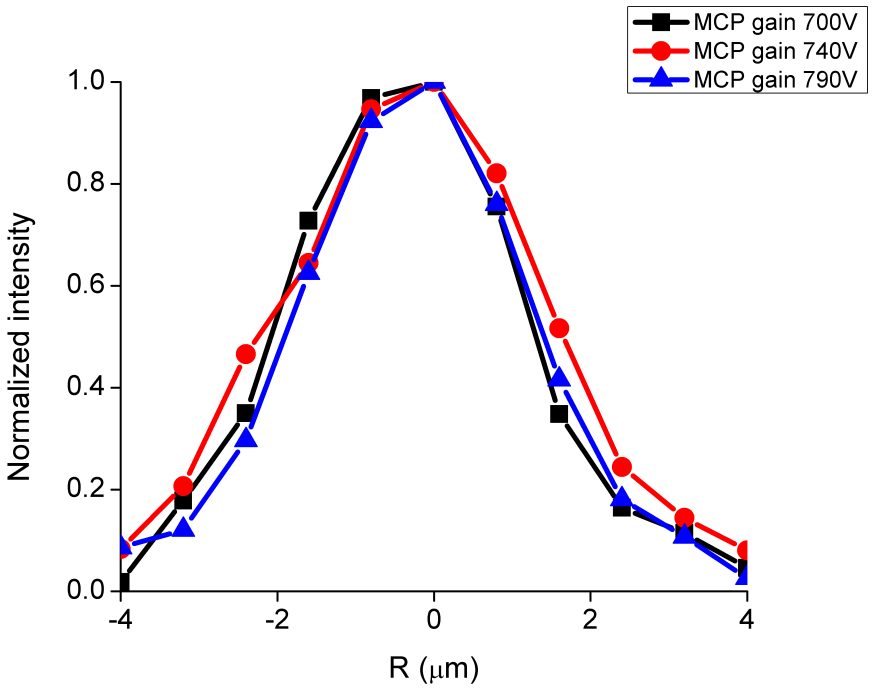

(a)

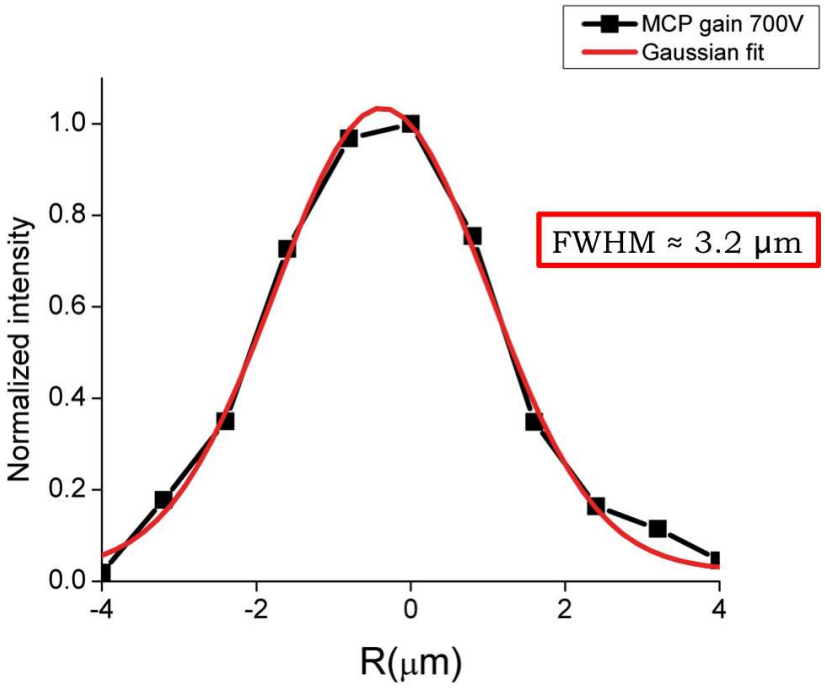

(b)

Figure III.6 – (a) Experimental bead profiles using a 20X (NA = 0.7) for different MCP gains. (b) Gaussian fit of the experimental bead (FWHM = 3.2 μm)

Figure III.6 presents the experimental bead profiles performed with different MCP gains.

The FWHM does not change with the MCP gain. Moreover, if we fit the data with a gaussian model, we obtain a FWHM equal to 3.2 μm, which is much larger than what we expect if only the bead dimensions and the objective limit the resolution (FWHM $\approx$ 0.65 μm).

The difference between our measurements and the expected value can be explained by different hypothesis :

- an approximate focus and spherical aberrations present if the imaged beads are not directly in contact with the coverslip,
- a bad conjugaison of the achromatic pairs which provides a magnification factor,
- aberrations induced by a possible misalignment of the optical axes of the various components in the detection bench.
- a decrease of the resolution due to the intensifier, noted HRI for High Rate Intensifier.

The images of the beads have been obtained after we set up and aligned the optical components to the best of our ability. We found the position of the sample that minimizes the images of the beads. At this point it is difficult to assert that one factor is responsible for the loss of resolution. All we can do for the next simulations is to define a transfer function for the HRI.

Indeed, among all these points, it is difficult to really improve the focus and determine which achromatic pair creates a magnification factor. We can limit the presence of spherical aberrations by using a corrected objective which allows the observation of samples deposited on a coverslip (here the objective used is corrected). However, the spherical aberrations can be observable if we do not image beads that are directly bonded to the microscope coverslip. But spherical aberrations are not responsible for such degradation of the resolution. Actually, according to the data sheet of the intensifier, the resolution depends on the mode used by the intensifier. Thus, the image obtained on the EMCCD camera can be written as:

$$Image = Object \bigotimes ObjectivePSF \bigotimes Intensifier \tag{III.2}$$

Densiset *et al* [96] have observed a loss of resolution using a comparable system and have clearly showed a degradation of the resolution when using a HRI.

For these reasons, we have performed a simulation where we defined a transfer function for the HRI depending on the HRI cutoff frequency. We have considered that the channel radius depended on the cutoff frequency of the intensifier and provided us a 2D gaussian PSF. The equation III.2 can now be written as :

$$Image = Object \bigotimes Objective\ PSF \bigotimes Intensifier\ gaussian\ PSF \qquad \text{(III.3)}$$

We fitted our experimental bead profile data with modeled profile using a cut-off frequency of 10 lp/mm, which is consistent with the HRI datasheet. Figure III.7 presents the experimental bead profile and the modelled profile obtained using Eq.III.3. Both curves are more or less superimposed and the remaining difference between the simulation and the experimental data can be attributed to the spherical aberrations and the magnification factor error that are not taken into account in the modelling.

To conclude this part, the resolution of the optical set up is not limited by the diffraction of the objective pupil. The intensifier appears to be responsible for the loss of resolution. Our model allowed us to determine the cutoff frequency of the intensifier that fits well with our experimental data. Even if the resolution is not as important as a classical wide field microscope (about 500 nm), as we want to track 10 μm-size cells, the resolution is sufficient for our application.

III.3.2 Noise sources

As the goal of the project is to detect rare and individual events, it is critical to characterize noise sources in order to optimize the intensifier parameters. This section presents the intensifier noise sources in order to better understand its behaviour and enhance the set up sensitivity.

There are many parameters that can modify the background noise level :

- the gain associated to the conversion photons- electrons at the entrance of the intensifier, called RF gain,
- the gain associated to the electrons amplifications, called MCP gain,
- the integration time,

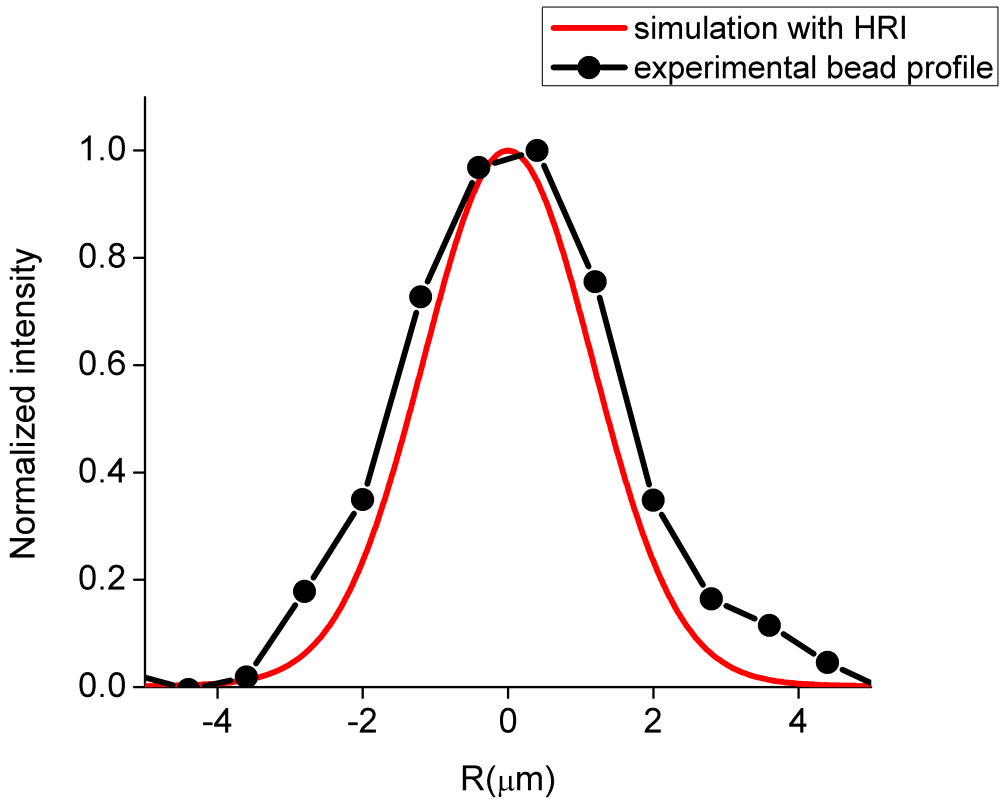

Figure III.7 – Comparison of the experimental bead profile (in black) and the simulated profile (in red) according to the equation III.2 with a cut frequency of 10 lp/mm.

- the gate width,

- the camera gains.

In this part, I will focus on the intensifier parameters and their influence on the level of detection noise. To perform detection noise quantification, we have recorded a stack of 30 images and measured the standard deviation for each pixel using the plugin Z Project of Image J. This process provided us an image for which each pixel corresponds to the standard deviation of the intensity of the same pixel on the stack of images. Then we chose a region of interest (ROI) (typically a region illuminated by the laser spot) and measured the average of the standard deviation per pixel in this ROI. These measurements correspond to the measurements of the detection noise and have been performed varying one by one each parameter previously mentioned.

Dependency on the gate width and the integration time

By fixing many parameters such as the MCP gain, the RF gain, the camera gains and the laser/gate repetition rates, we measured the influence of the gate width and the integration time on the detection noise level. We have performed detection noise measurements in order to better understand the HRI behaviour. Figure III.8 (a) presents the detection noise as a function of the gate width for different integration times. Figure III.8 (b) presents the detection noise as a function of the integration time for a gate width fixed. As illustrated in this figure, the detection noise slowly depends on the gate width. For each integration times, the ratio between the average of the detection noise for the larger gate and the detection noise for the shorter gate is conserved. This can be attributed to a transient noise caused by the opening and/or the closing of the gate.

However, the detection noise increases with the integration time. The variation is proportional to the square root of the integration time as shown in the Table III.1. As the variation slowly depends on the gate width, the increase with the integration time is due to photons created by the electron amplification in the intensifier. If the photons were "ambient photons" the value of standard deviation would be linear with the gate width. But here, we do not observe such a variation. We can conclude that the intensifier creates "photon noise" due to an amplification of electrons in the intensifier.

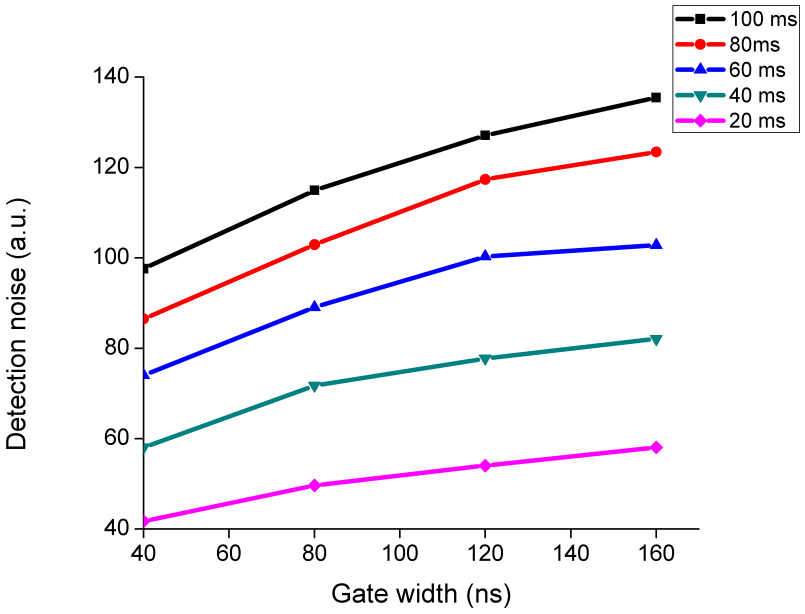

(a)

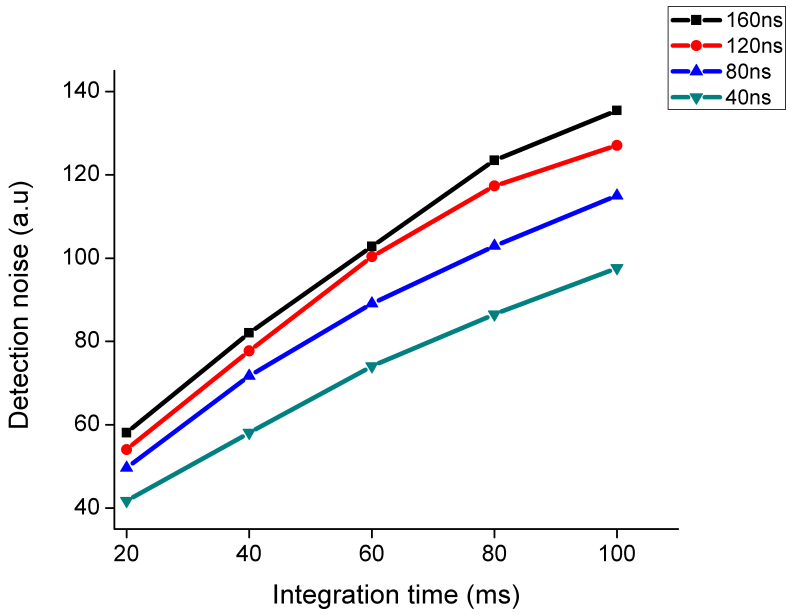

(b)

Figure III.8 – Influence of (a) the gate width and (b) the integration time on the background noise.

Gate width (ns)	160	120	80	40
DN/$\sqrt{100}(\sqrt{ms})$	13.5	12.7	11.5	9.7
DN/$\sqrt{80}(\sqrt{ms})$	13.8	13.1	11.5	9.7
DN/$\sqrt{60}(\sqrt{ms})$	13.3	12.9	11.5	9.6
DN/$\sqrt{40}(\sqrt{ms})$	13	12.3	11.3	9.2
DN/$\sqrt{20}(\sqrt{ms})$	13	12.1	11.1	9.3

Table III.1 – Detection noise (noted DN in the table) divided by the square root of the integration time for each gate width for a repetition rate of 5 MHz.

Dependency on the intensifier gains

We wanted to determine the effect of the intensifier gains (RF gain and MCP gain) on the "noise signals". The measurement procedure is the same as previously explained. Figure III.9 shows how the detection noise depends on the MCP or the RF gains. The variation is linear with the MCP gain whereas the RF gain does not affect it. We can relate these results to the previous ones. The RF gain does not create 'noise electrons' that are created in the amplification process by the MCP.

Dependency on the camera gains

We also wanted to determine the effects of the camera parameters on the noise sources. In a EMCCD camera, two types of gain can be settled : the CCD gain and the EMCCD one. The CCD gain represents the conversion factor from electrons to digital counts, or Analog-Digital Units (ADU). Gain is expressed as the number of electrons that get converted into a digital number, or electrons per ADU. It corresponds to the ratio between the number of electrons per pixel and the number of counts per pixel. The EMCCD gain corresponds to an electron amplification. Figure III.10 presents the detection noise regarding the camera gains. We fixed the exposure time to 100 ms and for the CCD gain variation, the EMCCD gain was fixed to zero whereas for the EMCCD gain variation, the CCD gain was fixed to 3. As illustrated in Fig. III.10, the detection noise slowly increases with the CCD gain but varies linearly with the EMCCD gain.

III.3.3 Influence of the noise signal on the signal-to-noise ratio (SNR)

We wanted to determine the SNR profile compared to the noise and signal ones. We deposited NIR QDs on a coverslip and measured the emmitted signal making sure

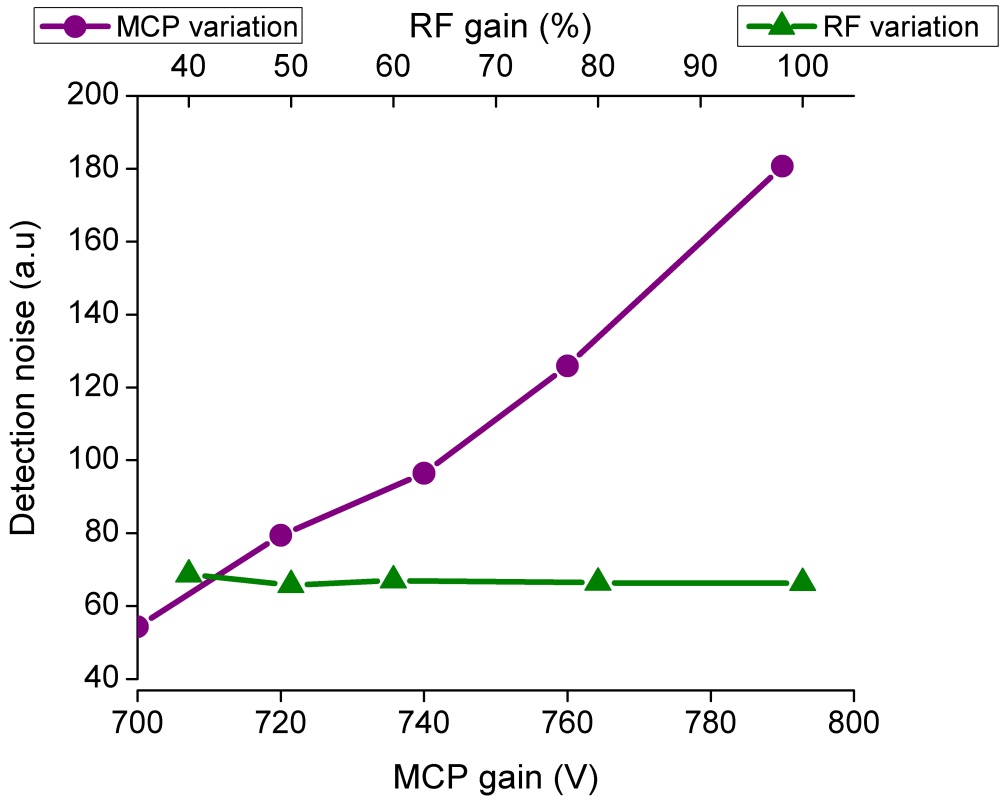

Figure III.9 – Detection noise regarding the MCP gain (in purple) and the RF gain (in green).

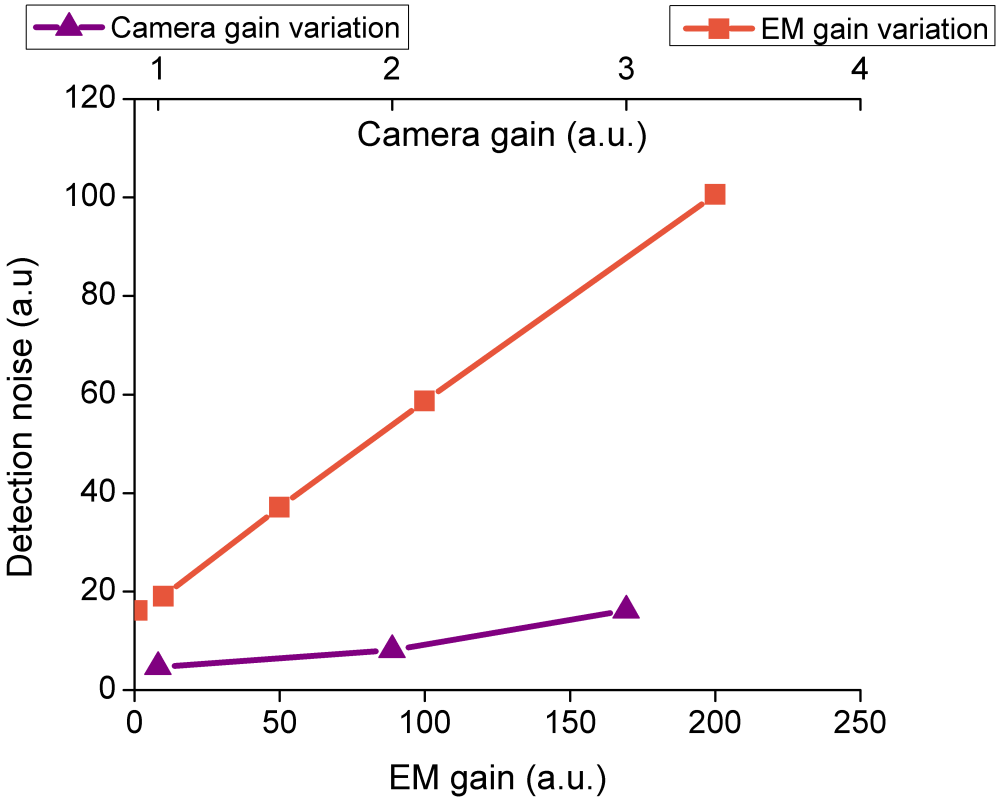

Figure III.10 – Detection noise regarding the CCD gain (in purple) and the EMCCD gain (in orange).

to previously substract the background. Figure III.11 shows the evolution of the SNR for different onfigurations: by changing the value of the RF gain or the MCP one. The SNR slowly depends on the RF gain and increases when the MCP gain also increases. Even if the high voltage of the MCP gain makes noise increase, the SNR is also improved. In brief, it is interesting to work with the highest MCP gain.

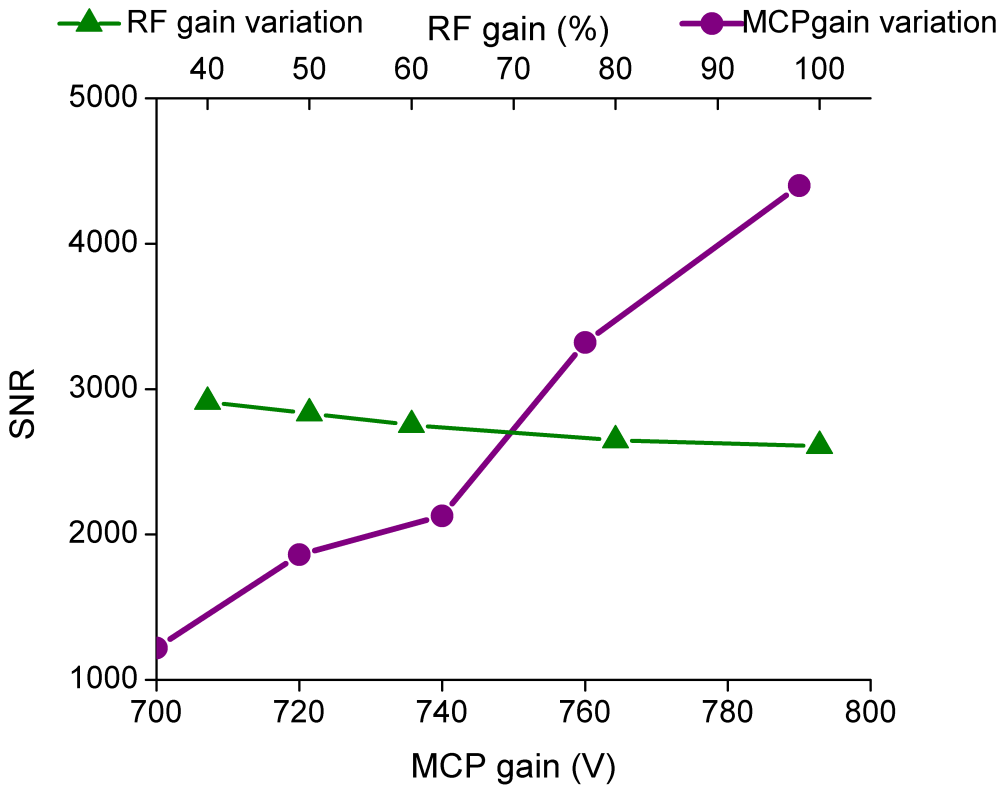

Figure III.11 – Signal-to-noise ratio of NIR QDs deposited in a coverslip.

III.3.4 Detection noise conclusion

To summarize, we observed that the intensifier creates "noise electrons" due to a non controlled amplification. These electrons strike a phosphor screen and their kinetic energy is converted into photons. These photons are then detected by a EMCCD camera. Thus, because they are created at the intensifier level, the gate width does not affect the detection noise whereas it varies with the square root of the integration time as a typical photon noise. The SNR increases with the voltage applied in the microchannel plates. Therefore, SNR can be improved by using the highest voltage of the MCP gain. The different noise sources identified here are :

- an instrumental noise due to the opening and/or closing gate that varies with the number of gates during an image,
- a dominant noise that increases with the square root of the exposure time,
- a noise due to the voltage applied to the microchannel plate of the intensifier,
- a noise due to the camera gains.

III.4 Fluorescence lifetime measurements

As previously mentioned, the optical set up developed can also be used to perform fluorescence lifetime measurements. For fluorescence lifetime measurements, the detection gate is delayed regarding the excitation. Here, we present fluorescence lifetime measurements carried out using our optical set up. These measurements aim to verify if our NIR QDs keep their fluorescence lifetime properties in different media and in the cell cytoplasm with time.

III.4.1 Principle

The intensifier is used in a mode that is suited to perform time-gated detection as well as fluorescence intensity decay measurements. Photoluminescence (PL) intensity decays are measured by acquiring a sequence of images, while phase shifting a 200-ns width gate trigger signal with respect to the laser trigger, as illustrated in Fig III.12. This introduces a controllable time delay, τ, between the laser impulsion and the beginning of the detection gate. Thus, for each delay of the gate, an image is acquired using a Matlab program developed by Vincent Loriette. This program allows to synchronize the HRI with the camera and to acquire an image for each gate position.

A common region of interest (ROI) for all images is selected and for each image, the average intensity of the ROI pixels is measured. The image offset, induced by the camera or by the external light sources, is eliminated by recording a sequence without laser excitation and subtracting the average of the pixels intensity of the same ROI from the original sequence. The results are then normalized to the measurement obtained after the laser pulse at zero delay. For fluorescence decay measurements, we typically use a radio frequency gain at 50% and Micro Channel Plate gain at 700 V and an input driving peak to peak voltage of 4 V.

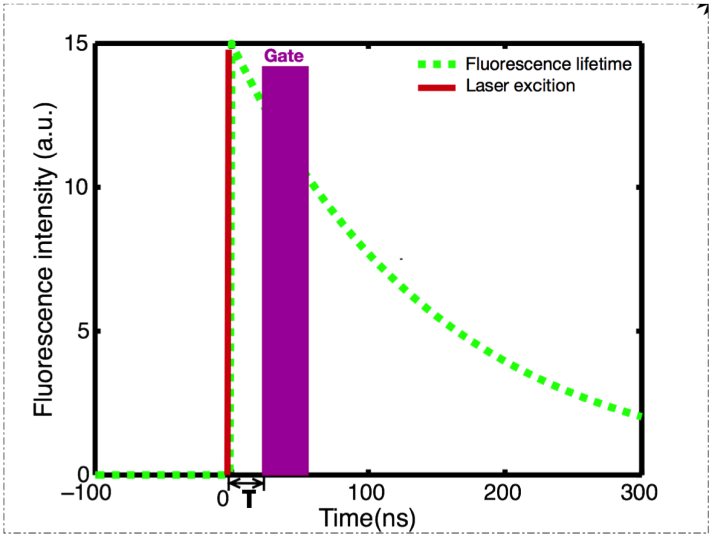

(a)

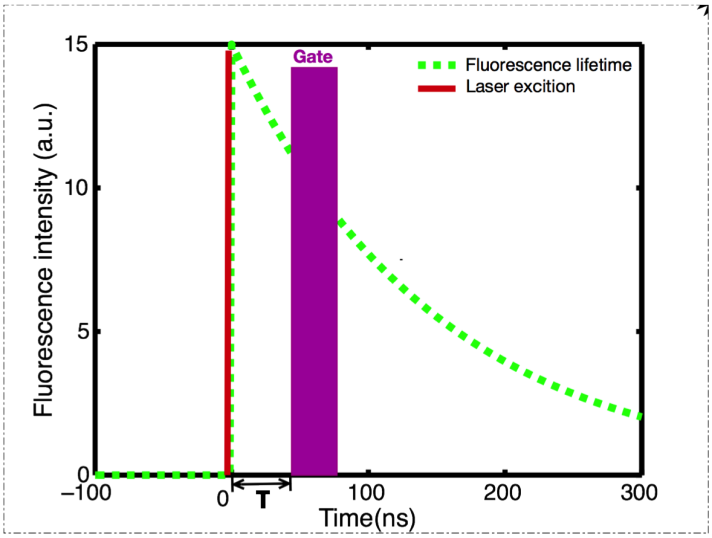

(b)

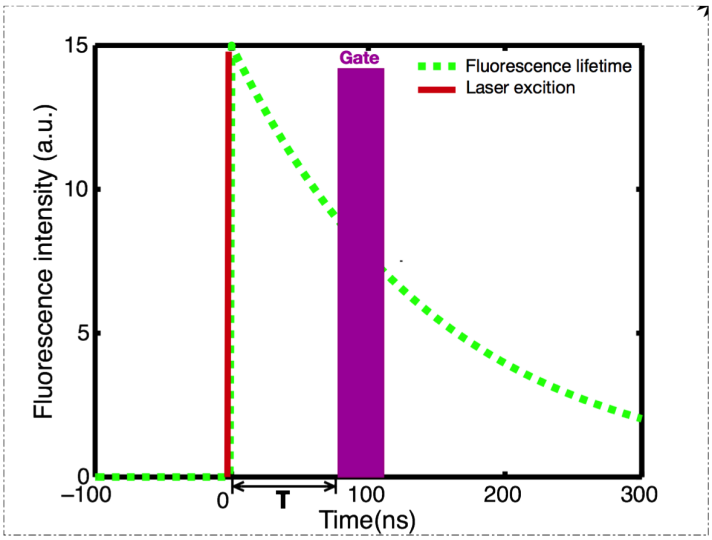

(c)

Figure III.12 – Scheme of the principle of fluorescence intensity decay measurements.

III.4.2 Influence on the gate width for the lifetime mesurements

As we want to track cells over a few day, NIR QDs long fluorescence lifetime need to be preserved in the cells for a week at least. For this reason, PL intensity decay measurements on QDs were carried out for different samples. The gate width has an influence on the lifetime measurements when the fluorescence lifetime of the molecule is not monoexponential[96]. For our NIR QDs, the long component represents at least 80 % of the decay. Thus, by assuming that the decay is monoexponential the gate width has no influence on the fluorescence lifetime.

In a general case, the measurable signal is given by:

$$S_m(t) = F_0 + A \times \exp\left(-\left[t + t_0\right]/\tau\right)$$

Where F_0 corresponds to the background level offset and A is the signal amplitude. The values F_0 and A are given counts (or electrons, or binary levels) per second. We measure this signal during the opening gate $[t, t+\Delta]$ where Δ is the gate width

$$S_d(t) = \int_t^{t+\Delta} F_0 + A \times \exp\left(-\left[t + t_0\right]/\tau\right) dt$$

$$S_d(t) = F_0\Delta - A\tau \exp\left(-\left[t + t_0\right]/\tau\right)\left(\exp\left(-\Delta/\tau\right) - 1\right)$$

If we detect N pulses per image, the detected signal is given by:

$$S_d(t) = F_{ccd} + NF_0\Delta - NA\tau \exp\left(-\left[t + t_0\right]/\tau\right)\left(\exp\left(-\Delta/\tau\right) - 1\right)$$

We note $\gamma_0 = NA\tau\left[1 - \exp\left(-\Delta/\tau\right)\right]\exp\left(-t_0/\tau\right)$ and $\Sigma_0 = F_{ccd} + NF_0\Delta$ corresponds to the total offset

If there is no background signal:

$$S(t) = S_0(t)$$

that can be also written:

$$S_0(t) = \gamma_0 \exp\left(-t/\tau\right)$$

If we calculate the log of S_0

$$\ln\left(S_0(t)\right) = \Gamma - \frac{t}{\tau}$$

with $\Gamma = \ln(\gamma_0)$. The lifetime is given by:

$$\tau = -\left(\frac{\mathrm{d}\ln(S_0(t))}{\mathrm{dt}}\right)^{-1}$$

If the background signal is low, that can be the case because we record a sequence of images without any fluorescent sample and substracte it to the original sequence we can write:

$$\ln(S(t)) \approx \ln(S_0) + \Sigma_0/S_0 = \gamma_0 - \frac{t}{\tau} + \frac{\Sigma_0}{\gamma_0}\exp(t/\tau)$$

and

$$\frac{\mathrm{d}\ln(S(t))}{\mathrm{dt}} \approx \frac{-1}{\tau}\left(1 - \frac{\Sigma_0}{\gamma_0}\exp(t/\tau)\right)$$

and we estimate

$$\tau^* \approx \frac{\tau}{1 - \frac{\Sigma_0}{\gamma_0}\exp(t/\tau)} \approx \tau\left(1 + \frac{\Sigma_0}{S_0(t)}\right)$$

This formula is valid when $\Sigma_0 \ll \gamma_0 \exp(-t/\tau)$.

The error depends on the value of Σ_0 compared to S_0. While $S_0(t)$ is higher than Σ_0 the estimated value τ^* is similar to the theoretical value τ. Thus, the most important point to obtain an experimental value of τ close to the true one is to use condition in which Σ_0 is lower than S_0.

III.4.3 Measurements on QDs in different media and in the cell cytoplasm with time

We measured the fluorescence intensity decays on three different samples in order to observe the influence of the QDs surrounding medium on their fluorescence lifetime. Lifetime measurements have been performed as described above. Figure III.13 shows fluorescence intensity decays obtained for three NIR QD samples: in hexane, in water (after ligand exchange), and in the cytoplasm of living cells. We performed the same experiment to measure fluorescence decays in the cell cytoplasm at different times after the electroporation (5, 24, and 48 h). We have fitted the fluorescence decay curves by a multiexponential curve with two major components and presented the different parameters in Table III.2. As shown in this table, more than 80 % of the decay is represented by the long component. The resulting values of τ_1 and τ_2 are equatable from one curve to another, taking into account the standard deviations. This experiment shows that the decay kinetics remain unchanged not

Sample	α_1	τ_1 (ns)	α_2	τ_2 (ns)
QDs in hexane	0.05	28 ±1.8	0.95	138 ±2
QDs in water	0.05	25 ±1.8	0.95	134 ±2.7
QDs in cell cytoplasm	0.15	60 ±25	0.85	177 ±78
5 h	0.2	39 ±10	0.8	142 ±35
24 h	0.15	60 ±25	0.85	177 ±78
48 h	0.05	31 ±11	0.95	197 ±37

Table III.2 – Numerical values of τ_1 and τ_2 used to fit our fluorescence decay curves in Fig. III.13 and Fig. III.14 and their respective weights, α_1 and α_2.

only in different media (Fig. III.13) but also in the cell cytoplasm even three days after electroporation (Fig. III.14). These results reflect the long-term stability of QDs in the cytoplasmic medium, and confirming the possibility to use them to label cells for long-term tracking applications.

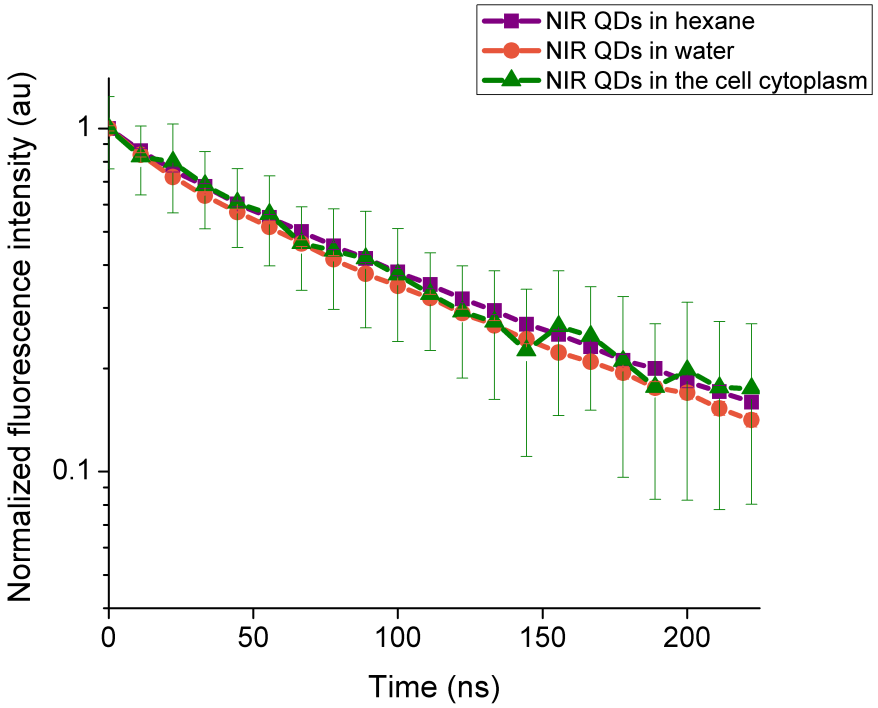

Figure III.13 – Normalized fluorescence intensity decay measurements of NIR QDs in different media (hexane, water, and cell cytoplasm)

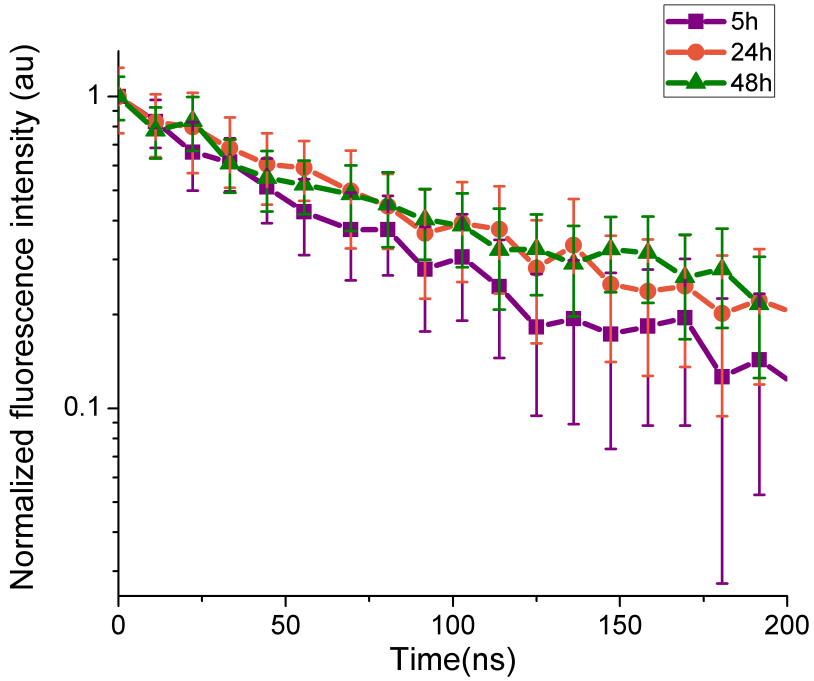

Figure III.14 – Normalized fluorescence intensity decay measurements of NIR QDs in the cell cytoplasm at different times after the electroporation (5, 24, and 48 h).

III.5 Conclusion

The optical set up I developed allows carrying out time-gated detection and fluorescence intensity decay measurements. This system allows to temporally shift the detection regarding the excitation in order to overcome short fluorescence lifetime signals. The resolution is affected by the intensifier but is still compatible with unique 10 μm diameter cell detection. The HRI creates "noise electrons" that are converted in "noise photons" by the phosphor screen. The optical set up allowed us to perform fluorescence lifetime measurements in order to verify the conservation of the long decay component. We showed that NIR QDs keep their long fluorescence decay in different media, including in the cell cytoplasm of living cells, at least for 48 h. These results reflect the long-term stability of NIR QDs in the cytoplasmic medium, and confirm the possibility to use them to label cells for long-term tracking applications. NIR QDs can be coupled to time-gated detection and we will determine the optimal parameters in order to increase the SNR and permit the detection of single cell in an autofluorescent environment.

IV

Time-gated detection for autofluorescence rejection

IV.1 Introduction

There are three main factors that limit the ability of a wide field microscope to detect rare and isolated events within tissue:

- the autofluorescence signal coming from the illuminated volume can be much larger than the signal of interest,
- the light absorption by the tissue that lies between the markers and the objective reduces the number of emitted photons that can be collected by the microscope,
- the scattering degrades the spatial resolution, and as a side effect also degrades the sensitivity because for a given number of detected photons, the signal is spread over more camera pixels.

In order to reduce these limitations, the fluorescence signal peak wavelength should lie in an absorption and diffusion free region and should be distinguishable, either spectrally or temporally, from the autofluorescence background.

Time-gated detection technique is used to isolate a time-decaying signal from other signals having a different, longer or shorter decay times. It is usually employed to get rid of the autofluorescence signal and enhance sensitivity [38][40][39][97]. In order to be highly efficient for the time-gated detection, the markers should have a lifetime at least one order of magnitude longer/shorter than the autofluorescence lifetime (< 5 ns) (see scheme in Fig.IV.1). Classical markers (fluorescent proteins or cyanine dyes) are thus not adapted to this technique because their lifetime is too close to the autofluorescence one [98][99]. Moreover, in order to enhance the sensitivity, the marker should also have optical properties adapted to tissue imaging (emission and absorption in the 'optical therapeutic window').

In this chapter, we will present *in vitro*, *ex vivo* and preliminary *in vivo* experiments that show short lifetimes rejection and NIR QDs detection enhancement using the optical system developed and presented in the previous chapter. The efficiency of the time-gated detection strongly depends on the gate characteristics (width and delay between the laser pulse and the beginning of the detection), on the relative magnitude of autofluorescence and probe signals and on the noise signal level. In order to better characterize the effect of all parameters we developed a model presented in the last section of this chapter.

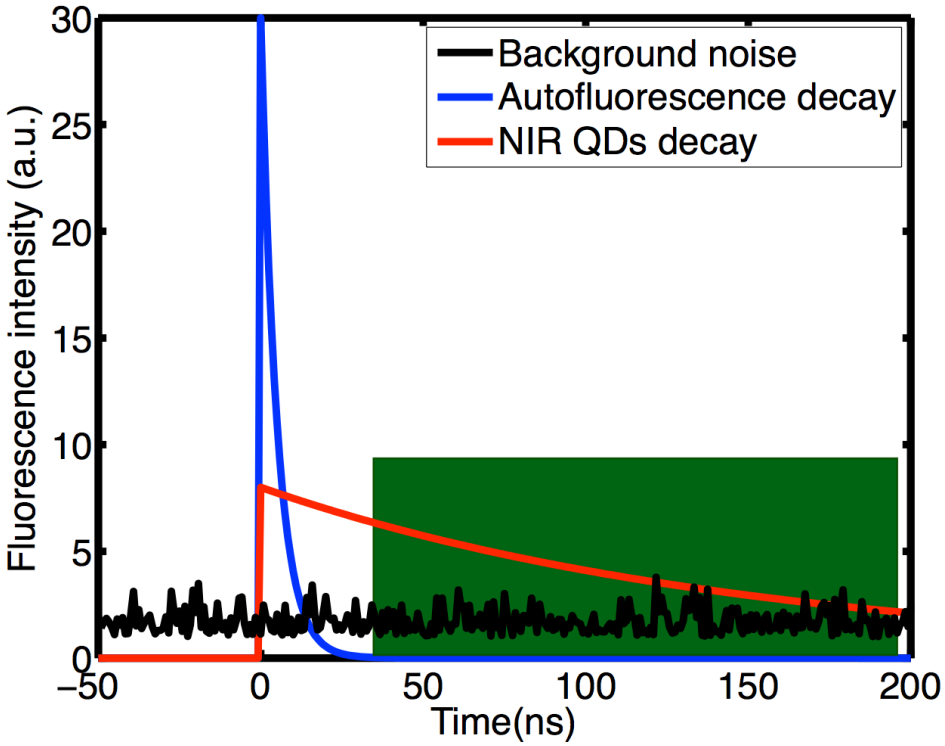

Figure IV.1 – Plot of the time-gated detection signals. In green, an adapted detection window to the removal of the autofluorescence signal.

IV.2 Short lifetime rejection

The optical set up described above can also be used to perform time-gated detection. Several groups have worked on time-gated detection in order to reduce autofluorescence signals. Time-gated detection can be performed by using Time-Correlated Single Photon Counting (TCSPC) or by using an intensifier. TCSPC has the advantage to be highly sensitive (detection of unique photons). However it is a scanning technique and first requires to construct a lifetime curve and secondly necessitates a computer program to build an image from a collection of detected events. Therefore, this method is not usable to track single dynamic events. The other solution is to use an intensifier that acts like a gate with programmable width and time shift with respect to the laser pulses. This method gives a time-gated (TG) image without necessarily perform a lifetime measurement and is thus better adapted for dynamic cell tracking. In this chapter, I will focus on the first results that show we can efficiently discriminate short lifetime signals from our NIR QDs' long fluorescence lifetime. I will also present the model we developed in order to better understand the influence of all parameters in the autofluorescence rejection efficiency.

IV.2.1 Description of the ratio $R(\tau, \Delta)$

In order to characterize the efficiency of the gate, we defined a scalar function of time, noted $R(\tau, \Delta)$, which corresponds to the ratio between the QD signal and all the other sources of signals that are considered undesirable. These signals are technical noises from the gate or the camera, photon noise and autofluorescence signals. The parameter τ corresponds to the time delay between the laser excitation and the beginning of the detection gate and Δ corresponds to the gate width of the detection. The signal given by a quantum dot on a camera pixel per laser pulse, noted ϕ_{QD} is :

$$\phi_{QD} = \varphi_{QD} \exp\left(-t/\tau_{QD}\right)$$

in counts per second. The value of ϕ_{QD} can be determined experimentally but depends strongly on the particular experimental conditions (exposure time, laser repetition rate, intensifier gains). φ corresponds to the amplitude of the signal.

If the detector exposure time is long compared to τ_{QD}, the signal in classical

fluorescence images, called here continuous wave images (CW) is :

$$S_{QD_{CW}} = \tau_{QD}\varphi_{QD}$$

Now, if we consider a gated detection with a gate width noted Δ and a delay τ between the excitation and the beginning of the detection, the integrated signal during an opening gate is given by :

$$S_{QD} = \int_{\tau}^{\tau+\Delta} \phi_{QD} \mathrm{d}t = \tau_{QD}\varphi_{QD} \exp\left(-\tau/\tau_{QD}\right)\left[1 - \exp\left(-\Delta/\tau_{QD}\right)\right]$$

The autofluorescence contribution can be described by the same way:

$$S_{a_{CW}} = \tau_a \varphi_a$$

and with a time-gated detection:

$$S_a = \tau_a\varphi_a \exp\left(-\tau/\tau_a\right)\left[1 - \exp\left(-\Delta/\tau_a\right)\right]$$

Therefore we define a general ratio, $R\left(\tau, \Delta\right)$, as:

$$R(\tau, \Delta) = \frac{S_{QD}}{S_{off} + S_a}$$

where S_{QD} and S_a correspond respectively to the signal of quantum dots and autofluorescence and S_{off} corresponds to the noise signal. If we use a gated-detection R becomes:

$$R(\tau, \Delta) = \frac{\tau_{QD}\varphi_{QD} \exp\left(-\tau/\tau_{QD}\right)\left[1 - \exp\left(-\Delta/\tau_{QD}\right)\right]}{S_{off} + \tau_a\varphi_a \exp\left(-\tau/\tau_a\right)\left[1 - \exp\left(-\Delta/\tau_a\right)\right]}$$

We note $S_{QD}(0)$ and $S_a(0)$, respectively the signal from the quantum dots and autofluorescence at zero delay:

$$S_{QD}(0) = S_{QD}(\tau = 0, \Delta) = \tau_{QD}\varphi_{QD}\left[1 - \exp\left(-\Delta/\tau_{QD}\right)\right]$$

$$S_a(0) = S_a(\tau = 0, \Delta) = \tau_a\varphi_a\left[1 - \exp\left(-\Delta/\tau_a\right)\right]$$

Finally we obtain:

$$R(\tau,\Delta)=\frac{S_{QD}\left(0\right)\exp\left(\frac{-\tau}{\tau_{QD}}\right)}{S_{off}+S_{a}\left(0\right)\exp\left(\frac{-\tau}{\tau_{a}}\right)} \tag{IV.1}$$

In a classical sample, where autofluorescence signal and NIR QDs signal are spatially superimposed, if we consider a region of interest at QDs location, ROI_{QDs}, and a region of interest where there is only autofluorescence, ROI_a, for each gate position we measure:

$$ROI_{QD}=S_{QD}+S_a+S_{off}$$

and

$$ROI_a=S_a+S_{off}$$

The background signal on each ROI can be previously eliminated by recording a sequence of images without excitation and by subtracting it to the original one with excitation.

Therefore if we calculate the ratio between both ROI, we finally obtain:

$$\frac{ROI_{QD}}{ROI_a}=\frac{S_{QD}+S_a+S_{off}}{S_a+S_{off}}=R+1$$

In the next section I will present results obtained for three different samples: *in vitro* sample where short lifetime spurious signal (that mimics autofluorescence) was spatially separated to NIR QDs signal, *ex vivo* sample where a NIR QDs stained cell was deposited in an autofluorescent tissue and preliminary *in vivo* samples where a solution of NIR QDs was injected in the tail vein of a mouse and the blood vessels of its ear were imaged.

IV.2.2 Test with spatially separated short lifetime and long lifetime QD signals

In order to demonstrate the possibility to discriminate efficiently short lifetime signals using our time-gated detection, we made a sample that contained cells stained with organic fluorophores, and cells previously labelled with QDs.

We simultaneously imaged cells electroporated with NIR QDs and cells electroporated with NIR fluorescent beads (beads coated with NIR organic fluorophores, *F8780, Invitrogen*) with a very short fluorescence liftetime ($\tau < 5$ ns). Figure IV.2 is a plot of the normalized fluorescence intensity decay of the two cells shown in Fig.

IV.3. These measurements show that the NIR QDs fluorescence lifetime is at least one order of magnitude longer than the fluorescence lifetime of the organic beads. After electroporation, cells have been rinsed, mixed together and deposited on the same cover slip. We have illuminated the cells with the pulsed laser source at 1 MHz and imaged them through 200-ns-gate. For this study, we did not investigate the influence of these two parameters that have been fixed arbitrarily. The signal was averaged over the central 10x10 pixels area of each cell. Each image has been acquired using a different delay τ between 0 ns and 200 ns with 2.7 ns steps. The camera exposure duration was fixed to 150 ms. Figure IV.3 shows examples of time-gated images of two cells taken at delay 0 ns, 11 ns, 30 ns and 50 ns. The left cell was stained with NIR QDs and the right one with fluorescent beads.

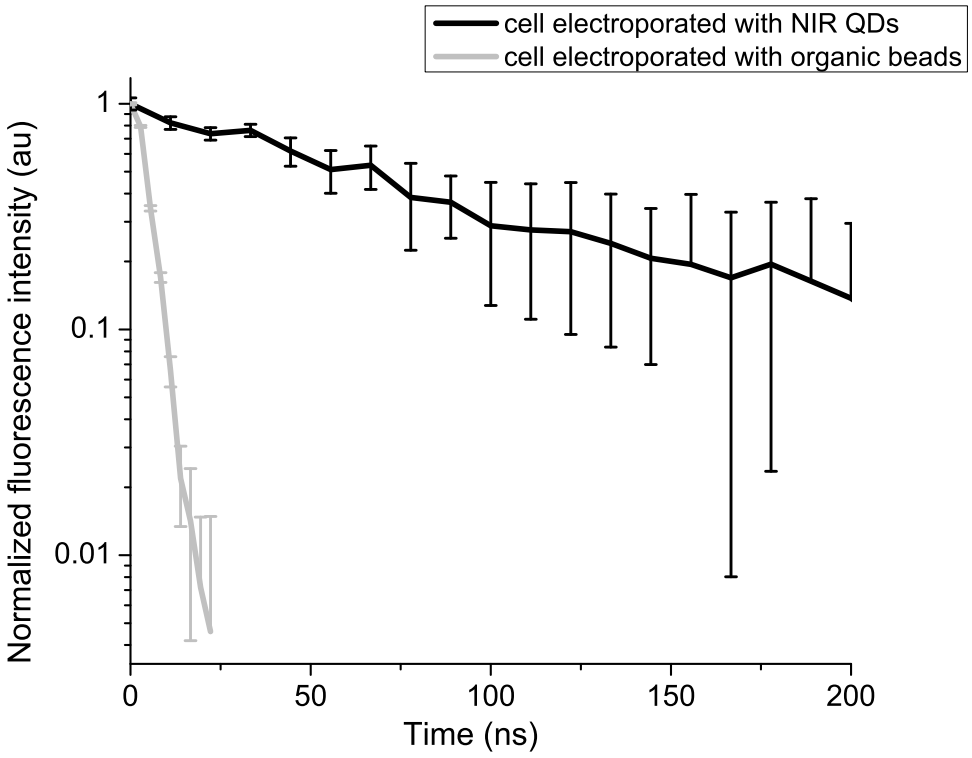

Figure IV.2 – Fluorescence intensity decay measurements of NIR QDs and fluorescent beads in cells.

We measured the ratio between NIR QDs and organic beads by defining a region of interest (ROI) on each cell. Here, both signals are spatially separated. Thus, on each ROI we measure a sum of QDs or beads signals and noise :

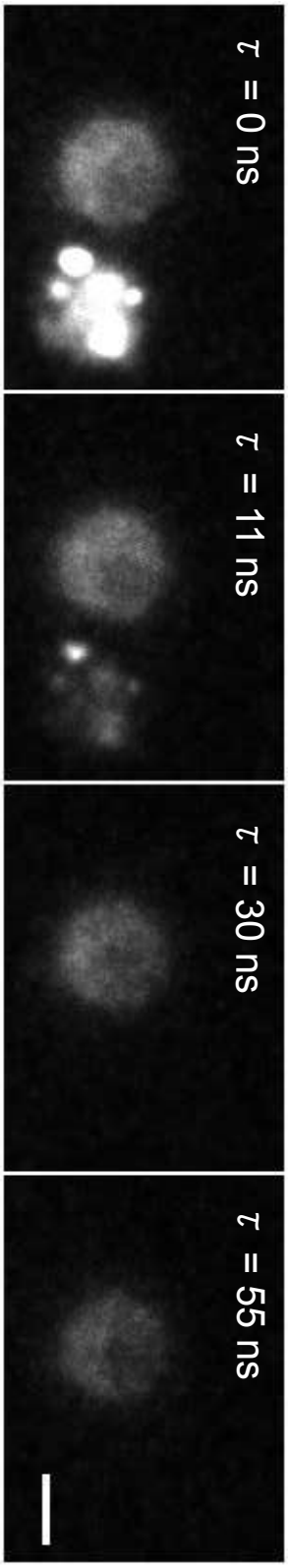

Figure IV.3 – Images of HeLa cells labeled with NIR QDs (cell on the left) or beads containing NIR fluorescent organic dyes (cell on the right) at different delays τ after the laser pulse (scale bar: 10 μm).

$$ROI_{QD} = S_{QD} + S_{off}$$

$$ROI_{beads} = S_{beads} + S_{off}$$

Therefore if we calculate the ratio between both ROI, we obtain:

$$R_{measured} = R + \frac{S_{off}}{S_{off} + S_{beads}\,(0) \exp\left(\frac{-\tau}{\tau_a}\right)}$$

The noise is estimated as the standard deviation of the background level previously defined. The second term of the equation is negligible when τ is short. When τ is high, S_{bead} contribution is very low and the term tends to 1.

Figure IV.4 presents the plot of R measured on the images presented in Fig. IV.3, as a function of the delay.

The fit allowed us to estimate a maximum R(τ) ratio obtained at $\tau = 28\,\text{ns}$. We consider the gain as the ratio between $R(\tau_{optimal})$ and $R(\tau = 0)$. Here, the R(τ) ratio increases by two orders of magnitude between $R(\tau = 0\,\text{ns}) = 0.44$ and $R(\tau = 28\,\text{ns}) = 40$. Experimentally, we found $R(\tau = 28\,\text{ns}) = 38$ At a delay of 27 $\pm$ 2.7 ns, the fluorescent beads signal goes below the noise level. This is thus, the optimal delay for opening the gate.

As long as the denominator in Equation IV.1 is dominated by the spurious fluorescence, the R(τ) ratio increases as $\exp(\tau\,(1/\tau_{fluo} - 1/\tau_{QD}))$. If on the contrary the background noise is dominant, the R(τ) ratio decreases as $\exp(-\tau/\tau_{QD})$.

For this experiment, we have recorded a stack of 402 images. Typically one image is recorded per second, thus the sample has been illuminated during *ca.* 6 minutes. We can wonder about a possible photobleaching of the organic dye fluorescence. For this reason, we have recorded sequences of images by increasing and then decreasing the delay of the opening of the gate as illustrated in Fig. IV.5. As previously performed, one image is acquired for each gate position. We measured the average intensity of a ROI and plotted it in the graph in Fig. IV.6. Indeed, the fluorescence of near-infrared emitting beads is decreased by photobleaching. Nevertheless, after 6 minutes of illumination, the signal has decreased by a factor of 1.5 but it is still 10 times larger than the background level. Therefore, the progressive disappearance of the cell stained with the fluorescent beads (right) clearly illustrates the rejection of the short lifetime signal when the delay increases and is not mainly induced by the photobleaching.

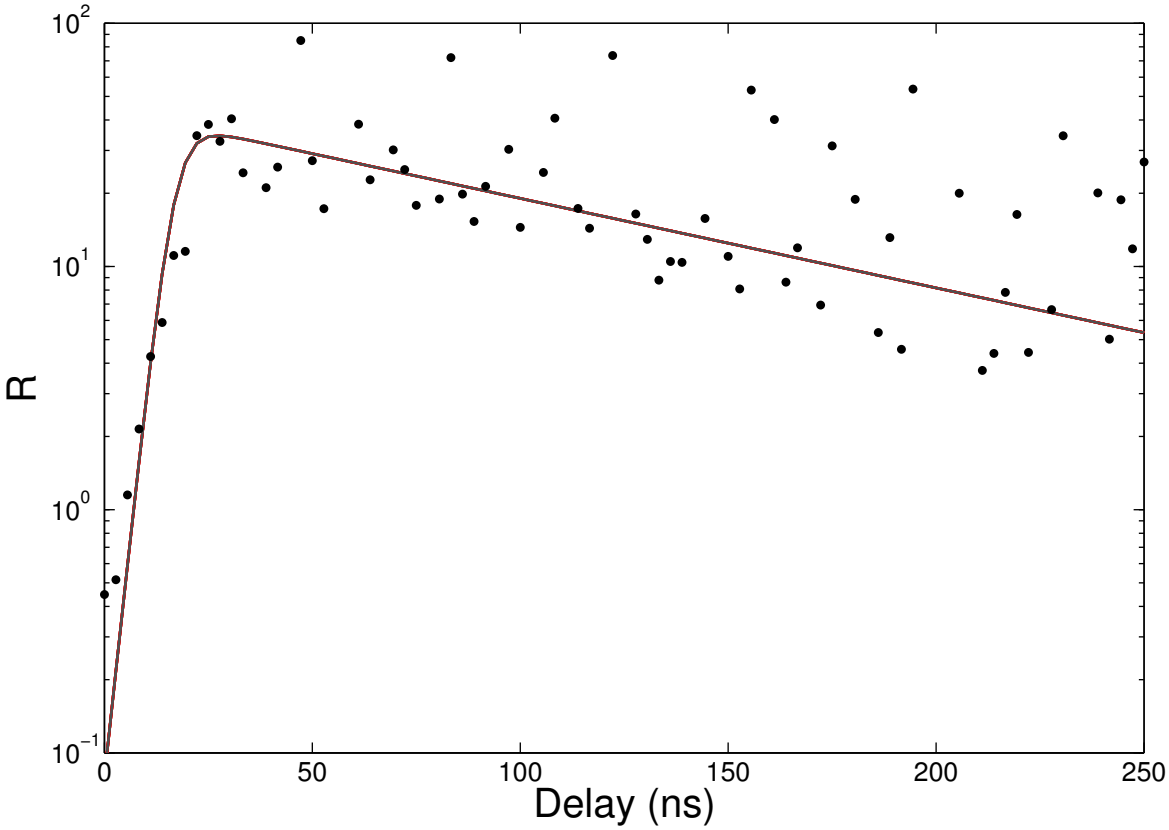

Figure IV.4 – Ratio R for our data (dots) and best (curve) fit using Eq. IV.1 as the fitting function.

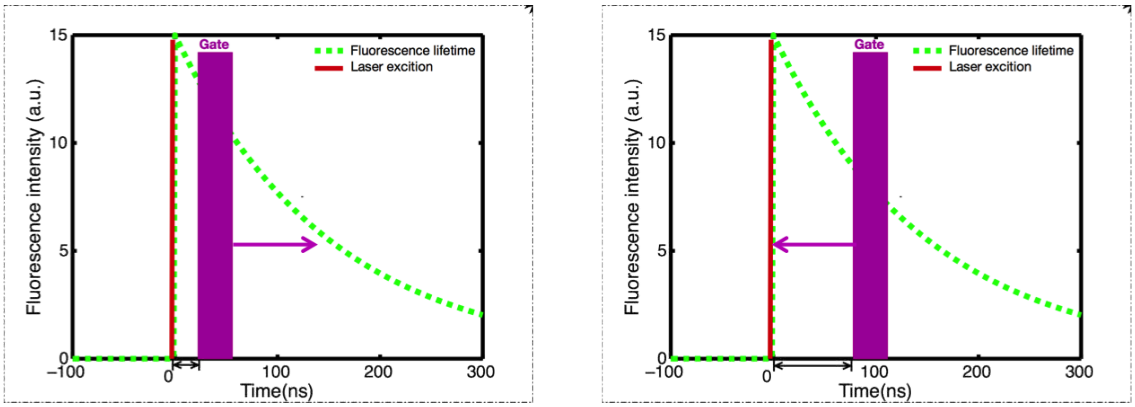

Figure IV.5 – Principle of "back and forth" measurements.

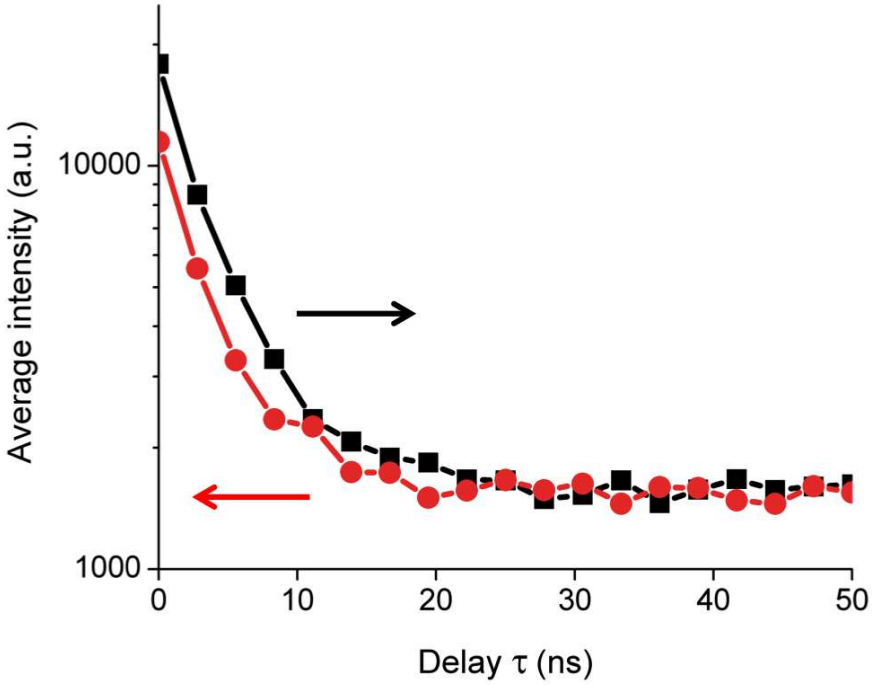

Figure IV.6 – Fluorescent intensity decay measurement of near infrared beads after "back and forth" measurements.

IV.2.3 Test in a real autofluorescent sample

We have deposited HeLa cells previously electroporated with NIR QDs on a thin slice of *ex vivo* tissue of beef muscle. Here QDs' signal is superimposed to the autofluoresence one, compared to the previous experiments where both signals were spatially separated. We have illuminated the sample with the pulsed laser source at 5 MHz and imaged it through a 160 ns gate width. Here again, we did not investigate the influence of the repetition rate and the gate width that have been fixed arbitrary. All images have been acquired with an exposure time of 100 ms and each image corresponds to an open gate position relative to the laser pulse at the zero delay $\tau = 0$. Here, we defined a ROI that corresponds to the cell and and another one around the cell that corresponds to the autofluorescence. We made the assumption that the autofluorescence signal is homogeneous in all the sample surface. As previously mentioned, for this type of sample we measure R+1.

Figure IV.7 is a plot of the average intensity at the cell location (purple curve), the average intensity next to the cell location (yellow curve) and the ratio R(τ) as defined in the previous section (red curve). For $\tau =< 0$ ns, which corresponds to a gate that is open when the laser pulse illuminates the sample, the autofluorescence signal dominates the NIR QDs one. Thus, both signals are nearly constant

and we mainly detect signal from tissue autofluorescence. For positive values of τ, since autofluorescence has a short fluorescence lifetime (<5 ns), its contribution falls rapidly. At $\tau = 17.7$ ns, when the autofluorescence signal falls below the noise level, R reaches its highest value: $R(\tau = 17.7) = 15.4$. This maximum represents an increase by more than one order of magnitude compared to zero delay $R(\tau = 0) = 0.6$, demonstrating the important benefit of our system. Then, R decreases following the QDs' fluorescence decay. Figure IV.8 shows images of the sample for two different time delays. On the left image, the gate opens before the laser impulsion, and both fluorescence from the cell and fluorescence from the tissue (autofluorescence) contribute to the signal. On the right image, the gate opens with a delay $\tau = 17.7$ ns after the laser pulse, the background due to autofluorescence has been eliminated using time-gated detection.

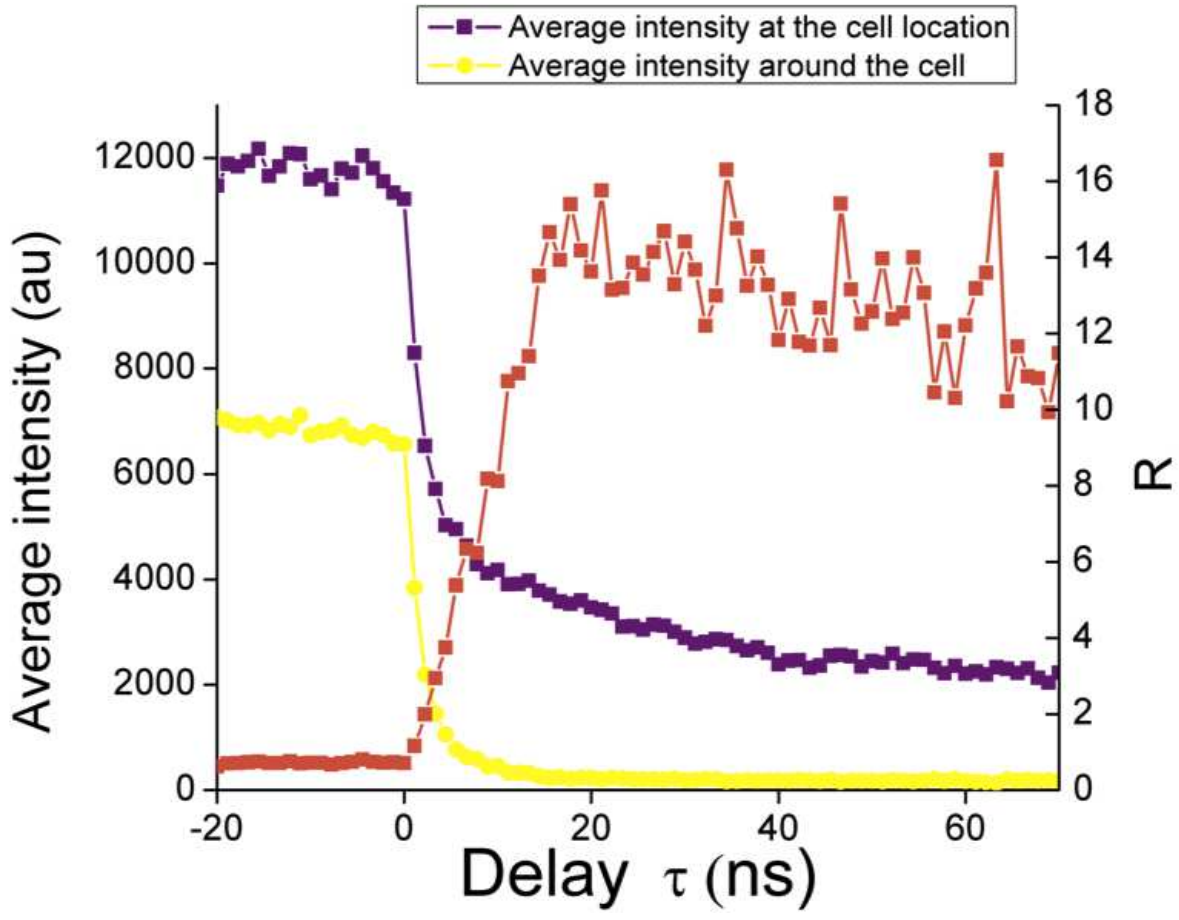

Figure IV.7 – Average intensity at the cell location (purple squares), average intensity of the autofluorescence (yellow circles). Evolution of the ratio R with the delay τ (red squares). ($\Delta = 160$ ns)

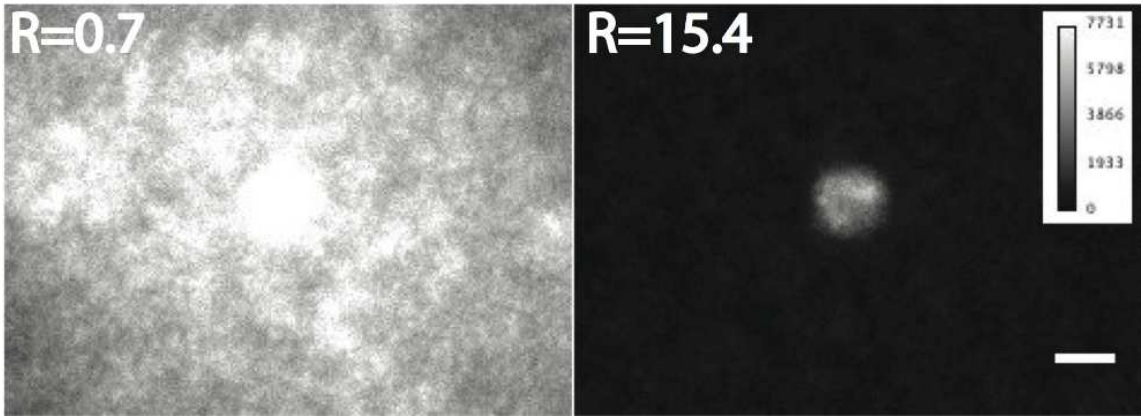

Figure IV.8 – Images of NIR QDs stained cell deposited in a thin slice of beef tissue for different positions of the gate detection (scale bar: 10 μm).

This experiment demonstrates the efficiency of autofluorescence rejection through time-gated detection of long lifetime NIR-QDs and the gain in sensitivity when a single stained cell is embedded within a strongly autofluorescent environment. Here, the gain has been multiplied by 25 compared to the measure obtained just after the laser pulse. The difference of gain between this experiment and the previous one is mainly due to the high value of the bead signal in the previous experiment. Indeed, as the gain inversely depends on the value of R($\tau = 0$), the more the spurious signal is high, the more the ratio R is low for $\tau = 0$ and the gain is high. The difference between the higher value of R strongly depends on the experimental conditions such as the repetition rate or the gate width and we did not optimize these parameters for both previous experiments.

IV.2.4 Preliminary results for *in vivo* experiments

We injected a solution of NIR QDs (about 1 nmol) in the tail vein of a mouse Balb/c and imaged the ear blood vessels using our time-gated detection. The repetition rate of the laser was fixed to 5 MHz and we imaged the mouse ear through a 40 ns-gate width. The gate width was chosen short because we investigated the fluorescence lifetime and wanted short gate width. The laser repetition rate was arbitrarily fixed to 5 MHz. Figure IV.9 depicts two images of a ear blood vessel of the mouse for different gate delays. The left image is acquired for a delay $\tau = 0$ ns and the right image is acquired for a delay $\tau = 7.7$ ns. On the left image we do not observe any blood vessel whereas on the right image the NIR QDs in the blood vessel are visible. As previously done, we calculated the ratio R for each image and obtained R($\tau =$

0) = 0.4 and R(τ = 7.7) = 2.9. Even if the value of R is not so high with the gated detection (less than 3), the gain using time-gated detection is multiplied by 7. Figure IV.10 is a plot of the average intensity at the vessel location and around the vessel as a function of the delay τ. Figure IV.10 also presents the evolution of R with the delay τ. As mentioned in the previous section, the ratio R reaches its maximum value when the autofluorescence signal falls bellow the noise. The short gain obtained here can be attributed to the short gate width compared to the previously described experiments.

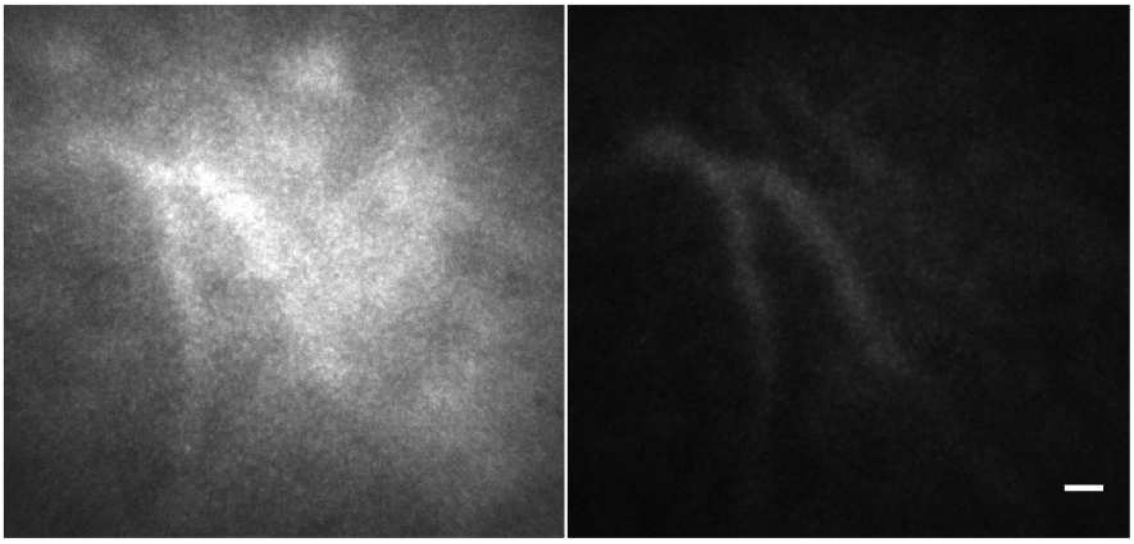

Figure IV.9 – Images of a ear blood vessel of a mouse for different gate delays. The left image is acquired for a delay $\tau = 0$ ns and the right image is acquired for a delay $\tau = 7.7$ ns. Scale bar : 20 μm.

These preliminary results are very encouraging and show that the gated-detection strongly enhances the sensitivity for *in vivo* NIR QDs detection. We now want to determine the best conditions in order to obtain the highest value of R.

In order to better understand the evolution of the ratio R and the gain obtained using the gated detection, we developed a model. This model takes into account the different noise sources, the gate width, the repetition rate of the laser diode, the NIR QDs and autofluorescence lifetimes.

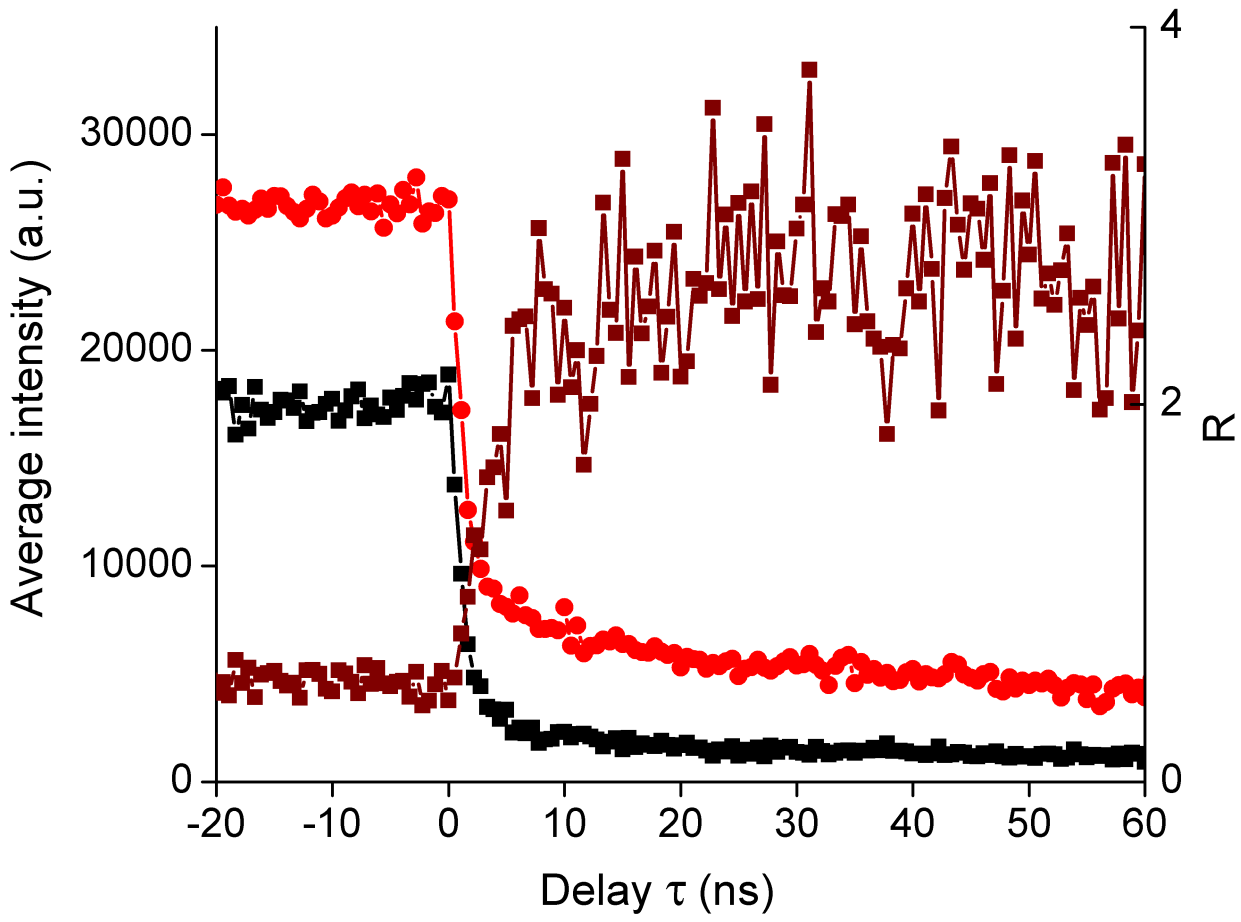

Figure IV.10 – Average intensity at the vessel location (in red) and around the vessel (in black). Evolution of the ratio R with the delay (in brown). (Δ=40 ns)

IV.3 Determination of optimal values of the different parameters

According to our definition of R, we have shown that it depends on five parameters (see Eq.IV.1):

1. The QDs fluorescence lifetime noted τ_{QD},
2. The autofluorescence lifetime noted τ_a,
3. The noise signal noted S_{off},
4. The gate width noted Δ,
5. The delay between the excitation and the beginning of the detection noted τ.

For the previous experiments we did not investigate the influence of the gate width and laser repetition rate. By deriving R versus τ, we can obtain the optimal value of τ when the derivative is equal to zero:

$$\frac{-1}{\tau_{QD}} S_{QD}(0) \exp(-\tau/\tau_{QD}) \left[S_{off} + S_a(0) \exp(-\tau/\tau_a)\right] + \frac{1}{\tau_a} S_{QD}(0) \exp(-\tau/\tau_{QD}) S_a(0) \exp(-\tau/\tau_a) = 0 \quad \text{(IV.2)}$$

This can also be written as:

$$\frac{-1}{\tau_{QD}} \left[S_{off} + S_a(0) \exp(-\tau/\tau_a)\right] + \frac{1}{\tau_a} S_a(0) \exp(-\tau/\tau_a) = 0$$

$$\left(\frac{1}{\tau_a} - \frac{1}{\tau_{QD}}\right) S_a(0) \exp(-\tau/\tau_a) = \frac{1}{\tau_{QD}} S_{off}$$

Thus we obtain:

$$\tau_{opt} = -\tau_a \left[\ln\left(\frac{S_{off}}{S_{a(0)}} \frac{\tau_a}{\tau_{QD} - \tau_a}\right)\right]$$

This formula is interesting because it shows that the optimal gate delay does not depend on the QDs concentration. If the first logarithm is dominant (which is consistent with the previous experiments where the autofluorescence dominates the

signal), then the value of τ_{opt} only depends on the autofluorescence and noise levels and lifetime. Thus we write τ_{opt} as :

$$\tau_{opt} = \tau_a \left[\ln \left(\frac{S_a(0)}{S_{off}} \right) \right]$$

We now consider a sum of impulsions for an integration time given for the EM-CCD camera. Figure IV.11 depicts the chosen configuration. We note Δ_{ccd} the exposure time and f_{mod} the repetition rate of the laser. The repetition rate can also be written as :

$$f_{mod} = (\tau_{opt} + \Delta)^{-1}$$

For the calculations, we assume that Δ_{ccd} is a multiple of $1/f_{mod}$ and we consider that the last gate detection takes into account the entire NIR QDs decay. We note N the number of impulsions during Δ_{ccd}. We have $N = f_{mod}\Delta_{ccd}$. The NIR QDs and autofluorescence signals can be written as :

$$S_{QD} = N\tau_{QD}\varphi_{QD} \exp(-\tau/\tau_{QD}) [1 - \exp(-\Delta/\tau_{QD})]$$

$$S_a = N\tau_a\varphi_a \exp(-\tau/\tau_a) [1 - \exp(-\Delta/\tau_a)]$$

If we take into account that the NIR QDs signal may extend over several pulses we have :

$$S_{QD} = N\tau_{QD}\varphi_{QD} \sum_{p=0}^{\infty} \exp\left(- \left(\tau + \frac{p}{f_{mod}} \right) / \tau_{QD} \right) [1 - \exp(-\Delta/\tau_{QD})]$$

$$S_{QD} = N\tau_{QD}\varphi_{QD} \exp(-\tau/\tau_{QD}) [1 - \exp(-\Delta/\tau_{QD})] \times \sum_{p=0}^{\infty} \exp\left(\frac{-p}{f_{mod}\tau_{QD}} \right)$$

$$S_{QD} = N\tau_{QD}\varphi_{QD} \exp(-\tau/\tau_{QD}) [1 - \exp(-\Delta/\tau_{QD})] \times \frac{1}{1 - \exp\left(\frac{-1}{f_{mod}\tau_{QD}}\right)}$$

Thus, if we want to determine the optimal delay τ_{opt} we have now :

$$\tau_{opt} = -\tau_a \left[\ln \left(\frac{S_{off}}{S_{a(0)}} \frac{\tau_a}{\tau_{QD} - \tau_a} \right) \right]$$

$$\tau_{opt} = \tau_a \left[\ln \left(\frac{N \tau_a \varphi_a \left[1 - \exp \left(-\Delta / \tau a \right) \right]}{S_{off}} \right) + \ln \left(\frac{\tau_{QD} - \tau_a}{\tau_a} \right) \right]$$

τ_{opt} now depends on N that also depends on f_{mod} and f_{mod} depends on τ_{opt}. Indeed, this problem has no analytical solution. For this reason we performed a numerical analysis in order to better understand the time-gated efficiency depending on the noise value, on the autofluorescence signal, on the probe lifetime.

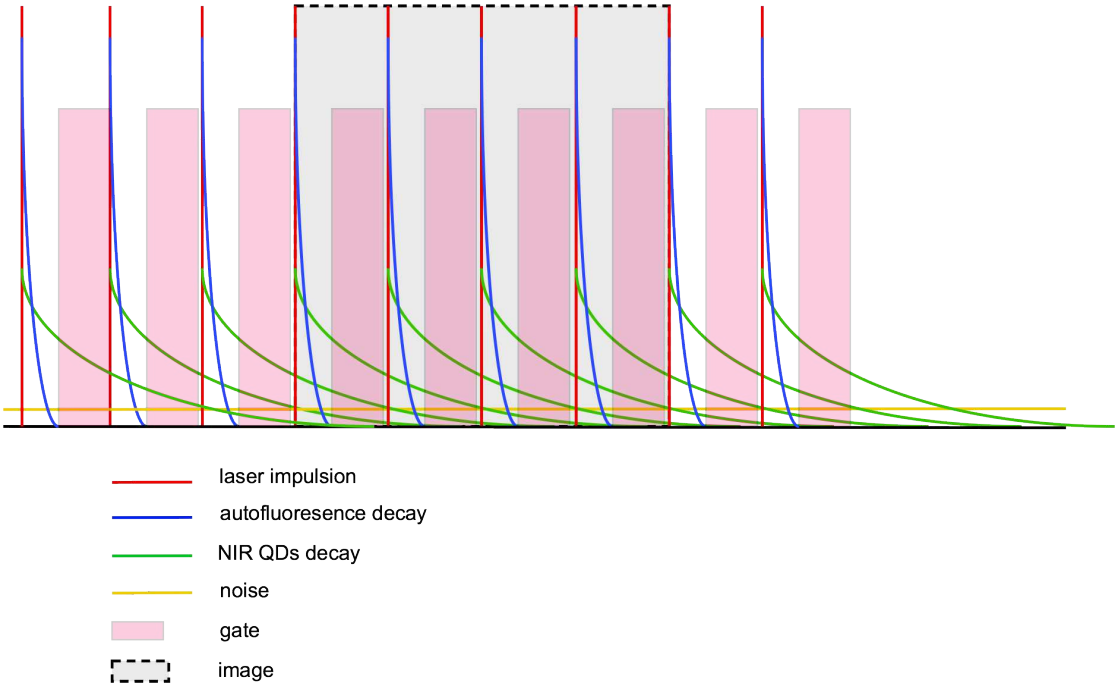

Figure IV.11 – Scheme of the chosen configuration for the calculations.

As mentioned in the previous chapter, the signal noise level can be written as:

- for time-gated images we have :

$$S_{off} = \sqrt{\left(\kappa_{off,N} \sqrt{N} \right)^2 + \left(\kappa_{CCD} \right)^2 + \left(\phi_{off} \sqrt{\Delta_{ccd}} \right)^2 + \left(S_{QD} \right)^2 + \left(S_a \right)^2 + \left(\kappa_{intensifier} \right)^2}$$

where S_{QD} and S_a are defined as following and are expressed in levels:

$$S_{QD} = N\tau_{QD}\varphi_{QD}\exp\left(-\tau/\tau_{QD}\right)\left[1-\exp\left(-\Delta/\tau_{QD}\right)\right] \times \frac{1}{1-\exp\left(\frac{-1}{f_{mod}\tau_{QD}}\right)}$$

$$S_a = N\tau_a\varphi_a\exp\left(-\tau/\tau_a\right)\left[1-\exp\left(-\Delta/\tau_a\right)\right]$$

where $\kappa_{off,N}\sqrt{N}$ corresponds to the noise component due to opening/closing gate, κ_{CCD} corresponds to the noise due to CCD camera, $\phi_{off}\sqrt{\Delta_{ccd}}$ corresponds to the noise that varies as the root square of the exposure time and $\kappa_{intensifier}$ is the noise due to the intensifier. κ constants are expressed in levels and ϕ_{off} is expressed in levels $\sqrt{Hz}$

- in classical images, when the gate is always opened we have :

$$S_{off} = \sqrt{\left(\kappa_{CCD}\right)^2 + \left(\phi_{off}\sqrt{\Delta_{ccd}}\right)^2 + \left(S_{QD}\right)^2 + \left(S_a\right)^2 + \left(\kappa_{intensifier}\right)^2}$$

where $S_{QD_{CW}} = N\varphi_{QD}\tau_{QD}$ and $S_{a_{CW}} = N\varphi_a\tau_a$ correspond to the signals values in continuous wave mode.

First, we fixed the noise signal level, the autofluorescence and NIR QDs levels and changed the fluorescence lifetime of the probes. In order to only observe the influence of the fluorescence lifetime on the final gain, we fixed the value of $S_{QD_{CW}}$. Here the gain is defined as the ratio between the QD signal and the autofluorescence signal, normalized by the same ratio without time-gated detection. We fixed the exposure time at 100 ms.

However, our developed model needs an order of magnitude for signal values. We used values obtained in a mode where the gate is permanently opened, as in classical fluorescence microscopy. Results are obtained for a repetition rate of 5 MHz. As the energy of one laser impulsion is constant, we can obtain the signal value for another repetition rate by multiplying the signal value by the corresponding multiple factor between both repetition rates. In our model we used this strategy and took $S_{a_{CW}} = 96200$ and $S_{QD_{CW}} = 37700$ counts, according to the data obtained for *in vivo* experiment. Moreover, constants $\kappa_{off,N}$, κ_{CCD}, ϕ_{off} are difficult to measure independently. For this reason, we chose values such as the ratio between S_a and S_{off} is equal to 100 for a delay $\tau = 0$ ns. This corresponds to the higher value of S_a and this assumption is relevant with our previous experimental data.

As we want to better identify the influence of the different parameters we decided to change separately the noise components, the signal components and lifetime components. The autofluorescence signal value was fixed for all simulations.

First, we varied the probe lifetime and determined the optimal parameters by assuming that the quantum efficiency is conserved even if the fluorescence lifetime varies. Thus, we fixed $S_{a_{CW}}$, $S_{QD_{CW}}$, S_{off} and varied the probe lifetime value. Our program allows calculating the optimal values of the repetition rate (noted $f_{mod,opt}$), the optimal delay (noted τ_{opt}), the value of R without and with time-gated (noted respectively R in CW, and R in TG) and the gain using time-gated detection (noted G). Here, the gain is defined as the ratio between the QD signal and the autofluorescence signal, normalized by the same ratio without time-gated detection. Table IV.1 presents the optimal parameters depending on the probe lifetime values. As shown in this table, the probe lifetime value has an influence on the final value of R in time-gated detection. Indeed, when the probe lifetime is too close to the autofluorescence lifetime the value of R is close to one. However, if the lifetime value increases the R value also increases. Nevertheless, the difference between a lifetime of 150 ns and a lifetime of 15 μs is not so high. Thus, in order to efficiently couple probes to time-gated detection they need to have a lifetime of one order of magnitude higher than the autofluorescence one.

Probe lifetime (ns)	R in CW	R in TG	Gain	τ_{opt} (ns)	$f_{mod,opt}$(MHz)
15	0.18	1.2	6.7	17	21
150	0.18	3.1	16	23	13
15000	0.18	3.3	18	24	13

Table IV.1 – Parameters values depending on the probe fluorescence lifetime

We fixed the autofluorescence and QDs lifetimes and signals and varied the value of the noise signal. Table IV.2 presents the optimal parameters for different ratios S_a/ S_{off}. Noise signal has an influence on the R value in time-gated detection. It also shows that for a low S_a/ S_{off} the repetition rate increases compared to a configuration where S_a/ S_{off}. Indeed, for low ratios S_a/ S_{off} the optimal τ is shorter and the gate is opened during few nanoseconds in order to not accumulate noise signal. Using our previously mentioned conditions, we found a S_a/ S_{off} ratio limit value of 35 in order to provide a SNR equal to 1 in time-gated detection.

Then we fixed the signal of autofluorescence and varied the QDs signal in order to understand the optimal values modifications. Table IV.3 presents the different

Ratio S_a/ S_{off}	R in CW	R in TG	Gain	τ_{opt} (ns)	$f_{mod,opt}$(MHz)
1000	0.35	22	63	30	13
100	0.18	3.1	16	23	13
50	0.12	1.7	13	20	15
10	0.033	0.43	13	10	29

Table IV.2 – Parameters values depending on the ratio S_a/ S_{off}.

parameters for different ratios S_a/S_{QD}. The value of R for time-gated detection strongly depends on the ratio S_a/S_{QD}, almost linearly. This shows that it is crucial to label cells with a high quantity of probes in order to increase S_{QD} and R in time-gated. We can also determine the limit of QD signal value in order to obtain a value of R equal to 1. We found a S_a/S_{QD} limit ratio of 7.7.

Signal values	R in CW	R in TG	Gain	τ_{opt} (ns)	$f_{mod,opt}$(MHz)
$S_a = 5 \times S_{QD}$	0.099	1.6	13	23	14
$S_a = 3 \times S_{QD}$	0.16	2.5	13	23	14
$S_a = S_{QD}$	0.41	7.8	19	23	14

Table IV.3 – Parameters values depending on the values of S_a and S_{QD}.

All these simulations were performed for previously defined values of lifetimes and signals that corresponded to previous experimental conditions. The developed model allows a determination of optimal parameters regarding fixed signal and lifetime values. By fixing the autofluorescence value and changing noise and QD values it permits to determine the best conditions for time-gated detection and to optimize R. These simulations revealed that in many cases the optimal repetition rate is in the range between 12 and 15 MHz, which corresponds to a repetition rate three times more important that the one we used for our experiments. The next experiment will consist in using a pulsed laser repetition rate between 12 and 15 MHz and checking if the measurements are coherent with the model. Then we can use this model to design the *in vivo* experiment where I will inject QD stained A20 cells into the mouse bloodstream and use our time gated detection to visualize them.

IV.4 Conclusion

In this chapter, we have shown we could efficiently discriminate long fluorescence lifetimes from short fluorescence decays spatially separated using our optical set up.

We have also shown we could efficiently enhance sensitivity (multiplied by 25) when a stained cell was embedded in an autofluorescent tissue. We also presented preliminary *in vivo* results: we injected a solution of NIR QDs in a mouse bloodstream and also strongly enhanced sensitivity using time-gated detection to visualize the vessels. In the last section, we presented a model developed in order to better characterize the influence of each parameter on the efficiency of time-gated detection. We have shown that, as mentioned previously, the probe fluorescence lifetime, the noise signal level and the ratio S_a/S_{QD} are crucial parameters for the final value of R. Now, we would like to validate this model by comparing these simulations with experimental data. Finally, we want to inject massively loaded cells with NIR QDs in a mouse bloodstream and determine the optimized parameters to enhance their detection using our time-gated detection. We also plan to inject different ranges of known cell concentrations in order to verify if our system is also quantitative.

V

Protocols

V.1 Synthesis of near-infrared-emitting quantum dots

This protocol describes the synthesis of near infrared emitting quantum dots based in I III VI materials.

Core synthesis

The synthesis of Zn-Cu-In-Se/ZnS core/shell quantum dots is inspired by Cassette et al. In our core synthesis, all precursors (0.4 mmol of CuCl, 0.4 mmol of InCl3, 0.8 mmol of selenourea, 0.8 mmol of Zn acetate) are introduced in a three-necked flask with 10 mL of octadecene (ODE) and 4 mL of trioctylphosphine (TOP), and briefly sonicated. Then, 4 mL of oleylamine (OAm) and 2 mL of dodecanethiol are added. The solution becomes pink and is stirred and degassed for 30 min under vacuum. The flask is then filled with argon and the solution heated progressively up to 260°C by steps of 5°C. During the rise in temperature, the solution becomes colorless and then red and finally black indicating the formation of nanocrystals. Heating is stopped immediately after the target temperature is reached and the flask is cooled down to room temperature. The Zn-Cu-In-Se cores are precipitated twice with ethanol and then dispersed in 10 mL of hexane.

ZnS precursors preparation

Zinc oleate, $Zn(OA)_2$, was prepared from hexahydrate $Zn(NO_3)_2$ and Na(OA). 30 mmol (m=8.91 g) of $Zn(NO_3)_2$,$6H_20$ (M = 297 g/mol) are dissolved in methanol and 60 mmol (m=18.27 g) of Na(OA) (M=304 g/mol) are also dissolved in methanol. When the two solutions are perfectly clear , they are mixed slowly. The resulting white precipitate was isolated by filtration and dried one night under vacuum.

Zinc ethylxanthate, $Zn(EtX)_2$, was prepared from hexahydrate $Zn(NO_3)_2$and K(EtX) as follows: 10 mmol of hexahydrate $Zn(NO_3)_2$ and 20 mmol of K(EtX) (M=160 g/mol) were separatly dissolved in distilled water. The solution were slowly mixed under stirring to form a white precipitate that was isolated and washed several times with water and dried overnight at 60°C.

Shell synthesis

For the shell synthesis, 4 mL of as-prepared cores are dispersed in 4 mL of ODE and 1 mL of OAm into a new three-necked flask. The mixture is degassed under vacuum at 40° C. A solution of zinc ethylxanthate and zinc oleate (respectively 0.13 mmol

and 0.8 mmol) dissolved in ODE (2 mL), TOP (3 mL), and dioctylamine (1 mL) is loaded into an heated injection syringe. The flask is heated to 190°C and these ZnS precursors are added dropwise in 1 h under argon atmosphere. The injection is introduced when the temperature reaches 130°C in order to be sure that at 190°C this is well underway. At the end of the injection, the reaction flask is cooled down to room temperature. The resulting Zn-Cu-In-Se/ZnS QDs are finally precipitated with ethanol and redispersed in 10 mL of hexane.

Synthesis of the PDSB ligand

Synthesis of the monomer A

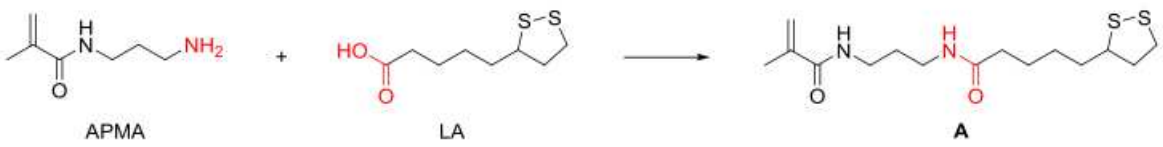

Figure V.1 – Scheme of the synthesis of the PDSB ligand [85].

To a suspension of APMA-HCl (2 g, 11.2 mmol) in dichloromethane (20 mL) was added triethylamine (2.5 mL, 17.9 mmol). Methanol (2 mL) was introduced to obtain complete solubilization. A solution of LA (2.76 g, 13.4 mmol) in dichloromethane (5 mL) was then added, followed by NHS (1.58 g, 13.8 mmol) in one portion. The reaction mixture was cooled down to 0°C with an ice bath and a solution of DCC (3.00 g, 14.4 mmol) in dichloromethane (10 mL) was injected dropwise. The medium was warmed up to room temperature and further stirred overnight. A pale yellow solution containing a white precipitate was obtained. The solution was washed by a 0.1 M aqueous HCl solution (2 × 50 mL), deionized water (1 × 50 mL) and a 0.2 M aqueous NaOH solution (2 × 50 mL). The organic phase was separated, dried over $MgSO_4$, filtrated and concentrated under reduced pressure. The crude residue was purified by chromatography on silica (eluent: hexane/ethyl acetate 1/4, then hexane/acetone 1/1) to give A (2.88 g, 8.71 mmol, 78%) as a pale yellow solid.

Synthesis of the polymer A+B

To a solution of B (SPP, 1.17 g, 4 mmol, 4 equiv.) in deionized water (20 mL) was added a solution of A (331 mg, 1 mmol, 1 equiv.) in THF (20 mL). A solution of

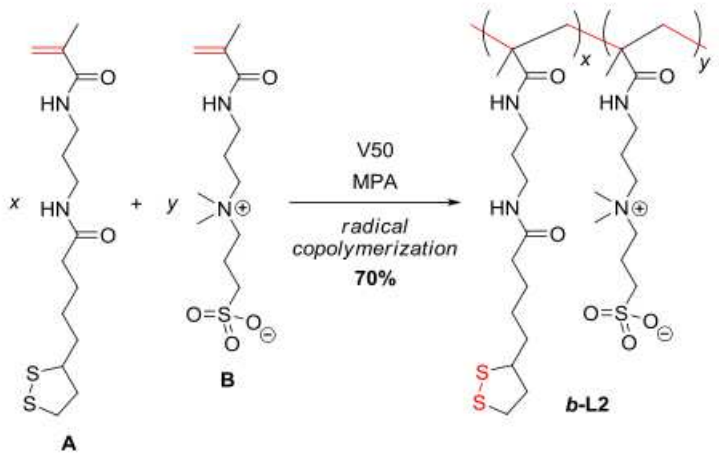

Figure V.2 – Scheme of the synthesis of the PDSB ligand [85].

V50 (130 mg, 0.5 mmol, 0.5 equiv.) in deionized water (2 mL) was further added in one portion. The pale yellow mixture was stirred and degassed by argon bubbling for 40 min. MPA (42 μL, 0.5 mmol, 0.5 equiv.) was injected into the reaction medium, which was stirred overnight at 60°C under argon atmosphere. THF was evaporated under reduced pressure; the residual solution was extracted with 20 mL of dichloromethane and the aqueous phase was separated. A 9-fold excess of ethanol was poured into the latter phase to precipitate the polymer, which was separated by centrifugation (50-mL centrifuge tubes, 2,800 g, 10 min) and further dried overnight under vacuum in the presence of P_2O_5 as a desiccant. The polymer was obtained as an off-white solid (1.05 g, 70%).

V.2 Solubilization in water: ligand exchange

As decribed previously, the NIR QDs synthesis occurs in organic media. In order to obtain biocompatible QDs, the solubilization in water is performed thanks to a ligand exchange.

400 μL of core/shell nanocrystals are precipitated with ethanol and resuspended in 150 μL of mercaptopropionic acid (MPA) overnight at 60°C. The QDs are dissolved in dimethylformamide (1 mL) and precipitated using potassium tert-butoxide. QDs are resuspended in basic water (sodium tetraborate 10 mM, pH 9.2) and mixed with a solution of PDSB ligands previously reduced by $NaBH_4$ (in order to open the dithiol function) for 12 h at 60°C (see Fig.II.21). After the ligand exchange, the QDs are purified using ultrafiltration (thanks to 30 KDa vivaspins) and ultra-

centrifugation (at 50 000 rpm, during 25 minutes in a 10-40 % sucrose gradient). After the ultracentrifugation, a tiny band of nanocrystals with same morphological properties is isolated. This solution is then purified by ultrafiltration. The QDs are finally resuspended in a 20 mM aqueous solution of NaCl.

V.3 Electroporation of HeLa cells

QDs are diluted in Dulbecco's Modified Eagle Medium (DMEM) enriched with 10 % Fetal Bovine Serum (FBS) and 1% penicillin-streptomycin antibiotics, later referred as complete medium. About 500,000 HeLa cells are previously precipated by centrifugation (2000 rpm, 5 minutes) and then suspended with 10 μM of QDs in a final volume of 100 μL in a 2-mm electroporation cuvette. The cuvette is subjected to 0.15 kV for about 30 ms pulse using a Gene Pulser (Biorad) electroporator. Juste after the electroporation, 1 mL of warm complete medium is added in the electroporation cuvette. The solution is then transfered in a 2 mL-ependorf and cells are rinsed 5 times with warm complete medium by centrifugation (1200 rpm, 5 minutes). Cells are then deposited in a 4-wells LabTek and are kept at least for 1 h at 37°C under a 5% CO2 atmosphere before imaging.

V.4 Chemical and biological products used

V.4.1 Chemical products

Product	Abreviation	Assay	Origin	Storage
Copper chlorure(I)	CuCl	>99%	Sigma-Aldrich	-
Indium chlorure	$InCl_3$	99.999%	Sigma-Aldrich	Glove box
Zinc acetate	-	99.99%	Aldrich	-
Selenourea	SeU	>98%	Acros Organics	4°C glove box
Sodium oleate	Na(OA)	>82%	Riedel-de Heen	-
Zinc nitrate	$Zn(NO_3)_2$	> 98%	Riedel-de Heen	-
Potassium Ethylxanthogenate	K(EtX)	>98%	Sigma-Aldrich	-
Potassium *tert*-butoxide	-	>97%	Fluka	-
Oleylamine	OAm	96%	Acros Organics	-
Dioctylamine	DOA	98%	Acros Organics	-
Trioctylphosphine	TOP	>95%	Cytop-380	Glove box
Dodecanthiol	DDT	>97%	Sigma-Aldrich	-
Mercaptopropionic Acid	MPA	>99%	Sigma-Aldrich	-

V.4.2 Chemical solvents

Solvent	Abreviation	Assay	Origin
1-Octadecene	ODE	90%	Sigma-Aldrich
Hexane	-	-	VWR
Ethanol	EtOH	-	VWR
Methanol	MetOH	RE	Carlos Herba
Dimethylformamide	DMF	anhydrous 99.8%	Sigma-Aldrich

V.4.3 Biological products

Product	Abreviation	Origin
Dulbecco's Modified Eagle Medium	DMEM	Life technologies
Roswell Park Memorial Institute 1640	RPMI	Life technologies
Fetal Bovine Serum	FBS	Life technologies
Penicillin-streptomycin	-	Life technologies
Hygromycine	-	Life technologies
Dulbecco's Phosphate-Buffered Saline	DPBS	Life technologies
Trypsine	-	Life technologies
Electroporation cuvette	-	Eurogentec

V.4.4 Preparation of cell medium for HeLa cells

HeLa cell complete medium was prepared with :

- 1 bottle of 500 μL of DMEM medium Glutamax+,
- 50 mL of FBS,
- 5 mL of Penicillin-streptomycin,

All the preparation is filtered using 22 μm membrane filters. The HeLa cell complete medium is conserved at 4°C.

V.4.5 Preparation of cell medium for A20 cells

HeLa cell complete medium was prepared with :

- 1 bottle of 500 μL of RPMI medium Glutamax+,
- 50 mL of FBS,
- 5 mL of Penicillin-streptomycin,
- 1 mL of pyruvate .

All the preparation is filtered using 22μm membrane filters. The A2O cell complete medium is conserved at 4°C. If A20 are tranfected with luciferase, 1% of hygromycine is added in the medium. The luciferase gene is often next to a restance gene for hygromycine, it allows to preferentially select cells Luciferase +.

Conclusion

The detection of individual and rare cells *in vivo* remains a challenge and is crucial to better understand metastatic migration pathways and processes. Indeed, it requires a highly sensitive imaging instrument to detect circulating tumour cells that leave the primary tumour to invade another site. Fluorescence imaging is a sensitive technique but its sensitivity is limited by the low visible light penetration depth because of absorption and scattering of tissues and the tissue autofluorescence.

During my PhD thesis, I have worked on the development of a sensitive fluorescence imaging technique using an exogenous labelling with nanoparticles for *in vivo* cell tracking. I have optimized the synthesis of near-infrared emitting quantum dots in order to enhance their fluorescence quantum yield. We noticed that the incorporation of zinc in the core synthesis has provided us brighter quantum dots. We attributed this to defect passivation and a filling of vacancy sites by Zn atoms inside cores. Using our synthesis we have obtained nanoparticles with an emission wavelength centred at 800 nm in the "optical therapeutic window" where absorption and scattering are minimal and with a fluorescence quantum yield up to 35% in hexane. These nanoparticles have been water solubilized using a new co-polymer developed in the lab that provides nanoparticle stable in a biological environment up to one week after their incorporation. These type of quantum dots also have a long fluorescence lifetime (around 150 ns) compared to tissue autofluorescence (<5 ns). We used this property to couple them to a time-gated detection in order to reduce autofluorescence signal that degrades contrast in fluorescence imaging.

The second part of my project was to develop a wide-field fluorescence microscope to perform time-gated detection. This technique was used to isolate a time-decaying signal from other signals having a different time decay. The detection developed allowed a cell scale resolution and permitted to realize both time-gated detection and fluorescence lifetime measurements. The optical set up is based on an intensifier that acts like a gate that opens and closes with a controllable delay after the laser

impulsion. We performed *in vitro* and *ex vivo* experiments and enhanced sensitivity by a multiplied factor of 25. This allowed us to detect a unique cell embedded in an autofluorescent signal. We also performed preliminary *in vivo* experiments by injecting a solution of NIR QDs in a mouse bloodstream via the tail vein and then imaging ear vessels with enhanced sensitivity and signal-to-noise ratio. These results are promising and we managed to enhance the signal-to-background by a factor 7. Moreover, all the parameters were not optimized regarding this application. We also developed a model in order to better understand the influence of the different gate parameters on the signal-to-noise ratio.

In perspective of this work we want to inject A20 cells previously electroporated with near-infrared quantum dots in a mouse bloodstream via the tail vein and determine if our technique is sensitive enough to detect an individual stained cell. We plan to inject massively loaded cells at different concentrations. This will allow determining experimental conditions to detect *in vivo* isolated cells and the final sensitivity gain. In the case of no cell is detected we plan to change our spot laser geometry in order to increase the excitation power. This can be performed efficiently because with our actual experimental conditions and NIR QDs are not saturated by the excitation. An other strategy to increase the sensitivity is to perform binning even if it provides a loss of resolution. Then, once signal detected, we also want to determine the lower NIR QDs concentration that can be detected in order to correlate it to the number of cell divisions and the number of days we will be able to detect QDs stained A20 cells for the PIOL application.

In the longer term, an other project in collaboration with a research team in Nancy is the staining of specific tumour cells and detection of small metastases, which are not detectable with classical imaging techniques. Finally, in collaboration with the Commissariat Ãă l' Energies Atomique et aux Energies Alternatives we would like to evaluate applications in stem cell transplants. Stem cells will be labelled with our NIR QDs and transplanted in a mouse brain. The aim is to observe these stem cells over a few days and, by using a second staining with a specific neuron differentiation dye, we will be able to correlate their differentiation into neurons with the number of cell divisions.

To conclude, many biological applications require high detection sensitivity. The development of our imaging system could be useful for many other cases.

Bibliography

[1] B. S. Harrison and A. Atala, "Carbon nanotube applications for tissue engineering.," *Biomaterials*, vol. 28, pp. 344–53, Jan. 2007.

[2] J.-Q. Gao, N. Okada, T. Mayumi, and S. Nakagawa, "Immune cell recruitment and cell-based system for cancer therapy.," *Pharmaceutical research*, vol. 25, pp. 752–68, Apr. 2008.

[3] N. Howlader, "SEER cancer statistics review 1975âĂŞ2008. National Cancer Institute [online] http:// seer.cancer.gov/csr/1975_2008/ (2011).."

[4] N. Mackiewicz, E. Gravel, A. Garofalakis, J. Ogier, J. John, D. M. Dupont, K. Gombert, B. Tavitian, E. Doris, and F. Ducongé, "Tumor-targeted polydiacetylene micelles for in vivo imaging and drug delivery.," *Small*, vol. 7, pp. 2786–92, Oct. 2011.

[5] B. Psaila and D. Lyden, "The metastatic nich: adapting the foreign soil," *Nature Reviews Cancer*, vol. 9, no. 4, pp. 285–293, 2009.

[6] J. a. Joyce and J. W. Pollard, "Microenvironmental regulation of metastasis.," *Nature Reviews Cancer*, vol. 9, pp. 239–52, Apr. 2009.

[7] A. Schroeder, D. a. Heller, M. M. Winslow, J. E. Dahlman, G. W. Pratt, R. Langer, T. Jacks, and D. G. Anderson, "Treating metastatic cancer with nanotechnology.," *Nature Reviews Cancer*, vol. 12, pp. 39–50, Jan. 2012.

[8] T. Ashworth, "A case of cancer in which cells similar to those in the tumours were seen in the blood after death,," *The Medical Journal of Australia,*, vol. 14, pp. 146–147, 1869.

[9] M. C. Miller, G. V. Doyle, and L. W. M. M. Terstappen, "Significance of Circulating Tumor Cells Detected by the CellSearch System in Patients with Metastatic Breast Colorectal and Prostate Cancer.," *Journal of oncology*, vol. 2010, p. 617421, Jan. 2010.

[10] M. Cristofanilli, T. Budd, M. Ellis, A. Stopeck, J. Matera, M. C. Miller, J. M. Reuben, G. V. Doyle, W. Allard, L. W. M. M. Terstappen, and D. F. Hayes, "Circulating Tumor Cells, Disease Progression, and Survival in Metastatic Breast Cancer," *The New Journal of Medicine*, pp. 781–791, 2004.

[11] J. a. Hanson, D. Alexandru, and D. a. Bota, "The evaluation and treatment of primary intraocular lymphoma," *Journal of Cancer Therapeutics and Research*, vol. 2, no. 1, p. 15, 2013.

[12] K. Peterson, K. a. B. Gordon, M.-H. Heinemann, and L. M. DeAngelis, "The clinical spectrum of ocular lymphoma.," *Cancer*, vol. 72, pp. 843–9, Aug. 1993.

[13] D. S. Bardenstein, "Intraocular Lymphoma.," *Cancer control : journal of the Moffitt Cancer Center*, vol. 5, pp. 317–325, July 1998.

[14] C.-C. Chan and D. J. Wallace, "Intraocular lymphoma: update on diagnosis and management.," *Cancer Control*, vol. 11, no. 5, pp. 285–95, 2007.

[15] G. S. Vosganian, S. Boisot, K. I. Hartmann, W. R. Freeman, R. W. Sharpe, P. Tripuraneni, and A. Saven, "Primary intraocular lymphoma: a review.," *Journal of neuro-oncology*, vol. 105, pp. 127–34, Nov. 2011.

[16] V. Touitou, C. Daussy, B. Bodaghi, S. Camelo, Y. de Kozak, P. Lehoang, M.-C. Naud, A. Varin, B. Thillaye-Goldenberg, H. Merle-Beral, W. H. Fridman, C. Sautes-Fridman, and S. Fisson, "Impaired Th1/Tc1 Cytokine Production of Tumor-Infiltrating Lymphocytes in a Model of Primary Intraocular B-Cell Lymphoma," *Investigative Ophthalmology & Visual Science*, vol. 48, pp. 3223–3229, July 2007.

[17] H. Hong, Y. Yang, Y. Zhang, and W. Cai, "Non-invasive cell tracking in cancer and cancer therapy," *Current Topics in Medicinal Chemistry*, vol. 10, no. 12, pp. 1237–1248, 2010.

[18] R. Weissleder and M. J. Pittet, "Imaging in the era of molecular oncology.," *Nature*, vol. 452, pp. 580–9, Apr. 2008.

[19] G. B. Saha, "Basics of PET Imaging," pp. 97–117, 2010.

[20] E. T. Ahrens and J. W. M. Bulte, "Tracking immune cells in vivo using magnetic resonance imaging.," *Nature Reviews Immunology*, vol. 13, pp. 755–63, Oct. 2013.

[21] I. J. M. de Vries, W. J. Lesterhuis, J. O. Barentsz, P. Verdijk, J. H. van Krieken, O. C. Boerman, W. J. G. Oyen, J. J. Bonenkamp, J. B. Boezeman, G. J. Adema, J. W. M. Bulte, T. W. J. Scheenen, C. J. a. Punt, A. Heerschap, and C. G.

Figdor, "Magnetic resonance tracking of dendritic cells in melanoma patients for monitoring of cellular therapy.," *Nature Biotechnology*, vol. 23, pp. 1407–13, Nov. 2005.

[22] M. A. Paley and J. A. Prescher, "Bioluminescence: a versatile technique for imaging cellular and molecular features," *MedChemComm*, vol. 5, no. 3, pp. 255–267, 2014.

[23] T. Ozawa, H. Yoshimura, and S. B. Kim, "Advances in fluorescence and bioluminescence imaging.," *Analytical Chemistry*, vol. 85, pp. 590–609, Jan. 2013.

[24] A. Dunne, N. A. Marshall, and K. H. G. Mills, "TLR based therapeutics.," *Current Opinion In Pharmacology*, vol. 11, pp. 404–411, Aug. 2011.

[25] R. Ben Abdelwahed, J. Cosette, S. Donnou, L. Crozet, H. Ouakrim, W. H. Fridman, C. Sautès-Fridman, A. Mahjoub, and S. Fisson, "Lymphoma B-cell responsiveness to CpG-DNA depends on the tumor microenvironment.," *Journal of Experimental & Clinical Cancer Research*, vol. 32, pp. 1–9, Jan. 2013.

[26] F. Leblond, S. C.Davis, P. A.Valdés, and B. W.Pogue, "Preclinical Whole-body Fluorescence Imaging: Review of Instruments, Methods and Applications," vol. 98, no. 1, pp. 77–94, 2013.

[27] J. Lakowicz, *Principles of fluorescence spectroscopy*. plenum pre ed., 1983.

[28] D. Elson, S. Webb, J. Siegel, K. Suhling, D. Davis, J. Lever, D. Phillips, A. Wallace, and P. French, "Applications of Fluorescence Lifetime Imaging," *Optics and Photonics News*, 2002.

[29] T. F. Massoud and S. S. Gambhir, "Molecular imaging in living subjects : seeing fundamental biological processes in a new light," *Genes and development*, pp. 545–580, 2003.

[30] J. V. Frangioni, "In vivo near-infrared fluorescence imaging," *Current Opinion in Chemical Biology*, vol. 7, pp. 626–634, Oct. 2003.

[31] Q. Ma and X. Su, "Near-infrared quantum dots: synthesis, functionalization and analytical applications.," *The Analyst*, vol. 135, pp. 1867–77, Aug. 2010.

[32] G. A. Wagnieres, W. M. Star, and B. C. Wilson, "ln Vivo Fluorescence Spectroscopy and Imaging for Oncological Applications," *Photochemistry and Photobiology*, vol. 68, no. 5, pp. 603–632, 1998.

[33] R. Richards-Kortum and E. Sevick-Muraca, "Quantitative optical spectroscopy for tissue diagnosis.," *Annual Review of Physical Chemistry*, vol. 47, pp. 555–606, Jan. 1996.

[34] L. S. Fournier, V. Lucidi, K. Berejnoi, T. Miller, S. G. Demos, and R. C. Brasch, "In-vivo NIR autofluorescence imaging of rat mammary tumors.," *Optics express*, vol. 14, pp. 6713–23, July 2006.

[35] G. Weagle, P. E. Paterson, J. Kennedy, and R. Pottier, "The nature of the chromophore responsible for naturally occuring fluorescence in mouse skin," *Journal of Photochemistry & Photobiology, B: Biology*, vol. 2, pp. 313–320, 1988.

[36] M. A. Funovics, R. Weissleder, and U. Mahmood, "Catheter-based in vivo imaging of enzyme activity and gene expression: feasibility study in mice.," *Radiology*, vol. 231, pp. 659–666, June 2004.

[37] A.-S. Montcuquet, *Imagerie spectrale pour l'étude de structures profondes par tomographie optique diff usive de fluorescence*. PhD thesis, 2010.

[38] M. Dahan, T. Laurence, F. Pinaud, and D. S. Chemla, "Time-gated biological imaging by use of colloidal quantum dots," *Optics letters*, vol. 26, no. 11, pp. 825–827, 2001.

[39] A. May, S. Bhaumik, S. S. Gambhir, C. Zhan, and S. Yazdanfar, "Whole-body, real-time preclinical imaging of quantum dot fluorescence with time-gated detection.," *Journal of Biomedical Optics*, vol. 14, no. 6, 2009.

[40] L. Gu, D. J. Hall, Z. Qin, E. Anglin, J. Joo, D. J. Mooney, S. B. Howell, and M. J. Sailor, "In vivo time-gated fluorescence imaging with biodegradable luminescent porous silicon nanoparticles," *Nature Communications*, vol. 4, pp. 1–7, 2013.

[41] J.-h. Park, L. Gu, G. V. Maltzahn, E. Ruoslahti, N. Sangeeta, and M. J. Sailor, "Biodegradable luminescent porous silicon nanoparticles for in vivo applications," *Nature materials*, vol. 8, no. 4, pp. 331–336, 2009.

[42] O. Faklaris, D. Garrot, V. Joshi, F. Druon, J.-P. Boudou, T. Sauvage, P. Georges, P. a. Curmi, and F. Treussart, "Detection of single photoluminescent diamond nanoparticles in cells and study of the internalization pathway.," *Small*, vol. 4, pp. 2236–2239, Dec. 2008.

[43] Y. Y. Hui, L.-J. Su, O. Y. Chen, Y.-T. Chen, T.-M. Liu, and H.-C. Chang, "Wide-field imaging and flow cytometric analysis of cancer cells in blood by fluorescent nanodiamond labeling and time gating.," *Scientific Reports*, vol. 4, Jan. 2014.

[44] X. He, J. Gao, S. S. Gambhir, and Z. Cheng, "Near-infrared fluorescent nanoprobes for cancer molecular imaging : status and challenges," *Trends in Molecular Medicine*, vol. 16, no. 12, pp. 574–583, 2010.

[45] A. Foucault-Collet, K. a. Gogick, K. a. White, S. Villette, A. Pallier, G. Collet, C. Kieda, T. Li, S. J. Geib, N. L. Rosi, and S. Petoud, "Lanthanide near infrared imaging in living cells with Yb3+ nano metal organic frameworks.," *Proceedings of the National Academy of Sciences*, vol. 110, pp. 17199–17204, Oct. 2013.

[46] U. Resch-Genger, M. Grabolle, S. Cavaliere-Jaricot, R. Nitschke, and T. Nann, "Quantum dots versus organic dyes as fluorescent labels.," *Nature Methods*, vol. 5, pp. 763–775, Sept. 2008.

[47] P. Reiss, M. Protière, and L. Li, "Core/Shell semiconductor nanocrystals.," *Small*, vol. 5, pp. 154–168, Feb. 2009.

[48] X. Michalet, F. F. Pinaud, L. A. Bentolila, J. M. Tsay, S. Doose, J. J. Li, G. Sundaresan, A. M. Wu, S. S. Gambhir, and S. Weiss, "Quantum dots for live cells, in vivo imaging, and diagnostics," *Science*, vol. 307, no. 5709, pp. 538–544, 2005.

[49] M. Bruchez Jr., M. Moronne, P. Gin, S. Weiss, and A. P. Alivisatos, "Semiconductor Nanocrystals as Fluorescent Biological Labels," *Science*, vol. 281, pp. 2013–2016, Sept. 1998.

[50] E. Cassette, M. Helle, L. Bezdetnaya, F. Marchal, B. Dubertret, and T. Pons, "Design of new quantum dot materials for deep tissue infrared imaging.," *Advanced Drug Delivery Reviews*, vol. 65, pp. 719–731, May 2013.

[51] J. M. Tsay, M. Pflughoefft, L. a. Bentolila, and S. Weiss, "Hybrid approach to the synthesis of highly luminescent CdTe/ZnS and CdHgTe/ZnS nanocrystals.," *Journal of the American Chemical Society*, vol. 126, pp. 1926–7, Feb. 2004.

[52] S.-W. Kim, J. P. Zimmer, S. Ohnishi, J. B. Tracy, J. V. Frangioni, and M. G. Bawendi, "Engineering InAs(x)P(1-x)/InP/ZnSe III-V alloyed core/shell quantum dots for the near-infrared.," *Journal of the American Chemical Society*, vol. 127, pp. 10526–32, Aug. 2005.

[53] S. Kim, Y. T. Lim, E. G. Soltesz, A. M. De Grand, J. Lee, A. Nakayama, J. A. Parker, T. Mihaljevic, R. G. Laurence, D. M. Dor, L. H. Cohn, M. G. Bawendi, and J. V. Frangioni, "Near-infrared fluorescent type II quantum dots for sentinel lymph node mapping," *Nature Biotechnology*, vol. 22, no. 1, pp. 93–97, 2004.

[54] L. Li, M. Protière, and P. Reiss, "Economic synthesis of high quality InP nanocrystals using calcium phosphide as the phosphorus precursor," *Chemistry of Materials*, vol. 20, pp. 2621–2623, Apr. 2008.

[55] R. Xie and X. Peng, "Synthetic scheme for high-quality InAs nanocrystals based on self-focusing and one-pot synthesis of InAs-based core-shell nanocrystals.," *Angewandte Chemie*, vol. 47, pp. 7677–80, Jan. 2008.

[56] L. Li, T. J. Daou, I. Texier, T. T. Kim Chi, N. Q. Liem, P. Reiss, T. K. C. Tran, and Q. L. Nguyen, "Highly luminescent CuInS 2 /ZnS core/shell nanocrystals: cadmium-free quantum dots for in vivo imaging," *Chemistry of Materials*, vol. 21, pp. 2422–2429, June 2009.

[57] T. Pons, E. Pic, N. Lequeux, E. Cassette, L. Bezdetnaya, F. Guillemin, F. Marchal, and B. Dubertret, "Cadmium-free CuInS2/ZnS quantum dots for sentinel lymph node imaging with reduced toxicity.," *ACS nano*, vol. 4, pp. 2531–8, May 2010.

[58] E. Cassette, T. Pons, C. Bouet, M. Helle, L. Bezdetnaya, F. Marchal, B. Dubertret, and L. Bolotine, "Synthesis and characterization of near-infrared Cu-In-Se/ZnS core/shell quantum dots for in vivo imaging," *Chemistry of Materials*, vol. 22, no. 22, pp. 6117–6124, 2010.

[59] C. J. Stolle, T. B. Harvey, D. R. Pernik, J. I. Hibbert, J. Du, D. J. Rhee, V. A. Akhavan, R. D. Schaller, and B. A. Korgel, "Multiexciton Solar Cells

of CuInSe 2 Nanocrystals," *The Journal of Physical Chemistry Letters*, vol. 5, pp. 304–309, Jan. 2014.

[60] R. Klenk, J. Klaer, R. Scheer, M. Lux-Steiner, I. Luck, N. Meyer, and U. Rühle, "Solar cells based on CuInS2- an overview," *Thin Solid Films*, vol. 480-481, pp. 509–514, June 2005.

[61] S. L. Castro, S. G. Bailey, R. P. Raffaelle, K. K. Banger, and A. F. Hepp, "Synthesis and characterization of colloidal CuInS2 nanoparticles from a molecular single-source precursor," *The Journal of Physical Chemistry B*, vol. 108, pp. 12429–12435, Aug. 2004.

[62] J. J. Nairn, P. J. Shapiro, B. Twamley, T. Pounds, R. von Wandruszka, T. R. Fletcher, M. Williams, C. Wang, and M. G. Norton, "Preparation of ultrafine chalcopyrite nanoparticles via the photochemical decomposition of molecular single-source precursors.," *Nano Letters*, vol. 6, pp. 1218–23, June 2006.

[63] C. Sun, J. S. Gardner, E. Shurdha, K. R. Margulieux, R. D. Westover, L. Lau, G. Long, C. Bajracharya, A. Thurber, A. Punnoose, R. G. Rodriguez, and J. J. Pak, "A high-yield synthesis of chalcopyrite CuInS2 nanoparticles with exceptional size control," *Journal of Nanomaterials*, vol. 2009, pp. 1–7, 2009.

[64] W. Du, X. Qian, J. Yin, and Q. Gong, "Shape- and phase-controlled synthesis of monodisperse, single-crystalline ternary chalcogenide colloids through a convenient solution synthesis strategy.," *Chemistry a European Journal*, vol. 13, pp. 8840–8846, Jan. 2007.

[65] P. M. Allen and M. G. Bawendi, "Ternary I-III-VI quantum dots luminescent in the red to near-infrared.," *Journal of the American Chemical Society*, vol. 130, pp. 9240–9241, July 2008.

[66] H. Zhong, Y. Zhou, M. Ye, Y. He, J. Ye, C. He, C. Yang, and Y. Li, "Controlled Synthesis and Optical Properties of Colloidal Ternary Chalcogenide CuInS 2 Nanocrystals," *Chemistry of Materials*, pp. 6434–6443, 2013.

[67] R. Xie, M. Rutherford, and X. Peng, "Formation of high-quality I-III-VI semiconductor nanocrystals by tuning relative reactivity of cationic precursors.," *Journal of the American Chemical Society*, vol. 131, pp. 5691–7, Apr. 2009.

[68] J. Park, C. Dvoracek, K. H. Lee, J. F. Galloway, H.-E. C. Bhang, M. G. Pomper, and P. C. Searson, "CuInSe/ZnS core/shell NIR quantum dots for biomedical imaging.," *Small*, vol. 7, pp. 3148–3152, Nov. 2011.

[69] T. Pons, E. Pic, N. Lequeux, F. Marchall, F. Guillemin, and B. Dubertret, "Water Soluble CuInS 2 / ZnS Core / Shell Quantum Dots for Near Infrared Biomedical Imaging," no. Figure 1, pp. 2–4.

[70] L. Li, A. Pandey, D. J. Werder, B. P. Khanal, J. M. Pietryga, and V. I. Klimov, "Efficient synthesis of highly luminescent copper indium sulfide-based core/shell nanocrystals with surprisingly long-lived emission.," *Journal of the American Chemical Society*, vol. 133, pp. 1176–9, Feb. 2011.

[71] R. Hardman, "A Toxicologic Review of Quantum Dots: Toxicity Depends on Physicochemical and Environmental Factors," *Environmental Health Perspectives*, vol. 114, pp. 165–172, Feb. 2006.

[72] S. B. Brichkin and E. V. Chernykh, "Hydrophilic semiconductor quantum dots," *High Energy Chemistry*, vol. 45, pp. 1–12, Jan. 2011.

[73] B. Dubertret, P. Skourides, D. J. Norris, V. Noireaux, A. H. Brivanlou, and A. Libchaber, "In vivo imaging of quantum dots encapsulated in phospholipid micelles.," *Science*, vol. 298, pp. 1759–62, Nov. 2002.

[74] H. Mattoussi, J. M. Mauro, E. R. Goldman, G. P. Anderson, V. C. Sundar, F. V. Mikulec, and M. G. Bawendi, "Self-assembly of CdSe-ZnS quantum dot bioconjugates using an engineered recombinant protein," *Journal of the American Chemical Society*, no. 8, pp. 12142–12150, 2000.

[75] B. Chen, H. Zhong, W. Zhang, Z. Tan, Y. Li, C. Yu, T. Zhai, Y. Bando, S. Yang, and B. Zou, "Highly emissive and color-tunable CuInS2-based colloidal semiconductor nanocrystals: off-stoichiometry effects and improved electroluminescence performance," *Advanced Functional Materials*, vol. 22, pp. 2081–2088, May 2012.

[76] J. Zhang, R. Xie, and W. Yang, "A simple route for highly luminescent quaternary Cu-Zn-In-S nanocrystal emitters," *Chemistry of Materials*, pp. 3357–3361, 2011.

[77] C. Rincon and R. Marquez, "Defect physics of the CuInSe 2 chalcopyrite semiconductor," *Journal of Physics and Chemistry of Solids*, vol. 60, pp. 1865–1873, 1999.

[78] E. Muro, A. Fragola, T. Pons, N. Lequeux, A. Ioannou, P. Skourides, and B. Dubertret, "Comparing intracellular stability and targeting of sulfobetaine quantum dots with other surface chemistries in live cells.," *Small*, vol. 8, pp. 1029–37, May 2012.

[79] H. S. Choi, W. Liu, P. Misra, E. Tanaka, J. P. Zimmer, B. Itty Ipe, M. G. Bawendi, and J. V. Frangioni, "Renal clearance of quantum dots.," *Nature Biotechnology*, vol. 25, pp. 1165–70, Oct. 2007.

[80] W. C. W. Chan and S. Nie, "Quantum Dot Bioconjugates for Ultrasensitive Nonisotopic Detection," *Science*, vol. 281, pp. 2016–2018, Sept. 1998.

[81] J. K. Jaiswal, E. R. Goldman, H. Mattoussi, and S. M. Simon, "Use of quantum dots for live cell imaging.," *Nature Methods*, vol. 1, pp. 73–78, Oct. 2004.

[82] H. T. Uyeda, I. L. Medintz, J. K. Jaiswal, S. M. Simon, and H. Mattoussi, "Synthesis of compact multidentate ligands to prepare stable hydrophilic quantum dot fluorophores.," *Journal of the American Chemical Society*, vol. 127, pp. 3870–8, Mar. 2005.

[83] W. Liu, H. S. Choi, J. P. Zimmer, E. Tanaka, J. V. Frangioni, and M. G. Bawendi, "Compact cystein-coated CdSe(ZnCdS) QDs for in vivo applications," *Journal of the American Chemical Society*, vol. 129, no. 47, pp. 14530–14531, 2008.

[84] E. Muro, T. Pons, N. Lequeux, A. Fragola, and N. Sanson, "Small and stable sulfobetaine zwitterionic quantum dots for functional live-cell imaging," *Journal of the American Chemical Society*, vol. 132, pp. 4556–4557, 2010.

[85] E. Giovanelli, E. Muro, G. Sitbon, M. Hanafi, T. Pons, B. Dubertret, and N. Lequeux, "Highly enhanced affinity of multidentate versus bidentate zwitterionic ligands for long-term quantum dot bioimaging.," *Langmuir*, vol. 28, pp. 15177–84, Oct. 2012.

[86] J. B. Delehanty, C. E. Bradburne, K. Boeneman, K. Susumu, D. Farrell, B. C. Mei, J. B. Blanco-Canosa, G. Dawson, P. E. Dawson, H. Mattoussi, and I. L.

Medintz, "Delivering quantum dot-peptide bioconjugates to the cellular cytosol: escaping from the endolysosomal system.," *Integrative Biology*, vol. 2, pp. 265–77, June 2010.

[87] E. Muro, *Quantum Dots pour le Ciblage en Cellules Vivantes et la Microscopie HiLo Bi-couleur*. PhD thesis, 2011.

[88] Neumann E, S.-R. M, W. Y, and P. Hofschneider, "Gene transfer into electric fields," *The EMBO Journal*, vol. 1, no. 7, pp. 841–845, 1982.

[89] T. Y. Tsong, "Electroporation of cell membranes.," *Biophysical Journal*, vol. 60, pp. 297–306, Aug. 1991.

[90] L. Ye, K.-T. Yong, L. Liu, I. Roy, R. Hu, J. Zhu, H. Cai, W.-C. Law, J. Liu, K. Wang, J. Liu, Y. Liu, Y. Hu, X. Zhang, M. T. Swihart, and P. N. Prasad, "A pilot study in non-human primates shows no adverse response to intravenous injection of quantum dots.," *Nature Nanotechnology*, vol. 7, pp. 453–8, July 2012.

[91] Y. Wang, R. Hu, G. Lin, I. Roy, and K.-T. Yong, "Functionalized quantum dots for biosensing and bioimaging and concerns on toxicity.," *Applied Materials & Interfaces*, vol. 5, pp. 2786–99, Apr. 2013.

[92] Y. Lu, Y. Su, Y. Zhou, J. Wang, F. Peng, Y. Zhong, Q. Huang, C. Fan, and Y. He, "In vivo behavior of near infrared-emitting quantum dots.," *Biomaterials*, vol. 34, pp. 4302–8, June 2013.

[93] L. Schermelleh, R. Heintzmann, and H. Leonhardt, "A guide to super-resolution fluorescence microscopy.," *The Journal of Cell Biology*, vol. 190, pp. 165–75, July 2010.

[94] B. N. G. Giepmans, S. R. Adams, M. H. Ellisman, and R. Y. Tsien, "The fluorescent toolbox for assessing protein location and function.," *Science*, vol. 312, pp. 217–224, Apr. 2006.

[95] C. A. Leatherdale, W. K. Woo, F. V. Mikulec, and M. G. Bawendi, "On the absorption cross section of CdSe nanocrystal quantum dots," *Journal of Physical Chemistry B*, vol. 106, no. 31, pp. 7619–7622, 2002.

[96] A. Deniset, *Imagerie 3D résolue en temps pour l'aide au diagnostic médical : développement d'un système de microscopie de fluorescence multipoints sous excitation à deux photons*. PhD thesis, 2008.

[97] G. Mandal, M. Darragh, Y. A. Wang, and C. D. Heyes, "Cadmium-free quantum dots as time-gated bioimaging probes in highly-autofluorescent human breast cancer cells.," *Chemical Communications*, vol. 49, pp. 624–6, Jan. 2013.

[98] V. Buschmann, K. D. Weston, and M. Sauer, "Spectroscopic study and evaluation of red-absorbing fluorescent dyes.," *Bioconjugate Chemistry*, vol. 14, no. 1, pp. 195–204, 2003.

[99] M. Y. Berezin and S. Achilefu, "Fluorescence lifetime measurements and biological imaging," *Chemical Reviews*, vol. 110, no. 5, pp. 2641–2684, 2010.

Appendix A : Vegard's law and estimation of QDs concentration

A.1 Vegard's law

Vegard's law allows us to determine the percentage of each material that composes an alloy. Using the position of each experimental diffraction peaks and the Bragg's law, we can determine the distance $d_{h,k,l}$. Bragg's law is given by :

$$d_{h,k,l} sin(2\theta) = \lambda$$

where θ is the diffraction angle, λ is the wavelength of the X-rays that interact with the sample. Here λ corresponds to the K_α of the copper which is 1.54 Å. For a cubic structure a relationship between $d_{h,k,l}$ and the lattice parameter noted a is given by

$$d_{h,k,l} = \frac{a}{\sqrt{h^2 + k^2 + l^2}}$$

Thus, for each diffraction peak we have obtained the values given in the Table V.1

hkl	peak position (2θ in °)	$d_{h,k,l}$ (Å)	a_{alloy} (Å)
111	27.5	3.24	5.61
220	45.5	1.99	5.62
311	54.0	1.70	5.62

Table V.1 – Experimental values of the different parameters obtained for each diffraction peak.

Finally using the Vegard's law we have :

$$a_{alloy} = xa_{ZnSe} + (1-x)a_{CuInSe_2}$$

We found $x = 0.44$ on average on the three peaks. Therefore, our cores are composed of 44% of ZnSe and 56% of $CuInSe_2$.

A.2 Estimation of the cores concentration

In order to calculate the cores concentration we will make several assumptions : the core size monodispersity and spherical shape. We also consider that all precursors are consumed during the reaction.

The different parameters used to calculate the core concentration are :

- The Avogadro number noted Na,
- The final solution volume noted V,
- The core diameter value obtained by TEM 4 nm,
- The volumic mass of the cores noted ρ,

$$\rho = 0.56 \times \rho_{CuInSe_2} + 0.44 \times \rho_{ZnSe} = 5.91 g/cm^{-3}$$

- The nanoparticule volume noted $V_{NP} = 3.3 \times 10^{-20} cm^3$
- The molar mass of the cores noted M= 252 g/mol,
- The introduced copper moles noted n(Cu) = 0.4 mmol.

First we determine the mass of a nanoparticule, noted m_{NP}:

$$m_{NP} = \rho \times V_{NP} = 1.95 \times 10^{-19} g$$

Secondly we determine the number of copper moles by nanoparticules:

$$n = 0.56 \times \frac{m_{NP}}{M}$$

We can now calculate the number of copper by nanoparticules given by :

$$N_{Cu/NP} = n \times Na = 257 Cu/NP$$

Finally, we can estimate the cores concentration :

$$C_{cores} = \frac{n(Cu) \times Na}{N_{Cu/NP}} \times \frac{1}{Na} \times \frac{1}{V} = 156\mu M$$

A.3 Estimation of the core/shell nanocrystals concentration

For the shell synthesis, we introduce 4 mL of cores, which are finally resuspended in 10 mL of hexane. Therefore the final estimated concentration of the core/shell nanocrystals is given by :

$$C_{QD} = \frac{C_{cores}}{2.5} = 62\mu M$$

Appendix B : Optical set up characteristics

B.1 Optical set up components

B.1.1 Filters properties

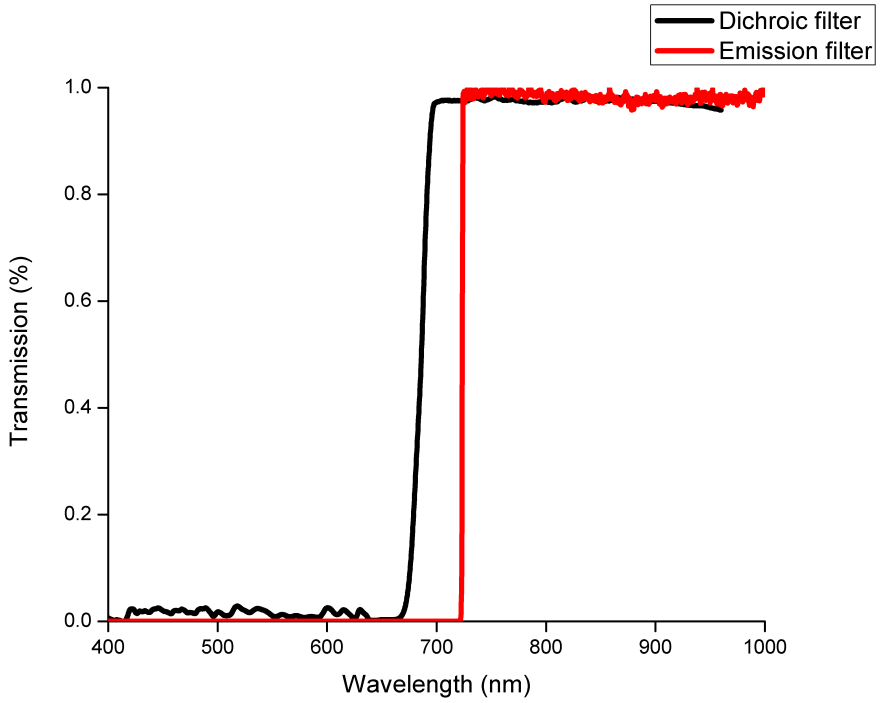

Figure V.3 – Filters transmission as function of the wavelength.

B.1.2 High Rate Intensifier quantum efficiency

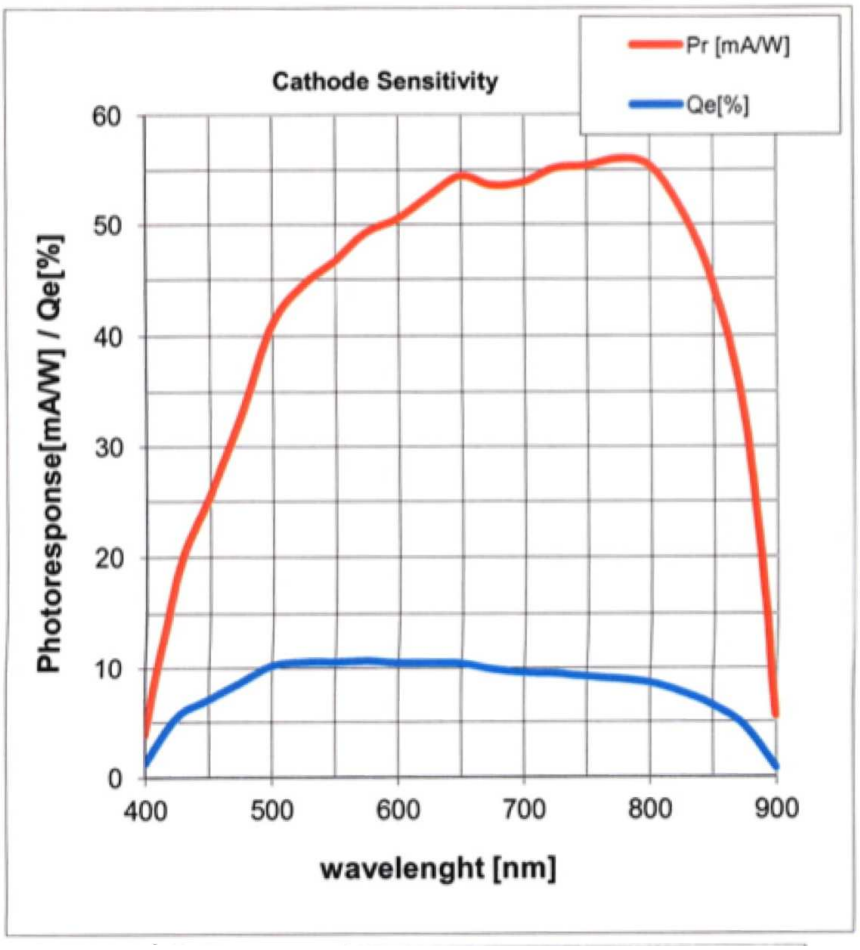

Figure V.4 – Quantum efficiency of the intensifier as function of the wavelength.

B.1.3 EMCCD camera efficiency

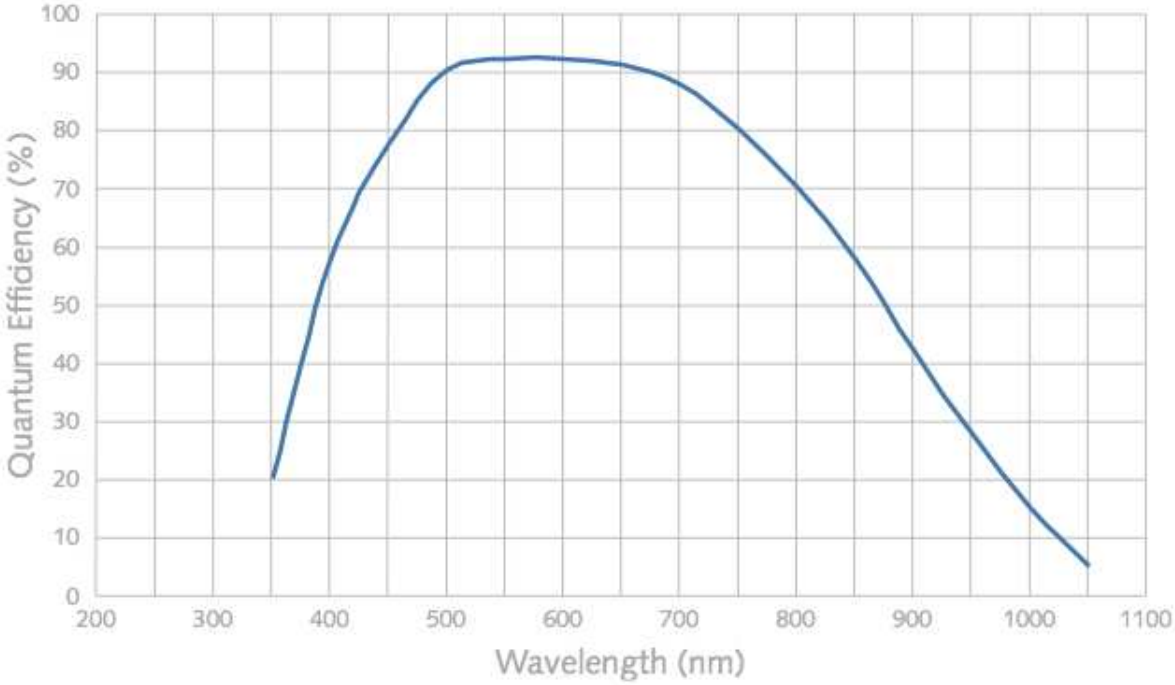

Figure V.5 – Quantum efficiency of the EMCCD camera *Quantem 512 SC* as function of the wavelength.

Journal of Biomedical Optics

SPIEDigitalLibrary.org/jbo

Time-gated cell imaging using long lifetime near-infrared-emitting quantum dots for autofluorescence rejection

Sophie Bouccara
Alexandra Fragola
Emerson Giovanelli
Gary Sitbon
Nicolas Lequeux
Thomas Pons
Vincent Loriette

SPIE

Journal of Biomedical Optics 19(5), 051208 (May 2014)

Time-gated cell imaging using long lifetime near-infrared-emitting quantum dots for autofluorescence rejection

Sophie Bouccara, Alexandra Fragola, Emerson Giovanelli, Gary Sitbon, Nicolas Lequeux, Thomas Pons, and Vincent Loriette*
Laboratoire de Physique et d'Etude des Matériaux, UMR 8213, ESPCI Paristech, CNRS, UPMC, 10 rue Vauquelin, Paris, France

Abstract. Fluorescence imaging is a promising technique for the detection of individual cell migration. Its sensitivity is, however, limited by a high tissue autofluorescence and a poor visible light penetration depth. In order to solve this problem, the fluorescence signal peak wavelength should lie in an absorption and diffusion free region and should be distinguishable, either spectrally or temporally, from the autofluorescence background. We present, here, the synthesis and characterization of low toxicity Zn–Cu–In–Se/ZnS core/shell quantum dots. Their fluorescence emission wavelength peaks around 800 nm, where the absorption and scattering of tissues are minimal. They are coated with a new ligand, which yields small, stable, and bright individual probes in the live cell cytoplasm, even 48 h after the labeling. Furthermore, these near-infrared-emitting quantum dots have a long fluorescence lifetime component (around 150 ns) compared to autofluorescence (<5 ns). Taking the advantage of this property and coupling these probes to a time-gated detection, we demonstrate efficiently the discrimination between the signal and short lifetime fluorescence such as the autofluorescence. This technique is supported by a method we developed, to massively stain cells that preserves the quantum dot stability and brightness for 48 h. [DOI: 10.1117/1.JBO.19.5.051208]

Keywords: quantum dots; fluorescence; microscopy; detection; cells.

Paper 130546SSRR received Jul. 31, 2013; revised manuscript received Dec. 5, 2013; accepted for publication Dec. 5, 2013; published online Jan. 6, 2014.

1 Introduction

Several *in vivo* cell tracking techniques based on the magnetic resonance imaging or positron emission tomography[1] have been developed but remain challenging for rare and individual cell detection, mainly because of their low-spatial resolution. On contrary, the fluorescence microscopy allows a cell scale detection, but is limited by a low sensitivity. Indeed, absorption and scattering of visible light, as well as tissue autofluorescence degrade image contrast. Time-gated detection has been developed for fluorescence lifetime imaging microscopy measurements[2] and also allows the rejection of short lifetime signals such as tissue autofluorescence.[3–6]

In the last few years, quantum dots have been used as probes for biological applications[7,8] because they combine a high resistance to photobleaching with interesting optical properties: broad absorption cross section, tunable emission wavelength (according to their size and composition) and high fluorescence quantum yields (QY). For fluorescence imaging, there is indeed an "optical therapeutic window" (from 700 to 900 nm), where the absorption and scattering of major tissue chromophores are minimum.[9,10] In this range of wavelengths, *in vivo* fluorescence imaging has been performed due to near-infrared-emitting quantum dots (NIR QDs).[11] Recently, NIR QDs based on I–III–VI materials have emerged[12–14] and exhibit a long fluorescence lifetime (around 150 ns).[15–17] Moreover, unlike other semiconductor nanoparticles emitting in the IR (PbSe, CdTe), they are made of low toxicity materials.[18] Nevertheless, the current challenge in this range of wavelengths consists of synthesizing probes with high fluorescence QY.[12,15,19–22] Moreover, for cell tracking applications, cells have to be loaded with numerous probes, which have to be equally distributed between the two daughter cells to preserve homogeneous population labeling.

We present here a new synthesis of NIR QDs made of low toxicity materials, emitting at 800 nm, and with fluorescence QY up to 35% in hexane. Their emission wavelength allows an excitation with a red-emitting laser, giving a better light penetration depth in tissues. The quantum dots are coated with a copolymeric ligand we recently developed,[23] which allows one to obtain bright, stable, and homogeneously distributed probes in the cell cytoplasm at least for 48 h. Furthermore, our NIR QDs exhibit a long fluorescence lifetime (around 150 ns) compared to tissue autofluorescence (<5 ns). Due to these unique properties and a time-gated detection on a widefield microscope, these QDs allow significant enhancement of the detection sensitivity of individual cells by efficiently rejecting short fluorescence lifetime signals.

2 Materials and Methods

2.1 *Synthesis of NIR QDs*

The synthesis of Zn–Cu–In-Se/ZnS core/shell quantum dots is inspired by Cassette et al.[14] In our core synthesis, all precursors (0.4 mmol of CuCl, 0.4 mmol of $InCl_3$, 0.8 mmol of selenourea, and 0.8 mmol of Zn acetate) are introduced in a three-necked

*Address all correspondence to: Vincent Loriette, E-mail: sophie.bouccara@espci.fr

0091-3286/2014/$25.00 © 2014 SPIE

flask with 10 mL of octadecene (ODE) and 4 mL of trioctylphosphine (TOP), and briefly sonicated. Then, 4 mL of oleylamine (OAm) and 2 mL of dodecanethiol are added. The solution is stirred and degassed for 30 min under vacuum. The flask is then filled with argon and the solution is heated progressively up to 260°C in, typically, 10 min. Heating is stopped immediately after the target temperature is reached and the flask is cooled down to room temperature. The Zn–Cu–In–Se cores are precipitated with ethanol and then dispersed in 10 mL of hexane.

For the shell synthesis, 4 mL of as-prepared cores is dispersed in 4 mL of ODE and 1 mL of OAm into a new three-necked flask. The mixture is degassed under vacuum at 40°C. A solution of zinc ethylxanthate and zinc oleate (respectively, 0.13 mmol and 0.8 mmol) dissolved in ODE (2 mL), TOP (3 mL), and dioctylamine (1 mL) is loaded into an injection syringe. The flask is heated to 190°C and these ZnS precursors are added dropwise in 1 h under argon atmosphere. At the end of the injection, the reaction flask is cooled down to room temperature. The resulting Zn–Cu–In–Se/ZnS QDs are finally precipitated with ethanol and redispersed in 10 mL of hexane. Optical spectroscopy characterization is performed using a F900 Edinburgh spectrometer.

2.2 *Solubilization in Water*

The solubilization in water is performed due to a ligand exchange. Four hundreds microliters of the Zn–Cu–In–Se/ZnS QDs are precipitated with ethanol and resuspended in 100 μL of mercaptopropionic acid overnight at 60°C. The QDs are dissolved in dimethylformamide (1 mL) and precipitated using potassium *tert*-butoxide. QDs are resuspended in basic water (sodium tetraborate 10 mM, pH 9.2) and mixed with a solution of poly(dithiol-*co*-sulfobetaine) zwitterionic ligands[23] for 12 h at 60°C. After the ligand exchange, the QDs are purified as previously described by Giovanelli et al. using ultrafiltration and ultracentrifugation. The QDs are finally resuspended in a 20 mM aqueous solution of NaCl.

2.3 *Cell Labeling*

QDs are diluted in Dulbecco's modified Eagle medium enriched with 10% fetal bovine serum and 1% penicillin–streptomycin antibiotics, later referred to as complete medium. About 500,000 HeLa cells are suspended with 10 μM of QDs in a final volume of 100 μL in a 2-mm electroporation cuvette. The cuvette is subjected to 0.15 kV for a 30-ms pulse using a Gene Pulser (Biorad, Hercules) electroporator. The cells are rinsed five times with warm complete medium, dispersed in a nonfluorescent imaging medium (OptiMEM® with no phenol red, Life technologies, Carlsbad, California) and deposited on a microscope coverslip (25 mm in diameter). The cells are kept at least for 1 h at 37°C under a 5% of CO_2 atmosphere before imaging.

2.4 *Optical Setup*

The light source used for time-gated imaging (setup shown in Fig. 1) is a picosecond pulsed laser diode (Picoquant PDL 800, Berlin, Germany), emitting at 659 nm, with a 1 or 5 MHz repetition rates injected in the epi-illumination path of a commercial microscope body (Olympus BX51WIF, Shinjuky, Japan). The beam spot size and position on the sample are controlled by an external telescope and periscope. We use a 60× water immersion Olympus objective (NA = 1) and a 40× Olympus objective (NA = 0.6). We use emission filters to discriminate between the QDs fluorescence and the excitation signal. A relay achromatic pair matches the image size to the intensifier and gate surface (Picostar HRI, LaVision, Goettigen, Germany). The same relay system is placed head to tail between the intensifier and the electron multiplying charge-coupled device (EMCCD) camera (Roper QuantEM 512 C, Photometrics, Tucson, Arizona) to preserve the nominal microscope magnification factor. The laser

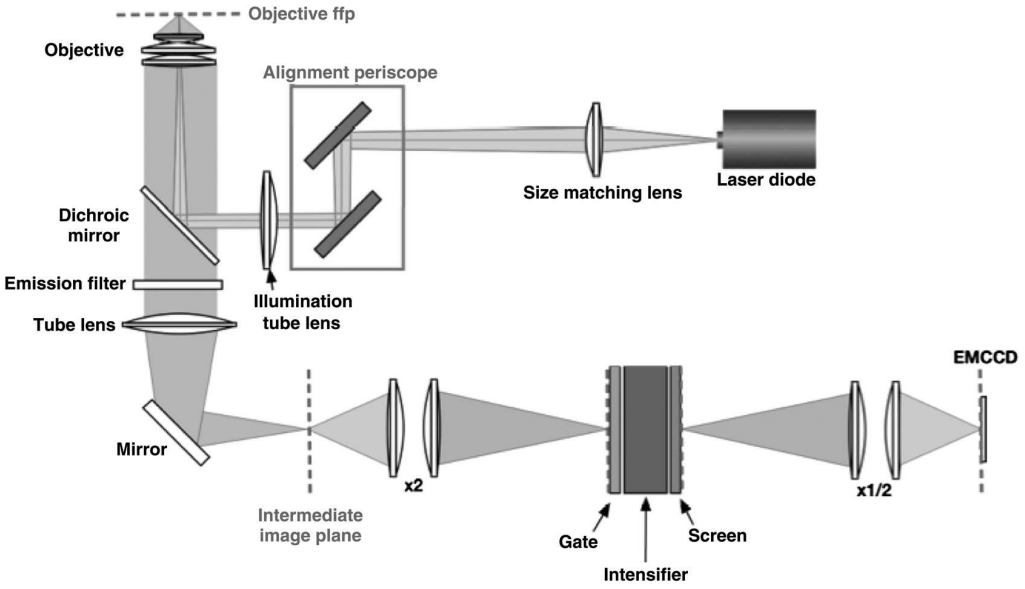

Fig. 1 Optical setup. The sample is illuminated by a pulsed laser diode with a 1 or 5 MHz repetion rate and emitting at 659 nm. The laser and the intensifier are synchronized by two phase-locked function generators.

diode and the intensifier are synchronized by two phase-locked function generators (Agilent 33120A and Agilent 33220A).

2.5 *Photoluminescence Intensity Decay Measurements*

The system described above can be used to carry out photoluminescence (PL) intensity decay measurements. The intensifier is used in a mode in which the gate is driven by a waveform synthesizer. This mode is suited to perform time-gated detection as well as fluorescence intensity decay measurements. PL intensity decays are measured by acquiring a sequence of images, while phase shifting a 200-ns width gate trigger signal with respect to the laser trigger, as illustrated in Fig. 2. This introduces a controllable time delay, τ, between the laser excitation and the beginning of the detection gate. Thus, for each gate position, an image is acquired. A common region of interest (ROI) for all images is selected and for each image, the average intensity of the ROI pixels is measured. The image offset, induced by the camera or by the external light sources, is eliminated by recording a sequence without laser excitation and substracting the average of the pixel intensity of the same ROI from the original sequence. The results are then normalized to the measure obtained after the laser pulse. For fluorescence decay measurements, we typically use radio frequency gain at 30% and Micro Channel Plate gain at 700 V and an input driving peak to peak voltage of 2 V.

3 Results and Discussion

3.1 *NIR QDs as Stable Probes for Cell Imaging*

3.1.1 *Spectroscopic characterization of NIR QDs*

We have developed and optimized the synthesis of NIR emitting Zn–Cu–In–Se/ZnS core/shell QDs. Compared to the previously reported Cu–In–Se/ZnS QDs,[14,24] we note that the incorporation of zinc during the core synthesis improves their fluorescence QY, and provided us with brighter core/shell QDs, as already noted with Zn–Cu–In–S QDs.[13,20,25] This has been putatively attributed to defect passivation and filling of vacancy sites by Zn atoms inside the QD cores. The QD size is estimated at typically 3 nm by electron microscopy and x-ray diffraction (data not shown). The initially hydrophobic QDs are solubilized in water as described in Sec. 2. These ligands provide suitable long-term colloidal and intracellular stability for our NIR QDs as will be demonstrated below.

Figure 3 presents the emission spectra of our NIR QDs in hexane and water, as well as the PL intensity decays. The emission (with an FWHM of around 130 nm) is centered around 800 nm, which corresponds to the "optical therapeutic window" for *in vivo* fluorescence imaging, in which the tissue penetration is maximal.[9,10] Fluorescence QY measurements gave typical values of 35% for QDs in hexane and 20% for QDs in aqueous solution after ligand exchange. We have observed that the emission is slightly blue shifted after ligand exchange, which could be attributed to a slight etching of the QD surface, or to better PL QY preservation of bluer-emitting QDs during the ligand exchange.

PL decays are multiexponential with a slow component, typically from 150 to 200 ns, compared to II–VI QDs, which usually decay in <20 ns.[4,26] This slow component is dominant. It can be related to a donor–acceptor transition and defect recombination. In fact, the localization of the exciton electron on Cu atoms strongly reduces the exciton overlap in these QDs and yields longer excitonic lifetimes.[15] This type of recombination also explains the broad emission spectra compared to II–VI QDs.[16] A shorter component between 10 and 60 ns is

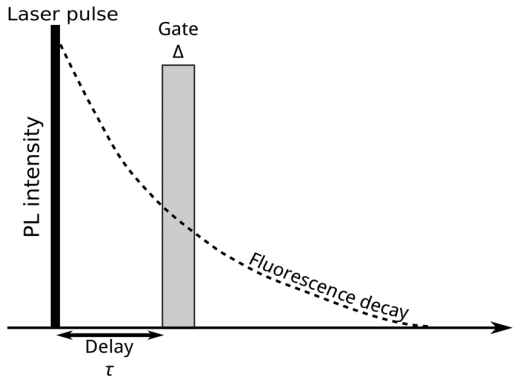

Fig. 2 Principle of photoluminescence intensity decay measurements. For each gate position, an image is acquired and the intensity of a region of interest is measured.

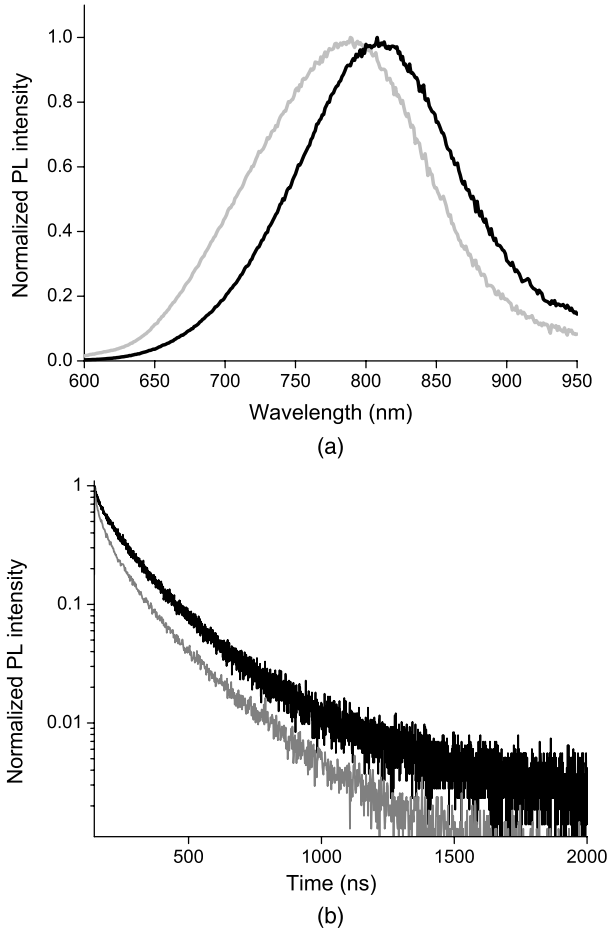

Fig. 3 (a) Normalized photoluminescence spectra. (b) Normalized photoluminescence intensity decays of near-infrared-emitting quantum dots (NIR QDs) in hexane (black) and water (gray).

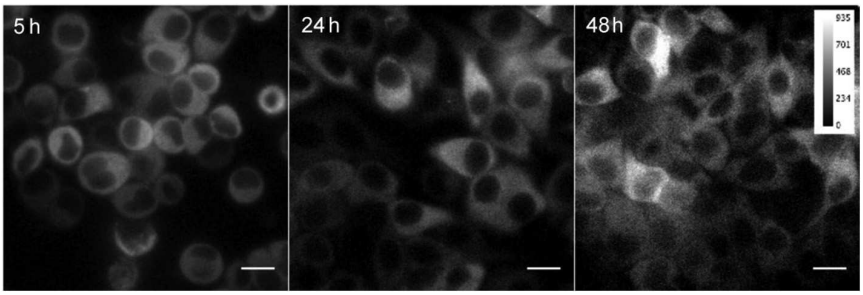

Fig. 4 Fluorescence microscopy images of HeLa cells electroporated with NIR QDs at different times after the electroporation: 5, 24, and 48 h (scale bar: 16 μm).

mainly due to intrinsic recombination of initially populated core states or surface states.[16]

3.1.2 *Labeling of live cells and NIR QDs stability*

As we aim to track cells over a few days, they need to be stained with a very high concentration of probes. Indeed, the cell division leads to a QDs dilution between two daughter cells. For this reason, we choose electroporation within the several techniques[27] because it allows one to obtain cells which are massively loaded with QDs in their cytoplasm.

Moreover, cell tracking experiments require highly stable intracellular probes. QDs have to remain individual and freely diffusing in order to be equally distributed in two daughter cells. Muro et al.[28] observed that the cytoplasmic aggregation kinetics depend strongly on the nanoparticle surface chemistry. Consequently, we have chosen to coat our quantum dots with a multidentate ligand which allows a high stability in cells for visible emitting quantum dots during several days.[23] Figure 4 shows images of living HeLa cells electroporated with NIR QDs, obtained at different times after the electroporation (5, 24, and 48 h). In order to visually compensate for the diminution of the fluorescence signal induced by QD dilution after each cell division, the intensity level of the middle image (24 h) was doubled and the level of the last image (48 h) was quadrupled according to the number of cell divisions. The original images exhibit average levels compatible with one and two division stages and no leaking of QDs. The images in Fig. 4 show that NIR QDs coated with this surface chemistry stay bright and homogeneously distributed in the cell cytoplasm for several days. Moreover, while initial free-floating cells are round (Fig. 4, 5 h), they become adherent on the coverslip the day after the electroporation (Fig. 4, 24 h). This, together with their preserved mitotic activity, is coherent with an expected low level of toxicity.[29]

As we intend to couple these probes to a time-gated detection, we have to verify that they keep their long fluorescence lifetime in different media and in the cell cytoplasm with time. We have measured the fluorescence intensity decays on three different samples in order to observe the influence of the QDs surrounding medium on their fluorescence lifetime. The lifetime measurements have been performed as described above in Sec. 2.5. Figure 5(a) shows fluorescence intensity decays obtained for three NIR QD samples: in hexane, in water (after ligand exchange), and in the cytoplasm of living cells. We performed the same experiment to measure fluorescence decays in the cell cytoplasm at different times after the electroporation (5, 24, and 48 h). We have fitted the fluorescence decay curves by a multiexponential curve with two major components and presented the different parameters in Table 1. The corresponding values of each parameter τ_1 and τ_2 are equatable from one curve to the other, taking into account the standard deviations.

The decay kinetics remain unchanged not only in different media [Fig. 5(a)] but also in the cell cytoplasm even after

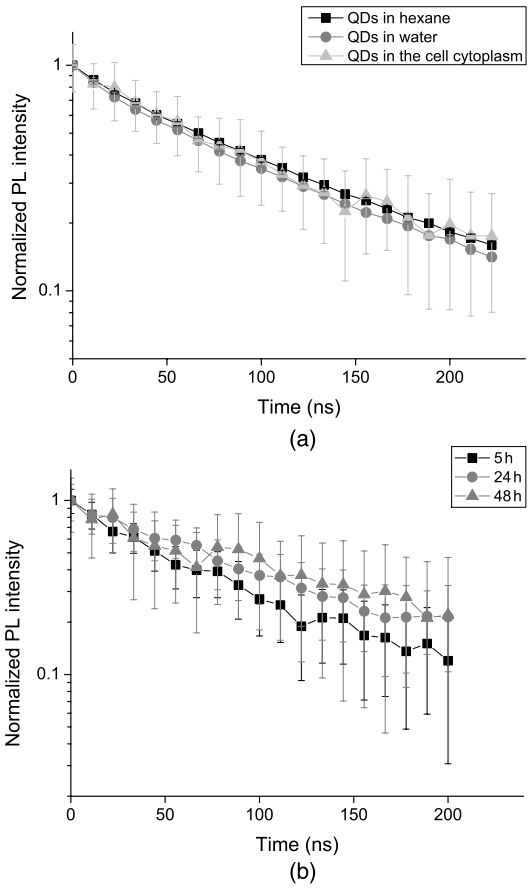

Fig. 5 (a) Normalized fluorescence intensity decay measurements of NIR QDs in different media (hexane, water, and cell cytoplasm). (b) Normalized fluorescence intensity decay of NIR QDs in the cell cytoplasm at different times after the electroporation (5, 24, and 48 h).

Table 1 Numerical values of τ_1 and τ_2 used to fit our fluorescence decay curves in Fig. 5 and their respective weights, α_1 and α_2.

Sample	α_1	τ_1 (ns)	α_2	τ_2 (ns)
QDs in hexane	0.05	28 ± 1.8	0.95	138 ± 2
QDs in water	0.05	25 ± 1.8	0.95	134 ± 2.7
QDs in cell cytoplasm	0.15	60 ± 25	0.85	177 ± 78
5 h	0.2	39 ± 10	0.8	142 ± 35
24 h	0.15	60 ± 25	0.85	177 ± 78
48 h	0.05	31 ± 11	0.95	197 ± 37

3 days [Fig. 5(b)], reflecting the long-term stability of QDs in the cytoplasmic medium, and confirming the possibility to use them to label cells for tracking applications.

3.2 *NIR QDs Coupled to Time-Gated Detection for Short Lifetime Autofluorescence Rejection*

3.2.1 *Proof of principle*

We demonstrate the increase of sensitivity by combining time-gated fluorescence detection with cells labeled with our long PL lifetime NIR QDs. To this end, we have imaged simultaneously cells electroporated with NIR QDs and cells electroporated with NIR fluorescent beads (beads coated with NIR organic fluorophores, F8783, Invitrogen, Life technologies, Carlsbad, California) with a very short fluorescence lifteime ($\tau < 5$ ns). The cells have been rinsed, mixed together, and deposited on the same coverslip. As described in Sec. 2, we have illuminated the cells with the pulsed laser source at 1 MHz and imaged them through 200-ns gate. For this study, we did not investigate the influence of these two parameters that have been fixed arbitrarily. Each image has been acquired using a different delay τ, between the laser pulse excitation and the opening of the gate. We have varied this delay between 0 and 200 ns with 2.7 ns steps. The camera exposure duration was fixed to 150 ms. Figure 6 shows examples of time-gated images of two cells taken at delay 0, 11, 30, and 50 ns. The left cell was stained with NIR QDs and the right one with fluorescent beads. The progressive disappearance of the cell stained with the fluorescent beads (right) clearly illustrates the rejection of the short lifetime signal as the delay increases. Figure 7 is a plot of the fluorescence intensity decay of the two cells shown in Fig. 6. The signal was averaged over the central 10×10 pixels area of each cell. At zero delay, the ratio between the fluorescent beads signal and the QD signal is 2.5. At a delay of 27 ± 2.7 ns, the fluorescent beads signal goes below the noise level. This is thus the optimal delay for opening the gate. We

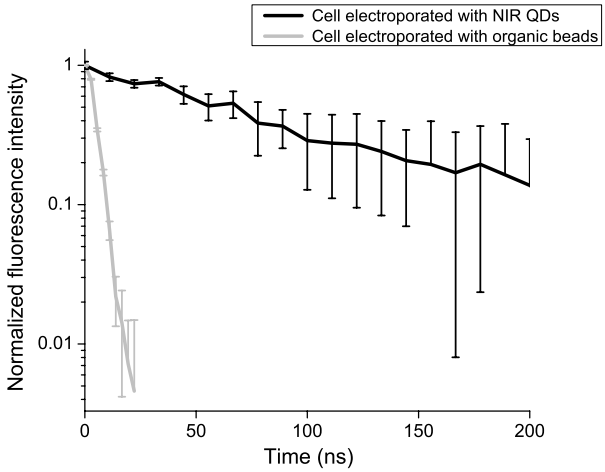

Fig. 7 Fluorescence intensity decay measurements of NIR QDs and fluorescent beads in cells.

characterized the efficiency of the gated detection by defining a parameter $R(\tau)$ which corresponds to the ratio of the signal from NIR QDs on the background noise and the spurious fluorescence signal corresponding to short lifetime signal. It can be written as

$$R(\tau) = \frac{S_{\mathrm{QD}}(0)\exp\left(\frac{-\tau}{\tau_{\mathrm{QD}}}\right)}{N + S_{\mathrm{fluo}}(0)\exp\left(\frac{-\tau}{\tau_{\mathrm{fluo}}}\right)}, \tag{1}$$

where $S_{\mathrm{QD}}(0)$ and $S_{\mathrm{fluo}}(0)$ are, respectively, the signal from the quantum dots and fluorescent beads at zero delay, N is the background noise level, and τ is the gate delay. N depends on the gate width but not on the delay. τ_{QD} and τ_{fluo} are the fluorescence lifetimes of QDs and short lifetime fluorophores, respectively. As long as the denominator in Eq. (1) is dominated by the spurious fluorescence, the $R(\tau)$ ratio increases as $\exp[\tau(1/\tau_{\mathrm{fluo}} - 1/\tau_{\mathrm{QD}})]$. If, on the contrary, the background noise is dominant, the $R(\tau)$ ratio decreases as $\exp(-\tau/\tau_{\mathrm{QD}})$; This behavior is illustrated in Fig. 8, where we plotted R measured on the images presented in Fig. 6, as a function of the delay. The solid gray curve is a fit of the data with the function of Eq. (1). The fit allowed us to estimate the fluorescence lifetimes: we found $\tau_{\mathrm{fluo}} = 2.7 \pm 0.3$ ns and $\tau_{\mathrm{QD}} = 120 \pm 30$ ns and a maximum $R(\tau)$ ratio obtained at $\tau = 28$ ns. The $R(\tau)$ ratio increases by two orders of magnitude: at $R(\tau = 0\ \mathrm{ns}) = 0.44$ and $R(\tau = 28\ \mathrm{ns}) = 40$.

In order to quantify the time-gated detection efficiency, we define a fluorescence rejection factor as the ratio between the QD signal and the spurious fluorescence signal, normalized by the same ratio without time-gated detection. It can be written as

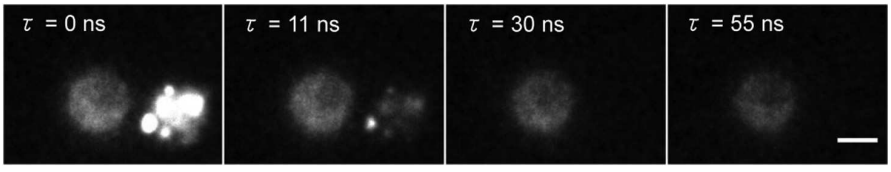

Fig. 6 Images of HeLa cells labeled with NIR QDs (cell on the left) or beads containing NIR fluorescent organic dyes (cell on the right) at different delays τ after the laser pulse. (scale bar: 10 μm).

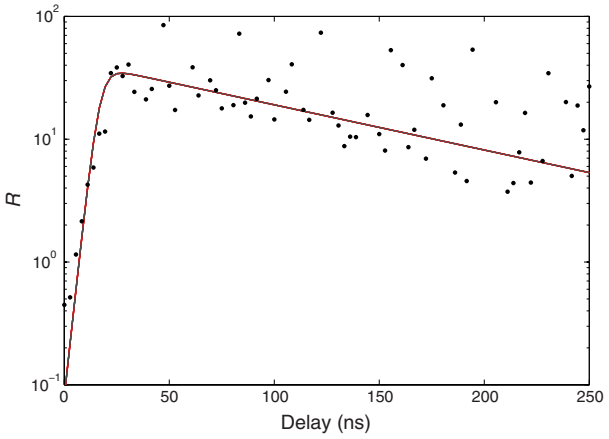

Fig. 8 Ratio R for our data (dots) and best (gray curve) fit using Eq. (1) as the fitting function.

$$G(\tau) = \frac{1 - \exp\left(-\frac{\Delta}{\tau_{\text{fluo}}}\right)}{1 - \exp\left(-\frac{\Delta}{\tau_{\text{QD}}}\right)} \frac{\exp\left(-\frac{\tau}{\tau_{\text{QD}}}\right)}{\exp\left(-\frac{\tau}{\tau_{\text{fluo}}}\right)}, \quad (2)$$

with Δ the gate width. Using the estimated values of the lifetimes, we obtain $G(\tau = 28\ \text{ns}) = 3.4 \times 10^4$. The high value of the rejection factor is obtained due to the long fluorescence lifetime of NIR QDs in the cell cytoplasm. The optimal gate delay is fixed by spurious fluorescence level and lifetime and by the background noise level. It depends only weakly on the QDs' lifetime and can be optimized independently on the QD characteristics.

3.2.2 *Ex vivo experiment*

We have deposited HeLa cells previously electroporated with NIR QDs on a thin slice of *ex vivo* tissue of beef muscle. This corresponds to a situation where the QDs' signal is superimposed to the autofluoresence one, compared to the previous experiments where both the signals were spatially decorrelated. We have illuminated the sample with the pulsed laser source at 5 MHz and imaged it through a 160 ns gate width. All images have been acquired with an exposure time of 100 ms and each

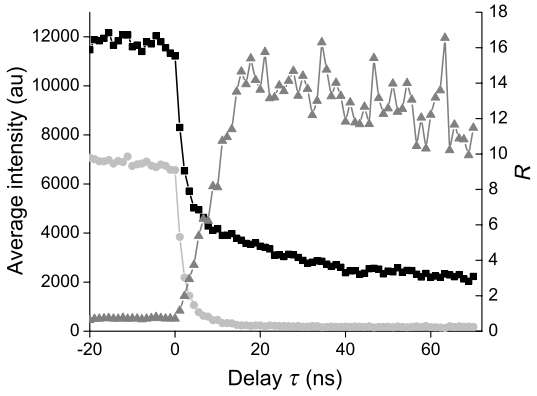

Fig. 9 Average intensity at the cell location (black squares), average intensity of the autofluorescence (gray circles), and ratio R (dark gray triangles).

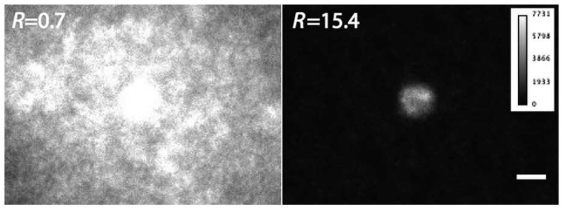

Fig. 10 Images of NIR QDs stained cell for different positions of the gate detection (scale bar: 10 μm).

image corresponds to an open gate position relative to the laser pulse at the zero delay $\tau = 0$.

Figure 9 is a plot of the average intensity at the cell location (NIR QDs and tissue autofluorescence and noise) (black curve), the average intensity next to the cell location (tissue autofluorescence and noise) (gray curve) and the ratio $R(\tau)$ as defined in the previous section.

For $\tau < 0$ ns, which corresponds to a gate that is open when the laser pulse illuminates the sample, the autofluorescence signal dominates the NIR QDs one. Thus, both the signals are nearly constant and we mainly detect signal from tissue autofluorescence. For positive values of τ, since autofluorescence has a short fluorescence lifetime (<5 ns), its contribution falls rapidly. At $\tau = 17.7$ ns, when the autofluorescence signal falls below the noise level, R reaches its highest value: $R(\tau = 17.7) = 15.4$. This maximum represents an increase by more than an order of magnitude compared to zero delay $[R(\tau = 0) = 0.6]$, demonstrating the important benefit of our system. Then, R decreases following the QDs' fluorescence decay.

Figure 10 shows images of the sample for two different time delays. On the left image, the gate opens before the laser impulsion, and both fluorescence from the cell and fluorescence from the tissue (autofluorescence) contribute to the signal. On the right image, the gate opens with a delay $\tau = 17.7$ ns after the laser pulse.

This experiment demonstrates that autofluorescence rejection through time-gated detection of long lifetime NIR-QDs exhibits performances and gain in sensitivity when a single cell is embeded within a strongly autofluorescent environment.

4 Summary

We have synthesized and characterized new biocompatible NIR QDs for *in vivo* fluorescence imaging. These probes remain stable, bright, and homogeneously distributed in the cell cytoplasm. They also keep their long fluorescence decay in different media, including in the cell cytoplasm of living cells, at least for 48 h. Due to these properties, we demonstrated that we could couple these probes to a widefield time-gated imaging and efficiently discriminate between NIR QDs emission and spurious short lifetime signals, such as autofluorescence in an *ex vivo* sample. This combination of probes and widefield time-gated detections could be functional for *in vivo* cell tracking, where the autofluorescence is the main limitation.

Acknowledgments

Part of this work was funded by "les Laboratoires Servier" and the "Investissement d'Avenir project Nano-CTC." We would like to thank Anne Simon for her help on cell culture and Aurore Bournigault-Nuquet for her help on the instrument characterization.

References

1. H. Hong et al., "Non-invasive cell tracking in cancer and cancer therapy," *Curr. Top. Med.* **10**(12), 1237–1248 (2010).
2. D. Elson et al., "Biomedical applications of fluorescence lifetime imaging," *Opt. Photonics News* **13**(11), 36–32 (2002).
3. R. Richards-Kortum and E. Sevick-Muraca, "Quantitative optical spectroscopy for tissue diagnosis," *Ann. Rev. Phys. Chem.* **47**, 555–606 (1996).
4. M. Dahan et al., "Time-gated biological imaging by use of colloidal quantum dots," *Opt. Lett.* **26**(11), 825–827 (2001).
5. A. May et al., "Whole-body, real-time preclinical imaging of quantum dot fluorescence with time-gated detection," *J. Biomed. Opt.* **14**(6), 060504 (2009).
6. G. Mandal et al., "Cadmium-free quantum dots as time-gated bioimaging probes in highly-autofluorescent human breast cancer cells," *Chem. Commun.* **49**(6), 624–626 (2013).
7. X. Michalet et al., "Quantum dots for live cells, in vivo imaging, and diagnostics," *Science* **307**(5709), 538–544 (2005).
8. M. Bruchez, Jr. et al., "Semiconductor nanocrystals as fluorescent biological labels," *Science* **281**(5385), 2013–2016 (1998).
9. Q. Ma and X. Su, "Near-infrared quantum dots: synthesis, functionalization and analytical applications," *Analyst* **135**(8), 1867–1877 (2010).
10. J. Frangioni, "In vivo near-infrared fluorescence imaging," *Curr. Opin. Chem. Biol.* **7**(5), 626–634 (2003).
11. S. Kim et al., "Near-infrared fluorescent type II quantum dots for sentinel lymph node mapping," *Nat. Biotechnol.* **22**(1), 93–97 (2004).
12. L. Li et al., "Highly luminescent $CuInS_2$/ZnS core/shell nanocrystals: cadmium-free quantum dots for in vivo imaging," *Chem. Mater.* **21**(12), 2422–2429 (2009).
13. T. Pons et al., "Cadmium-free $CuInS_2$/ZnS quantum dots for sentinel lymph node imaging with reduced toxicity," *ACS Nano* **4**(5), 2531–2538 (2010).
14. E. Cassette et al., "Synthesis and characterization of near-infrared Cu–In–Se/ZnS core/shell quantum dots for in vivo imaging," *Chem. Mater.* **22**(22), 6117–6124 (2010).
15. L. Li et al., "Efficient synthesis of highly luminescent copper indium sulfide-based core/shell nanocrystals with surprisingly long-lived emission," *J. Am. Chem. Soc.* **133**(5), 1176–1179 (2011).
16. H. Zhong et al., "Controlled synthesis and optical properties of colloidal ternary chalcogenide CuInS2 nanocrystals," *Chem. Mater.* **20**(20), 6434–6443 (2008).
17. T. K. C. Tran et al., "Time-resolved photoluminescence study of $CuInS_2$/ZnS nanocrystals," *Adv. Nat. Sci.: Nanosci. Nanotechnol.* **1**(2), 025007 (2010).
18. A. L. Rogach et al., "Infrared-emitting colloidal nanocrystals: synthesis, assembly, spectroscopy, and applications," *Small* **3**(4), 536–557 (2007).
19. B. Chen et al., "Highly emissive and color-tunable $CuInS_2$-based colloidal semiconductor nanocrystals: off-stoichiometry effects and improved electroluminescence performance," *Adv. Funct. Mater.* **22**(10), 2081–2088 (2012).
20. J. Zhang, R. Xie, and W. Yang, "A simple route for highly luminescent quaternary Cu–Zn–In–S nanocrystal emitters," *Chem. Mater.* **23**(14), 3357–3361 (2011).
21. H. Nakamura et al., "Tunable photoluminescence wavelength of chalcopyrite $CuInS_2$-based semiconductor nanocrystals synthesized in a colloidal system," *Chem. Mater.* **18**(14), 3330–3335 (2006).
22. P. M. Allen and M. G. Bawendi, "Ternary I–III–VI quantum dots luminescent in the red to near-infrared," *J. Am. Chem. Soc.* **130**(29), 9240–9241 (2008).
23. E. Giovanelli et al., "Highly enhanced affinity of multidentate versus bidentate zwitterionic ligands for long-term quantum dot bioimaging," *Langmuir* **28**(43), 15177–15184 (2012).
24. J. Park et al., "CuInSe/ZnS core/shell NIR quantum dots for biomedical imaging," *Small* **7**(22), 3148–3152 (2011).
25. L. De Trizio et al., "Strongly fluorescent quaternary CuIn–Zn–S nanocrystals prepared from $Cu_{1-x}InS_2$ nanocrystals by partial cation exchange," *Chem. Mater.* **24**(12), 2400–2406 (2012).
26. J. A. Kloepfer, S. E. Bradforth, and J. L. Nadeau, "Photophysical properties of biologically compatible CdSe quantum dot structures," *J. Phys. Chem. B* **109**(20), 9996–10003 (2005).
27. A. Derfus, W. Chan, and S. Bhatia, "Intracellular delivery of quantum dots for live cell labeling and organelle tracking," *Adv. Mater.* **16**(12), 961–966 (2004).
28. E. Muro et al., "Comparing intracellular stability and targeting of sulfobetaine quantum dots with other surface chemistries in live cells," *Small* **8**(7), 1029–1037 (2012).
29. M. Helle et al., "Visualisation of sentinel lymph node with indium-based near infrared emitting quantum dots in a murine metastatic breast cancer model," *PLoS One* **7**(8), e44433 (2012).

Sophie Bouccara is currently a PhD student at the Laboratoire de Physique et d'Étude des Matériaux. She received her MSc in optics for biomedical applications from the Université Pierre et Marie Curie in 2011. Her research focuses on the combination of the synthesis of near-infrared fluorescent biological probes with time resolved widefield microscopy in order to follow metastatic cells migration *in vivo*.

Alexandra Fragola is an assistant professor at Pierre et Marie Curie University, where she obtained a PhD in 2003 under the supervision of Claude Boccara and Lionel Aigouy in near-field microscopy. At the Laboratoire de Physique et d'Étude des Matériaux, she is currently developing super-resolution fluorescence microscopes for live cell and *in vivo* imaging, using time-gated detection, structured illumination techniques, and adaptive optics.

Emerson Giovanelli is currently a teaching assistant in the quantum dot group of the Laboratoire de Physique et d'Etude des Matériaux at ESPCI ParisTech. He graduated from the French Grande Ecole Chimie ParisTech, together with a MSc in organic chemistry from University of Paris VI (2003), and received his PhD from University of Paris XI (2008). His research focuses on quantum dots' surface chemistry and functionalization for water solubilization and *in vivo* applications.

Gary Sitbon is currently a PhD student at the Physics and Materials Study Laboratory, Paris. He received his Msc in nanomaterials science from Pierre and Marie Curie University, Paris, in 2011. His current research focuses on the synthesis of magnetic and fluorescent nanocrystals for biomedical applications in order to guide the surgical intervention.

Nicolas Lequeux is a professor of solid chemistry at the Ecole Supérieure de Chimie et Physique Industrielles of Paris. He received a PhD degree from University Paris-Sud (1990) and has been at ESPCI since 1991. His research focuses on chemistry of materials (ceramics and cements) and more recently on inorganic nanoparticle synthesis and functionnalization.

Thomas Pons is a research scientist at the Laboratoire de Physique et d'Étude des Matériaux. He received his PhD in 2004 from Université Pierre et Marie Curie under the supervision of Jerome Mertz. After a postdoctoral fellowship at the Naval Research Laboratory under the direction of Hedi Mattoussi, he joined the LPEM where he is currently developing multifunctional quantum dot and nanoparticle probes for biological applications, including cellular and *in vivo* imaging.

Vincent Loriette is a research scientist at the Laboratoire de Physique et d'Étude des Matériaux. He received his PhD in astrophysics in 1995 from Université Denis Diderot under the supervision of Claude Boccara. Until 2007, he was developing the optical metrology instruments for the Virgo project (gravitational wave detector). He is currently developing fluorescence microscopes with the extended spatial resolution or wide field optical sectioning properties.

Nanoscale

PAPER

View Article Online
View Journal | View Issue

Multimodal Mn-doped I–III–VI quantum dots for near infrared fluorescence and magnetic resonance imaging: from synthesis to *in vivo* application†

Cite this: *Nanoscale*, 2014, **6**, 9264

Gary Sitbon,[abc] Sophie Bouccara,[abc] Mariana Tasso,[abc] Aurélie Francois,[d] Lina Bezdetnaya,[d] Frédéric Marchal,[d] Marine Beaumont[e] and Thomas Pons*[abc]

Received 25th April 2014
Accepted 14th June 2014

DOI: 10.1039/c4nr02239d

www.rsc.org/nanoscale

The development of sensitive multimodal contrast agents is a key issue to provide better global, multi-scale images for diagnostic or therapeutic purposes. Here we present the synthesis of Zn–Cu–In–(S, Se)/$Zn_{1-x}Mn_xS$ core–shell quantum dots (QDs) that can be used as markers for both near-infrared fluorescence imaging and magnetic resonance imaging (MRI). We first present the synthesis of Zn–Cu–In–(S, Se) cores coated with a thick ZnS shell doped with various proportions of Mn. Their emission wavelengths can be tuned over the NIR optical window suitable for deep tissue imaging. The incorporation of manganese ions (up to a few thousand ions per QD) confers them a paramagnetic character, as demonstrated by structural analysis and electron paramagnetic resonance spectroscopy. These QDs maintain their optical properties after transfer to water using ligand exchange. They exhibit T1-relaxivities up to 1400 mM^{-1} [QD] s^{-1} at 7 T and 300 K. We finally show that these QDs are suitable multimodal *in vivo* probes and demonstrate MRI and NIR fluorescence detection of regional lymph nodes in mice.

Introduction

Noninvasive molecular imaging is being increasingly used both as a scientific tool to study biological processes in living organisms and as a diagnostic tool to provide clinicians with an otherwise inaccessible image of a specific marker distribution.[1–3] Each imaging modality presents complementary advantages in terms of sensitivity, spatial resolution, imaging depth and ease of use.[4,5]

Near infrared fluorescence imaging (NIRFI), in particular, is attracting increasing attention due to its high sensitivity, low cost, non-invasiveness and easy implementation. It is however limited to near surface tissues, since its imaging depth does not exceed a few centimeters. Its spatial resolution varies from the micrometer scale using microscopy on cell samples to centimeters in thick tissues, due to light diffusion. Magnetic resonance imaging (MRI), on the other hand, provides whole body images with a homogeneous millimeter-resolution, albeit with a lower sensitivity. Nanotechnology offers the potential to design probes that offer contrast in both imaging modalities and combine the best of each, therefore providing a more comprehensive picture of the biological markers of interest. In particular, fluorescent semiconductor quantum dots (QDs) represent an attractive platform to integrate different contrast agents.

During the past decade, visible emitting QDs have increasingly been used for cellular imaging due to their unique optical properties such as their high brightness, photo-stability and multiplexing capabilities. They have for example enabled long term tracking of single molecules or simultaneous labeling of many different biomolecular targets.[6,7] QDs are also being increasingly used for *in vivo* imaging to improve detection sensitivities.[8,9] For *in vivo* applications, however, QDs should emit in the NIR range, typically between 700 nm and 1000 nm, in order to minimize light absorption and diffusion and therefore maximize imaging depth.[10] While no signs of acute toxicity have been observed after the injection of large doses of Cd-based QDs,[11] safer, heavy-metal free QDs have been developed in order to minimize toxicity. Recently developed silicon-based QDs,[12,13] as well as QDs based on I–III–VI_2 materials such as $CuInS_2$ or $CuInSe_2$ (ref. 14–17) provide attractive fluorescent probes for biomedical applications due to their low toxicity and high detection sensitivities.

[a]*LPEM, PSL Research University, ESPCI-ParisTech, 10 rue Vauquelin, F-75231, Paris Cedex 5, France. E-mail: thomas.pons@espci.fr*
[b]*CNRS, UMR 8213, F-75005, Paris, France*
[c]*Sorbonne Universités, UPMC Univ Paris 06, F-75005, Paris, France*
[d]*Centre de Recherche en Automatique de Nancy (CRAN), ICL, Université de Lorraine, UMR 7039, Campus Sciences, BP 70239, 54506 Vandoeuvre-lès-Nancy Cedex, France*
[e]*CIC-IT de Nancy, CHU de Nancy, Hôpitaux de Brabois, rue du Morvan, 54511, Vandoeuvre-lès-Nancy, France*

† Electronic supplementary information (ESI) available: Determination of Mn content; magnetization measurements; additional TEM and spectroscopic data; additional NIR fluorescence image; MTT assay results. See DOI: 10.1039/c4nr02239d

Several strategies have been used to bring together fluorescence and MR contrast into one nanoprobe using I–III–VI QDs. For example, Hsu *et al.* incorporated $CuInS_2$/ZnS QDs and superparamagnetic iron oxide nanoparticles in silica beads.[18] However, the resulting size is much larger than the original nanoparticles, which may hinder access to confined spaces. In order to obtain more compact nanoprobes, Cheng *et al.* have encapsulated $CuInS_2$/ZnS QDs in an amphiphilic polymer, to which they coupled Gd^{3+}-chelates.[19] In addition to the relatively low number of Gd conjugated per QD, leading to a small relaxivity per QD, this strategy may suffer from the weak non-covalent link between the QD and the paramagnetic ion. Indeed, the QD organic surface chemistry may easily detach with time from the QD surface due to its interaction with the complex *in vivo* environment, as has been shown for example for micelle encapsulated QDs.[20] Even relatively strong dithiol-containing ligands have been shown to exhibit a fast desorption rate from the QD surface, on the order of 1 h^{-1}.[21] The dissociation between the fluorescent QDs and the magnetic species linked to the surface ligands therefore represents a strong limitation to the use of this type of multimodal probe for *in vivo* imaging.

We have therefore chosen to directly incorporate the paramagnetic ion into the QD inorganic shell to ensure that at all times the fluorescent and magnetic species remain colocalized. Doping of QDs with Mn^{2+} ions has been reported earlier in II–VI QDs.[22] Wang *et al.* demonstrated the use of Mn-doped CdSe/ZnS QDs for *in vitro* fluorescence and MR imaging of macrophages.[23] More recently, several groups reported the synthesis of Mn-doped $CuInS_2$ or $AgInS_2$ QDs.[24–26] However, none of these QDs emit in the NIR. In addition, they were only able to incorporate a small number of Mn per QD, leading to a low MR sensitivity. These two limitations precluded their use for *in vivo* imaging. Here we report the synthesis and characterization of Zn–Cu–In–(S, Se)/$Zn_{1-x}Mn_xS$ QDs designed for *in vivo* imaging: the emission of these QDs is tunable in the NIR range for optimal fluorescence imaging and they contain up to 3000 Mn atoms. This very high Mn loading leads to relaxivities in the μM $(QD)^{-1}$ s^{-1} range and allows QD-based multimodal *in vivo* imaging. As an illustration, we demonstrate *in vivo* MRI and fluorescence detection of regional lymph nodes in mice.

Materials and Methods

Chemicals

All chemicals were purchased from Sigma-Aldrich and used as received without further purification. Zinc ethylxanthogenate ($Zn(EtX)_2$) and zinc oleate ($Zn(OA)_2$) were prepared from zinc nitrate, potassium ethylxanthogenate and sodium oleate according to previously reported methods.[16] HeLa cells were obtained from ATCC and cultured using supplemented DMEM medium (DMEM, high glucose, GlutaMAX, pyruvate, 10 vol% FBS, 1 vol% penicillin–streptomycin) from Gibco.

Synthetic procedures

Synthesis of Zn–Cu–In–S cores. In a typical synthesis of Zn–Cu–In–S cores, 1 mmol of copper(I) iodide (190 mg), 1 mmol of indium acetate (291 mg) and 0.1 mmol of zinc acetate ($Zn(OAc)_2$, 18 mg) were introduced in a three-neck flask with 5 ml of dodecanethiol (DDT) and degassed under vacuum at 40 °C for 30 min. The yellow turbid suspension was then placed under argon flow and heated to 120 °C for 10 min. The resulting clear yellow solution was subsequently further heated to 220 °C. After approximately 15 minutes, the mixture was quickly cooled to room temperature. The obtained 780 nm emitting Zn–Cu–In–S cores were then collected by precipitation with ethanol (EtOH) and washed three times by successive redispersion and precipitation in hexane–EtOH. The final precipitate was redispersed in 10 ml of hexane.

Synthesis of Zn–Cu–In–Se cores. In a typical synthesis of Zn–Cu–In–Se cores, 1 mmol of CuCl (99 mg), 1 mmol of $InCl_3$ (221 mg), 2 mmol of $Zn(OAc)_2$ (367 mg) and 2 mmol of selenourea (246 mg) were introduced in a 100 ml three-neck flask with 10 ml of trioctylphosphine and 25 ml of octadecene (ODE). After sonicating the suspension for a few minutes, we added 5 ml of DDT and 10 ml of oleylamine (OAm). The resulting pink solution is degassed for 30 minutes at 40 °C. The solution is then heated at 230 °C and turned from pink to black. After 80 minutes of heating, 800 nm emitting Zn–Cu–In–Se cores were obtained and purified as described above. The final black precipitate was redispersed in 10 ml of hexane.

Growth of a $Mn_xZn_{1-x}S$ shell. We used a dropwise injection for the growth of a $Mn_xZn_{1-x}S$ shell on Zn–Cu–In–E (E = S or Se) cores. The first solution (solution 1) was composed of 2.5 mmol of $Zn(EtX)_2$ (768 mg), 3 ml of OAm and 7 ml of ODE. It resulted in a white turbid solution. The second solution (solution 2) is prepared in a 100 ml three-neck flask. We introduced 2,5-*x* mmol de $Zn(OA)_2$, 2 ml OLA and 8 ml ODE. The solution was degassed under vacuum at 120 °C for 10 minutes. After the solution was cooled to room temperature, we introduced *x* mmol of manganese(II) acetate and the solution was then degassed again under vacuum at 120 °C for 10 minutes. The orange solution is kept under argon prior to the injection.

In a 100 ml three-neck flask, we mixed 1 ml of core QD solution prepared as mentioned above and 10 ml of ODE. The solution was degassed under vacuum at 50 °C for 40 minutes and then heated at 200 °C under argon. Solution 1 and solution 2 were then injected simultaneously in 2 hours. After cooling at room temperature, QDs were purified as described above and redispersed in 10 ml of hexane.

Water solubilization. QDs can be transferred in water by cap exchange with polyethylene glycol (PEG) modified-dihydrolipoic acids (DHLA-PEG) prepared according to a literature method with commercially available Jeffamine M-1000 polyetheramine (Huntsman).[27] A two-step surface modification was first performed to facilitate the subsequent water solubilisation. For that, 1 ml of QD solution was precipitated with ethanol and resuspended in chloroform. They were left overnight at 60 °C in the presence of 200 μl OAm. QDs were then precipitated with acetone and redispersed in chloroform. We then added 100 mg $Zn(OA)_2$ and the solution was heated to 60 °C for 2 hours. After precipitation with acetone to remove excess ligands and redispersion in chloroform, cap exchange and purification were done as reported before.[15]

Characterization

Optical characterization. Absorption spectra were performed using a UV-Visible Varian Cary-5E spectrometer. Photoluminescence excitation spectra were performed using a Horiba Jobin Yvon Fluoromax-3 spectrofluorometer. Photoluminescence spectra and fluorescence lifetime measurements were performed using an Edinburgh Instruments FSP920 spectrofluorometer. The excitation source was either an Edinburgh Instruments EPL375 laser diode with an emission wavelength at 376 nm or a xenon 450 W arc lamp. The detector used for the experiments was a Hamamatsu R2658P side window photomultiplier. Photoluminescence quantum yields (QY) were measured using zinc phthalocyanine as reference, according to a previously reported method.[15]

Structural characterization. TEM/HRTEM images were acquired using a JEOL 2010 TEM equipped with a Gatan camera. XRD powder diffraction patterns were acquired using a Philips X'Pert diffractometer with a Cu K_α source. We determined the size of crystalline domain, d, using Scherrer's law:

$$d = \frac{K\lambda}{\mathrm{FWHM}\cos\theta},$$

where K is a dimensionless shape factor (a typical value of 0.9 for spherical objects was used as a first approximation), β is the FWHM of the peak (in radians) and θ is the Bragg angle of the corresponding peak.

EPR measurements were performed using a Bruker EMX spectrometer operating at X band frequency (9.7 GHz).

Elemental analysis was performed by energy-dispersive X-ray spectroscopy (EDX) on a Hitachi S-3600N scanning electron microscope operated at 15 keV. ICP-AES analyses were performed by Repsem analytical platform in Strasbourg. Samples are prepared by dissolving dried QDs with nitric acid.

Dynamic light scattering (DLS) was carried out on a CGS-3 goniometer system equipped with HeNe laser illumination at 633 nm and an ALV/LSE-5003 correlator (Malvern). Purified QD solutions are filtered (0.2 μm) and measured at five different angles between 45° and 120°.

Zeta potentials were measured in triplicate in water using a Malvern Zetasizer.

Manganese ions leaching. Manganese leaching was measured by colorimetry using 3,3′,5,5′-tetramethylbenzidine (TMB) as described by Bosch-Serrat.[28] Purified hydrophilic quantum dots were dispersed in cell culture medium (optiMEM reduced serum, no phenol red medium, Gibco) at a concentration of 1 μM and left at 37 °C. After different incubation times, free manganese ions are separated from QDs by ultrafiltration (100 kDa cutoff), quantified using TMB absorbance at 450 nm and standard calibration solutions.

Relaxivity characterization. Spin-lattice relaxivities (r_1) were measured at 7 T and room temperature using a Bruker ASX 300 MHz NMR spectrometer. A solution containing QDs was introduced in a 200 μl Teflon sample holder and put in the spectrometer. We then used an inversion recovery protocol with various time delays, τ, between the 180°-inversion pulse and the 90°-reading pulse. The NMR signal, M, for a given time delay τ, is given by

$$M(\tau) = M_0\left(1 - \exp\left(-\frac{\tau}{T_1}\right)\right),$$

where M_0 is the NMR signal before inversion. T_1 is obtained from the above equation (see Fig. S6a in ESI†). Relaxation measurements were performed at different QD concentrations to obtain the relaxivity of each QD sample (Fig. S6b†).

Cell viability assay. To assess the cytotoxicity of our probes, we performed a colorimetric MTT assay on HeLa cells. The assay is based upon the reduction of yellow 3-(4,5-dimethylthiazol-2-yl)-2,5-diphenyltetrazolium bromide to its purple formazan by viable cells. HeLa cells were seeded on a 96-well plate at a density of 10 000 cells per well. After overnight incubation at 37 °C and 5% CO_2, culture medium was removed and cells were rinsed with phosphate buffer saline (PBS) solution. Then, 100 μl of culture medium containing QDs at various concentrations were added. These QD solutions were pre-filtered (0.2 μm) for sterilization. After 24 hours of incubation at 37 °C and 5% CO_2, medium was removed and cells were rinsed with PBS. We then added 100 μl of culture medium and 20 μl of a solution of MTT in water (5 mg ml^{-1}). After 2 hours incubation, culture medium was removed and cells were rinsed with PBS. 150 μl of a 10% vol Triton X-100 in isopropanol was added to cells. After 30 minutes incubation, absorbance at 550 nm was measured on an absorbance microplate reader. Three replicates for each condition were considered, as well as (i) a blank control with only cell medium, and (ii) a control with the highest evaluated nanoparticle concentration in cell medium. This latter control intended to assess eventual (and parasitic) MTT reagent conversion induced by QD nanoparticles.[29,30] In our assays, such an effect was not observed: the absorbance of the only-QDs control was similar to the one of the blank with only medium. Furthermore, all reported absorbance values are increments relative to the absorbance of the blank.

In vivo experiments

Animals and QD administration. All animal experiments were conducted in agreement with the Principles of Laboratory Animal Care (National Institutes of Health publication no. 86-23, revised 1985) and approved by the regional ethics committee. Female C57/BL6 mice (Janvier, Le Genest-Isle, France) were used in this study and maintained under specific pathogen-free conditions. 300 μl of a 40 μM stock solution of $CuInSe_2/Zn_{0.8}Mn_{0.2}S$ QDs was ultrafiltered and the pellet was dissolved in 60 μl of PBS. All experiments were performed under anesthetic using intraperitoneal injection of 0.01 ml g^{-1} of body weight of a solution containing 9 mg ml^{-1} of ketamine (Ketalar®, Panpharma, Fougères, France) and 0.9 mg ml^{-1} of xylazine (Rompun®, Bayer Pharma, Puteaux, France). Female C57/BL6 mice (Janvier, France) were injected subcutaneously in the distal part of the left anterior paw with 20 μl of QD solution. After product delivery, the left paw was kneaded to improve product migration. Immediately after injection, animals were placed in the MR scanner, in the same position as before QD injection.

Magnetic resonance imaging. MRI was performed on a 3T MR scanner (SIGNA HDxt, General Electric, Milwaukee, WI)

using a four channel volume coil for reception (RAPID Biomedical, Rimpar, Germany). T1-weighted images were acquired using a fast spin-echo sequence with the following parameters: TE/TR = 12/500 ms; acquisition matrix = 480 × 320; field of view = 120 mm^2 and 17 1 mm thick slices. Acquisitions were performed pre and post (20 min) QD injection.

Near-infrared fluorescence imaging. *In vivo* optical imaging of QDs was performed using a Fluobeam® (Fluoptics, Grenoble, France) NIR imaging system. A 750 nm longpass emission filter is used. The regions of interest (ROIs) were depilated using a commercial hair removal cream before imaging. The CCD camera shows the specificity to adjust the fluorescence signal on the pixel which presents the strongest fluorescence intensity. Thus, the injection point of QDs was hidden if necessary, allowing thereby a better ROI visualization. *In vivo* fluorescence of axillary lymph nodes and lateral thoracic was acquired after MRI experiments, about 1 h after QD administration.

Results and discussion

Growth of thick zinc sulfide shell on Zn–Cu–In–S cores

We first synthesized Zn–Cu–In–S core QDs using a protocol adapted from Li *et al.*[14] We added a small amount of zinc precursors to the core synthesis as this improved the core photoluminescence quantum yield (PL QY),[15] without restricting the tunability of the emission in the NIR region due to the increase of the bang gap. The Zn content was indeed typically limited to 25% compared to the Cu content, as estimated from EDS, and the Cu–In ratio was close to one. The obtained Zn–Cu–In–S cores typically emitted at 780 nm, with a FWHM of 100 nm, and a PL QY of 30%. While the size of these cores was difficult to estimate from TEM images due to low contrast, X-ray diffractograms were consistent with a core size of about 3 nm using Scherrer's law (see Materials and methods section).

Our objective was then to grow a thick ZnS shell to be able to incorporate at later stages a maximal number of paramagnetic Mn^{2+} ions in the shell. Layer by layer deposition of ZnS on quantum dots following a SILAR protocol[31] required elevated temperatures (>240 °C) to activate low reactivity precursors (zinc oleate and sulfur dissolved in octadecene). At these temperatures however, QD cores were rapidly etched, while lower temperatures resulted in an absence of growth. Previously described protocols were able to yield thin (1 nm) ZnS shell around Zn–Cu–In–S cores using dropwise injection of more reactive zinc ethylxanthate or dithiocarbamate precursors.[14,15] However the injection of additional precursors resulted in secondary nucleation of ZnS nanocrystals without increasing the shell thickness. We found that adjusting (see Materials and methods for details) the amount of oleylamine and the injection speed helped growing thicker monocrystalline shells, in the range of 2–3 nm, corresponding to about 10 ZnS monolayers, as shown in Fig. 1a by TEM (8 ± 2 nm in diameter) and XRD (7 ± 1 nm).

The resulting QDs retained their emission properties in the near infrared (Fig. 1b), with a small blue shift which could be attributed to the incorporation of Zn in the core due to cation exchange and/or Zn interdiffusion.[15,32] Photoluminescence excitation (PLE) spectrum showed a sharp rise below 350 nm, corresponding to the contribution of ZnS. This confirms the growth of a thick ZnS shell on the fluorescent QD cores. Comparison of PLE and absorption spectra indicates a limited secondary nucleation (typically less than 10%). Fluorescence decays showed a long lifetime component around 200 ns (see Fig. S1 in ESI†), which is typical for these I–III–VI QDs.[14,33]

Incorporation of manganese in the shell

To incorporate manganese in the ZnS shell, we simply replaced zinc oleate with manganese acetate in the injection solution using different ratios of Mn to Zn. To avoid oxidation of manganese, the solution was carefully degassed under vacuum before adding the manganese precursor, as was previously described by Yang *et al.*[34] We thus synthesized samples with 1, 2, 5, 10, 20 and 30% of manganese precursor in the injection of solution.

Incorporation of Mn in the ZnS shell is evidenced by X-ray diffractograms, as shown in Fig. 2. The nanocrystals retain their

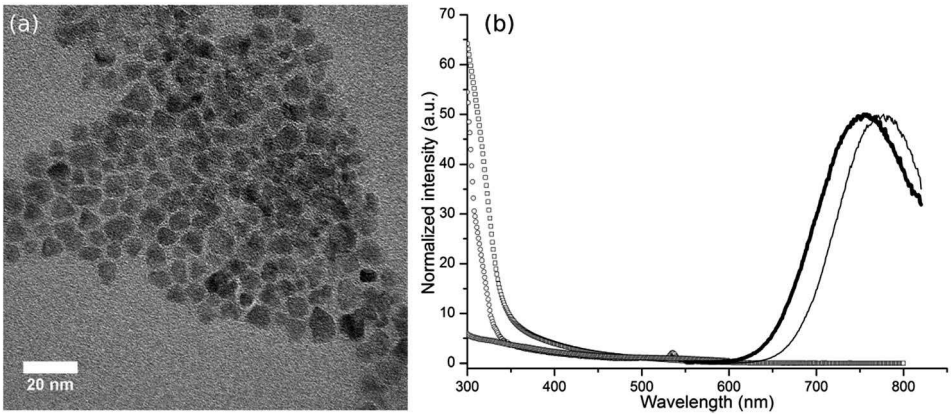

Fig. 1 (a) TEM images of Zn–Cu–In–S/ZnS core–shell QDs; (b) normalized PL spectra of Zn–Cu–In–S core (gray) and Zn–Cu–In–S/ZnS core–shell QDs (black), absorbance spectra of core (triangles) and core–shell (squares), and PLE spectrum of Zn–Cu–In–S/ZnS core–shell QDs (circles).

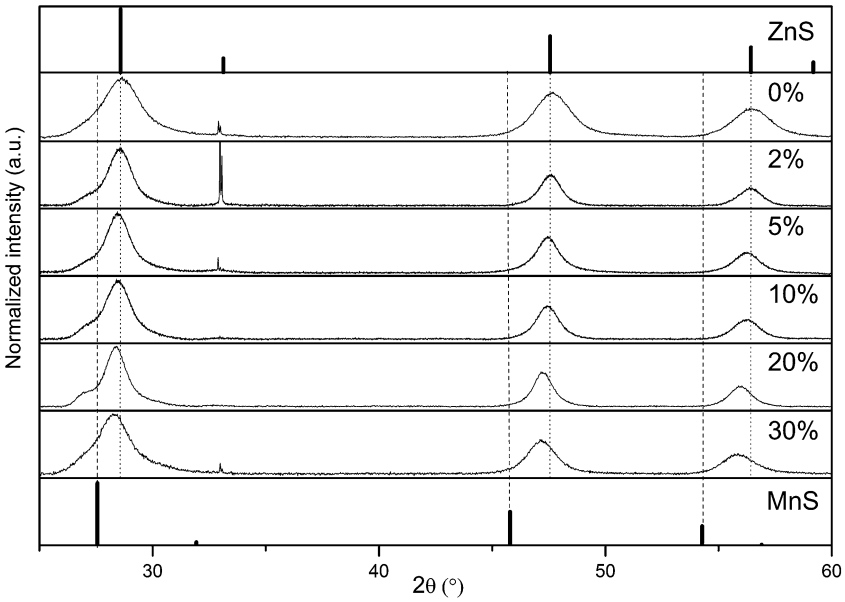

Fig. 2 XRD patterns obtained for different Mn concentrations in the injection solution. Patterns for zinc blende ZnS (JCPDS 03-065-5476) and MnS (JCPDS 03-065-2884) are indicated for reference.

sphalerite structure, with narrow diffraction peaks indicative of large monocrystalline nanoparticles. Using Scherrer's law (see Materials and methods section), the derived crystallite size is around 7 nm for all samples. The diffraction peaks deviate from pure ZnS towards MnS at smaller angles with increasing Mn content in the injection solution. The position of the XRD peaks may be used to determine the final Mn content in the nanocrystals using Vegard's law. In the range of 2% to 30% of Mn compared to the total cation content (Zn + Mn), the Mn proportion measured in the final nanocrystals using XRD closely follows the composition of the injection solution. This was confirmed by elemental analysis using EDS on nanocrystal powders, as shown in Table S1 in ESI.†

In addition, the incorporation of manganese in the ZnS shell is probed using electron paramagnetic resonance (EPR). EPR spectra for samples with different manganese contents are presented in Fig. 3. We observed a classical structure for manganese in zinc sulfide.[35] At very low Mn concentration, up to 2%, these spectra exhibit a six-line hyperfine structure, with a 71 G splitting at 9.7 GHz corresponding to Mn in ZnS.[35] This structure gradually disappears when the manganese content is increased, due to Mn–Mn interactions.[36] Magnetometry measurements at room temperature show a paramagnetic behavior for all samples (see Fig. S2 in ESI†). This, together with the above results, confirms that Mn is incorporated inside the shell and not only adsorbed at the surface of the QDs.

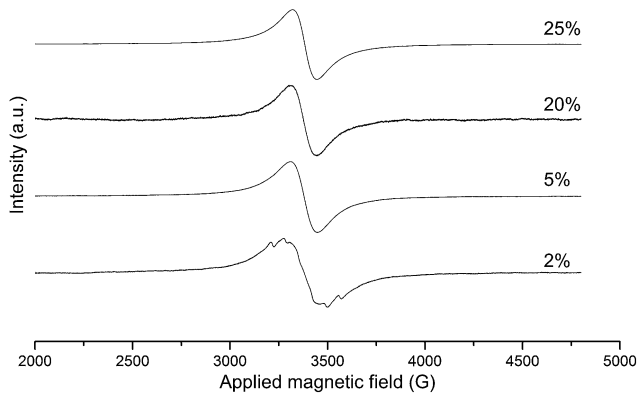

Fig. 3 EPR spectra of Zn–Cu–In–S/$Zn_{1-x}Mn_xS$ QDs obtained for various Mn contents.

Incorporation of Mn in the shell did not influence the size or the shape of the nanocrystals: TEM images (Fig. 4a) show nearly spherical nanoparticles of around 9 ± 3 nm in diameter (see Fig. S3(c) in ESI for size distribution†), corresponding to a 2–3 nm $Mn_xZn_{1-x}S$ shell thickness. Diffraction patterns observed by high resolution TEM confirm the cubic sphalerite crystalline structure of the core–shell nanocrystals (Fig. S3 in ESI†).

We investigated the influence of Mn : Zn ratio on the optical properties of Zn–Cu–In–S/$Zn_{1-x}Mn_xS$ QD. These properties remain quite similar to Zn–Cu–In–S/ZnS QDs, as shown in Fig. 4b and S4 in ESI.† Absorption and photoluminescence excitation spectra show a high absorption at small wavelength, below 350 nm, which reflects the growth of a thick ZnS shell. Similarly to Zn–Cu–In–S/ZnS QDs, the growth of the shell induces a small blue shift due to a limited incorporation of zinc in the core. No systematic additional shift was observed for different Mn content. For these QDs, the bandgap energy is lower than the $^4T_1$–$^6A_1$ ligand-field Mn transition,[37] which prescribes energy transfer from the QD bandgap to the Mn centers, so that the QDs retain their core emission properties.[38]

Relaxivity measurements

There are mainly two strategies to transfer quantum dots into water: encapsulation and ligand exchange.[39] The encapsulation

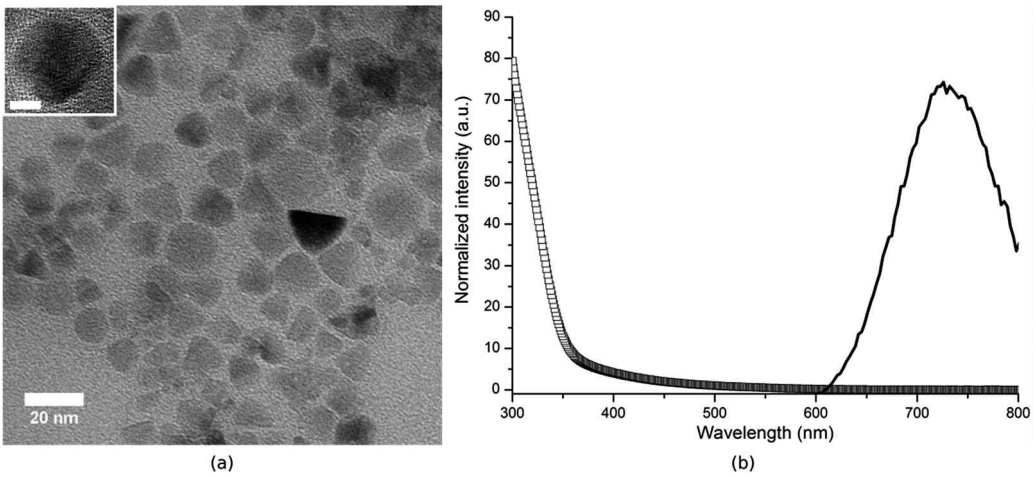

Fig. 4 (a) Typical TEM image (inset: HRTEM image, scale bar: 5 nm), (b) absorbance (squares) and PL (black) spectra of Zn–Cu–In–S–$Zn_{1-x}Mn_xS$ core–shell QDs.

process requires the use of amphiphilic molecules, whose hydrophobic part interacts with the initial hydrophobic ligands of the QD and hydrophilic part ensures water solubility and colloidal stability. This strategy possesses the advantage of an excellent preservation of the fluorescence properties, since the QD surface chemistry is kept unmodified. Their PL stability in water is also superior, as the hydrophobic layer prevents water, ions and small solutes from accessing the QD surface. However, this would potentially limit the MRI response of these probes, as water protons would not be able to reach the close proximity of the paramagnetic Mn ions located in the ZnS shell. In contrast, exchanging the original hydrophobic ligand with new hydrophilic ligands may decrease the PL quantum yields of the QDs due to suboptimal surface passivation and oxidation. However, it enhances proton access to the QD surface, which should translate into better MRI response. Since we expect that the fluorescence sensitivity achieved by our QDs will be higher than for MRI, we chose to use the latter strategy. In addition, ligand exchange generally offers more compact probes compared to encapsulation strategies. We therefore exchanged the original (xanthogenates, oleylamine and/or oleate) ligands by polyethylene glycol (PEG) modified-dihydrolipoic acids (DHLA-PEG).[27] These ligands provide colloidal stability in a wide range of buffers with a reduced non-specific biomolecule adsorption. QDs were then purified using ultrafiltration to remove excess of unbound ligands and possibly desorbed ions, as well as using centrifugation to remove small aggregates. The optical properties remained similar in water (see Fig. S5 in ESI†) and we obtained quantum yields up to 20%. The hydrodynamic radius of our QDs capped with DHLA-PEG was measured by DLS and was found to be 10.8 ± 0.7 nm (see Fig. S6 in ESI†), consistently with the size of our QDs and of the DHLA-PEG ligands. Zeta potential measurement indicated that our probes were neutral (0.5 ± 0.2 mV), as expected from PEG-coated nanoparticles.

We then measured the r_1 relaxivity of Zn–Cu–In–S–$Zn_{1-x}Mn_xS$ QDs with different manganese contents using ^1H NMR in pure water under a 7 T static magnetic field at 300 K. The relaxation rate of water protons increased linearly with the QD concentration for all samples (see Fig. S7 in ESI†). We measured the absolute concentration of manganese, indium and zinc using ICP-AES, then normalized by the Mn concentration to derive relaxivity values in mM $(Mn)^{-1}$ s^{-1}, as shown in Fig. 5. At low Mn content, we observe a strong increase in relaxivity with increasing Mn content, from about 0.01 mM $(Mn)^{-1}$ s^{-1} for QDs containing 1% Mn to 0.5 mM $(Mn)^{-1}$ s^{-1} for QDs containing 20% Mn at 7 T. This increase suggests that several Mn participate cooperatively in the relaxation dynamics of water protons diffusing near the surface of the nanoparticle: when the Mn concentration is higher, each Mn participates more efficiently to the water relaxivity. Interestingly, the optimal Mn concentration in ZnS, 20%, is above the solubility of MnS in ZnS at the synthesis temperature (7.5% for bulk materials).[40] It is unclear whether our continuous growth method actually

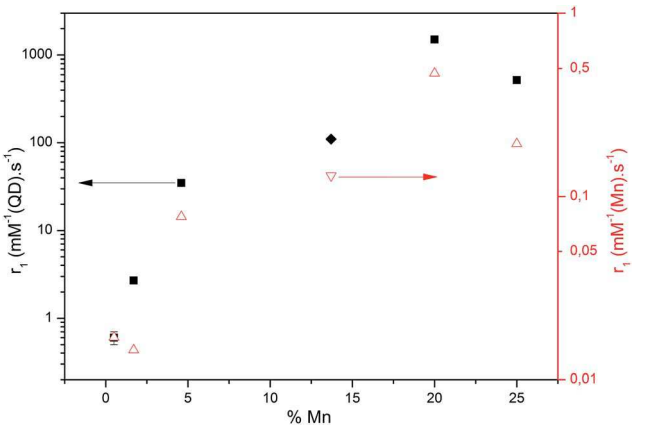

Fig. 5 Longitudinal relaxivity r_1 of Zn–Cu–In–(S, Se)/$Zn_{1-x}Mn_xS$ QDs normalized to the Mn (S: triangles; Se: inverted triangles, right axis) or QD (S: squares; Se: diamonds, left axis) concentration as a function of the Mn content in the shell.

leads to epitaxial growth of small MnS nanoclusters or if the Mn ions are dispersed homogeneously in the shell. While bulk MnS is antiferromagnetic,[41] very small MnS clusters may contain uncompensated spins at their boundaries, which could interact with nearby water protons and accelerate their relaxation. With more concentrated samples (such as $Zn_{0.75}Mn_{0.25}S$), the effective relaxivity per mmol of manganese decreases. This may be due to the increase of antiferromagnetic coupling between neighbouring manganese atoms.[42]

With respect to the application of our Mn-doped QDs to MRI, it is interesting to consider their "per QD-relaxivity" in mM $(QD)^{-1}$ s^{-1}, obtained by multiplying the per Mn-relaxivity by the number of Mn per QD, as determined by elemental analysis. This will indeed dictate the local concentration of doped QDs needed to obtain a T1 contrast in a specific tissue. Fig. 5 shows that the per-QD relaxivity first strongly increases with the doping rate, since both the per-Mn relaxivity and the number of Mn per QD increase. The optimal sample, corresponding to a $Zn_{0.8}Mn_{0.2}S$ shell, presents a r_1 value of 0.5 mM $(Mn)^{-1}$ s^{-1} and 1500 mM $(QD)^{-1}$ s^{-1} at 7 T. The per-Mn relaxivity is lower than for single ion probes such as Gd-DTPA (3.1 mM^{-1} s^{-1} at 7 T (ref. 43)) and slightly lower than previously reported Mn-doped Si QDs,[44] $Zn_{0.9}Mn_{0.1}S$ nanocrystals[45] and $CdSe/Zn_{0.94}Mn_{0.06}S$ QDs.[23] We attribute this difference to the fact that the effect of Mn ions on water protons decreases with the distance to the shell surface, so that Mn ions deeply buried in the shell do not contribute much to the overall relaxivity. On the other hand, our thick shell allows the incorporation of much more Mn ions (3000 Mn/QD for the optimal sample), leading to a maximal relaxivity of 1500 mM $(QD)^{-1}$ s^{-1} at 7 T. This high relaxivity should provide a high detection sensitivity for low density biomolecular markers.

Ideally, QDs for *in vivo* imaging should not only emit in the NIR transparency window (700–900 nm) but also be capable to efficiently absorb light in the same region, so that excitation light could efficiently penetrate the tissue and excite the probes. If we select for this purpose an excitation wavelength around 700 nm, optimal NIR QDs should emit further than the 700–750 nm range obtained for our $CuInS_2$-based probes in order to optimize their absorption cross-section at 700 nm and be able to efficiently discriminate between excitation back reflection and fluorescence emission. We therefore chose to synthesize Zn–Cu–In–Se/$Zn_{0.8}Mn_{0.2}S$ core–shell QDs, based on previously reported protocols for cores[16] and protocols similar to those used for Zn–Cu–In–S for the $Zn_{1-x}Mn_xS$ shell. This allowed us to obtain Mn-doped QDs with smaller shell thicknesses (around 1.5 nm) and manganese content (see Table S1 in ESI†), but with an 800 nm centered emission (see Fig. S8 in ESI†), which was better adapted for *in vivo* imaging. The relaxivity of Zn–Cu–In–Se/$Zn_{0.86}Mn_{0.14}S$ QDs was estimated to be 110 mM $(QD)^{-1}$ s^{-1} and 0.13 mM $(Mn)^{-1}$ s^{-1}. The relaxivity per Mn atom (Fig. 5, inverted triangle) is comparable with the ones obtained with Zn–Cu–In–S cores. Nonetheless, the per QD relaxivity (Fig. 5, diamond) is lower due to a smaller number of Mn ions incorporated in each QD (around 1000 Mn/QD) and a smaller surface of QDs.

Mn leaching and cytotoxicity

To ensure a prolonged colocalization of the MRI and fluorescence signals and limit toxicity due to Mn leaching, the paramagnetic Mn dopants must remain inside the QD nanocrystals even after prolonged exposition in a biological medium. Zn–Cu–In–Se/$Zn_{0.86}Mn_{0.14}S$ QDs were incubated in culture medium at 37 °C and the released Mn ions were quantified by colorimetry. The release of Mn ions was indeed found to be extremely slow: $(1.3 \pm 0.8)‰$ after 3 days and $(2.6 \pm 0.9)‰$ after 7 days.

We investigated the cytotoxicity of our probes with or without Mn in the shell using a common colorimetric MTT assay after a 24 h incubation (Fig. S9 in ESI†). Interestingly, the presence of manganese in the QD shell does not increase significantly the cytotoxicity of our QDs, even at millimolar concentrations of Mn. Cellular viability remains above 80% for QD concentrations up to 1 μM, which shows the low toxicity of these QD probes. In comparison, other QDs reported a much stronger toxicity with IC_{50} values around 100 nM, such as CdSe/ZnS (45 nM),[46] CdTe/ZnS (100 nM)[47] or InAs/InP/ZnS (≈100 nM).[48] This lower toxicity may be attributable to the large inert ZnS shell and to the virtual absence of released free Mn ions from the QDs at this timescale. We also note that *in vitro* toxicity results cannot be directly extrapolated to *in vivo* toxicity, since it depends on the overall biodistribution and organ specific doses.[49] For example, an absence of acute toxicity has been demonstrated after intravenous injection of relatively high doses of CdSe-based QDs.[11] Since our Cd-free QDs show lower *in vitro* toxicity, we assume that they will also present limited *in vivo* toxicity, even though a comprehensive *in vivo* study is required to fully understand the *in vivo* biological response to our nanoprobes.

In vivo imaging

As a simple proof-of-principle, we chose to demonstrate detection of regional lymph nodes in mice. This required no further functionalization for specific targeting of the QDs, since nanoparticles injected subcutaneously are partly drained through lymph vessels and captured by macrophages in the lymph nodes. In addition, lymph node detection represents a potential clinical application of such probes, as lymph node resection is a common diagnostic procedure in the treatment of breast cancer. A solution containing 4 nmol of Zn–Cu–In–Se/$Zn_{0.88}Mn_{0.12}S$ QDs emitting at 810 nm and coated with DHLA-PEG was prepared in phosphate buffer saline solution (PBS) and injected in the anterior left paw of a mouse. As previously demonstrated with other PEG-coated NIR emitting QDs, the probes migrated very rapidly to the regional lymph nodes.[15] Using MRI, a strong signal enhancement was clearly visible on T1-weighted images, acquired 20 min after QD injection (Fig. 6), compared to pre-injection images. Near infrared fluorescence images acquired a few minutes later (Fig. 6c) clearly show the two regional lymph nodes previously detected in MRI. Here, the injection point was hidden to increase the contrast. However, the nodes were also visible without hiding it, as shown in Fig. S10 in ESI.† These results demonstrate the good

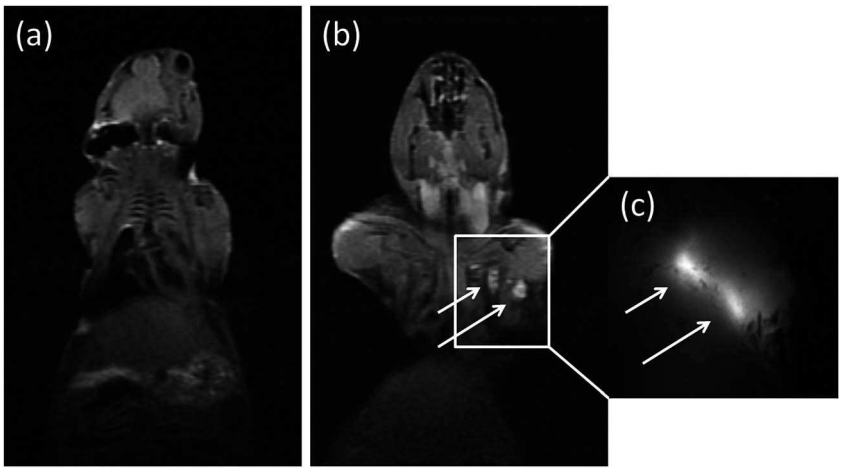

Fig. 6 T1-weighted MRI images of a mouse before (a) and after (b) injection of a solution of Zn–Cu–In–Se/$Zn_{0.9}Mn_{0.1}S$ QDs and the corresponding NIRF image (c).

colocalization of MR and NIRF contrast in the regional lymph nodes due to the uptake of the Mn-doped QDs.

Conclusion

In this work, we have described the synthesis of core–shell Zn–Cu–In–(S, Se)/$Zn_{1-x}Mn_xS$ bimodal probes for both near infrared fluorescence imaging and MRI, based on low-toxicity materials. By varying the size and composition of the cores, we were able to tune the emission wavelength of these QDs throughout the "therapeutic window", the spectral range corresponding to minimum absorption and diffusion of blood and tissues. The growth of a thick shell of $Zn_{1-x}Mn_xS$ on fluorescent cores not only preserves their fluorescence in water but also confers a paramagnetic character to our probes. Optimization of the nanoparticle size and Mn content leads to r_1 relaxivities in water ranging from 1 to 1500 mM $(QD)^{-1}$ s^{-1}, allowing sensitive MR and NIRFI detection. Finally, we have demonstrated the use of these probes *in vivo* for imaging the regional lymph nodes in mice in both NIRFI and MRI. These probes represent promising tools for *in vivo* biological and biomedical imaging due to their high sensitivities and to the well-developed toolbox available for QD functionalization. Further biodistribution and toxicity studies will be required before translating these probes to the medical field.

Acknowledgements

The authors would like to thank X. Xu for help with TEM, G. Lang for EPR, B. Bresson for NMR and B. Leridon for SQUID. Part of this work was supported by a SESAME grant from Région Ile-de-France and by the Investissement d'avenir project NanoCTC from the Ministère de l'enseignement supérieur et de la recherche (France).

References

1 R. J. Gillies, *J. Cell. Biochem.*, 2002, **87**, 231–238.
2 T. F. Massoud and S. S. Gambhir, *Genes Dev.*, 2003, **17**, 545–580.
3 R. Weissleder and M. J. Pittet, *Nature*, 2008, **452**, 580–589.
4 J. Cheon and J.-H. Lee, *Acc. Chem. Res.*, 2008, **41**, 1630–1640.
5 E. T. Ahrens and J. W. M. Bulte, *Nat. Rev. Immunol.*, 2013, **13**, 755–763.
6 X. Michalet, F. F. Pinaud, L. A. Bentolila, J. M. Tsay, S. Doose, J. J. Li, G. Sundaresan, A. M. Wu, S. S. Gambhir and S. Weiss, *Science*, 2005, **307**, 538–544.
7 H. Mattoussi, G. Palui and H. Bin Na, *Adv. Drug Delivery Rev.*, 2012, **64**, 138–166.
8 S. Kim, Y. T. Lim, E. G. Soltesz, A. M. De Grand, J. Lee, A. Nakayama, J. A. Parker, T. Mihaljevic, R. G. Laurence, D. M. Dor, L. H. Cohn, M. G. Bawendi and J. V. Frangioni, *Nat. Biotechnol.*, 2004, **22**, 93–97.
9 E. Cassette, M. Helle, L. Bezdetnaya, F. Marchal, B. Dubertret and T. Pons, *Adv. Drug Delivery Rev.*, 2013, **65**, 719–731.
10 J. Mobley and T. Vo-Dinh, in *Biomedical Photonics Handbook*, ed. T. Vo-Dinh, CRC Press, Boca Raton, FL, 2003.
11 L. Ye, K. Yong, L. Liu, I. Roy, R. Hu, J. Zhu, H. Cai, W. Law, J. Liu, K. Wang, J. Liu, Y. Liu, Y. Hu, X. Zhang, M. T. Swihart and P. N. Prasad, *Nat. Nanotechnol.*, 2012, **7**, 453–458.
12 X. Li, Y. He, S. S. Talukdar and M. T. Swihart, *Langmuir*, 2003, **19**, 8490–8496.
13 F. Erogbogbo, K. Yong, I. Roy, R. Hu, W. Law, W. Zhao, H. Ding, F. Wu, R. Kumar, M. T. Swihart and P. N. Prasad, *ACS Nano*, 2011, **5**, 413–423.
14 L. Li, T. J. Daou, I. Texier, T. T. Kim Chi, N. Q. Liem and P. Reiss, *Chem. Mater.*, 2009, **21**, 2422–2429.
15 T. Pons, E. Pic, N. Lequeux, E. Cassette, L. Bezdetnaya, F. Guillemin, F. Marchal and B. Dubertret, *ACS Nano*, 2010, **4**, 2531–2538.
16 E. Cassette, T. Pons, C. Bouet, M. Helle, L. Bezdetnaya, F. Marchal and B. Dubertret, *Chem. Mater.*, 2010, **22**, 6117–6124.
17 K.-T. Yong, I. Roy, R. Hu, H. Ding, H. Cai, J. Zhu, X. Zhang, E. J. Bergey and P. N. Prasad, *Integr. Biol.*, 2010, **2**, 121–129.

18 J.-C. Hsu, C.-C. Huang, K.-L. Ou, N. Lu, F.-D. Mai, J.-K. Chen and J.-Y. Chang, *J. Mater. Chem.*, 2011, **21**, 19257.
19 C. Cheng, K. Ou, W. Huang, J. Chen, J. Chang and C. Yang, *ACS Appl. Mater. Interfaces*, 2013, **5**, 4389–4400.
20 F. Ducongé, T. Pons, C. Pestourie, L. Hérin, B. Thézé, K. Gombert, B. Mahler, F. Hinnen, B. Kühnast, F. Dollé, B. Dubertret and B. Tavitian, *Bioconjugate Chem.*, 2008, **19**, 1921–1926.
21 E. Giovanelli, E. Muro, G. Sitbon, M. Hanafi, T. Pons, B. Dubertret and N. Lequeux, *Langmuir*, 2012, **28**, 15177–15184.
22 R. Bhargava, D. Gallagher, X. Hong and A. Nurmikko, *Phys. Rev. Lett.*, 1994, **72**, 416–419.
23 S. Wang, B. R. Jarrett, S. M. Kauzlarich and A. Y. Louie, *J. Am. Chem. Soc.*, 2007, **129**, 3848–3856.
24 G. Manna, S. Jana, R. Bose and N. Pradhan, *J. Phys. Chem. Lett.*, 2012, **3**, 2528–2534.
25 Q. Liu, R. Deng, X. Ji and D. Pan, *Nanotechnology*, 2012, **23**, 255706.
26 B. Lin, X. Yao, Y. Zhu, J. Shen, X. Yang, H. Jiang and X. Zhang, *New J. Chem.*, 2013, **37**, 3076–3083.
27 B. C. Mei, K. Susumu, I. L. Medintz, J. B. Delehanty, T. J. Mountziaris and H. Mattoussi, *J. Mater. Chem.*, 2008, **18**, 4949.
28 F. B. Serrat, *Mikrochim. Acta*, 1998, **129**, 77–80.
29 N. A. Monteiro-Riviere, A. O. Inman and L. W. Zhang, *Toxicol. Appl. Pharmacol.*, 2009, **234**, 222–235.
30 S. Wang, H. Yu and J. K. Wickliffe, *Toxicol. In Vitro*, 2011, **25**, 2147–2151.
31 J. J. Li, Y. A. Wang, W. Guo, J. C. Keay, T. D. Mishima, M. B. Johnson and X. Peng, *J. Am. Chem. Soc.*, 2003, **125**, 12567–12575.
32 J. Park and S.-W. Kim, *J. Mater. Chem.*, 2011, **21**, 3745–3750.
33 T. K. C. Tran, Q. P. Le, Q. L. Nguyen, L. Li and P. Reiss, *Adv. Nat. Sci.: Nanosci. Nanotechnol.*, 2010, **1**, 025007.
34 Y. Yang, O. Chen, A. Angerhofer and Y. C. Cao, *J. Am. Chem. Soc.*, 2008, **130**, 15649–15661.
35 T. Kennedy, E. Glaser, P. Klein and R. Bhargava, *Phys. Rev. B: Condens. Matter Mater. Phys.*, 1995, **52**, R14356–R14359.
36 Y. Ishikawa, *J. Phys. Soc. Jpn.*, 1966, **21**, 1473–1481.
37 D. Langer and H. Richter, *Phys. Rev.*, 1966, **146**, 554–557.
38 R. Beaulac, P. I. Archer, X. Liu, S. Lee, G. M. Salley, M. Dobrowolska, J. K. Furdyna and D. R. Gamelin, *Nano Lett.*, 2008, **8**, 1197–1201.
39 S. B. Brichkin and E. V. Chernykh, *High Energy Chem.*, 2011, **45**, 1–12.
40 C. Sombuthawee, S. B. Bonsall and F. A. Hummel, *J. Solid State Chem.*, 1978, **25**, 391–399.
41 L. Corliss, N. Elliott and J. Hastings, *Phys. Rev.*, 1956, **104**, 924–928.
42 S. H. Koenig and R. D. Brown, *Prog. Nucl. Magn. Reson. Spectrosc.*, 1990, **22**, 487–567.
43 C. Kalavagunta, S. Michaeli and G. J. Metzger, *Contrast Media Mol. Imaging*, 2014, **9**, 169–176.
44 C. Tu, X. Ma, P. Pantazis, S. M. Kauzlarich and A. Y. Louie, *J. Am. Chem. Soc.*, 2010, **132**, 2016–2023.
45 M. Gaceur, M. Giraud, M. Hemadi, S. Nowak, N. Menguy, J. P. Quisefit, K. David, T. Jahanbin, S. Benderbous, M. Boissière and S. Ammar, *J. Nanopart. Res.*, 2012, **14**, 932–938.
46 S. Deka, A. Quarta, M. G. Lupo, A. Falqui, S. Boninelli, C. Giannini, G. Morello, M. De Giorgi, G. Lanzani, C. Spinella, R. Cingolani, T. Pellegrino and L. Manna, *J. Am. Chem. Soc.*, 2009, **131**, 2948–2958.
47 Y. Su, Y. He, H. Lu, L. Sai, Q. Li, W. Li, L. Wang, P. Shen, Q. Huang and C. Fan, *Biomaterials*, 2009, **30**, 19–25.
48 R. Xie, K. Chen, X. Chen and X. Peng, *Nano Res.*, 2008, **1**, 457–464.
49 K. M. Tsoi, Q. Dai, B. A. Alman and W. C. W. Chan, *Acc. Chem. Res.*, 2013, **46**, 662–671.

Résumé

Le suivi de cellules *in vivo* est essentiel afin de déterminer par exemple les voies de migration de cellules tumorales circulantes ou encore pour suivre l'activité de cellules immunitaires. La microscopie de fluorescence assure une bonne résolution ainsi qu'une grande sensibilité et semble adaptée à la détection de cellules uniques *in vivo* dans un modèle de souris. Néanmoins, sa sensibilité est limitée par deux principaux facteurs: le signal d'autofluorescence des tissus d'une part, et l'absorption et la diffusion de la lumière visible dans les tissus d'autre part.

Nous présentons la synthèse et la caractérisation optique des quantum dots Zn-Cu-In-Se/ZnS composés de matériaux peu toxiques. Ces nanoparticules possèdent un maximum d'émission centré autour de 800 nm, où l'absorption et la diffusion par les tissus biologiques sont limitées. Elles sont rendues biocompatibles grâce à une chimie de surface développée au laboratoire qui permet d'obtenir des sondes petites, brillantes et stables en milieu intracellulaire pendant plusieurs jours.

Grâce à leur temps de vie fluorescence beaucoup plus long (150 ns) que celui de l' autofluorescence des tissus ($<$ 5ns), nous avons développé un microscope de fluorescence résolu en temps qui permet de sélectionner le signal d'une cellule isolée marquée par des quantum dots et rejeter l'autofluorescence du tissu environnant. Nous présentons également les premières images *in vivo* de veines marquées avec ces sondes et observées avec notre microscope.

Abstract

In vivo cell tracking is a promising tool to improve our understanding of certain biological processes (circulating tumour cells migration, immune cells activity). Fluorescence microscopy ensures a high resolution and a good sensitivity. The latter is however limited by the high tissue autofluorescence and poor visible light penetration depth.

We present the synthesis and characterization of Zn-Cu-In-Se / ZnS (core/shell) QDs made of low toxicity materials. These QDs exhibit a bright emission centred around 800 nm, where absorption and scattering of tissues are minimal. These nanocrystals are coated with a new surface chemistry, which yields small and bright probes in the cell cytoplasm for several days after labelling.

These QDs also present a fluorescence lifetime much longer (150 ns) than the tissue autofluorescence ($<$ 5 ns). By combining a pulsed excitation source to a time-gated fluorescence imaging system, we show that we can efficiently discriminate the intracellular QDs signal from autofluorescence in an *ex vivo* sample and thus increase the detection sensitivity of labelled cells into tissues. We also report preliminary results obtained in an *in vivo* sample.